Politecnico di Torino

ScuDo
Scuola di Dottorato ~ Doctoral School
WHAT YOU ARE, TAKES YOU FAR

Doctoral Dissertation
Doctoral Program in Energy Engineering (35^{th} cycle)

Development and experimental validation of a novel CFD approach for the simulation of high-pressure accidental gas releases

By

Alberto Moscatello

******

Supervisor(s):
Prof. Andrea Carpignano

Doctoral Examination Committee:
Prof. Valentina Busini, Politecnico di Milano
Prof. Gabriele Landucci, Università di Pisa
Dr. Massimo Marro, École Centrale de Lyon
Prof. Nicola Pedroni, Politecnico di Torino
Prof. Pietro Salizzoni, École Centrale de Lyon

Politecnico di Torino
18 May, 2023

Declaration

I hereby declare that, the contents and organization of this dissertation constitute my own original work and does not compromise in any way the rights of third parties, including those relating to the security of personal data.

Alberto Moscatello
18 May, 2023

* This dissertation is presented in partial fulfillment of the requirements for **Ph.D. degree** in the Graduate School of Politecnico di Torino (ScuDo).

It is better to fail in originality,
than to succeed in imitation.

(Herman Melville)

Acknowledgements

I would like to acknowledge and give my sincere thanks to my supervisor prof. Andrea Carpignano for guiding me on this journey, and for what he gave me in terms of professional and personal growth.

I wish to thank the SEADOG people, since without their collaboration this work would not have been possible. Thanks to Raffaella Gerboni and Anna Chiara Uggenti for the support they gave me during all the research activities, and thanks to Gianmario Ledda for all the moments shared in the SEADOG laboratory facing CFD convergence issues and for being such a good friend. I wish to thank also prof. Gaetano Iuso, Dr. Domenic D'Ambrosio and Dr. Gioacchino Cafiero from the Department of Mechanical and Aerospace Engineering and prof. Nicola Pedroni from the Energy Department for the technical support, useful discussions and collaborations we had during these years. I wish to thank also the reviewers of the thesis for their suggestions, which have certainly improved the quality of the final product.

I also wish to thank all the guys with whom I shared the office for all the *funny jokes* we had every day. In particular, thanks to Nicolò Abrate, for the fruitful collaboration we had during these years, and to Giuseppe Francesco Nallo (GFN10) for the useful technical suggestions on CFD topics (well repaid by my technical support on the football pitch) and the moral support on *PhD-life issues*.

Thanks to all the fellows, researchers and professors of the Energy Department who shared part of their time with me.

Thanks to my parents Ada and Donato, my brother Dario and my sister Fiorella for their immeasurable support, that I constantly feel despite my natural inclination to face things by myself. Thanks to *nonna* Cesaria for being a living example of resilience.

Finally, a *special* thank to Paola. Thank you for having supported me in all the difficult times I have faced during these years and thank you for inspiring me every day with your positive attitude.

Grazie,
Alberto

Abstract

Current regulations impose strict constraints on the safety of risk-relevant facilities as process plants involving flammable and/or toxic substances, Oil & Gas plants and nuclear plants. For all the aforementioned cases, a Quantitative Risk Assessment (QRA) or Probabilistic Risk Assessment (PRA) is mandatory to demonstrate the achievement of the required safety level. One of the main steps of the QRA/PRA is the consequences assessment of the critical accidental scenarios coming from the preliminary hazard's identification analysis. The simulation of these major hazards events is required to estimate the associated consequences effects. The state-of-practice for the consequences analysis relies on the use of integral models or empirical models based on massive measurements and few theoretical principles. The real geometry is neglected, and the physical phenomenon is roughly approximated, permitting the simulations of a huge number of accidental scenarios in a short time and with a low computational effort. Due to the extremely simplified assumptions, these models tend to highly overestimate the damage areas, especially when the complexity of the geometry plays a key role in the development of a hazardous scenario (e.g., influencing a gas cloud dispersion), leading to an oversizing of the structures and the safety barriers with a consequent money and resource waste. This is the case of offshore Oil & Gas platforms, where a reduced amount of space is available for the equipment, and nuclear plants since most of the equipment is confined in the containment building for safety reasons. More accurate approaches, like computational fluid dynamics (CFD) ones, can be employed to accurately predict the accident evolution, but they still have too high computational cost. For this reason, they are used only for the verification of few critical scenarios, whereas they cannot provide timely results to drive the plant design.

The present work proposes a CFD approach able to guarantee a suitable accuracy-computational cost trade-off, investigating the feasibility of an effective CFD-QRA integration. The model, developed in ANSYS Fluent, is targeted for the simulation

of high-pressure gas releases in large, congested geometries. These scenarios lead to the formation of underexpanded jets, that are likely to impinge part of the equipment near the leak point, hence it is crucial to consider the gas-geometry interactions also within the first centimeters. In literature, several CFD-based methodologies are available to model such scenarios, but most of the works propose the use of empirical correlations to account for the initial jet expansion, thus neglecting possible impingements in the nearfield zone of the jet.

The basic idea of the model here proposed, is the splitting of the accidental scenario in *two-steps*: the supersonic compressible jet near the leak source, defined here as the *release*, and the incompressible subsonic *dispersion* in the plant. The first part is simulated in a small domain, the Source Box (SB), sized according to the criterion of assuring negligible compressibility effects at its outlet boundaries. Its results are then used as gas source boundary conditions for the second part, the gas dispersion simulation in the plant geometry. The approach is called Source Box Accident Model (SBAM) and allows to simplify the overall simulation process, since the complexity of the initial underexpanded jet (1^{st} step) can be addressed separately, in an *ad hoc* domain. Furthermore, the possibility to get the SB results in few seconds, realizing a Reduced Order Model (ROM) reproducing its behavior, was investigated at a preliminary stage giving promising results. As a consequence, a strong computational cost saving is expected, since the dispersion simulation (2^{nd} step) is largely faster and easier than the SB one as discussed in the results.

Once the SBAM main features, applicability range and novelties are introduced, a *numerical benchmark* analysis and the model *experimental validation* are presented. For these purposes, SBAM is applied to several case studies involving the accidental high-pressure methane release on an offshore platform.

The benchmark CFD simulation is based on the state-of-the-art practices for ANSYS Fluent, and does not imply the splitting of the phenomenon, indeed, both the release and the dispersion are modelled in the plant geometry. Comparing this last simulation with SBAM on the same case study, results show a good agreement as small relative errors are obtained on several risk-oriented parameters, e.g. the flammable volume. The comparison involves also the implementation features and simulation time, hinting that the splitting of the phenomenon can represent a strong advantage in terms of computational effort and simulation implementation.

The experimental validation concerns the reproduction of several high-pressure methane releases on a platform under wind condition. The SEASTAR WT, an open cycle subsonic wind tunnel, was employed to reproduce the wind field. A 1/10 scaled platform mockup, equipped with gas sensors, was realized to represent the real environment. Several case studies, obtained changing the wind direction, the release pressure and the release position and direction, are considered. To assure the fluid dynamic similarity between the real scale and the model scale, a *scaling procedure* tailored on gaseous critical flows under wind conditions was developed. This methodology is based on the preservation of a dimensionless parameter, the dimensionless discharge momentum flux, which includes the wind velocity and the gas release parameters. Predicted and observed values of concentrations at sensors locations are at first directly compared to analyze the qualitative gas distribution in the domain. Secondly, a more robust methodology for gas dispersion models validation is employed to verify the SBAM performance. This last approach uses some statistical parameters to account for random and systematic errors and to quantify the correlation between the two sets of data. From the analysis of the results, it can be deduced that the model predictions are in good agreement with the measured values, hinting similar gas distributions with a slight overestimation tendency. Basing on the statistical parameters criteria, a preliminary validation of SBAM is achieved, since its predictions result acceptable in most of the test cases.

To conclude, the main outcomes of this study are presented. The work offers a new perspective on the accident simulation methodologies related to the QRA for congested layout plants, proposing a CFD approach to accurate model high-pressure gas impinging jets without a prohibitive computational effort. Furthermore, to overcome the lack of suitable methodologies for the realization of scaled experiments involving critical gaseous flows under wind conditions, a novel scaling approach is presented. This procedure allows to relate the scaling of fluid dynamic parameters, the wind velocity and the gas release pressure, to the geometry scaling factor. Finally, a relevant contribution was given to the wind tunnel calibration as well as to the gas sensing system optimization, and useful insights on the realization of high-pressure gas releases experiments under wind conditions are provided.

Contents

List of Figures

List of Tables

Chapter 1

Introduction

1.1 Safety and Industry

1.1.1 Risk analysis

Technological developments of the last decades led to increasingly complex systems designs. The energy production and process industry sectors have seen a dramatic increment in the complexity of the plant design as well as of the transportation and storage systems. Larger quantities of energy and process substances are increasingly involved in these sectors, therefore, the possibility the provoke accidents must be carefully considered. Moreover, analyzing the more promising novel technological solutions related to climate change challenges, another aspect arises. For example, CO_2 capture and storage systems, involve its injection in exhausted oil/gas reservoirs at high pressure (80 bar) [1]. Large scale renewable energy production claims for sustainable storage systems solutions, as high pressure H_2 tanks (350 or 700 bar) [2, 3], as well as low emissions fuel cell vehicles need small scale high pressure H_2 storage systems [3]. Moreover, one of the more promising futurable solution for the energy production is represented by nuclear fusion reactors working at extremely high temperatures ($\sim 10^6$ K) [4]. It can be noted that, each of them involve increasingly extreme operating conditions (e.g. extremely low/high pressure or temperature) which represent potential drivers of physical hazards, and dangerous substances (toxic, flammable or radioactive materials) which can lead to chemical hazards if a release occur. These potential hazards are not expected in plants or,

more in general, in systems where the design, construction and operation are based on state-of-the-art safety technologies. According to Hauptmanns [5] the design of a plant/system must assure the containment of hazardous substances inside the plant, e.g. vessels, pipes, reactors. This translates in an adequate mechanical resistance of the components, and the introduction of safety systems able to guarantee the integrity of containment, like pressure relief, emergency trips, emergency cooling systems. In parallel to this, the design phase accounts also for an optimized use of resources (materials and money), thus an optimal compromise between performance and safety must be pursued. This last is the main objective of the *Risk Analysis*. The concept of risk can be referred to many fields as economics, business, sport, industry, etc. hence, a possible definition specifically related to the industry world can be "*risk is a measure of human injury, environmental damage or economic loss in terms of both the incident likelihood and the magnitude of the loss or injury*" [6]. A general mathematical formulation of the risk (R) can be the one shown in Eq. 1.1.

$$R = f(L;D) \tag{1.1}$$

R can be expressed as a general function of the likelihood of an event (L) and the related damage (D). The likelihood or frequency of occurrence of accidental events is related to the frequency of occurrence of the initiating events which can be estimated through a PRA (Probabilistic Risk Assessment) [7]. L represents the number of occurrence of an event in a certain amount of time, and is expressed as events per year (ev/y). D quantifies the loss of people, money or the impact on the environment associated to the scenario, and can be expressed in deaths, money, released oil (or any dangerous substance for the environment) per event (deaths/ev, $/ev). It is important to emphasize that R can be estimated rather than calculated, since a certain level of uncertainty must be always taken into account due to a lack of precise data about the accidental events. The procedure followed during a risk analysis devoted to the safety demonstration of an industrial plant can be schematically represented as in figure 1.1 [6]. The first step is the identification of potential hazards. This is made analyzing possible external hazards, historical analysis by studying previous accidents in similar systems (based on databases) and performing an HAZOP (Hazard and operability) analysis to identify all the possible initiating events coming from the abnormal operation or failure of components. Successively, the effects (thermal radiation, overpressures, etc.) related to an initiating event must be evaluated through the accident simulation. By applying vulnerability models, the

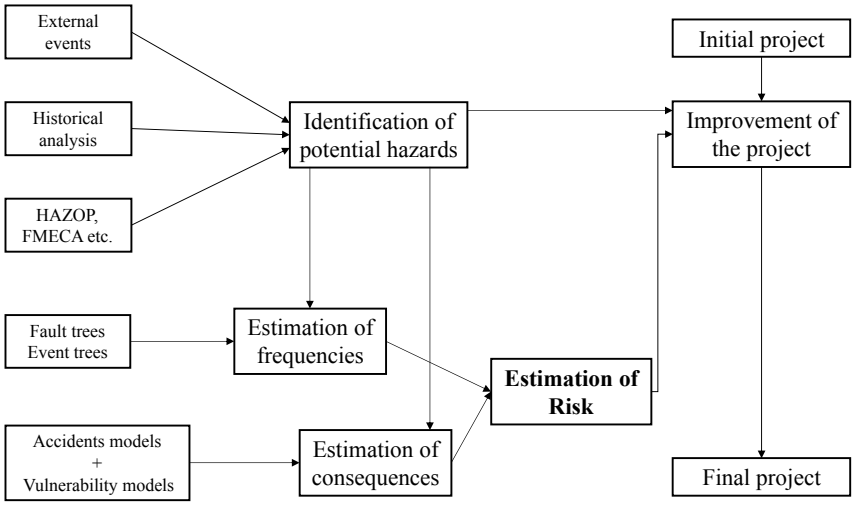

Fig. 1.1 Risk Analysis flowchart. Inspired from [6].

consequences of the accident can be assessed by identifying the distribution of the vulnerable elements (population, equipment), thus quantifying the damage due to the physical effects of the accident. The expected frequencies of the different potential scenarios are then evaluated through event tree and fault tree analyses. Combining the estimation of frequencies and consequences, the risks associated to each scenario can be evaluated. The final risk values are compared to the acceptable, ALARP (As Low As Reasonably Practicable) and non-acceptable thresholds, and the results are used to improve the safety of the project. Among all the possible type of accidents, this work focuses, on *Major* ones, which translates in the possibility of having *Major Hazards* for people and environment. These lasts are related to exceptional events leading to severe consequences, which consist in the release of large amounts of substances and energy in a short amount of time. The effects of a major accident can affect the external environment and the population, while in the majority of the cases (minor accidents) the risk is relevant only for some of the onsite workers. A more specific definition of major accidents, provided in [8], is: "*the occurrence of a major emission, fire or explosion resulting from uncontrolled developments in the course of the operation of an establishment*". Several types of major accidents can be identified [6]:

- *Pool fires*: steady state combustion of a pool of flammable liquid
- *Jet fires*: steady state combustion of a turbulent free jet

- *Flash fires*: fire caused by the ignition of a flammable mixture of air and flammable gas
- *Explosions*: mechanical explosion due to the expansion of a pressurized gas, or chemical reactions
- *Vapor Cloud Explosions (VCE)*: chemical explosions involving a flammable vapour/gas-air mixture
- *BLEVE (Boiling Liquid Expanding Vapour Explosion)*: physical explosion of a vessel containing liquefied gases by pressure or temperature
- *Dust explosions*: fast combustion of oxidizable particulate solids
- *Release of toxic/flammable materials*: dispersion of flammable unignited or toxic gas clouds in the environment due to the loss of containment.

Over the years, the attention to major risks control measures especially in the industrial field is considerably increased. Regulations evolved in order to enhance the safety level of the plants, especially those related to major accidents. One of the most impacting regulations is the "Seveso Directive" which prescribes the adoption of a Major Accident Prevention Policy (MAPP) and Safety Management System (SMS) by the operator of installations [9]. This directive prescribes that authorities must guarantee to the community that operators fulfil their duties and decrease the vulnerability of the external environment. Another relevant regulation is the European Union Offshore Safety Directive of 2013 [10], where the Quantitative Risk Assessment (QRA) is designated as the instrument to adequately demonstrate the safety of risk relevant plants. Furthermore, QRA should be integrated in the design phase of the plant, leading to a safety-driven design and it should be also at the basis of the decision making process for land use planning and emergency planning. QRA methodologies were widely discussed [11], nonetheless due to the increase of technology complexity and safety standards, novel approaches are needed to enhance the accuracy of the risk estimation.

1.1.2 Quantitative Risk Assessment - Accident simulation

As mentioned in the previous section, the QRA is defined as the appropriate methodology for the safety demonstration of major accident industrial plants by the European Union (EU) Offshore Safety Directive 2013/30/EU [10]. This methodology permits to identify the possible accidental scenarios caused by normal operating component failure, external events, human errors, etc. and to quantify the related risks. The possible accidental scenarios associated to a big plant can be in the hundreds, and the risk estimation passes through the quantification of the damage associated to all of them. The consequences of an accident can be quantified in term of risk measures, e.g. flammable/toxic areas, high thermal flux areas, and to obtain these data, the simulation of the event is an essential step. Since such a large number of events must be analyzed in a time compatible with the design project schedule of the plant, the necessity to adopt fast-response and simple methods for the simulation arises. In other words, the choice of suitable simulation methodologies for QRA purposes must respond to a principle expressible as *fast-calculation and simple-use*. For this reason, the state-of-the-art for the consequences estimation in the QRA rely on the use of semi-empirical tools and integral models. Their simplicity permits fast evaluations with a low computational effort, moreover, their employment does not require a deep understanding of the physical phenomena involved in the event. In the past, empirical or integral models were formulated for several phenomena as turbulent free-jets [12, 13], gas dispersion [14], jet fires [15, 16], explosions [15] and VCE [17]. Software implementing these models are available for companies in order to perform a QRA, e.g. PHAST [18] and ALOHA [19]. On the other hand, these methods are developed for specific phenomena in specific conditions, therefore they cannot be applied outside their range of validity. Moreover, they completely neglect the actual geometry of the domain, i.e. only free-jets/fires are considered, and the interaction with the object is not accounted. Despite this approach seems acceptable for most of the existing industrial plants, in some cases neglecting the actual layout complexity, can have relevant consequences on the final safety design. Considering a leak of gas from high pressure conditions as an industrial accidental scenario, the situation of a congested area or, more in general, of a geometrically complex environment surrounding the leak position, is likely to happen. The gas-object interaction plays a key role on the final gas cloud configuration, since the gas is likely to impinge as soon as it is released an its spreading can be consistently different with respect to a free jet

case. This can be the case of Oil & Gas (O&G) offshore platforms or nuclear plants, considering the part in the containment building. The limit of integral/empirical models in that situations was widely studied and it was demonstrated that they tend to overestimates damage areas [20–24]. In [25, 26] Gerbec et al. present a comparison between the semi empirical tool PHAST and ANSYS Fluent by simulating a Liquefied Petroleum Gas (LPG) release in a geometrical complex environment. The results show that the flammable cloud is largely overestimated by PHAST, and the authors concluded that this outcome can be ascribed to the Unified Dispersion Model (UDM) employed by the software, which cannot account for the presence of the obstacles. In [27] several dispersion simulations are realized through both a CFD and an integral model for the development of a multi-criteria optimization strategy for the positioning of gas detectors in a complex industrial layout. The authors state that the results given by the integral model are excessively over predictive, and the level of accuracy of the CFD predictions is necessary for the methodology. A similar outcome is derived by Landucci et al. in [28], where the potential of CFD models in simulating dispersion scenarios is investigated by comparing the results to the real data related to the Viareggio accident [29]. The CFD models resulted highly accurate in predicting the real data demonstrating their strong reliability for the gas dispersion simulation in geometrically complex environments. Moreover, the authors present a comparison with an integral model highlighting how this last tend to extremely overestimate the accident consequences. In [30], Shen et al. present a literature review about application of integral models and CFD in process safety and loss prevention. More than one hundred papers, related to the most relevant scenarios for industrial safety, such as fires (jet/pool fire), dispersion of flammable and/or toxic gases and explosion scenarios (VCE, BLEVE, dust explosions) are analyzed. This review highlights how empirical or integral models are employed for the study of free space scenarios, as well as experimental campaign are realized for free-field tests, whilst only CFD-based analyses are performed considering realistic geometries. It is emphasized how the limitations of empirical/integral models lead to damage areas and volumes overestimations, and consequently to an oversized safety design. i.e. a waste of resources, money and a relevant mechanical overload of the structures. In this cases, Shen et al. suggest more accurate methodologies like numerical methods, to predict the phenomena with the requested accuracy. Among all the others, CFD tools are indicated as the more appropriate, since allow to consider the real geometry and can resolve complex physical phenomena with a high level of detail. On the

other hand, this approach requires a deep knowledge about the physical phenomena and the numerical methods adopted for the calculations, and most of all, a high computational effort. For this reason, the employment of the CFD in a QRA is still prohibitive, and its use is limited for the verification of the most critical scenarios, often at the end of the design, when changes are no longer applicable. This work, seeks to provide a possible answer to the CFD-QRA integration issue, by providing an alternative approach able to guarantee a suitable computational cost-accuracy trade-off without losing sight of the *fast-calculation and simple-use* principle.

1.2 Background and motivation

1.2.1 Framework of this thesis

The framework of this work is a project funded by the Italian Ministry of Economic development (MiSE) in 2015 to enhance safety in the O&G offshore sector, as well as to provide new perspectives on the futurable uses of this kind of infrastructures. In fact, despite the energy transition towards low carbon solutions pushes for a growing renewable technologies employment, the O&G sector will play a key role in helping this process, representing a reliable energy source. With this perspective, strategies for the enhancement of their sustainability are investigated, e.g. coupling with Carbon Capture and Storage systems [31]. Moreover, potential re-uses of depleted reservoirs envisage for the storage of captured CO_2 as well as H_2 which can play a key role in the decarbonization of the transport sector [32]. Among the others, one of the main goals of this project is the definition/design of novel methodologies for a suitably accurate simulation of accidental scenarios, since as highlighted in section 1.1.2, the commonly used empirical or integral methods lead to highly inaccurate results especially in the case of complex geometries, such as offshore platforms. With these motivations, this work proposes a CFD based method targeted for QRA purposes, for the simulation of high-pressure gas leakage scenarios in complex geometries. The choice of considering gaseous releases is driven by the fact that the majority of Italian offshore plants treat natural gas, and that potential future uses involve gaseous substances as well (e.g. CO_2, H_2). More specifically, the CFD model is intended for high-pressure releases from small holes. In fact, QRAs for such a kind of plants are mainly devoted to that kind of scenarios since

it is likely to have leakages from small ruptures rather than guillotine ones [33], as well as equipment normally work at high pressure (at least 5 bar) [34]. Lastly, the proposed model is targeted for the analysis of big plants characterized by congested geometries exactly like a platform or also like the portion of nuclear plant inside the containment building, where impinging jets are likely to happen on small/large length objects.

1.2.2 Safety-oriented CFD: present-day solutions

Before introducing the aims of the present work, a brief overview of the available literature about CFD simulation of high-pressure gas releases in complex geometries is necessary to highlight potential gaps related to its application for safety purposes. Several authors propose a combined empirical method-CFD methodology, where the initial expansion of the gas jet is resolved through a simplified model to evaluate a pseudo-source to be used as input data for the CFD simulation. Deng et al. [35] and Liu et al. [36] studied a natural gas and a CO_2 release from high pressure pipelines to predict the hazardous cloud extension. In both works, the initial expansion of the gas jet was treated through the Birch model [37], which permits to evaluate a pseudo-velocity and a pseudo-diameter in correspondence of the complete gas expansion location, i.e. when its pressure equals the ambient one. These values are then used as input for a RANS based CFD simulation. A similar approach is proposed by Tolias et al. in [38], where the best practices for the simulation of H_2 release in automotive scenarios for safety assessment are discussed. In this case, instead of the Birch model, the authors recommend the use of the notional nozzle approach. Hu et al. studied the underexpanded jets impingement on vertical obstacles in [39], proposing a modified version of two simplified models to account for the jet expansion: the two layer partitioning model [40] and the Birch model. Colombini et al. propose a novel assessment tool to estimate the extent of high-pressure methane jets starting from CFD simulations in [41–43]. In all the three works an impinging jet is considered, respectively on a cylinder, a sphere and a pipe rack. The Birch model is chosen to account for the initial jet expansion. In [44] the interaction of an unintended H_2 release with a barrier is studied, a pseudo source approach is used also in this case. This approach is also adopted by some CFD safety-oriented software like FLACS by Gexcon US [45] and KFX by DNV-GL [46]. The first one is the industrial standard [47, 48] for explosions and it is validated for flammable

and toxic releases [49]. The latter is the leading CFD simulator of DNV GL, used to simulate dispersion of hazardous materials, fires and explosions. These are specific purpose tools, developed for safety analyses, and propose the integration of a semi-empirical model (Birch model) with a numerical one. A Porosity Distributed Resistance formulation of the governing equations is used, guaranteeing a consistent computational cost reduction with respect to general purpose codes. On the other hand, some limitations arise when dealing with gas-objects interaction, as discussed more in detail in appendix A. This brief overview highlights that all these works propose a simplified modeling of the initial compressible jet expansion, thus not permitting the simulation of an impingement with an obstacle located nearer with respect to the pseudo-source location. This could represent a limitation, since near impinging jets are likely to happen in highly congested environments, and the gas dispersion highly depends on the gas-surroundings interaction. This is especially true if the impingement occurs at high speed. On the other hand, this approach permits a faster evaluation of the consequences and it is suitable for most of the onshore plants where the geometry is not congested. To gain more accuracy, a possible strategy could be a full CFD approach, as proposed Wilkening et al. [50], where a pressurized hydrogen release is compared to a methane release under the same conditions. The simulation required a high-performance computing cluster, since a high computational cost arises from the constraints of dense mesh and small time step imposed by the initial expansion of the jet. Liu et al. [51] and De Souza et al. [52] propose similar approaches for the simulation of CO_2 and CH_4 high-pressure releases respectively. In both works, the initial expansion of the jet is numerically solved in a separate simulation, which results are used as input for the dispersion one. This strategy permits a simplification of the simulation process, but still maintain the issues related to the excessive computational burden. From the overview of these works presenting full numerical approaches, it can be deduced that if on the one hand this strategy give an answer to the accuracy issue, on the other hand it requires unsustainable computational efforts (from a QRA point of view). Moreover, in these works only free-jets are modeled, hence, considering an impingement near the leak source would make the situation even worse leading to even higher computational costs.

1.2.3 The need for alternative strategies

This brief overview highlights that this kind of simulations are approached mainly in two ways: on the one hand, empirical methods are employed to model the initial jet expansion for the sake of computational cost reduction, and on the other hand, full numerical models are employed for the sake of accuracy. The first ones, completely neglect what happens in the region between the release point and the location of complete jet expansion, thus not permitting to account for flow-object interactions in the first centimeters of the jet. This approximation could have a significant weight on the final estimations, since, the high inertia gas jet impingement near the release point has a strong influence on the final gas cloud configuration. The second ones, guarantee a higher level of accuracy, but require unsustainable computational efforts particularly seeking for a CFD integration in the QRA.

1.2.4 Aim of the work

In this thesis, the *high level* objective is to fill the gaps highlighted in the previous section, that can be translated in the need of a more accurate modeling of the near jet region with respect to empirical models, thus accounting also for near jet impingements, and by avoiding the huge computational burden of the already available full numerical solution strategies. In particular, this thesis proposes a CFD approach realized in ANSYS Fluent and called Source Box Accident Model (SBAM), that fits somewhere between the approach employing an empirical method for the initial jet expansion and the full numerical ones. Since the aim is to provide a QRA oriented CFD approach, the model design philosophy is based on a trade-off between simulation setup ease, computing speed and desired accuracy seeking for the aforementioned principle of *fast calculation and simple use*.

This *high level* objective is pursued by addressing several *low level* objectives. At first, the CFD approach (SBAM) [53] is developed according to the desired target applications, and suitably tailored on the physical phenomena of the accidental scenario under consideration. Moreover, a *numerical benchmark* analysis is performed to investigate advantages and disadvantages of the model with respect to a «classical» CFD approach and to investigate strategies aiming at a computational cost reduction. After the numerical model refinement, its experimental validation is addressed. Several representative case studies are defined and reproduced through scaled tests in a

wind tunnel, the SEASTAR WT [54]. This required the formulation of an *ad hoc* scaling procedure [55] targeted for high-pressure gas releases under wind conditions, as well as the calibration of the experimental devices [56], the data interpretation and finally, an investigation on the suitable methodology for the numerical-experimental data comparison to evaluate the model performance [57]. The link between the *high* and *low* level objectives is schematically represented in figure 1.2.

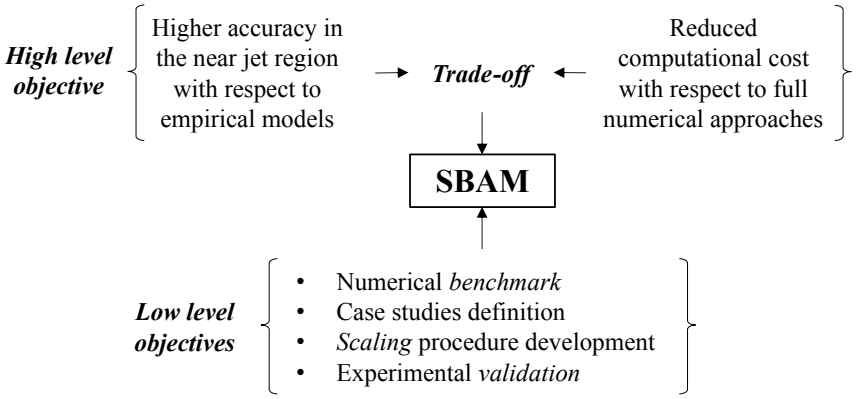

Fig. 1.2 *High* and *low* level objectives schematic representation.

1.3 Thesis structure

The following chapters are organized as follows.

Chapter 2 introduces the problem statement and an overview of the solution strategy. At first, the main features of the physical phenomena involved in high-pressure gas releases are described. Secondly, an overview of the proposed CFD approach is given with a list of requirements/challenges which guided its design and experimental validation.

Chapter 3 describes a set of case studies of accidental high-pressure gas releases on an offshore platform, which are considered in the numerical and experimental analyses. Considerations and assumptions made for the definition of such scenarios are discussed in detail.

Chapter 4 presents a detailed description of the proposed CFD approach, a numerical benchmark analysis and a sensitivity analysis on some model parameter. The Source Box Accident Model (SBAM) features are discussed in detail as well as its novelties and applicability range. Moreover, a numerical benchmark is performed

by comparing SBAM to a «classical» CFD approach, deriving insights on its strengths and weaknesses.

Chapter 5 is dedicated to the model experimental validation. At first, the experimental facility, domain mockup and measuring devices are described. Successively, an *ad hoc* scaling procedure for high-pressure gas releases is presented and used for the design of reduced scale case studies. The SBAM prediction capability is then tested by comparing numerical and experimental data through a set of statistical metrics.

In the end, chapter 6 presents several conclusions, future perspectives and a final discussion on the main outcomes of this work highlighting its strengths and limitations.

Chapter 2

Problem Statement

The present thesis focuses on one of the most common major accidents related to the process or energy industries: the loss of containment, a scenario that must be deeply investigated during a QRA to assure the plant capability to handle such abnormal situation. In particular, gas leakages in industrial complex geometries from high-pressure (HP) equipment (tanks, pipes) are considered. As described in section 1.2, this kind of phenomena are of large interest in the industry sector and were largely studied in the past, however, their numerical simulation still represent a challenge. This is true especially if the simulation is targeted for QRA purposes, where a trade-off between simulation setup ease, computing speed and desired accuracy has to be achieved.

The first objective of this chapter is to describe the main physics features of the phenomenon. The main features of HP gas releases are presented, with particular reference to the structure of the resulting *underexpanded jet*. The differences arising in the regions near and far the release point are highlighted in order to gain insights on the possible simulation strategy. These two regions are then characterized by evaluating the order of magnitudes of three dimensionless quantities, the Mach number (Ma), the Reynolds number (Re) and the Froude number (Fr). This last is just a simple and rough estimation based on several assumptions, but it provides a useful sketch of the features of the phenomenon.

The second and last objective of this chapter is to provide an overview on the model simulation strategy, also highlighting the main challenges addressed for its design, application and validation.

2.1 Critical flows and underexpanded jets

An accidental HP gas leakage, as suggested by the name itself, is defined by the involved pressure levels. In this respect, the first two parameters can be introduced: the gas total pressure inside the leaking equipment p_0 and the discharge ambient pressure p_a. An underexpanded jet may occur depending on the ratio of these two values, here defined as η_0 in Eq. 2.1.

$$\eta_0 = \frac{p_0}{p_a} \tag{2.1}$$

For the purposes of this work, the discharge ambient pressure (p_a) can be always assumed equal to 1 bar, considering that leakages happen from HP plant equipment towards the surrounding atmospheric pressure environment. Despite this assumption, which simplifies the discussion, each consideration derived for a certain η_0 value holds no matter the effective p_a value. Depending on η_0, the discharged flow could be critical or not. In the first case, a chocked flow condition verifies at the exit section, while not in the second. This can be judged *a priori* by comparing η_0 with the so-called critical pressure ratio R_{cr} defined by Eq. 2.2 [58]. This is a gas property since it is only a function of the adiabatic expansion coefficient of the gas γ.

$$R_{cr} = \left(\frac{2}{\gamma+1}\right)^{\frac{\gamma}{\gamma-1}} \tag{2.2}$$

A critical flow verifies if the condition shown by Eq. 2.3 is satisfied.

$$\frac{1}{\eta_0} = \frac{p_a}{p_0} < R_{cr} \tag{2.3}$$

Since R_{cr} is almost 0.5 for most of the gases [59–61] and remembering that $p_0 \geq 5$ bar, the condition 2.3 is always satisfied for the possible scenarios considered in this work. In fact, as introduced in section 1.2.1 this work considers leakages from small ruptures and pressure levels above 5 bar, since in O&G plants, gaseous substances are normally transported, stored and treated by high pressure equipment usually working at that pressure values [34]. A choked flow condition means that at the exit section (in correspondence of the release hole), the flow velocity is equal to speed of

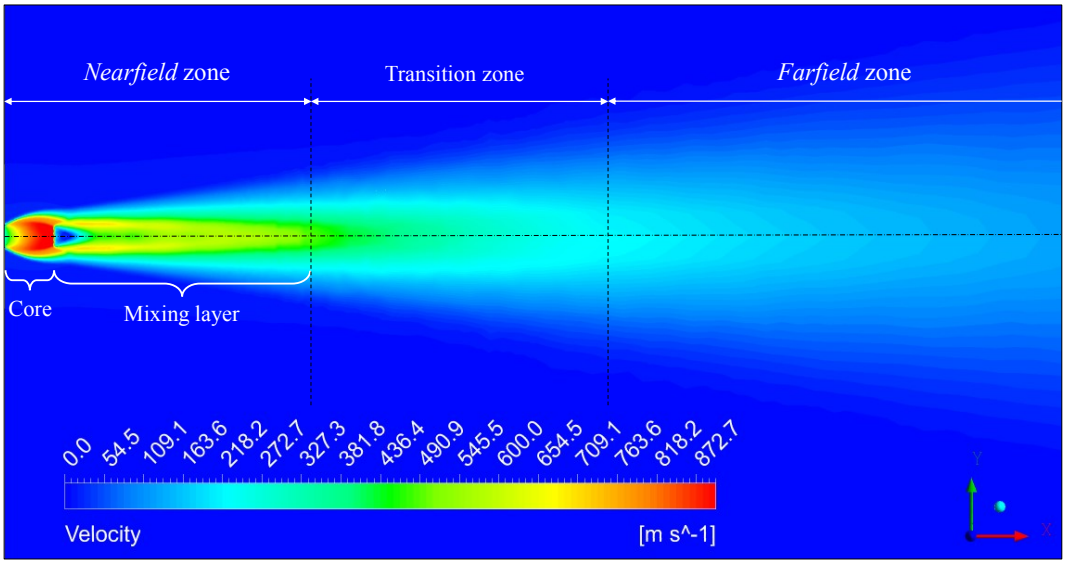

Fig. 2.1 Schematic representation of the free underexpanded jet structure.

sound and the exit pressure p_e (called also critical pressure) is given by Eq. 2.4.

$$p_e = R_{cr} \cdot p_0 \tag{2.4}$$

It is easily deducible that p_e will always be larger than p_a, hence, the gas needs to expand in the surrounding environment to reach the equilibrium. For these reason, the resulting jet is defined *underexpanded*. Three main spatial regions can be identified in a free underexpanded jet:

1. The *nearfield* zone
2. The transition zone
3. The *farfield* zone

Figure 2.1 helps to visualize the overall structure of a generic underexpanded jet and can be used for the following discussion. The *nearfield* zone, which is described in detail in section 2.1.1, can be further divided into the core and the mixing layer. The core is separated from the ambient fluid and its behavior is dominated by compressible effects. In this region, the gas undergoes an isentropic expansion and suddenly a compression phase, causing the formation of shock waves. In the mixing layer, large turbulent structures induce a mixing between the jet and the quiescent surrounding air. It can be observed that in this region, there is a high

velocity flow (in yellow) separated from the surrounding fluid, which tends to merge in a single jet. The *nearfield* zone ends when the mixing layer replace the inner part along the centerline. In the transition zone the mixing is enhanced since the longitudinal and radial variations of the variables are small, and it ends when the pressure finally homogenizes at the ambient value. In the *farfield* zone the jet is in pressure equilibrium with the environment and its velocity profile is fully developed, hence a self-similarity of all the flow variables verifies. Radial profiles of velocity and gas concentration can be described by Gaussian profiles centered with the axis, while longitudinally the variables are inversely proportional to the distance from the source point.

Summarizing, the jet can be roughly divided in a momentum dominated region and a buoyancy controlled one. In fact, as the inertia of the jet decays, buoyancy forces play a relevant role in the gas dispersion. This is true, unless the gas jet is immersed in an external flow field, e.g. a wind field. In fact, the gas flow, once has lost its pressure driven inertia, is driven by the external field inertia. In this case, the *farfield* can be described as a gas dispersion at a subsonic regime, driven by the external flow. Figure 2.2, which depicts a HP gas jet on a complex domain under a wind field, helps to visualize the *nearfield* zone and *farfield* zone, according to this different definition, which is the more representative of the context of this work.

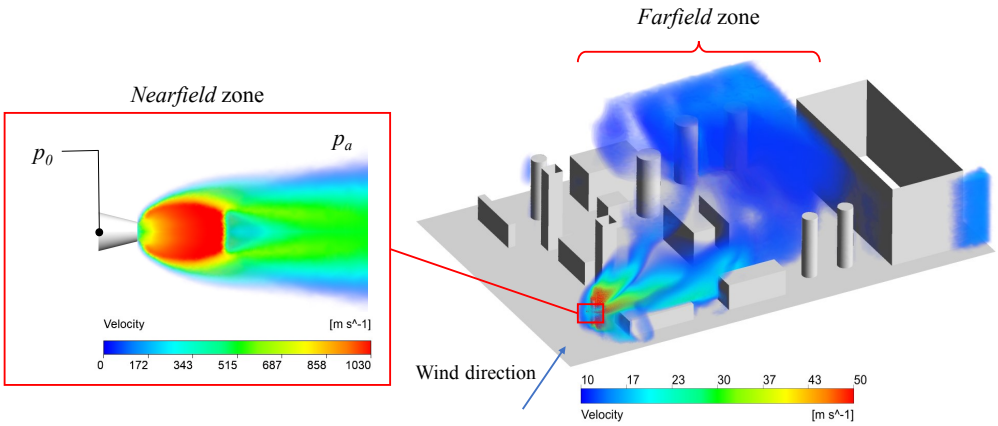

Fig. 2.2 *Nearfield* zone and *farfield* zone schematic representation for a HP gas release in a complex domain under a wind field.

2.1.1 *Nearfield* zone

The structure of the *nearfield* zone is quite complex and deserves a detailed description. Its structure changes according to the values assumed by η_0, which defines the level of underexpansion of the jet. In this respect, a classification is proposed by Franquet et al. [62] basing on several works available in literature [60, 63–68]:

1. *Moderately* underexpanded jets: $2 \lesssim \eta_0 \lesssim 4$
2. *Highly* underexpanded jets: $4 \lesssim \eta_0 \lesssim 7$
3. *Extremely* underexpanded jets: $\eta_0 \gtrsim 7$

The jet features for each η_0 range were studied in the past through a large number of experimental observations which permitted to gain detailed descriptions. The typical structure of a *moderately* underexpanded jet is shown in figure 2.3.

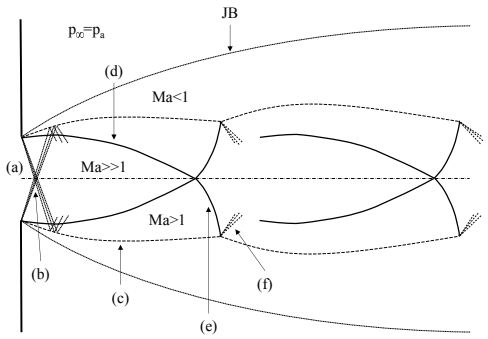

Fig. 2.3 Schematic representation of *moderately* underexpanded jets structure. Inspired from [62].

The picture shows that as soon as the jet exits from point (a), some expansion waves (b) are generated and reflected in correspondence of the line (c) which delimits the surrounding environment at a constant pressure equal to p_a. This reflection causes the generation of compression waves directed towards the inner side of the jet, which coalescence produce an oblique shock (d). In the region delimited by the oblique shocks a supersonic flow is registered, in fact the Mach number (Ma) that is the ratio between the local flow velocity and the speed of sound is highly larger than unity. Once these shocks intercept each other, novel shocks (e) are generated and again reflected by the boundary (c) generating another similar structure. The repetition of this pattern produce the typical *diamond* or *X* shape of these jets. Another supersonic

region ($Ma > 1$) between the oblique shocks (d) and the ambient pressure line (c) forms, and is surrounded by a subsonic region ($Ma < 1$) which extends until the jet boundary (JB). The structure of a *highly* underexpanded jet, shown in figure 2.4, is quite similar to the previous one, except for the absence of the oblique shocks interception.

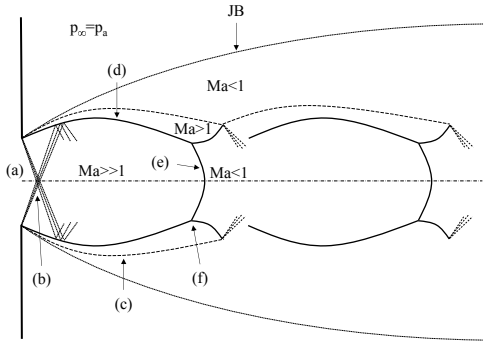

Fig. 2.4 Schematic representation of *highly* underexpanded jets structure. Inspired from [62].

Also in this case expansion waves (b) are generated and reflected by the boundary (c) generating oblique shocks (d). Moreover, a normal shock (e) called Mach disk (MD) appear, and intersect the oblique shocks in the so-called triple point (f). It can be noticed that a supersonic region ($Ma \gg 1$) is registered upstream the MD, and a subsonic one ($Ma < 1$) downstream, hinting the presence of a strong discontinuity in the flow field. The jet is then completed by a supersonic region with $Ma > 1$ between oblique shocks (d) and the ambient pressure line (c), and a surrounding subsonic ($Ma < 1$) region until the jet boundary (JB). Finally, the *extremely* underexpanded jet structure is shown in 2.5.

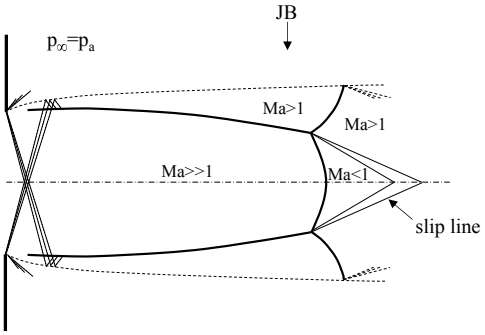

Fig. 2.5 Schematic representation of *extremely* underexpanded jets structure. Inspired from [62].

The structure of this last kind of jets is basically the same of the *highly* underexpanded jets, with the only difference that a unique normal shock (Mach disk) appear. For most of the industrial applications, especially those related to the O&G field, this last situation is likely to happen. As mentioned in the previous section, gas processing equipment is generally at pressure higher than 5 bar, in particular, for QRAs the range 5-100 bar is generally considered [34]. Therefore, the condition of $\eta_0 \gtrsim 7$ is likely to verify in most of the cases. For this reason and for other considerations related to the model applicability range, which are discussed at point 3 in section 4.1.4, only *extremely* underexpanded jets are considered for the purposes of the CFD model development. The main feature of these kind of jets is the formation of single supersonic cell, which ends with a normal discontinuity, the MD. This cell has a barrel like shape which is the result of the coalescence of the compression waves [69]. Downstream the MD, an annular region where $Ma > 1$ forms around a subsonic central region ($Ma < 1$). These two regions are separated by a *slip line* in the mixing layer, which becomes weaker until the two regions are perfectly mixed. Another important characteristic is the strong air entrainment caused by the extremely high inertia of the jet. According to numerous theoretical, numerical and experimental studies available in literature [59–61, 68, 70–73] several features about the MD could be derived. The most relevant for the present work is the MD location (L_{MD}), expressed as a distance from the release source. The authors of these works suggest that the MD position is mainly influenced by η_0 and the release diameter D_e while is almost independent by the type of fluid. Among all the possible correlations, the one proposed by [74] was validated for the larger pressure ratio range and is reported in Eq. 2.5.

$$L_{MD} = 0.645497 \cdot D_e \cdot \sqrt{\eta_0} \tag{2.5}$$

This parameter is important since it is an input of the CFD model design as discussed in section 4.1.1.

2.2 *Nearfield* and *farfield* zones - flow regimes

As described in section 2.1, the *nearfield* and the *farfield* of a HP jet can be easily distinguished due to their extremely different flow field features. Moreover, it is pointed out that for the purposes of this work, the term *farfield* refers to the region where the gas motion is driven by the an external field advection and it is influenced

also by the interaction with the domain objects, if the release occurs in a complex geometry. From now on, these two phases of the gas leakage will be identified respectively with the terms *release* instead of *nearfield* zone and *dispersion* for the *farfield* zone. An interesting exercise could be the evaluation of the order of magnitudes of some dimensionless numbers for both the *release* and the *dispersion* to gain some insights on their different features. The three following numbers are chosen:

- Froude number (Fr), which represents the ratio between inertial and buoyancy forces. It is useful to understand if the flow is momentum dominated or buoyancy effects are non negligible.
- Reynolds number (Re), which represents the ratio between inertial and viscous forces. It gives a measure of turbulence level of the flow.
- Mach number (Ma), which is the ratio between the local flow velocity and the speed of sound. It permits to define if the flow is compressible or not.

They can be evaluated respectively through Eqs. 2.6, 2.7 and 2.8.

$$Fr = \frac{u}{\sqrt{g \cdot L_{Fr}}} \tag{2.6}$$

$$Re = \frac{\rho \cdot u \cdot L_{Re}}{\mu} \tag{2.7}$$

$$Ma = \frac{u}{c} \tag{2.8}$$

Where c is the speed of sound in m/s, u is the flow velocity in m/s, ρ is the density in $\mathrm{kg/m^3}$, g is the gravitational acceleration in $\mathrm{m/s^2}$, μ is the dynamic viscosity in $\mathrm{Pa \cdot s}$, L_{Fr} and L_{Re} are respectively the reference lengths for the Fr and Re numbers in m. Several assumptions are made in order to define representative input values for the dimensionless number estimation in both the *release* and *dispersion* phases. Obviously, these are made according to the scenarios of interest for this work (see description in section 1.2.1). In the *release* phase, the gas velocity at the release section can be used as the reference one (u) for the calculations. Since this work considers only critical flows, i.e. a choked flow condition verifies in correspondence of the release hole, the gas velocity is equal to the speed of sound, hence $u = c$. The order of magnitude of the speed of sound for most of the gases is

100 m/s (as an example see the data collected in [75]), therefore, it can be assumed $u = 100$ m/s assuring that this is a suitably representative value. The density ρ can vary consistently considering heavier or lighter gases, nonetheless, considering HP releases means that the released gas density will be higher with respect to the value at ambient pressure. Following an underestimation approach, a value of 0.1 kg/m^3 can be assumed in order to be sure that the results are representative also in case of extremely light gases (e.g. H_2, He). The dynamic viscosity μ is assumed equal to 10^{-5} Pa·s, which is a representative value for most of the gases. The scenarios under analysis in this work deal with external flows, hence, the reference length for the *Re* number is here defined as the characteristic length of the objects invested by the released gas. According to the context of this work, this objects are represented by the plant equipment, e.g. pipelines, tanks, which dimension can vary in a wide range. To be the more complete as possible two values are considered, representing the minimum and maximum reasonable lengths $L_{Re} \sim 0.1 - 10$ m. The last parameter to be defined is L_{Fr}. Being the Fr number related to buoyancy effects, its reference length is defined as the characteristic dimension of the domain along the $\vec{g}$ direction, that is the direction in which the gas could be transported by buoyancy forces. Considering releases in big industrial plants, L_{Fr} can be defined as the order of magnitude of the height of compartments/rooms where the equipment is located or the inter-deck height in case of offshore platforms. According to that, a reasonable assumption can be L_{Fr}=1 m. The resulting values of the three dimensionless numbers for the *release* are then $Ma \geq 1$, $Re \sim 10^5 - 10^7$ and $Fr \sim 10$.

An analogous *iter* is followed for the calculation related to the *dispersion*. In this case the reference flow velocity u depends on the residual jet inertia and on the external field velocity, thus, assuming a representative value for this parameter is not trivial. It must be considered that the gas initially flows at sonic velocity, hence, it carries a large inertia which is gradually dissipated. However, assuming a flow velocity of the order of 10 m/s in most of the domain seems reasonable, especially if the release happens in big plants where the gas has enough space to slow down up to extremely low velocities. The external field is represented by a wind field, which velocity usually ranges from 1 to 30 m/s [34], thus, considering both contributions, u can be assumed of the order of 10 m/s. A value of 1 kg/m^3 is used for ρ since at this point the released gas, no matter it is extremely heavy or light, is strongly mixed with the surrounding air. For the remaining parameters, the same assumptions made for the *release* calculations hold. The resulting values of the three dimensionless

numbers for the *release* are then $Ma \sim 0.1$, $Re \sim 10^5 - 10^7$ and $Fr \sim 1$. Comments about the Ma values can be analyzed considering this thresholds [58]:

- Incompressible flow: $Ma \leq 0.3$
- Compressible subsonic flow: $0.3 < Ma < 1.0$
- Compressible supersonic flow: $Ma \geq 1.0$

In light of this, the first main difference between the *release* and the *dispersion* arises. In the first case the compressibility effects are non negligible and must be accounted in the numerical solution strategy, while in the second case the flow can be assumed incompressible. Comments on the Re can be derived by considering a threshold value related to external flows over blunt bodies. Taking a cylindrical shaped object as a reference blunt body, a Re value larger than $5 \cdot 10^4$ implies the formation of a turbulent boundary layer [58]. In both the *release* and the *dispersion* this threshold is overcome since $Re > 10^5$, hence the flow is largely turbulent in both cases. This consideration is strengthen, in the *release* phase, considering that Re is underestimated due to the low density value assumed, hence this will be especially true considering heavier gases (e.g CO_2). The Fr value obtained for the *release* phase suggests that the inertia forces are dominant with respect to the buoyancy forces at least by one order of magnitude, while in the *dispersion* phase inertial and buoyancy forces can be considered comparable, being their ratio $\sim$1. This interesting and rather approximate exercise is useful to highlight the main differences the two phases of the leakage which lead to a multi physics phenomenon where a compressible inertia driven flow coexists with an incompressible flow with relevant buoyancy effects. It must be emphasized that in presence of external velocity fields like the wind one, advection will overcome buoyancy effects, which could be relevant only in some extremely low velocity regions. A last comment regards the different gradients of flow variables appearing in the two phases. In the *release* phase, especially near the Mach disk region, strong flow field variable discontinuities appear, leading to steep gradients which needs to be accurately accounted for in the numerical grid generation. Differently, in the *dispersion*, the flow field is smoother and no large gradients are expected apart from the boundary layers arising near the walls. As discussed in section 4.1 this translates in a different effort in the mesh generation for the numerical solution calculation. Summarizing the previous considerations, two definitions can be given for this two stages of the scenario:

- The *release*: high inertia compressible flow near the leak point
- The *dispersion*: low inertia incompressible dispersion of gas in the plants/domain, driven by the wind advection.

2.3 Overview of the model and open points

The CFD model here proposed, is realized in ANSYS Fluent and provides that the different features of the *release* and the *dispersion* phases are handled in two different simulations. The logical scheme in figure 2.6 highlights the *two-steps* nature of the model.

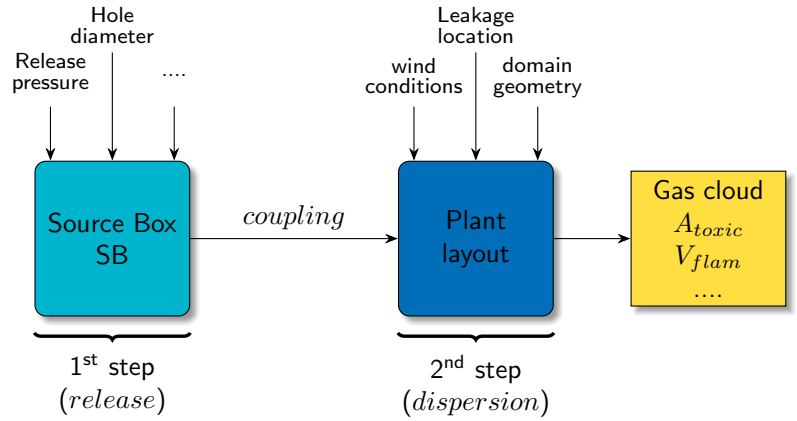

Fig. 2.6 Logical scheme of the Source Box Accident Model.

The *first step* represents the *release* phase simulation, which considers a small domain compared to the plant geometry, called Source Box (SB). It takes some input parameters as the release pressure and the hole size and accounts for the compressible, inertia dominated flow of the jet nearfield. For the sake of this discussion, the *release* simulation will hereafter be referred to as the SB simulation. The results of the SB simulation are stored and used as boundary conditions in the *second step*, the gas *dispersion* simulation in the case study environment, where the subsonic incompressible flow is modeled. Thus, the results of the SB represent the «leak source» in the dispersion domain, hence the name Source Box Accident Model (SBAM). This second simulation takes in input also other parameters as the

wind velocity and direction, the leak position and direction on the case study plant and obviously the geometry of the plant itself. The main output of the model is the prediction of the gas concentration in the domain, from which risk metrics such as the flammable/toxic cloud volume and areas at any elevation can be derived. The main aim of the model is to provide a more accurate estimate of these quantities, since strictly related to the identification of hazardous areas due to flammability (e.g. consequences area estimation associated to flash fires) or toxicity limits. In addition, other output values like the gas cloud mass are obtained as well, and could serve as *high-accuracy* input for explosion models (like the TNT equivalency one [15]) to evaluate peak over-pressures. The target applications for which SBAM is conceived can be ideally described by the following sentences:

- A gaseous release is involved
- The release pressure is such that an underexpanded jet occur ($\eta_0 > 2$)
- The domain layout is congested
- The required level of accuracy shall not exceed the one suitable for safety assessment

As one might guess, some limitations had to be applied to these desired targets, due to issues arising during the model design. In this respect, the actual model applicability range is then defined and presented in section 4.1.4. The development of the model followed the accomplishment of some requirements, which served also as a guide for the activity:

1. Define a qualitative criterion for the SB sizing and shaping
2. Translates this qualitative criterion in a systematic rule and successively in an equation
3. Define how to account for the gas jet impingement near the release point
4. Define a suitable methodology for the *coupling* of the two simulations
5. Define the numerical solution strategies for the SB and the dispersion simulations
6. Define a strategy to reduce the computational cost associated to the model

7. Assess the model performance with respect to a «classical» CFD approach and with respect to CFD safety oriented tools
8. Define the model applicability domain basing on the target applications and its limitations

These points are addressed in chapter 4 and appendices A and B, which are devoted to the design of the model and the numerical investigations. Moreover, the model validation required to address the following issues:

9. Define a suitable set of case studies basing on the model target applications
10. Define a scaling procedure for HP gas releases under wind conditions for deriving scaled parameters starting from real scale case studies
11. Calibrate the wind tunnel and investigate on the measuring devices working principles
12. Identify a suitable methodology for comparing the numerical data with the experimental one to evaluate the model quality

This last set of points are addressed in chapters 3 and 5, which are mainly related to the definition of the case studies and the experimental activities.

Chapter 3

Case studies definition

The analyses presented in sections 4.2, 4.3 and chapter 5 aim at assessing the model performances, and required the definition of a representative set of scenarios according to the model target applications description given in section 2.3, which is reprised here for convenience:

- A gaseous release is involved
- The release pressure is such that an underexpanded jet occur ($\eta_0 > 2$)
- The domain layout is congested
- The required level of accuracy shall not exceed the one suitable for safety assessment

Thus, basing on these criteria and on the specific context of this work, a set of HP gas leakage scenarios in an offshore platform is defined. In fact, as described in section 1.2.1, the activities carried out in this thesis fall within the framework of a project funded by the Italian Ministry of Economic development (MiSE) to enhance safety in the O&G offshore sector, considering the current and potential future uses. In particular, the need of novel methodologies for the consequences assessment for these kind of plants is the motivation for the development of SBAM. Having that the majority of Italian platforms treat natural gas, and that potential future uses regards the storage of CO_2 and H_2, this work focuses on accidental scenarios related to gaseous leakages. Based on this, the domain layout and a set of case studies are defined, adopting the philosophy of having a sufficiently diversified set of scenarios.

In fact, the objective of the numerical benchmark and especially of the experimental validation, is to evaluate the model accuracy and prediction capability, its limitations as well as differentiating between situations in which the model has better or worse performances. For these reasons, the basic idea is to consider several values for each parameter (pressure, hole size, wind conditions, leak position, etc.) and to combine them in the most various possible ways. However, since the case studies had to be reproduced experimentally, some practical constraints have driven the selection of a subset of scenarios to permit their testing.

3.1 Definition of the domain geometry and selection of the case studies

The considered geometry is inspired by a realistic oil rig design, with particular reference to natural gas extraction platforms located in the Adriatic Sea. Despite they normally consist of several decks, for the sake of the present work, only the central one, e.g. the production deck, is considered. In fact, in these kind of platforms an accidental gas release occurring in one deck would not affect the adjacent ones due to the presence of *plated* floors, which act as physical barriers avoiding the gas spreading across them. This permits to analyze a single deck and consequently to simplify the geometry. On the other hand, this geometrical arrangement could lead to a relevant gas accumulation in the deck with the potential formation of dangerous flammable and/or toxic spots, thus, generating highly relevant scenarios for a QRA. The geometry is shown in figure 3.1.

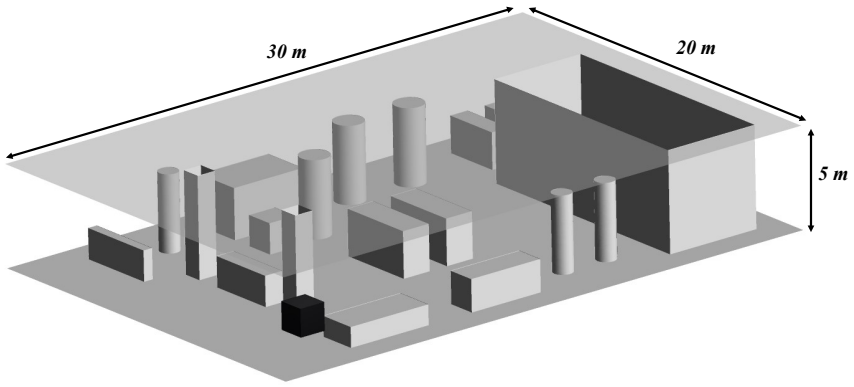

Fig. 3.1 Offshore platform deck CAD geometry with its size.

All the process equipment such as tanks, separators, compressors etc. are reproduced in the domain by simple geometrical shapes as parallelepiped and cylinders, while the secondary equipment (small pipelines, etc) is neglected. Despite the geometry can appear extremely simplified, it must be considered that integral or empirical models, which are now massively employed in QRA, completely neglect the geometry, hence a slight simplification of the domain still represent a relevant enhancement of the accuracy. To perform the analyses, a set of relevant gas release scenarios are identified according to Vivalda et al. [34]. In their work the authors proposed a methodology to identify a representative set of release scenarios to be simulated through CFD for safety assessment purposes, related to the normal operation and maintenance phase of an O&G platform. Several initiating events are identified starting from the review of the available literature on loss of containment accidents as well as reports of statistical analyses and incident investigations. Those events are related to valves failures, mal-operation of hoses, incorrect fitting of flanges, sealing failures, degradation of welded pipes, corrosion, overpressure, etc. which lead to HP gas leakages through small holes. As a final consideration, the authors state that the main influencing factors are the wind direction and intensity and the gas release rate and direction providing also some representative value ranges for some parameters. Hence, basing on [34] the values of release pressure and hole size that are more likely to happen in an accidental release in the O&G sector are:

- 5 bar$<p_0<$100 bar
- D_e=5-30-100 mm

According to that, in this work the release is characterized in terms of pressure and hole diameter (assuming only circular holes) taking values in the proposed ranges. The plausible gas leak positions in the domain are defined considering leakages in the internal part of the deck, where the wind inertia is less effective, and near the edge of the platform where the wind inertia is more effective. The gas leak direction and the wind direction are both defined with the aim to consider the worst scenarios, that is, considering the configurations in which the dangerous cloud spreading involves the largest portion of the domain, while neglecting scenarios in which the gas escapes as soon as it is released. According to the general framework, methane is chosen as leaked gas, and the wind intensity is defined according to the meteorological conditions referred to the Adriatic Sea [76]. Along with these theoretical considerations,

some practical constraints related to the experimental activities played a key role in the definition of the case study parameters. In fact, these tests employed a platform mockup (which is described in section 5.1.2) resembling the CAD geometry, and the realization of onboard gas releases is performed assembling a release nozzle on its floor. This required to have holes on the floor in correspondence of each release location, but since several Printed Circuit Boards had to be mounted under the mockup base to acquire the sensors signals, the available surface for these holes was reduced. At the end, considering both the theoretical requirements and the practical constraints, the leakage positions and directions and the wind directions ($\vec{U}_1$, $\vec{U}_2$) shown in figure 3.2 were selected.

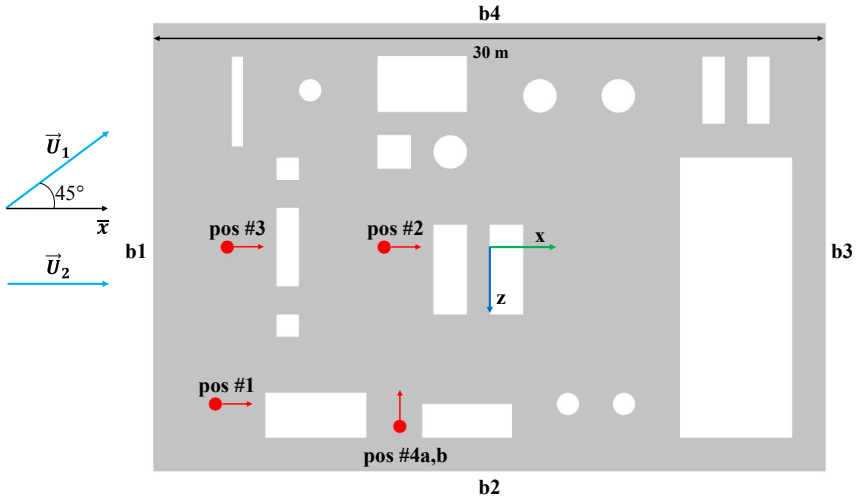

Fig. 3.2 Top view of the deck CAD geometry with a schematic representation of the leak positions and directions (red bullets/arrows) and wind directions (cyan arrows).

Table 3.1 summarizes the spatial coordinates of the leak points and the corresponding release directions, referring to the coordinate system shown in figure 3.2 which origin coincides with the center of the platform floor. Similarly, D_e and p_0 are defined starting from the previous theoretical considerations and some practical ones derived from several preliminary tests. It was observed that low values of D_e would lead to negligible gas concentrations levels, hardly detectable by the gas sensors, while high values of D_e and p_0 would lead to a fast depletion of the test gas inventory. Therefore, a value of 30 mm, the middle one is chosen for the diameter and a maximum value of 50 bar for the pressure. Three other pressure levels were chosen below this value in order to test also considering lower inertia releases. The last parameters, the wind intensity, is set equal to 6 m/s ($|\vec{U}_1|$=$|\vec{U}_2|$=6 m/s) basing

on the most frequent value in the Adriatic Sea [76]. At the end, the resulting case studies are the ones presented in table 3.2.

	x-coord. [m]	y-coord. [m]	z-coord. [m]	Release direction
position 1 (pos#1)	-12.23	1.5	7	$\vec{x}$
position 2 (pos#2)	-4.7	2.5	0	$\vec{x}$
position 3 (pos#3)	-11.7	2.5	0	$\vec{x}$
position 4a (pos#4a)	-4	2.5	8	$-\vec{z}$
position 4b (pos#4b)	-4	1.5	8	$-\vec{z}$

Table 3.1 Summary of the leak positions coordinates and correspondent release directions with respect to the Cartesian reference framework of figure 3.2.

case study (cs) tag	Release position/direction	p_0 [bar]	D_e [cm]	Wind
cs#1	pos#1	30	3	$\vec{U}_1$
cs#2	pos#1	40	3	$\vec{U}_1$
cs#3	pos#1	50	3	$\vec{U}_1$
cs#4	pos#2	30	3	$\vec{U}_2$
cs#5	pos#2	50	3	$\vec{U}_2$
cs#6	pos#3	30	3	$\vec{U}_2$
cs#7	pos#3	40	3	$\vec{U}_2$
cs#8	pos#3	50	3	$\vec{U}_2$
cs#9	pos#4a	30	3	$\vec{U}_1$
cs#10	pos#4a	50	3	$\vec{U}_1$
cs#11	pos#4b	30	3	$\vec{U}_1$
cs#12	pos#4b	40	3	$\vec{U}_1$
cs#13	pos#4b	50	3	$\vec{U}_1$

Table 3.2 Summary of case studies (cs) considered for the numerical and experimental analyses, with the corresponding parameters.

According to the general framework, methane is chosen as leaked gas for all the scenarios. Since the SBAM target is to provide some risk metrics useful for safety considerations, some properties related to the flammability of methane are here introduced for the sake of the results interpretation in the following chapters. In particular CH_4 flammability limits according to [77] are introduced:

- Low Flammability Limit (LFL): 0.05 by volume of air

- Upper Flammability Limit (UFL): 0.15 by volume of air

These values are important since the discussion of the consequences areas due to a flammable gas dispersion are strictly related to them. The concentration range between LFL and UFL defines the *ignition window* of a gas, that in this case is, if the percentage of methane in air is in this range it can be ignited causing fires ad consequently damages to people and structures. Starting from these two parameters, the following definitions could be given according to Italian regulations [78]:

- Irreversible Injuries (II) area, defined as the area where CH_4 mole fraction> 0.5·LFL
- High Lethality (HL) area, defined as the area where LFL<CH_4 mole fraction<UFL

The first one defines an area where, in case of ignition, serious injuries could happen to people and structures, while the second one defines an area were deaths could happen. These two risk metrics are crucial in a QRA since the calculation of the damage D in case of flammable substance leakage (see Eq. 1.1) is strictly related to them, hence, these will be used also in this work in the results discussion.

Chapter 4

Methodology and numerical investigations

The first part of this chapter is devoted to a detailed description of SBAM. The model features, the applicability range and the expected novelties are discussed. The second part is devoted to a numerical benchmark analysis where SBAM is compared to a «classical» CFD approach, and to sensitivity analysis on the *coupling* parameters. Part of the work presented in this chapter was previously published in Moscatello et al. [53].

4.1 Source Box Accident Model

As introduced in section 2.3, the model follows a *two-steps* approach where the *release* is simulated in the SB and the *dispersion* in the case study domain. This section goes into the details of SBAM by describing the SB features, the two simulations coupling methodology, highlighting the foreseen novelties and discussing its applicability range.

4.1.1 Source Box description

The SB is the domain where the initial expansion of the HP jet is simulated. Its design, starts from the consideration that the high inertia compressible part of the

phenomenon and the impingement on a near obstacle have to be modeled within its boundaries. Hence, these requirements can be formalized by these three sentences:

1. All the compressibility effects must be exhausted inside the SB, assuring that flow is incompressible at its outlet boundaries
2. The SB must contain an object in proximity of the leak to account for the space congestion
3. Inside the SB the underexpanded jet must be correctly reproduced

The starting point, is the research for a criterion to define the distance from the release point at which the compressibility effects are no more relevant. According to [74] for free extremely underexpanded jets, this distance is almost equal 10 times the Mach disk position (L_{MD}, see Eq. 2.5), hence a reference length for the SB can be defined as in Eq. 4.1.

$$L_{SB} = 10 \cdot L_{MD} = 10 \cdot 0.645497 \cdot D_e \cdot \sqrt{\eta_0} \tag{4.1}$$

To fulfil the first requirement, the SB is conceived as a cube with side length equal to L_{SB} as shown in figure 4.1.

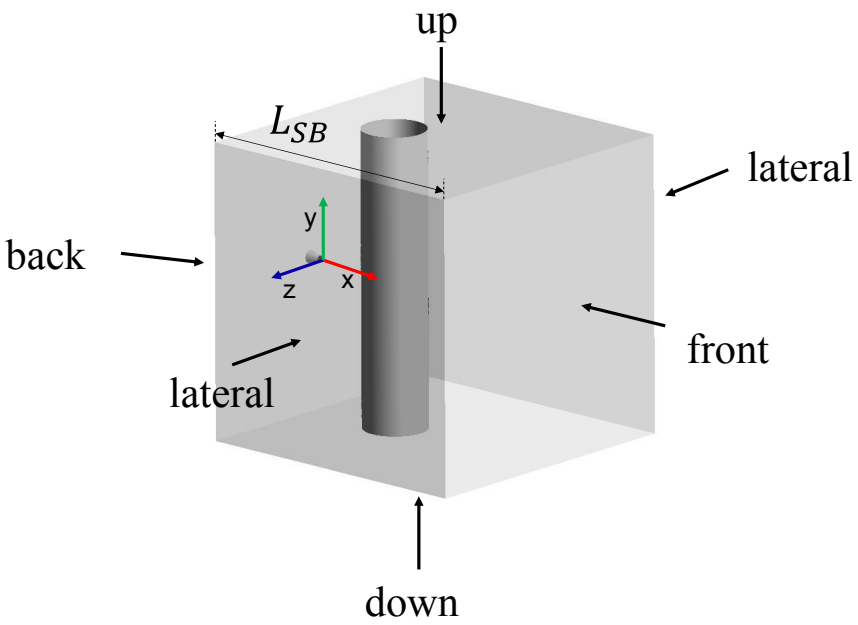

Fig. 4.1 SB face nomenclature and coordinate system.

The release hole is positioned at the center of a face, assuring that once the gas reaches the opposite outlet side it is subsonic, having traveled the distance L_{SB}. This is particularly reasonable considering that an obstacle is placed in front of the release hole and a faster inertia dissipation occurs with respect to a free jet. The choice to consider a cubic shape, instead of a generic parallelepiped, is made for the sake of simplification, in particular to simplify the *coupling* methodology. Eq. 4.1 suggests that, as expectable, the larger the leak hole or the release pressure, the bigger has to be the domain, since L_{SB} is proportional to D_e to the square root of η_0. To met the second requirement, an object is placed in the SB at a distance $l_{obs} < L_{SB}$ from the release point on the jet axis as shown by the cylinder in figure 4.1 as an example. The shape of the object can be a cylinder or a flat plate, depending on the equipment to be represented (small pipes, big aspect ratio tanks, etc.). Pipelines in front of the leak hole can be represented as cylinders with reference length d_{cyl} equal to their diameter, while bigger objects as big tanks can be approximated with a flat plate with reference length L_{fp}, that represent a transversal length with respect to the jet flow direction. Figure 4.1 introduces also a fixed denomination for the SB faces: *back* is the face where the release point is located (in the origin of the coordinate frame), *lateral* is the name of both faces on the right and left sides (the same tag is used due to symmetry purposes, see discussion in section 4.2.1), *up* and *down* are respectively the top and bottom faces and *front* is the face opposing to the release point. The release point is always positioned at the center of the face *back* as well as the release direction is always coincident with the x-axis as shown in the picture. The necessity to have a fixed denomination of the SB faces, release point and direction arises to facilitate the *coupling* with the dispersion and to standardize the procedure making it robust. Having a fixed release direction in the SB does not represent a constraint in the dispersion phase, since different release directions in the plant geometry can be simulated by rototranslating the SB and aligning the SB $\vec{x}$ direction any direction in the 3D space of the plant. The last SB requirement is achieved by using a fictitious nozzle to model the release hole. As suggested in [79], to obtain a correct modeling of an underexpanded jet in ANSYS Fluent, a convergent nozzle can be used to reproduce the gas discharge in the environment. Imposing the release conditions at the nozzle inlet (the condition inside the leaking equipment) permits to have the correct critical conditions at the nozzle exit (critical pressure, sonic velocity), which represents the release hole. The present work considers only circular holes, hence round nozzles are used to simulate the leakages. Figure 4.2

shows an example of possible SB configuration and helps a better understanding of the SB geometry. It considers a rupture in a pipeline (blue) causing an impinging jet on a parallel pipeline (red).

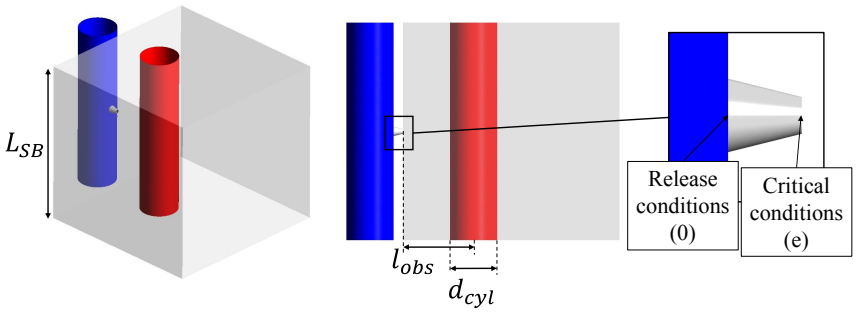

Fig. 4.2 *Left*: SB representing a leakage from a pipeline. *Center*: Visualization of the obstacle (parallel pipeline in red) with the distance l_{obs} and its dimension d_{cyl}. *Right*: Detailed view of the nozzle.

On the left, the SB is shown in light grey, in the center the obstacle distance l_{obs} and the obstacle dimension d_{cyl} are highlighted. In the case of a cylindrical obstacle, the distance is defined between the release point and the its axis. On the right, a detailed view of the nozzle is shown: at its inlet, the release conditions (0) are imposed, at its exit (e) the critical conditions are reproduced. Despite in this case a leak from a pipeline is considered, the release source can as well represent a leak from a tank, a rotating machines seal, a guillotine pipe rupture, etc. To summarize, the parameters characterizing the SB are listed below:

- Release pressure, p_0
- Release hole diameter, D_e
- Gas type
- Obstacle distance, l_{obs}
- Obstacle type, (cylinder, flat plate)
- Obstacle dimension, (d_{cyl}, L_{fp})

4.1.2 The *coupling* methodology

The term *coupling* refers to the interface between the SB and dispersion simulations. As mentioned in the model overview of section 2.3, the SB results represent the leak source in the dispersion, therefore, the *coupling* issue could be here translated in the necessity of defining which SB results to consider an how to use them. The simplest possible approach seems to consider the surface results on the outlet SB boundaries as boundary conditions (BCs) in the dispersion. At this point, it is crucial to identify a representative set of quantities and secondly define the simplest possible methodology to translate the SB results in a suitable form for the *dispersion*. Considering that the final aim of the analysis is the assessment of the accident consequences in terms of released flammable/toxic gas distribution in geometry, dangerous gas cloud volumes or areas at different heights, etc. the main interesting results of the dispersion simulation are the spatial distribution of the gas concentration and the velocity field. In the case of a HP gas leakage in an open environment, the development of the cloud is initially dominated by the jet inertia which is dissipated along the first part of the trajectory until its velocity becomes comparable to the wind one. In this sense, the leak source must be characterized by a velocity inlet in order to account for the inertia of the gas flowing in the SB. In addition, since the final gas concentration distribution is influenced by the initial quantity of pollutant released through the leak hole, the gas concentration in the SB is reasonably a crucial parameter too. It was decided to neglect the temperature field, after the observation that the strong mixing with the surrounding air causes the thermal equilibrium with the environment already within the SB, therefore thermal effects are not expected.

Basing on these considerations, the velocity field and the gas mass fraction distribution on the SB outlet faces, namely *back, lateral, front, up, down* in figure 4.1, are identified as the suitable quantities to be used as BCs in the dispersion simulation. For this purpose the gas leak source in the dispersion phase is modeled by a box with the same dimensions of the SB that is placed in correspondence of the leak point. On the faces of this box, the input BCs coming from the SB results are imposed, therefore, from the dispersion point of view it can be interpreted as a *black-box*, see figure 4.3.

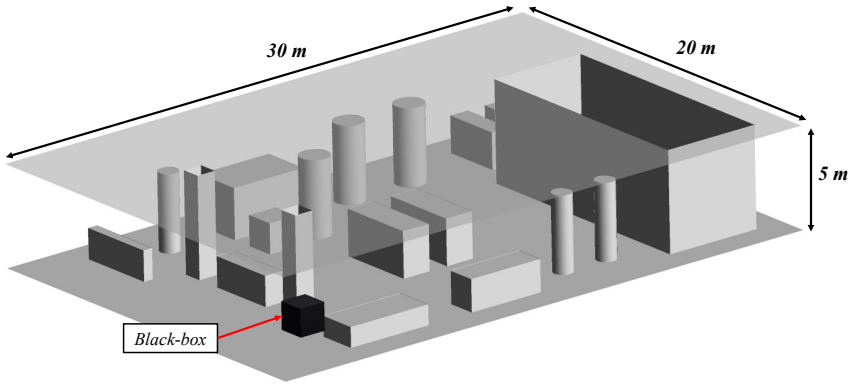

Fig. 4.3 Highlight on the *black-box* in the offshore platform deck CAD geometry.

Once the SB results are available, some manipulation of the data is necessary to make them suitable for the dispersion simulation. The gas mass fraction (m.f.) and velocity components on the SB outlet faces are saved and stored in a matrix with the corresponding coordinates (in the reference frame of the SB). Then, since only a quarter of the SB is simulated due to the exploitation of geometrical and BCs symmetries (see discussion in section 4.2.1), the m.f. and velocity profiles on the entire cubic surface are generated. Secondly, a rototranslation of the profiles is performed in order to correctly set the BCs according to the leak source and direction in the dispersion domain reference frame. In fact, the release direction in the SB is always along $\vec{x}$, while in the dispersion domain the release can have any orientation. All these manipulations are performed by a MATLAB script which generates a «.prof» file, suitable to be used in ANSYS Fluent as BCs. It is obvious that, the less is the data to process, the faster and simpler is the method. In this view, considering additional quantities which could be potentially relevant for the gas dispersion, for example related to turbulence, would be in contrast with the principle of making things the fastest and simplest possible. Hence, the model is tested considering only these two *coupling quantities* in the benchmark analysis from which it could be deduced if the accuracy of the coupling needs to be enhanced or if this approach is enough and can be maintained as it is. Another key point which has to be assessed concerns the level of accuracy needed for the dispersion BCs. In fact, the SB results on the outlet faces could be taken as area average values or detailed profiles storing the data for each grid node. On the one hand the first solution would largely simplify the method, on the other hand it could lead to relevant approximations. A sensitivity

analysis is presented in section 4.3 to define the best strategy according to the desired output accuracy.

4.1.3 Novelties of the model

At this point, having introduced all the main ingredients of the model, a more detailed representation of its logical scheme could be given as in figure 4.4.

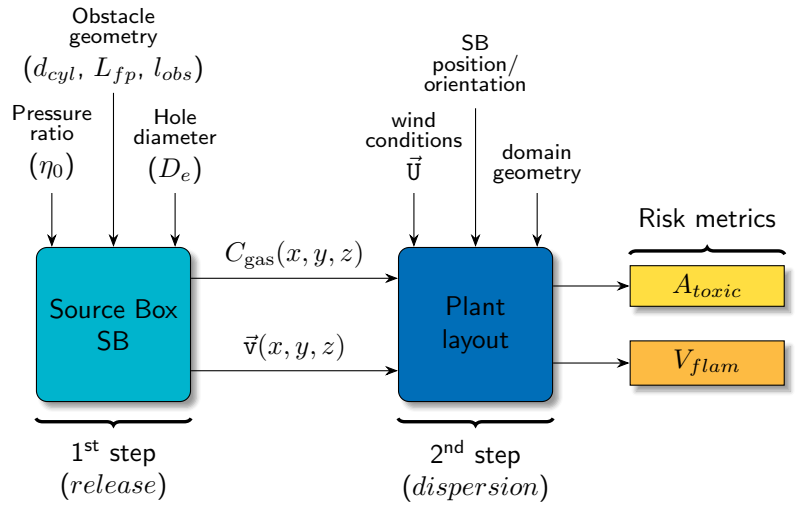

Fig. 4.4 Detailed logical scheme of SBAM.

The picture highlights the main SB inputs, the *coupling parameters*, which are the gas concentration ($C_{gas}(x,y,z)$) and velocity field ($\vec{v}(x,y,z)$) on the SB outlet faces and the dispersion simulation inputs. SBAM is realized in ANSYS Fluent and is intended for steady-state analysis. Referring to the SB, the transient until the underexpanded jet stabilization, takes $\sim$40 μs [69] that is a largely negligible time span from the safety analysis point of view, since monitoring system have a responding time of the order of seconds. Moreover, since the final target of the analysis is the evaluation of the consequences areas for a QRA, the steady-state configuration of the accidental scenario is of interest, i.e. when the gas cloud is fully developed and reaches its maximum extension. In this configuration, the results in terms of risk metrics as flammable cloud volume, toxic areas, etc., are obtained and can be used for safety considerations. With reference to the brief overview on literature of section 1.2.2, it comes out that there are mainly two approaches for

addressing these kind of scenarios through CFD: employing an empirical method for the initial jet expansion to evaluate an input for the CFD simulation [35, 36, 38–44] or using a full numerical approaches [50–52]. If the first ones are more oriented to a computational cost saving by approximating the underexpanded jet and the phenomenon occurring near the release point, the second ones guarantee a larger level of accuracy at the cost of huge computational efforts. SBAM is conceived to fit between these two approaches. Similarly to what is done in [35, 36, 38–44] the initial jet expansion is treated separately, but differently from these approaches it is resolved numerically seeking for a larger accuracy and permitting to consider an impingement near the release point. Moreover, splitting the scenario in two simulations permits to differentiate the numerical solution methods, and to employ *ad hoc* models for the compressible flow in the SB as well as to generate a sufficiently refined mesh to capture the underexpanded jet features. Whilst, similarly to what is proposed in [50–52] SBAM numerically solve the entire scenario, but seeking for a simplification of the simulation setup and a reduction of computational cost. To achieve this outcome, the SB, which is the key point of the model, is exploited. In fact, one of the advantages of SBAM is that one SB simulation can be used for several dispersion simulations by changing the position and directions of the source, i.e. the position of the *black-box* in the plant as well as its orientation, thus permitting the simulation of several initiators without re-calculating the SB. This lead to a considerable time saving both in the setup and calculation steps, since the dispersion simulation is easier and cheaper with respect to the SB one (as demonstrated in section 4.2), due to simpler physics assumptions and especially due to the absence of steep gradients which facilitates the mesh generation. Moreover, the same principle can be extended to a more general approach: the SB results can be used also for different case studies involving different installations. This last situation is realistic since despite each plant geometry differs from the others, the substances, the pressure levels, the typical rupture diameters, the type of equipment are similar, hence the SB can be representative for a wide range of industrial installations. For these purposes, a library of SB characterized by different input values could be generated in order to pick the results when it is necessary, or, in alternative a Reduced Order Model (ROM) of the SB could be designed to obtain results in few seconds. This last aspect is investigated in appendix B.

4.1.4 Model applicability range

At this point, with knowledge of the SBAM features and its target applications (described in chapter 3) some considerations about its limitations can be derived and its applicability range can be defined.

1. It can be applied only to gaseous releases. The model is tailored on HP gas releases and on their multi-physics nature, with particular attention to the modeling of the underexpanded jet phase. This kind of phenomenon is not relevant for liquid releases, while it could be for multiphase flows with extremely high gaseous percentages, which can be approximated to full gas releases. Multiphase flows with considerable liquid state percentages would lead to a different fluid dynamic behavior which can not be addressed by the model as it is.

2. Non reactant flows are considered. No chemical reactions are modeled in the SB or *dispersion* simulations, whilst only interaction of species. This could represent a possible follow up of the model, perhaps considering fires, but it would require new numerical benchmark analysis and additional validation activities.

3. Pressure ratio range $7 \leq \eta_0 \leq 100$. For the sake of simplicity, this criterion can be translated in terms of the release pressure assuming that the discharge ambient is p_a= 1 bar, and it becomes 7<p_0<100 bar. The upper limit can be extended ideally to any pressure, but for the moment is set due to the modeling capabilities of the SB simulations. In other words, the maximum pressure for which a convergent solution is obtained in the SB till now is 100 bar. As explained in appendix C, some convergence issues are experienced for the SB simulation due to its small size, as the release pressure is increased. On the other hand, the lower limit is set according to some *a priori* considerations. Having p_0>7 bar assure to have an extremely underexpanded jet which structure is characterized by a single normal shock in correspondence of the Mach disk (see section 2.1). Its position can be evaluated through an empirical correlation, and this permits to avoid a SB obstacle interaction with the Mach cell simply placing it at a distance l_{obs} larger than L_{MD}. Considering highly or moderately underexpanded jets where multiple shocks appear, would complicate the numerical solution since shocks-obstacle interactions could occur

and cannot be avoided by knowing *a priori* the shocks location. However, it must be remarked that the threshold of 7 bar comes from experimental observations, hence it is possible that also slightly lower pressure values lead to the formation of a single shock structure depending on the specific case (gas type, orifice shape, etc.). This means that the model is in principle applicable also to cases with $p_0 < 7$ bar, provided that a preliminary check on the numerical solution prove the formation of a single shock structure.

4. Limited SB length, L_{SB}. This limit is crucial to avoid that the SB size is comparable with the domain size, since in that case the splitting of the phenomenon in two steps would be meaningless. L_{SB} depends on D_e and η_0 (see Eq. 4.1), hence, a check on this criterion is necessary for each specific case study. As it is difficult to define a rigorous rule, a practical suggestion could be avoiding that the SB intersect domain objects, domain boundaries and assuring that L_{SB} is lower than the 20% of the domain longitudinal dimension.

5. Constraints on the dimension and distance of the SB obstacle. With reference to a cylindrical object, these two criteria have to be accomplished: $l_{obs} - d_{cyl}/2 > L_{MD}$ and $l_{obs} + d_{cyl}/2 < L_{SB}$. The first criterion is related to the discussion of point 3 about avoiding any Mach disk interaction with the obstacle. The second criterion is necessary to avoid that the object is tangent with the face *front* of the SB. In appendix B a more detailed discussion on this point is available.

6. The model is targeted for steady-state analysis. It would be impossible to couple the SB and the dispersion simulation in time. The only possibility is to use the SB steady-state solution as BC for a transient dispersion simulation, considering that the time scale of the release phase is negligible with respect to the dispersion one. But this last application would require some additional benchmark tests on the model to check for the final solution consistency.

7. The model is targeted to guarantee a suitable accuracy for QRA purposes, having in mind a massive use for hundreds of scenario. More specific analyses where the interest is not devoted to average estimations of the flow field are out of scope.

Note that with respect to the target applications defined in section 2.3, here some more restrictive limitations appear on the release pressure (point 3) and the geometry,

which is constrained by criteria 4 and 5. Finally, it must be remarked that despite the specific context (the O&G) in which SBAM is conceived, it is intended as a suitable model for any application which meets the applicability criteria.

4.2 Numerical benchmark analysis

The main objective of this analysis is to assess how the *two-steps* nature of SBAM affects the results, the simulation implementation and the computational cost with respect to a «classical» CFD approach. For this purpose, a reference simulation, here defined *benchmark* simulation, is realized in ANSYS Fluent according to a standard approach not involving the splitting of the phenomenon, but instead modeling the gas leakage directly in the case study environment. It was decided to perform the benchmark analysis considering case study cs#3 (see table 3.2) which main parameters are p_0=50 bar, D_e=3 cm and wind velocity $|\vec{U_2}|$=6 m/s. This is one with the largest degree of complexity, since involves non concordant release and wind directions and assures a strong gas cloud interaction with the platform equipment. A cylindrical obstacle is considered in front of the release point, at a distance l_{obs}=45 cm and with diameter d_{cyl}=30 cm to represent an impingement on a pipeline.

The benchmark simulation is realized with the philosophy of assuring the accuracy required by a QRA for the verification of a critical scenario. As an example, the turbulence closure problem is addressed through Reynolds Averaged Navier Stokes (RANS) models rather than more complex ones like Large Eddy Simulation (LES) or Direct Numerical Simulation (DNS), which are largely out of scope. In other words, having in mind the target accuracy, models, methods and mesh generation are tailored on the specific case study according to the state-of-the-art for CFD simulations. Hence, it can be stated that the benchmark simulation setup is conceived to be highly case study dependent. This philosophy is in opposition with the one of SBAM, which on the other hand is conceived to permit a simulation implementation the more independent as possible from the specific case study. The following sections present the simulations setup and a comparison between the SBAM dispersion simulation and the benchmark results, and also a discussion on practical advantages/disadvantages of SBAM.

4.2.1 SBAM simulations setup

Source Box simulation setup

At first the SB size is evaluated through Eq. 4.1 according to p_0=50 bar and D_e=3 cm, giving L_{SB}=1.38 m. It can be noted that the size is reasonably small and it is not in contrast with the point 4 of the model applicability range list (section 4.1.4). Before setting the simulation, the dimensionless numbers introduced in section 2.2 in Eq. 2.6, 2.7 and 2.8 are evaluated using the parameters of this specific case study in order to verify if the considerations derived on flow regimes are applicable. Since p_0=50 bar and the gas is discharged into atmospheric environment (p_a=1 bar) an *extremely* underexpanded jet forms (η_0=50), thus also requirement 3 of the model applicability range is fulfilled. Moreover, the condition $1/\eta_0 < R_{cr}$ is verified being $R_{cr} \sim 0.5$ for CH_4, hence, the resulting flow is critical and the gas discharge velocity u_e at the exit section (e) (see figure 4.2) is equal to the speed of sound. It is known that, having a chocked flow, the pressure in (e) is given by $p_e = R_{cr} \cdot p_0$. Assuming an adiabatic process between the inside conditions (0) and the exit section (e), the density ρ_e and the temperature T_e can be computed. Having that for methane γ=1.3 (adiabatic expansion coefficient) and $R \sim$519 J/(Kg·K) (gas constant), it results that $\rho_e = 20.2$ kg/m^3 and $u_e = \sqrt{\gamma \cdot R \cdot T_e}$=420.5 m/s. The remaining parameters are the dynamic viscosity of methane $\mu_e = 9.8 \cdot 10^{-6}$ Pa·s and the reference lengths assumed as $L_{Re} = d_{cyl}$ and $L_{Fr} = L_{SB}$, according to the definitions given in section 2.2. These values are obtained:

- $Fr \approx 114$
- $Re \approx 26 \cdot 10^7$
- $Ma = 1$

It can be noticed that the results are in line with the order of magnitude evaluated in section 2.2, in fact, Fr»1 suggests a highly inertia driven flow with no relevant buoyancy effects, Ma>0.3 hints that compressibility phenomena can not be neglected and Re>10^5 hints a highly turbulent flow. A *steady-state* formulation of the governing equations is solved and a *pressure-based* solver is employed. A Reynolds averaged formulation of the Navier-Stokes turbulent equations (RANS) is considered a proper compromise between accuracy and computational cost. A two-equations model,

the k-ω SST is employed as suggested by [80] for transonic flows (in the case of *extremely* underexpanded jets *Ma*»1 can verify). This model is validated for underexpanded jets in [51, 81] against the available experimental data [82]. The *viscous heating* term is considered in the turbulent model, as it is relevant for compressible flows [80]. A *species transport equation* is solved to model the gas species interaction without chemical reactions and the *ideal gas law* is used to compute the density at each iteration. The SB domain is reduced to $1/4$ due to the exploitation of some symmetries in the geometry and BCs. Two symmetry planes are defined, the *xy* and *xz* planes as shown in figure 4.5.

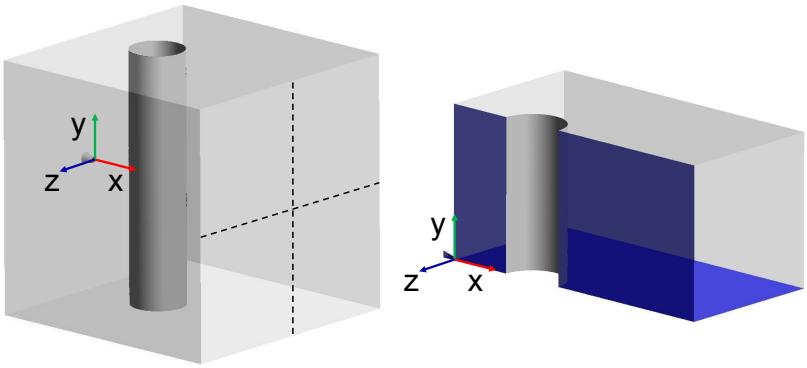

Fig. 4.5 Symmetries in the SB.

In particular, the symmetry plane *xy* can be defined since the turbulent wake past the cylinder is not in the Von Kármán vortex range, that is intrinsically non-symmetric. In fact, this effect is expected for $10<Re<10^4$, while in this case $Re>10^5$ suggest the presence of a fully developed turbulent wake [58]. Moreover, since a steady-state formulation of the RANS equations is solved, a steady-in-the-mean flow field is computed and fluctuations are neglected. This symmetry assumption is also confirmed by several authors dealing with a similar problem [83–85]. The BCs are imposed as in the following:

- Nozzle inlet: a *pressure inlet* is imposed. An absolute pressure equal to p_0 is prescribed, as well as a temperature equal to 300 K and a CH_4 mass fraction equal to 1
- SB faces: a *pressure outlet* is imposed. An absolute pressure equal to p_a is prescribed at the SB faces (back, front, lateral, up)

- Symmetry planes *xy* and *xz*: a *symmetry* boundary condition is imposed
- Cylinder and nozzle Walls: a *wall* with no-slip condition is imposed

A pressure-velocity *coupled* algorithm is employed. A *pseudo-transient* formulation of the governing equations is used to help the convergence of the solution by introducing the implicit relaxation terms. This helped the convergence by «relaxing» the solution but on the other hand made the required number of iterations grow. The solution convergence is judged considering the residuals and by monitoring two user defined quantities: the total released mass of CH_4 and the mean velocity on the outlet boundaries. A more detailed discussion on the governing equations and numerical methods is presented in appendix C. An unstructured mesh with tetrahedral elements in generated to optimize the elements distribution also in presence of round shapes [80]. The boundary layer on the cylinder wall is fully resolved, therefore a mesh refinement is generated through the *inflation layer* algorithm of ANSYS meshing assuring a y^+<1. A grid independence study was perform (see appendix C) to assess the solution independence from the grid size. The resulting mesh consisted in $\sim 4.5 \cdot 10^5$ elements with a minimum size of 1.75 mm near the release point and a maximum size of 0.4 m at the outlet faces.

Dispersion simulation setup

The domain of this simulation is shown in figure 3.1. Also in this case the flow regime is defined through Eqs. 2.6, 2.7 and 2.8. The wind intensity U_1 is assumed as a reference velocity and the properties of air at ambient conditions (since the mixture is mainly composed of air in the dispersion) are considered for the calculations: $\rho = 1.22$ kg/m^3, $\mu = 1.8 \cdot 10^{-5}$ Pa·s, $c = 347$ m/s. The reference length are here defined as L_{Re} =1 m (representative order of magnitude of the platform obstacles dimension) and $L_{Fr} = 5$ m (height of the deck). The resulting dimensionless numbers are:

- $Re \approx 4.07 \cdot 10^5$
- $Fr \approx 0.86$
- $Ma \approx 0.017$

Also in this case the results are in line with the order of magnitude evaluated in section 2.2. In fact, $Fr < 1$ hints that buoyancy forces can play a relevant role especially in the portion of the domain where the initial inertia of the jet is exhausted. It must be emphasized that the wind advection is the main driver of the gas species transport, therefore buoyancy can play a role only in some low inertia spots appearing behind the platform objects. Secondly, $Ma < 0.3$ assures that no compressible effects are expected in the domain and that the incompressibility assumption can be made for this simulation. Lastly, the flow is still in a fully turbulent condition since $Re > 10^5$. A *steady-state* solution is computed employing a *pressure-based* solver. The gravity forces term is included in the momentum equations. Also in this case RANS models are used for the turbulence closure problem, in particular, five different models are employed to make a comparison with the benchmark simulation: k-ω Standard, k-ω SST, k-ω BSL, k-ε Realizable (with standard wall functions), and k-ε RNG (with standard wall functions). The species interaction is modeled also in this case with a *species transport equation* neglecting chemical reactions. The BCs are set on the boundaries shown in figure 3.2 as in the following:

- b1-b2: a *velocity inlet* is imposed prescribing a velocity magnitude equal to U_1 and direction according to cs#3, and prescribing an absolute pressure equal to p_a
- b3-b4: a *pressure outlet* is imposed prescribing an absolute pressure equal to p_a
- Roof, ceiling and equipment sides: a *wall with no-slip condition* is imposed
- Black-box: a *velocity inlet* is imposed. The velocity components as well as the CH_4 m.f. profile obtained by the SB simulation (see example of results in figure 4.9) are prescribed.

The methods, numerical schemes and convergence criteria are analogous to the SB simulation one with the difference that no the relaxation terms are set fostering a fast convergence of the solution. The domain is discretized imposing a uniform mesh sizing in the core volume and setting face refinements on the objects faces. Moreover, a refinement on the walls is generated in order to obtain $30<y^+<300$, in such a way to employ wall functions for the boundary layer resolution with a consequent computational effort reduction with respect to a full numerical approach.

A tetrahedral unstructured mesh consisting of $\sim 4.5 \cdot 10^6$ elements is generated. A grid independence study is also performed to guarantee the spatial convergence of the solution. More details on models and mesh are discussed in appendix C.

4.2.2 Benchmark simulation setup

In this simulation the release is directly modeled in the case study domain, hence the nozzle discharges in the platform and the cylindrical obstacle is positioned in front of the release point, reproducing the same geometrical arrangement of the SB simulation (see figure 4.2). In figure 4.6 an enlarged view of the nozzle and the cylinder is shown.

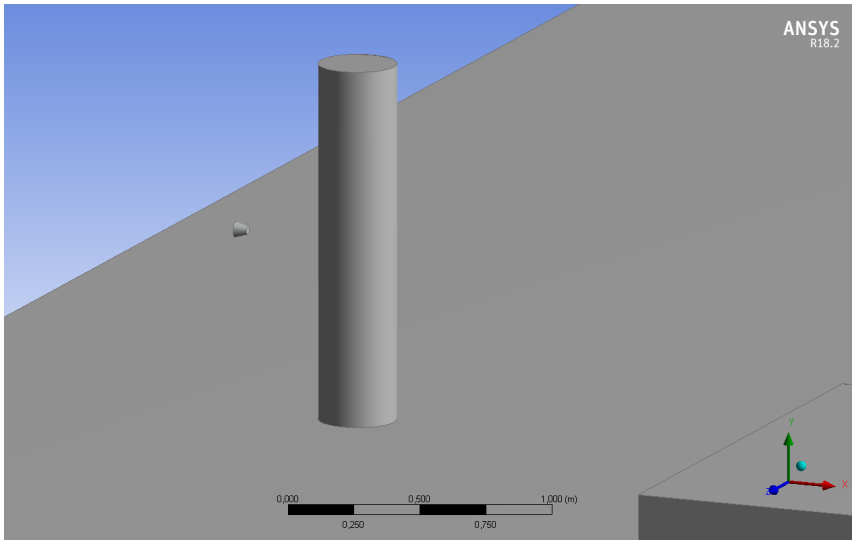

Fig. 4.6 Nozzle and cylindrical obstacle geometry in the benchmark simulation.

In this situation, the two flow regimes defined as the *release* and the *dispersion* are resolved in the same simulation, hence assumptions and models can not be differentiated. The mesh generation resulted the most challenging step of the analysis since a steep variation of the mesh elements dimension was necessary going from the release point to the far field region. A fine mesh is needed near the leak point to properly resolve the underexpanded jet, which consists of steep flow field gradients especially in the Mach disk region. On the other hand, far from the release point the flow field becomes smoother and a largely coarser mesh can be generated, especially in view of saving computational time or avoiding unsustainable memory requirements for the employed machine. The transition from the smallest to the

biggest cell had to be carefully addressed through the construction of several control volumes and the use of a 1.2 growth rate from one mesh region to the other. The smaller control volume is constructed around the nozzle and is characterized by a 0.005 m cell dimension while the biggest cell dimension reached in the domain is 0.4 m. A face refinement on the obstacles surfaces is realized setting the dimension at 0.15 m. A tetrahedral mesh consisting of $\sim 10^6$ elements is selected for the calculations after a grid independence study (see appendix C). Several attempts in the mesh construction were performed before reaching the optimal grid resolution to permit the calculations to converge. This was an extremely time consuming step in the pre-processing, and this hints the complexity of handling such a complex phenomenon. A *pressure-based* solver is used to obtain the *steady-state* solution. The *gravity forces* term in considered in the governing equations to capture the possible far field buoyancy phenomena. The k-ω SST model is employed as it is recommended for transonic flows (that in this case appear near the jet source) by [80] and the *viscous heating* term is enabled as it is relevant in compressible flows. A *species transport equation* is solved to model the CH_4-air interaction and the *ideal gas law* is selected to evaluate the density at each iteration. The BCs are set as in the following:

- Nozzle inlet: a *pressure inlet* is imposed. An absolute pressure equal to p_0 is prescribed, as well as temperature equal to 300 K and a CH_4 m.f. equal to 1
- b1-b2: a *velocity inlet* is imposed prescribing a velocity magnitude equal to U_1 and direction according to cs#3, and prescribing an absolute pressure equal to p_a
- b3-b4: a *pressure outlet* is imposed prescribing an absolute pressure equal to p_a
- Roof, ceiling and equipment sides: a *wall with no-slip condition* is imposed

The other setup parameters are setting analogously to the SB simulation and more details are available in appendix C.

4.2.3 Benchmark analysis results discussion

Source Box results

In figure 4.7(a) a 3D volume rendering, obtained by mirroring the solution with respect to the symmetry planes, is shown. The velocity distribution resembles the

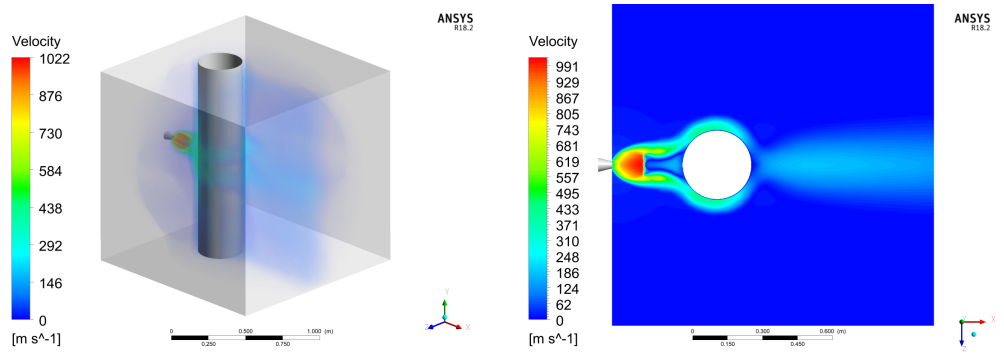

(a) 3D rendering of the extremely underexpanded jet.

(b) 2D contour plot of the extremely underexpanded jet.

Fig. 4.7 Benchmark analysis: Source Box results.

expected *extremely* underexpanded jet structure, in fact, the supersonic barrel shaped core is clearly visible in red. In this region the velocity grows up to over 1000 m/s and then rapidly decrease up to subsonic values (under 100 m/s). This strong discontinuity in the velocity field is representative of the Mach disk presence, where also a density, pressure an temperature discontinuity appear. These features are more appreciable from figure 4.7(b), in which a contour plot of the velocity on a transversal section (xz plane at y=0 m) of the SB is shown. From this plot it can be appreciated also that the largest inertia is concentrated in the near-field, while at the outer boundaries of the SB the flow is almost subsonic, thus confirming the first requirement for the SB sizing is met (see section 4.1.1). In addition, a strong Coanda effect [86] can be observed as the gas tends to attach to the cylinder and reconnects exiting from the domain as a single jet. To verify the solution consistency by a quantitative point of view the MD position obtained numerically is compared to the theoretical value evaluated through Eq. 2.5. Figure 4.8 shows the velocity profile along the jet axis in blue and the theoretical MD position in black. The discontinuity in the velocity profile is due to the presence of the cylindrical obstacle.

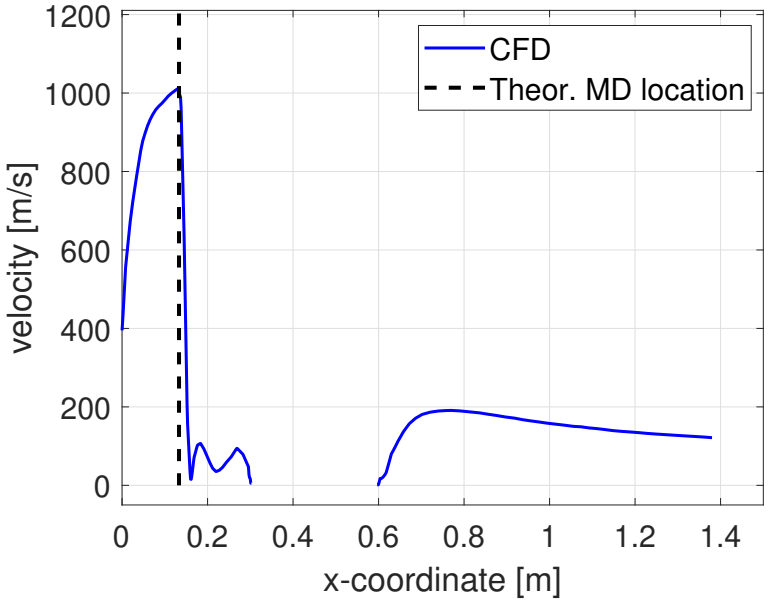

Fig. 4.8 Velocity profile along the jet centerline in the SB obtained through CFD and theoretical MD location evaluated through Eq. 2.5

The theoretical MD position is 0.133 m from the leak source, while the numerical one, evaluated as the velocity peak position, is 0.130 m, thus, its relative error with respect to the theoretical one is $\sim$2.5 %. This result hints that the solution has an acceptable accuracy and resembles the expected physical phenomenon. At this point, the discussion can be focused on the most relevant results of the SB, namely the velocity components and the CH_4 m.f. contours on the outlet faces. These lasts are of great importance since are used as BCs on the *black-box* in the dispersion simulation. Figure 4.9(a) and (b) show the velocity magnitude and CH_4 m.f. contours on the SB faces. Both the velocity and the gas concentration fields have peak values in the center. In fact the jet has enough space in the domain to reconnect downstream of the cylinder forming a single jet, which does not reach the lateral sides. On the other hand, the presence of the obstacle strongly deflects the jet upward and downward, generating a non-negligible exiting flow rate from the upper and lower faces. Its convergence was hardly reached especially due to the small dimensions of the domain, since outlet conditions are imposed too close to the high-inertia injection point and to the cylinder. In fact, in the case of external flows it is suggested to consider as bigger as possible domains, in order to impose the outlet BCs as far as possible from jet source locations and objects to permit a full development of the flow

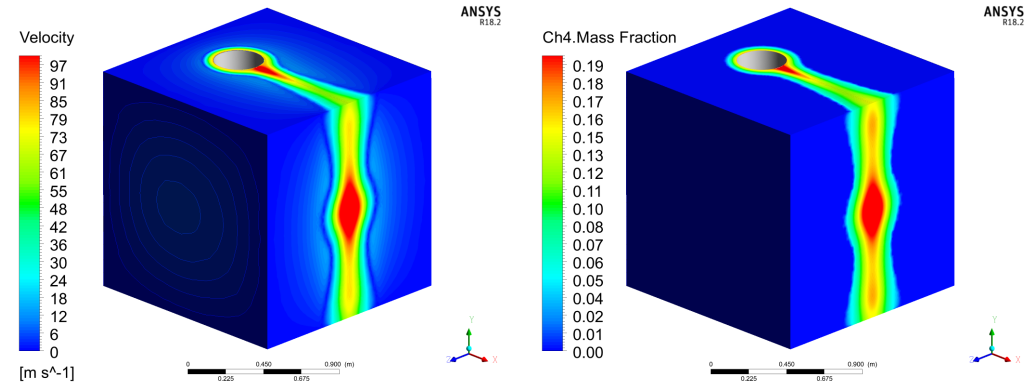

(a) Magnitude velocity contour plot on the outlet SB faces.

(b) CH_4 m.f. profile on the SB outlet faces.

Fig. 4.9 Source Box results: velocity and gas distribution on the outlet faces.

and avoiding high gradients at the boundaries. Convergence was helped by using low relaxation terms in the equations and the creating of a user defined function (udf) to handle the inlet high pressure ratio. The udf (see appendix C) permits to increase the inlet pressure linearly with the iterations in order to avoid a strong gradient at the first iterations and helping the solution stability. The simulation run took $\sim$24 h on a Dell Tower 7810 with a Intel Xeon e5-2630 CPU with a 2.4 GHz core frequency (8 cores-16 threads), a 64 GB RAM and 1 TB HDD. However, it must be remarked that the duration of this simulation is relatively irrelevant for the final considerations on the SBAM computational cost as the idea is to realize a library to store all the possible SB configurations (combinations of all possible values of D_e, p_0, d_{cyl}, l_{obs}) results making them ready for use for the analysis. In this sense only the dispersion simulation computational time must be considered. Alternatively, the feasibility of a Reduced Order Model of the SB is investigated in appendix B to obtain results in few seconds when necessary.

Numerical benchmark results

This analysis consists in the comparison of the SBAM dispersion simulations and the benchmark one in terms of quantitative and qualitative results, implementation flexibility, setup complexity and computational cost. As previously explained, five simulations are realized using SBAM employing the following turbulence models:

- k-ω Standard
- k-ω SST
- k-ω BSL
- k-ε Realizable (Standard Wall Functions)
- k-ε RNG (Standard Wall Functions)

The k-ε Standard model was not considered since nonphysical results were obtained. In fact, this model is mainly suggested for free-flows [80], and fails in modeling flow-objects interactions. At first, the solution of the benchmark simulation is discussed to check its physical consistency. In figure 4.10 a velocity contour plot is shown (b), with a zoomed view on the jet nearfield (a). The zoomed view on the nearfield highlights a strong discontinuity in the velocity field which reflects the presence of the MD after a potential core (in red). The structure of an extremely underexpanded jet is correctly reproduced hinting that the physical expectations are satisfied. This portion of the flow field appear similar to the one obtained in the SB simulation, but some differences arises in the flow downstream the cylinder. In fact, if on the one hand the Coanda effect can be appreciated also in this case, on the other hand the flow direction after the cylinder is no more aligned with the jet axis. This can be explained considering that the jet direction is influenced by the wind field as soon as the gas is released. This phenomenon is neglected in the SB simulation, where the wind is not considered and the jet is aligned with the release axis, see figure 4.7. The necessity to use the SB results as a source for any dispersion case study imposes to have the more generic approach possible in order to make the results adaptable to any configuration of external wind velocity. This approximation can be one of the causes of the differences arising between the SBAM and the benchmark results, which are quantified in terms of percentage errors on some relevant risk related quantities in

the following discussion. At first, the comparison is made on a qualitative basis by comparing the velocity field and the distribution of the gas cloud.

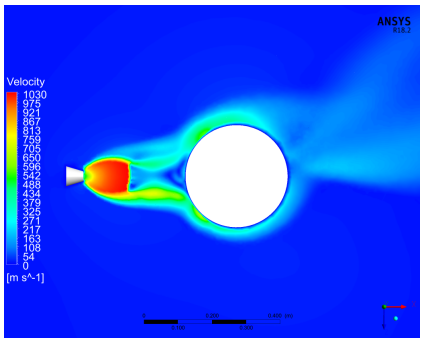

(a) Zoomed visualization of the velocity field near the release point on a *xz* section at *y*=1.5 m.

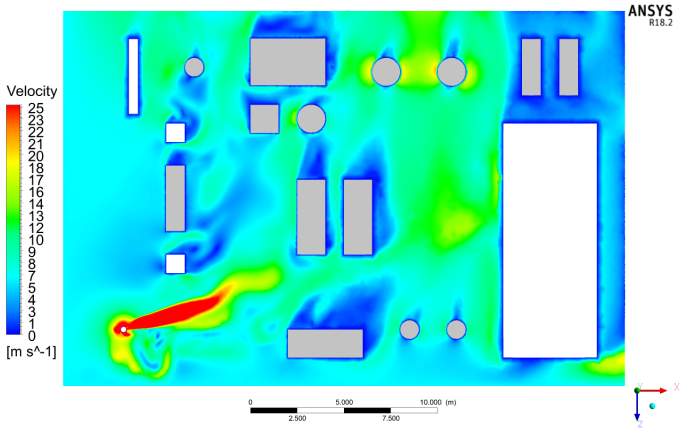

(b) Velocity contour plot on a *xz* section at *y*=1.5 m on the entire platform.

Fig. 4.10 Benchmark simulation velocity field.

The velocity streamlines on a transversal plane (*xz*) at *y*=1.5 m are compared in figure 4.11 to discuss the differences and analogies in the resulting flow fields. The black square in the bottom left corner of the SBAM plots is the *black-box* placed in correspondence of the leak location. The velocity field resemble the wind direction in all the simulations, and a high inertia region can be observed after the release point (in red) where the gas jet inertia is still dominant. Recirculation regions past the obstacles appear in all the simulations, due to the drop of pressure behind the objects. The velocity fields of the SBAM simulations are similar except for the k-ω BSL one which presents a faster dissipation of the initial jet inertia as the red zone

appear shorter and more influenced by the wind convection. Qualitatively the red high inertia region has a different shape in the benchmark simulation with respect to all the SBAM ones. In these lasts the inertia seems larger, as a plume shape can be observed, while in the benchmark one it is faster dissipated and these jet portion appears more distorted. The explanation could lie in the fact that the wind interacts in the nearfield of the jet, while applying SBAM, the portion of the jet simulated in the SB is not interacting with the wind inertia, so it maintains its own inertia till it exits the SB. Notwithstanding the approximation introduced splitting the phenomenon in two simulations, the overall flow field of the SBAM simulations qualitatively resemble the benchmark one. Going further, the CH_4 distribution is also compared in terms of High Lethality (HL) and Irreversible Injuries (II) areas, defined in chapter 3, on a *xz* plane at *y*=1.5 m, being this a reference height for safety considerations since is representative of human targets. In all the simulations the II areas, shown in figure 4.12, are obviously influenced by the wind inertia which transport the pollutant according to its direction. Almost the same platform area is involved, and the same elements are touched by this area except for the case of the SBAM k-ω BSL (figure 4.12 (d)) in which the area resulted smaller suggesting an underestimation with respect to the benchmark simulation. The HL areas, shown in figure 4.13, seem relevantly influenced by the high inertia region discussed before. The SBAM k-ε Realizable gives the more qualitatively similar result to the benchmark since the area extends till the boundary of the domain and the same elements of the platform are involved. The SBAM k-ω BSL has the worst performance also in this case confirming the results of the velocity field and the II areas since an underestimation is clearly noticeable.

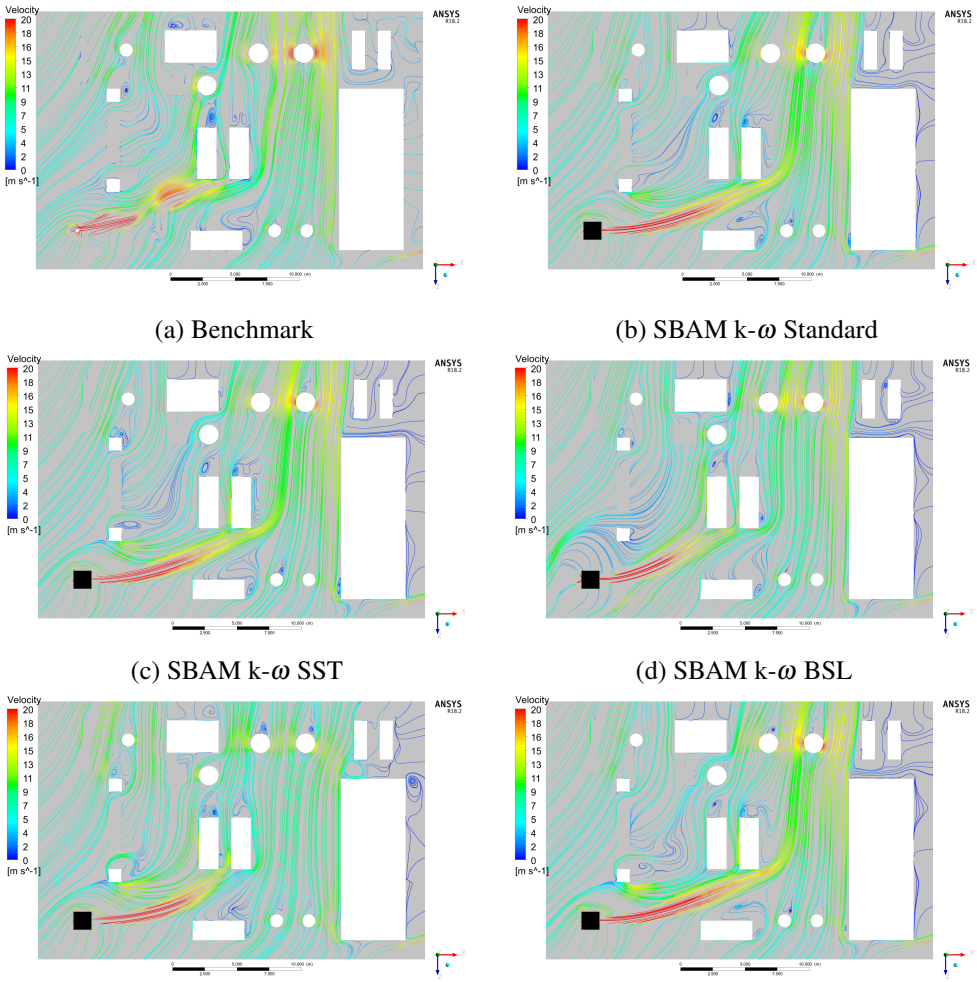

(a) Benchmark

(b) SBAM k-ω Standard

(c) SBAM k-ω SST

(d) SBAM k-ω BSL

(e) SBAM k-ε Realizable

(f) SBAM k-ε RNG

Fig. 4.11 Comparison of the velocity streamlines on a xz plane at y=1.5 m obtained in the benchmark and SBAM simulations.

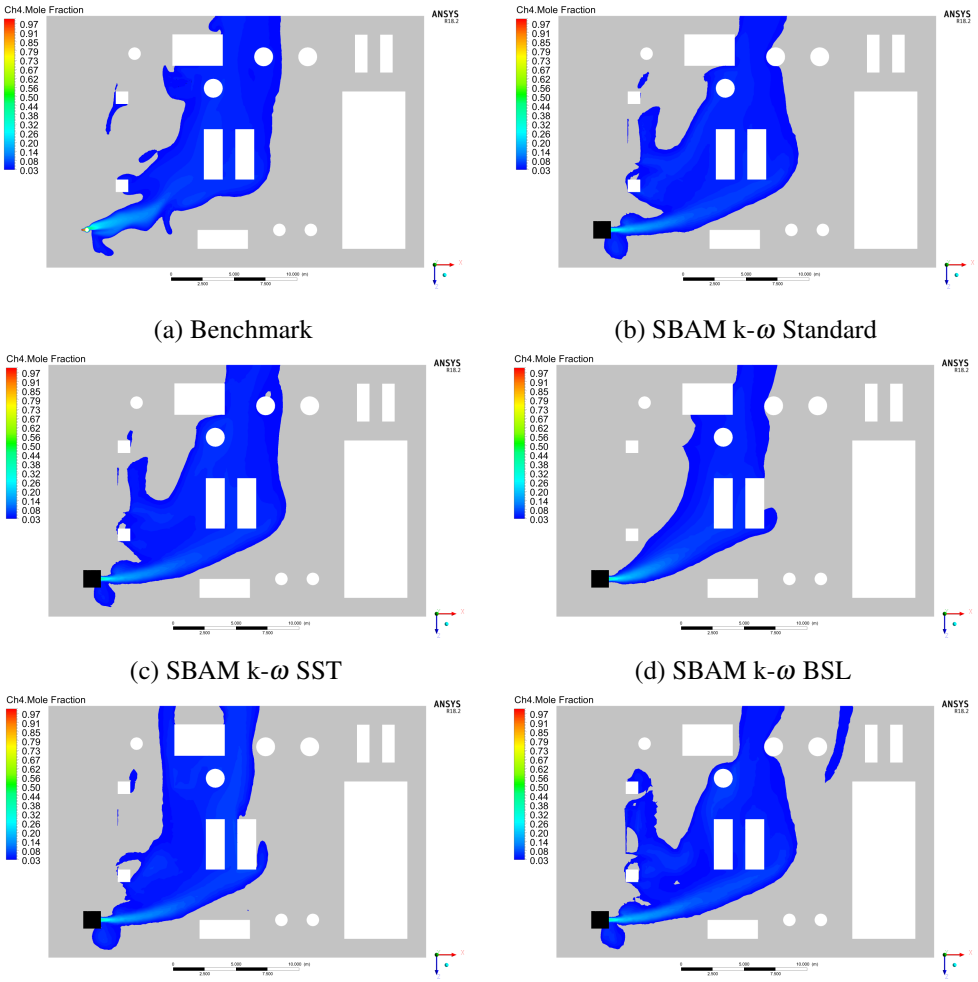

(a) Benchmark

(b) SBAM k-ω Standard

(c) SBAM k-ω SST

(d) SBAM k-ω BSL

(e) SBAM k-ε Realizable

(f) SBAM k-ε RNG

Fig. 4.12 Irreversible Injuries areas on a *xz* plane at *y*=1.5 m obtained in the benchmark and SBAM simulations.

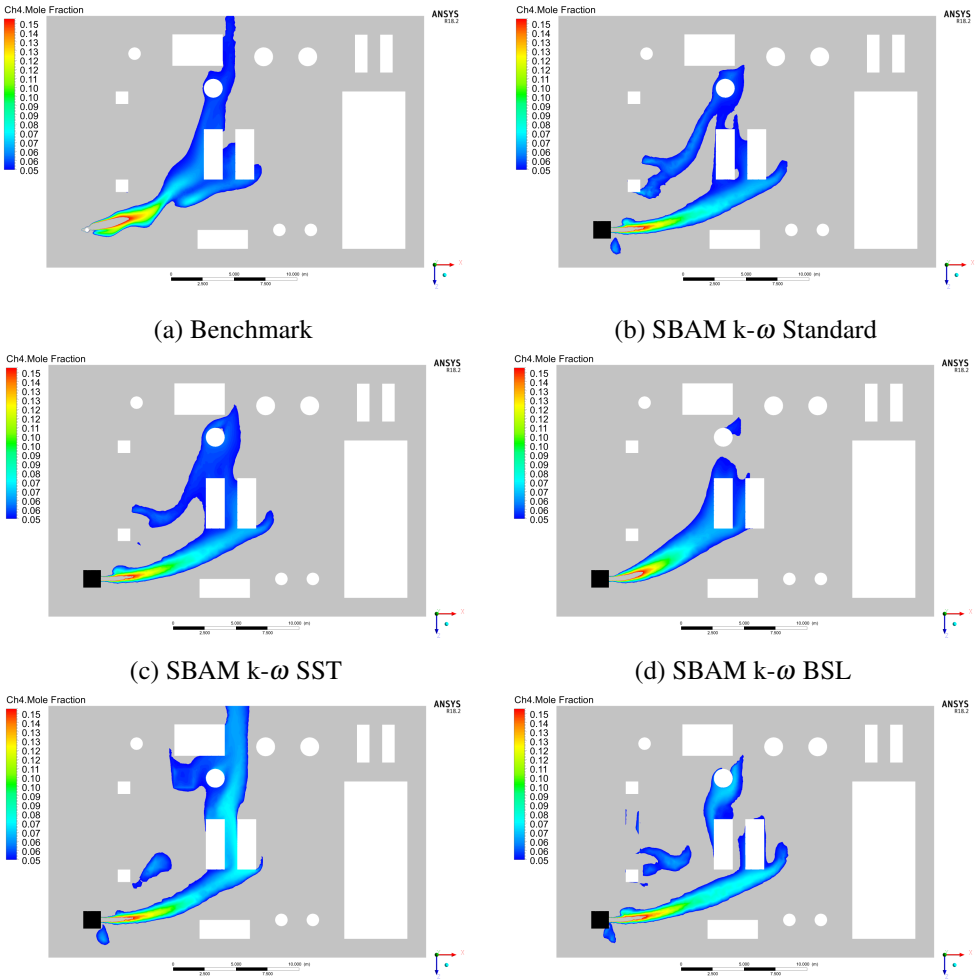

(a) Benchmark

(b) SBAM k-ω Standard

(c) SBAM k-ω SST

(d) SBAM k-ω BSL

(e) SBAM k-ε Realizable

(f) SBAM k-ε RNG

Fig. 4.13 High Lethality areas on a *xz* plane at *y*=1.5 m obtained in the benchmark and SBAM simulations.

A better visualization of the HL zones is given in figure 4.14, where the flammable cloud in shown in 3D.

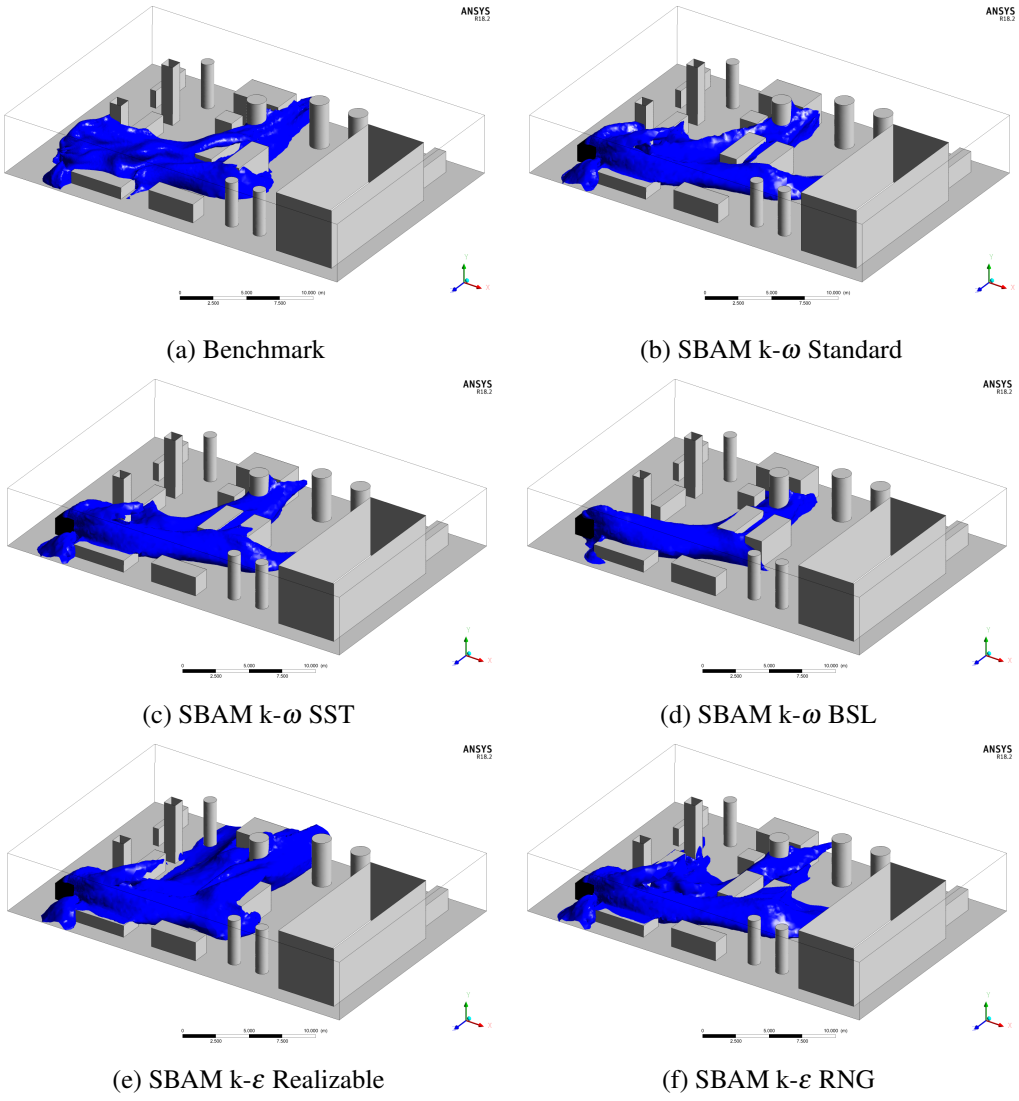

(a) Benchmark

(b) SBAM k-ω Standard

(c) SBAM k-ω SST

(d) SBAM k-ω BSL

(e) SBAM k-ε Realizable

(f) SBAM k-ε RNG

Fig. 4.14 Flammable volumes 3D rendering obtained in the benchmark and SBAM simulations.

From this pictures some new relevant information can be gained, the SBAM k-ε Realizable seems to overestimate the volume as the two blocks in the center of the platform are completely covered by the cloud. The SBAM k-ω BSL underestimation is more evident from this perspective and the k-ω SST and k-ω Standard give both similar results with respect to the benchmark. At least from a qualitatively point of view, the approximations introduced by SBAM especially due to the coupling

seem not relevantly affecting the final solution. The qualitative analysis of the results is useful to identify dangerous areas where an ignition can occur causing fires or explosions hence producing damages to workers/people and structures. Nonetheless, some risk related quantities must be evaluated to quantify the possible damages and to evaluate the energy involved in case of ignition. For these purposes some metrics are defined:

- M_{CH4} [kg], the total mass of CH_4 in the domain
- V_{flam} [m^3], the flammable cloud volume
- Σ_v [-], the ratio between the flammable cloud volume and the domain volume (V_{flam}/V_{domain})
- A_{flam} [m^2], the flammable area @ y=1.5 m
- $M_{CH4flam}$ [kg], the CH_4 mass contained in the flammable cloud
- Σ_m [-], the ratio between the CH_4 mass contained in the flammable cloud and the total mass of CH_4 in the domain ($M_{CH4flam}/M_{CH4}$)

Some quantities like M_{CH4}, V_{flam}, $M_{CH4flam}$ are useful for quantifying the effects of a possible fire or explosions through some empirical models as well as the A_{flam} which is typically used for safety considerations to establish the damage area. The other parameters, Σ_v and Σ_m can be useful risk metrics to give an idea on the proportions of the accident in relative terms. Table 4.1 summarize the results while table 4.2 presents the relative difference between SBAM and the benchmark. The considerations on the SBAM k-ω BSL deduced by the observations on the II, HL areas and flammable volume plots are confirmed also by the quantitative results as a clear underestimation of all the parameters is noticeable. Negative relative differences are obtained for all the parameters, hinting a systematic underestimation which cannot be accepted, hence, this model can be defined the worst performing one and it will be excluded from further analysis. M_{CH4} is consistently predicted by all the SBAM simulations guaranteeing at least a conservation of the total mass involved in the accident. The more different value is given by the SBAM k-ω Standard, overestimation by $\sim$3 kg (+18 %), while the more similar value is obtained with the k-ε Realizable (+8.6 %). On the other hand this model has the worst performance in all the other parameters, which are certainly more relevant for safety considerations.

	Benchmark	SBAM dispersion simulations				
		k-ω SST	k-ω Standard	k-ω BSL	k-ε Realizable	k-ε RNG
M_{CH4} [kg]	15.248	17.589	18.000	11.558	16.553	17.292
V_{flam} [m^3]	117.455	137.287	135.867	80.265	191.038	132.852
Σ_v [-]	0.046	0.054	0.053	0.031	0.075	0.052
A_{flam} [m^2]	39.493	44.024	41.034	27.086	52.592	36.770
$M_{CH4flam}$ [kg]	4.866	6.063	6.117	3.460	8.244	6.081
Σ_m [-]	0.319	0.345	0.340	0.299	0.498	0.352

Table 4.1 Risk metrics comparison between benchmark simulation and SBAM dispersions.

	SBAM dispersion simulations				
	k-ω SST	k-ω Standard	k-ω BSL	k-ε Realizable	k-ε RNG
M_{CH4} [kg]	+15.358 %	+18.051 %	-24.200 %	+8.560 %	+13.409 %
V_{flam} [m^3]	+16.885 %	+15.676 %	-31.663 %	+62.648 %	+13.109 %
Σ_v [-]	+16.885 %	+15.676 %	-31.663 %	+62.648 %	+13.109 %
A_{flam} [m^2]	+11.473 %	+3.902 %	-31.415 %	+33.167 %	-6.895 %
$M_{CH4flam}$ [kg]	+24.610 %	+25.711 %	-28.883 %	+69.429 %	+24.975 %
Σ_m [-]	+8.020 %	+6.488 %	-6.178 %	+56.068 %	+10.199 %

Table 4.2 Risk metrics percentage difference between benchmark simulation and SBAM dispersions.

This can be clearly observed in table 4.2 where extremely large relative errors appear. A_{flam} is overestimated by more than 30 %, while $M_{CH4flam}$, V_{flam} and Σ_v by more than 60 % hinting a not acceptable overestimation of the potential hazard. Among the remaining models, the k-ω Standard is the more accurate. In fact, the k-ε RNG has low relative errors with respect to the benchmark simulation, but it tends to underestimate A_{flam}, and this is in contrast with the conservative approach used in the safety field. The k-ω Standard resulted more accurate in 4 parameters out of 6 with respect to the k-ω SST and does not produce underestimations in any of the metrics. It can be deduced that the k-ω Standard is more suitable model to be employed in the SBAM dispersion simulations.

The last discussion concerns the implementation and computational time. The pre-processing, in particular the mesh generation, in the benchmark simulation was the most challenging step for the reasons described in section 4.2.2. Finding an optimal space discretization observing the constraints imposed by the necessity of a highly refined mesh in the jet nearfield region, and avoiding an unsustainable memory requirement for the employed machine was a time consuming task. On the other hand, SBAM permits to handle the mesh in a simpler way. In the SB, the optimal mesh size for the Mach disk region can be easily realized since the simulation domain is largely reduced with respect to the platform. Meanwhile in the dispersion simulation, where no steep variations of the variables are expected in the domain, a simple uniform core mesh with face refinements on the objects can be generated in a relatively short time. Concerning the computational time, the comparison regards the benchmark simulation and the SBAM dispersion simulations, since, in principle the SB results have to be considered already available in a database or provided by a Reduced Order Model (as explained in section 4.1.3). A direct comparison of the computational cost is possible since the same machine, a Dell Tower 7810 with a Intel Xeon e5-2630 CPU with a 2.4 GHz core frequency (8 cores-16 threads), a 64 GB RAM and 1 TB HDD, is employed for all the calculations. The benchmark simulation run took $\sim$24 h, while each SBAM dispersion run took $\sim$2 h to obtain the same level of convergence of the solution. This hints that the time employed for a single run using a standard CFD approach can be used for $\sim$10 SBAM runs obtaining a comparable accuracy in the results and a considerable simplification in the implementation, especially regarding the mesh generation. From this outcome, it can be deduced that with respect to classical full numerical approaches like the one proposed in [50–52] and to which the benchmark simulation is inspired, SBAM can effectively lead to a computational cost reduction.

It must be pointed out that all the previous considerations come from the analysis of a single case study, which cannot be considered representative of all the possible scenarios, hence, some of the outcomes can be generalized while others have a more restricted validity. On the other hand, the selection of this particular case study responded to the aim of considering one with the largest degree of complexity. The combination of release position, direction and wind direction is such that the dangerous cloud involve the largest part of the domain, causing a strong interaction with the platform equipment. Moreover, having a massive gas presence in the domain assured significant estimations on the risk metrics, permitting a reasonable

quantitative comparison through percentage deviations. In addition, considering non concordant release and wind directions adds an extra degree of complexity with respect to the concordant case. For this reasons, this single case study approach can be considered suitable for this analysis, and additionally because adopting a brute force approach by extending this analysis to several case studies would be unsustainable in terms of time and resources.

However, if on the one hand the outcomes about the accuracy of the results in terms of percentage differences on the risk metrics are highly case study dependent, on the other hand having considered one of the more complex configurations suggests that in simpler ones even lower discrepancies would be obtained. Moreover, considerations about the simplification of the implementation especially related to the mesh generation can be generalized, because are case study independent. No matter the case study, the splitting of the phenomenon lead to a simplification of the mesh generation in the case study environment, consequently having a lighter mesh causes a reduction of computational load, hence, consequently also considerations on the computational cost could be generalized.

4.3 Sensitivity study on *coupling* parameters

This sensitivity analysis has the aim to assess which level of detail is necessary in the coupling step, i.e. which level of detail to consider for the BCs to be imposed on the *black-box* in figure 3.1. These BCs are derived from the SB simulation by taking the velocity and m.f. values on the SB faces. These can be exported as area averages or detailed profile by storing data for each SB face grid point. This analysis aims at investigating the possibility of simplifying the *coupling* phase by using average values instead of detailed velocity and m.f. profiles by quantifying the impact of the different level of details of these BCs on the final results. The effect of velocity and the m.f. are studied independently, realizing two parallel analyses consisting of three simulations each. At first, three level of details are defined for the velocity BCs:

- Averages of the 3 velocity components
- Simple discretization of the 3 velocity components
- Continuous profiles of the 3 velocity components

Then, three level of details are defined for the m.f. BCs:

- Averages of the m.f.
- Simple discretization of the m.f.
- Continuous profiles of the m.f.

Average values are obtained as area weighted averages on the SB faces: this is the lowest possible level of detail. The profiles are the most detailed possible exportation of the results, which depends on the mesh grid of the SB simulation. The discretization is a rough representation of the profiles, both of the velocity components or the m.f., and represent a medium level of detail. It is obtained by roughly discretizing the profiles, basing on a qualitative analysis of the distribution on the SB faces. As an example, considering the SB faces nomenclature introduced in figure 4.1, the face *front* is taken as a reference and a possible discretization example for the velocity components is shown in figure 4.15.

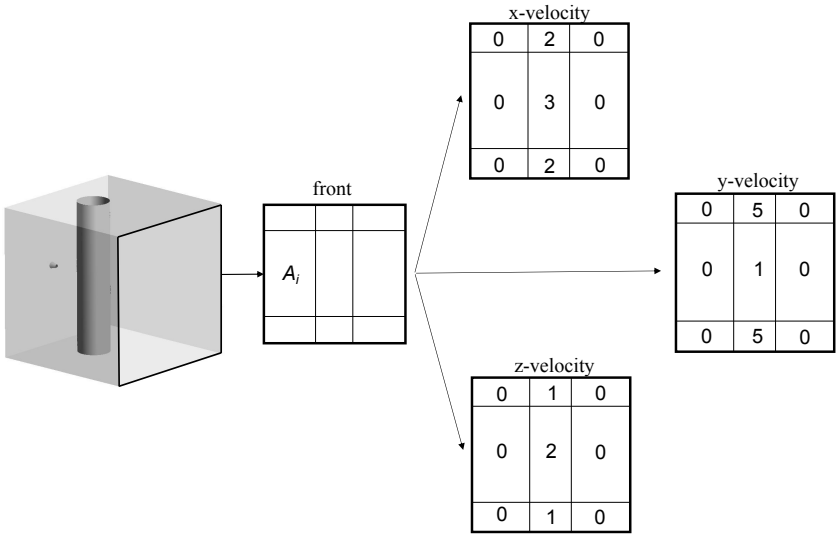

Fig. 4.15 Example of SB face discretization.

The face is discretized in smaller rectangles of area A_i, where the pedex i goes from 1 to N total number of rectangles. A different weight, $w_{j,i}$ is qualitatively assigned to each rectangle i to represent the j-th velocity component distribution on the face (the higher the value the higher the weight). In fig. 4.15 an example of weighting is shown for the 3 velocity components. For each rectangle i the relative

Simulation N°	Gas concentration BCs	Velocity BCs
1	Continuous profiles of m.f.	average of velocity components
2	Continuous profiles of m.f.	Simple discretization of velocity components
3	Continuous profiles of m.f.	average of velocity components

Table 4.3 BCs settings of the simulations for the sensitivity analysis on velocity BCs.

j-th velocity component value $u_{j,i}$ is derived according to the weight value $w_{j,i}$ by satisfying the flowrate balance in Eq. 4.2.

$$A_{face} \cdot u_{j,ave} = \sum_{i=1}^{N} A_i \cdot u_{j,i} \tag{4.2}$$

With A_{face} area of the considered face, in this case front, $u_{j,ave}$ j-th velocity component average value on that face, and N total number of discretization rectangles. The m.f. BCs are defined following the same procedure, with the difference that being the m.f. a scalar value, the procedure is simplified. The sensitivity analysis on the velocity BC is performed considering three simulation where the most detailed m.f. BCs are used and the velocity BCs are varied according to table 4.3. The third simulation is the most accurate, hence simulation 1 and 2 will be compared to this one in the discussion. A specular path is followed to realize the m.f. sensitivity analysis, as the velocity BC is kept constant at the most detailed level and the m.f. BC is varied according to table 4.4. It must be noted that simulations 3 and 6 coincides, as both employ the same BCs, but different names are assigned in order to simplify the discussion. Using average values or simple discretizations instead

Simulation N°	Gas concentration BCs	Velocity BCs
4	Average of m.f.	Continuous profiles of velocity components
5	Simple discretization of m.f.	Continuous profiles of velocity components
6	Continuous profiles of m.f.	Continuous profiles of velocity components

Table 4.4 BCs settings of the simulations for the sensitivity analysis on m.f. BCs.

of the profiles can represent an advantage in terms of coupling simplification. In fact, using the profiles requires to generate a refined mesh on the *black-box*, while in the case of average values, the mesh can be arbitrarily coarser and in the case of the discretization the mesh size can be at least equivalent to the discretization boxes size. Also this analysis, as for the *benchmark*, is carried out on the case study cs#3 described in 3.2 using d_{cyl}=30 cm and l_{obs}=45 cm. The numerical implementation is the same described in section 4.2.1, with the only difference that the BCs on the *black-box* are varied according to tables 4.3 and 4.4.

4.3.1 Sensitivity study results

At first the results related to the velocity BCs sensitivity analysis are discussed. The effects of the different BCs setting are evaluated in terms of two risk-relevant quantities that are the flammable volume V_{flam} and the flammable area at a 1.5 m height A_{flam}. Figure 4.16 show that both quantities tend to increase as the level of detail of the velocity BC increase.

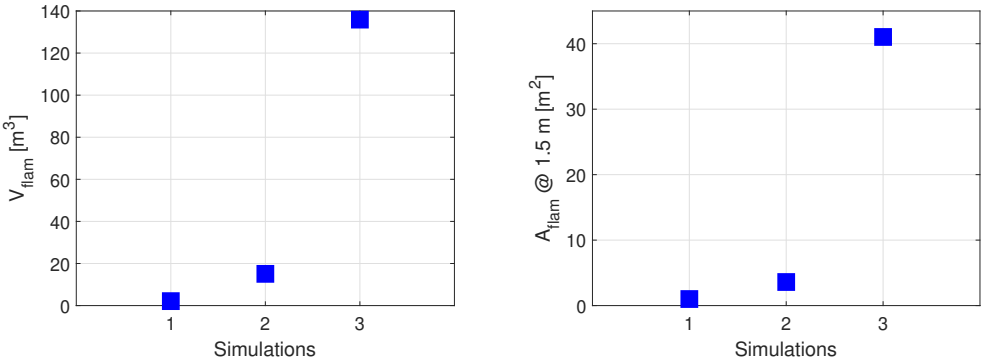

(a) Flammable volume variation as the velocity BCs level of detail increase

(b) Flammable area at 1.5 m variation as the velocity BCs level of detail increase

Fig. 4.16 Results of the sensitivity study on the velocity BCs imposed on the black-box

Furthermore, simulations 1 and 2 largely underestimate the flammable quantities with respect to simulation 3, which is the most accurate, by ∼7 times. The explanation of these large difference in the flammable quantities can be explained looking at the CH_4 m.f. distribution on the SB faces, figure 4.9(b). The peak concentration is in the center, while it steeply decreases going towards the lateral sides. In this sense it can be deduced that the central portion of the profile has a higher *importance*

with respect to the external one, as the largest part of the gas in concentrated here. The concept of *importance* is here referred to concentration levels of the release gas: from a consequences analysis point of view, regions with higher gas concentrations are more *important* than the other, in the sense that are more relevant. If this gas is transported by a uniform average velocity, as in simulation 1, all the gas regions on the face are equally transported and the mixture is carried out slowly in the domain, helping the mixing with the surrounding air. Differently, in case 3, the central m.f. peak region is transported with a higher velocity (see velocity profiles in figure 4.9(a)), meaning that the highest importance region is transported in the domain with a higher inertia leading to an more extended region with high concentration in the domain. Simulation 2 gives a coherent result since as the level of detail of the velocity BCs is slightly increased, the estimated V_{flam} and A_{flam} tend to increase with respect to simulation 1, nonetheless the underestimation remains unacceptable. Figure 4.17 show the results of the sensitivity analysis on the CH_4 m.f. BCs.

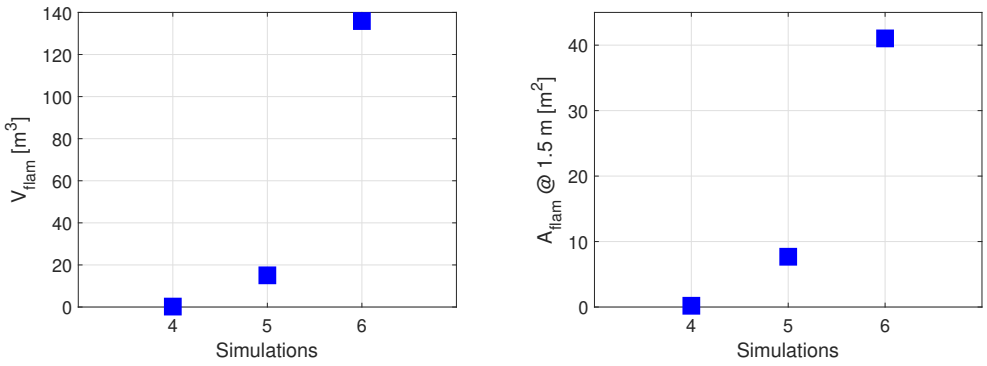

(a) Flammable volume variation as the CH_4 m.f. BCs level of detail increase

(b) Flammable area at 1.5 m variation as the CH_4 m.f. BCs level of detail increase

Fig. 4.17 Results of the sensitivity study on the CH_4 m.f. BCs imposed on the black-box

The results are in accordance with the previous ones, since a large underestimation of the two quantities is observed also in this case. Using a uniform averaged m.f. value as BC, as in simulation 4, causes a dramatic underestimation by two orders of magnitude of V_{flam} and by one order of magnitude of the A_{flam}. After the averaging process, the peak concentration values of the profiles, see figure 4.9(b), disappear as the gas is uniformly distributed on the faces. Since the concentrations levels are already lowered by the averaging process, it is easily understandable that regions with a concentration level larger than the LFL are unlikely to verify, as a

low CH_4 concentration mixture is spread into the domain. Coherently, simulation 5 gives a slight increment on the estimation of the flammable quantities since the level of detail of the CH_4 m.f. is enhanced, nonetheless the underestimation with respect to the simulation 6 is not acceptable. It can be concluded that the use of the velocity and CH_4 m.f. profiles as they are exported from the SB simulation is necessary. In fact, using averaged values lead to dangerous underestimations of the risk-relevant quantities which can not be accepted in a QRA view. On the other hand, it could have represented an advantage in terms of methodology simplification in the coupling phase and also in the mesh generation in the dispersion simulation. In fact, keeping the profiles as they are exported from the SB means generating a mesh refinement on the *black-box* faces suitable for a correct mapping of these lasts on the new mesh. On the contrary, using only the average values or rough representation of the profiles would not require such level of discretization refinement.

Chapter 5

Experimental investigations and model validation

In this chapter, the SBAM experimental validation is discussed. It is worth mentioning that the part of the work related to the experimental activities, would not be possible without the collaboration of the other members of the SEADOG group. The case studies introduced in chapter 3 are reproduced experimentally, and the results in terms of gas concentration in the domain are used as a reference for a comparison with the model output. At first, on overview on the experimental facility is given. Secondly, a scaling procedure for high-pressure gas releases under wind conditions is presented. The set of case studies introduced in table 3.2 is translated in the corresponding set to be reproduced in the experimental facility, assuring the fluid dynamic similitude. A brief description of the numerical setup of the scaled cases simulations is presented. Lastly, the numerical and experimental results are compared in terms of gas concentration in correspondence of the measuring points inside the platform and some statistical parameters are employed to discuss the SBAM prediction capabilities and to judge its accuracy. Part of the work presented in this chapter was previously published in Moscatello et al. [55, 57] and Gerboni et al. [56].

5.1 Experimental setup

5.1.1 Wind Tunnel

The tests were carried out in the SEASTAR wind tunnel (WT) [54], an infrastructure born in the framework of a research activity for the O&G sector safety enhancement, funded by the Italian Ministry of Economic Development (MiSE). It is an atmospheric subsonic open circuit wind tunnel with a rectangular open-jet test section, which schematic representation is proposed in figure 5.1.

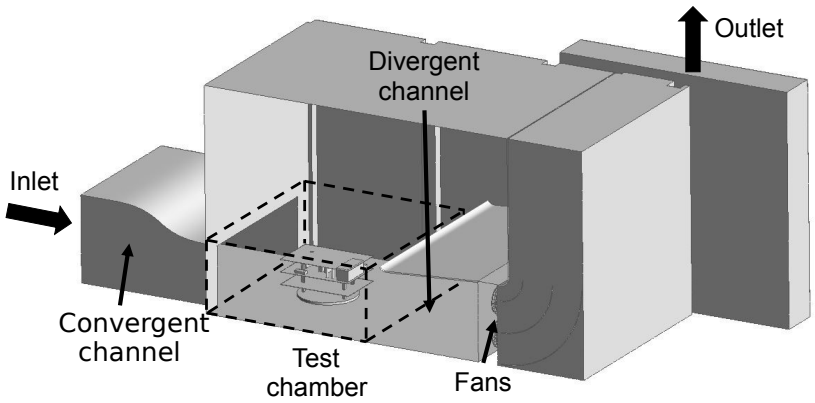

Fig. 5.1 Schematic representation of the SEASTAR wind tunnel.

It is composed of a contraction section (convergent channel), a test chamber and a diffusion section (divergent channel) which terminates in a panel encapsulating a set of ten fans, which can be appreciated in a frontal view from figure 5.2.

Fig. 5.2 SEASTAR wind tunnel picture from the inlet point of view.

The air is taken from the inlet through a honeycomb structure which homogenise and align the flow as well as blocks the biggest impurities from the external environment. The air flows through the convergent channel which assures an almost uniform flow in the test chamber, and it is later expelled outside the building from the outlet section. The fans work in suction mode, therefore the air is entrained inside the test chamber and forced outside. The facility is completed with a Control Room that is positioned above the test chamber so that operations in the tunnel can also be directly visible through a window. The useful dimensions of the test chamber are $6 \times 5 \times 2.5$ m, allowing to test and operate different kind of technologies which need a big volume of air around them (e.g., small wind turbines, drones). Its design is extremely versatile, thanks to the generous proportions and to the possibility to tune the fans frequency individually guaranteeing a fine tuning of the wind velocity of in the range 0-8 m/s. The flow field inside the test chamber was characterized by performing several measures through a Pitot tube rake. The details of the WT calibration are presented in Gerboni et al. [56], whilst in the following only a brief description is presented. The methodology was inspired by several works available in literature, where open-jet wind tunnel are calibrated by use of Pitot tube [87–90]. The velocity is evaluated starting from the dynamic pressure value (p_d) which results as the difference between the total (p_t) and static pressure (p_s) measured by the Pitot tube. The velocity can be found knowing that it is related to p_d by Eq. 5.1.

$$p_d = \frac{\rho \cdot velocity^2}{2} \tag{5.1}$$

The rake consists in ten Pitot tubes vertically arranged with a 25 cm spacing, identifying ten vertical coordinates (z_1-z_{10}), where z_1 is 20 cm away from the floor and z_{10} is at a 2.45 m height. Three vertical planes were identified in the test chamber, in correspondence of the points x_1, x_2, x_3 visible in figure 5.3 with x_1 located at 50 cm from the convergent channel end.

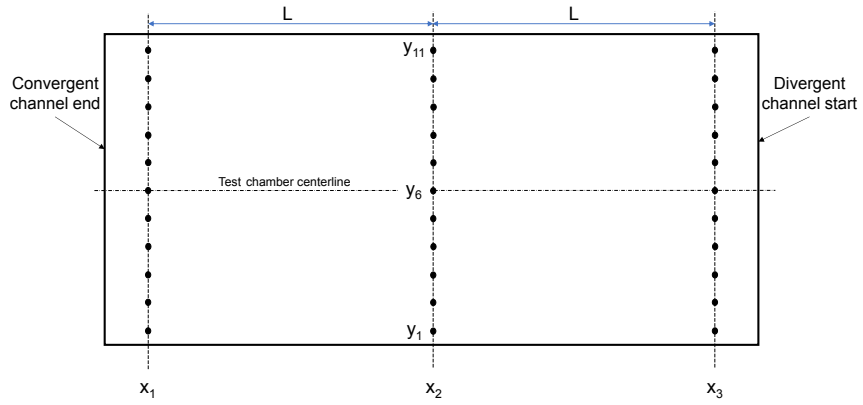

Fig. 5.3 Grid points on the test chamber floor for the calibration measurements through the Pitot tube rake.

Eleven points were considered (from y_1 to y_{11}) per each x coordinate, with a constant spacing of 50 cm covering up all the test chamber width. Considering that ten vertical point of measures (z_1-z_{10}) are available per each (x,y) couple, a total of 110 points are obtained for each plane. Three tests were performed imposing the same frequency to each fan to a value of 30, 40 and 50 Hz respectively. Once the frequency was set, the Pitot rake was positioned in one of the (x,y) couple point and the measures were obtained in the 10 vertical coordinates. Measures with a 40 Hz data rate were performed for 3 minutes, with a break of 15 minutes between each change of position to permit a flow stabilization after the operator intervention. An average value of velocity is evaluated per each point, and through a spline interpolation a velocity map is obtained for each plane. To analyze the flow homogeneity, a percentage deviation from a reference value, taken in the plane center at coordinates (y_6, z_6), is shown in the maps of figures 5.4, 5.5 and 5.6. As expected from theory, a reduction of the average velocity can be observed approaching the fans (from x_1 to x_3) as the greater values are expected after the convergent channel. Larger percentage discrepancies are observed in the lowest velocity test (30 Hz) as well as some asymmetries in the left and right borders of the section in all the three cases. These last effects had been attributed to the internal structure of the tunnel itself and some improvements were designed and implemented. All the velocity maps show a low velocity boundary at the bottom of the section, which can be ascribed to the presence of a 12 cm frame at the inlet base. This causes a blockage effect which is successively overcome by introducing an inclined polystyrene platform helping the boundary layer development. The non uniformities in the lateral sides were easily

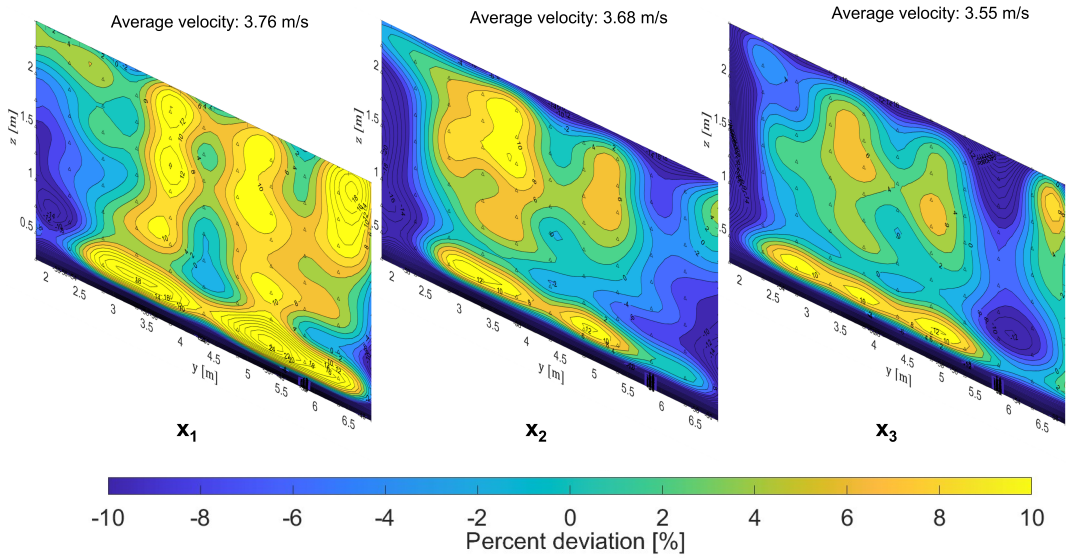

Fig. 5.4 Percent deviation map of velocities across planes x_1, x_2, x_3 for the 30 Hz case.

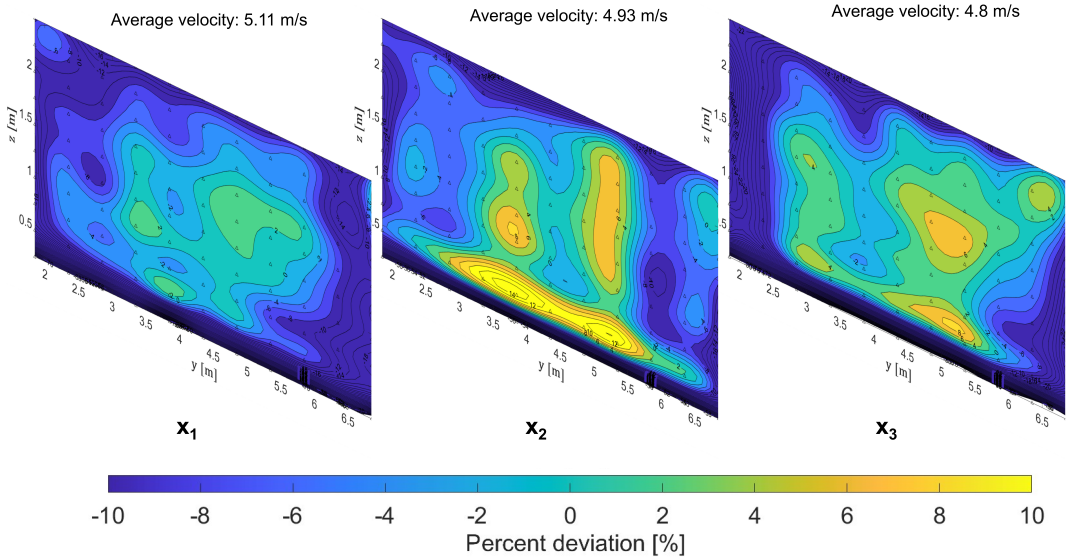

Fig. 5.5 Percent deviation map of velocities across planes x_1, x_2, x_3 for the 40 Hz case.

predictable due to the non-symmetric structure of the building. Polystyrene panels were used to smooth the lateral surfaces. The effect of the structural modifications, can be observed in figure 5.7. The uniformity of the flow field is largely improved especially in the central region, 2.5<y<6.5 m, that is the interest region for the tests, where the percent deviation varies between -2% and +2%. Further improvements in the flow field are obtained by tuning the frequency of each fan independently, as discussed in [56]. A last set of measures were performed to obtain a relation between

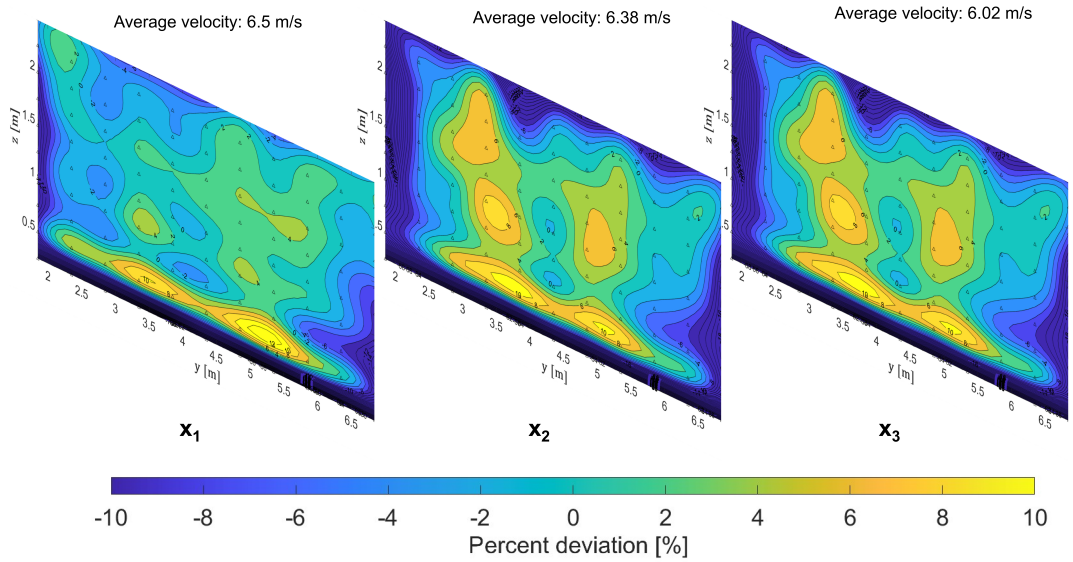

Fig. 5.6 Percent deviation map of velocities across planes x_1, x_2, x_3 for the 50 Hz case.

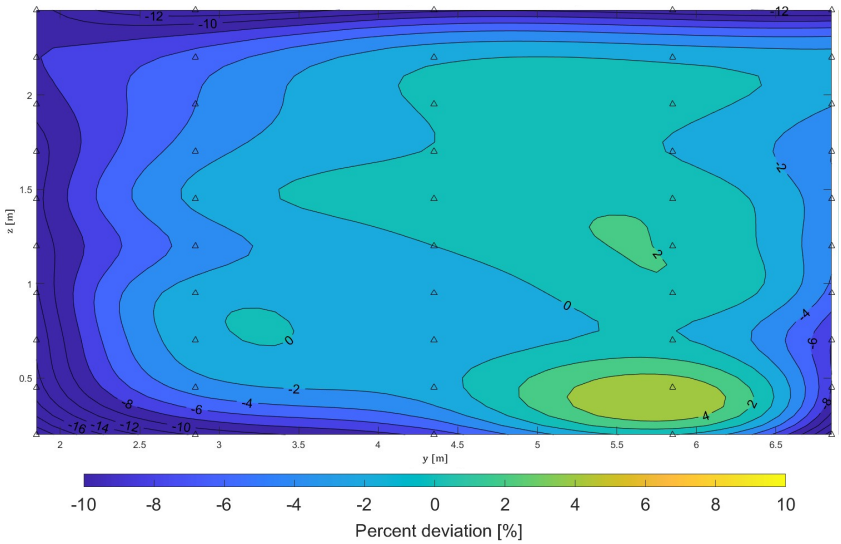

Fig. 5.7 Percent deviation map of velocities across plane x_2 at 50 Hz after structural improvements.

the fans frequency and the air velocity at the test chamber center (x_2,y_6,z_6) in order to permit an easy regulation of the velocity inside the tunnel. As shown in figure 5.8, measurements were performed varying the frequency from 5 to 60 Hz, obtaining an almost linear behavior except for the first step.

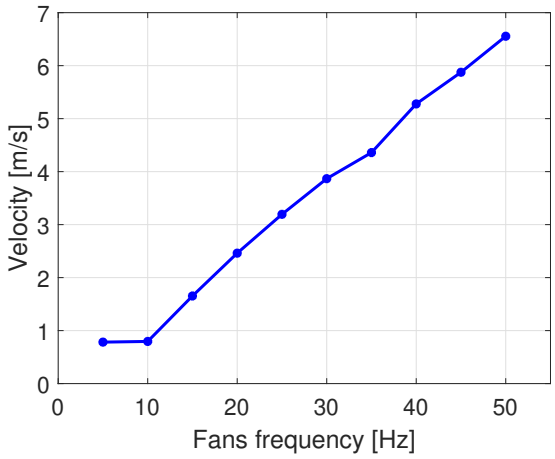

Fig. 5.8 Velocity variation in the test chamber centre (x_2,y_6,z_6) as a function of the fans frequency.

5.1.2 Platform mockup and measuring devices

The tests were carried out on a 1/10 scaled mockup of the platform, see figure 5.9.

Fig. 5.9 Platform mockup picture.

The platform considered in these tests is defined on the model of the structures normally found in the Adriatic Sea and is characterized by a three-storey emerged structure. The intermediate level is the reproduction of the CAD geometry shown in figure 3.1, and it is the only one instrumented as it represents the production deck, on which the study of the present work focuses. The plane dimensions of each floor of the mockup are 3×2 m and each inter-deck distance is 50 cm. The

structure has wheels to permit its rotation and movement and four telescopic lifting columns to regulate its height. The gas measurements were performed by 38 gas sensors sparsely placed on the platform central deck, which were embedded in the objects to avoid any interference with the flow field and which locations are shown in figure 5.10. Pellistor type sensors were employed for the measurements as

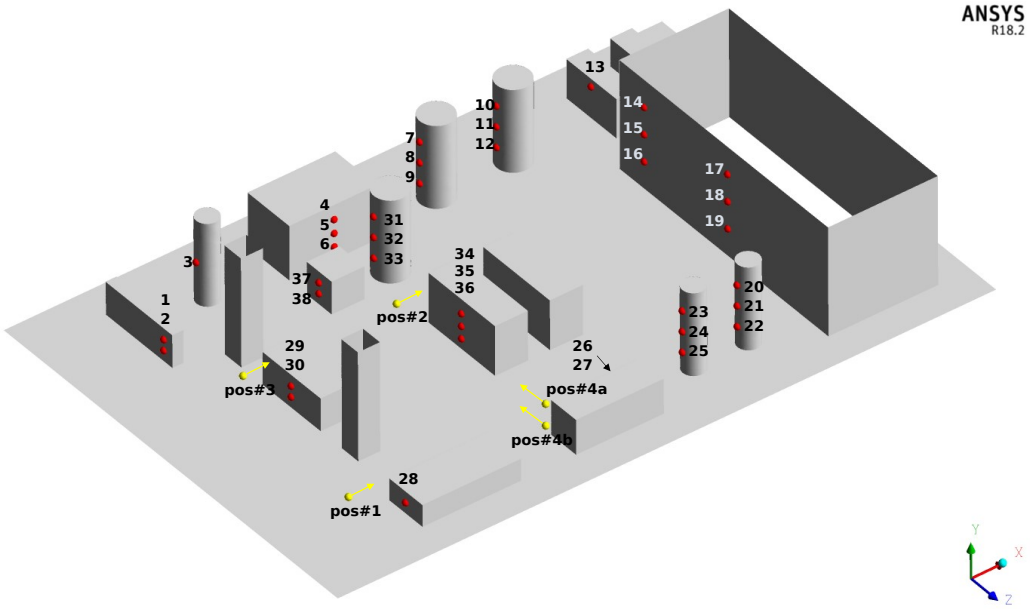

Fig. 5.10 Graphical representation of the gas sensors positions in the platform deck (red bullets) with the corresponding number tags, and release positions and directions considered in the case studies (yellow bullets and arrows).

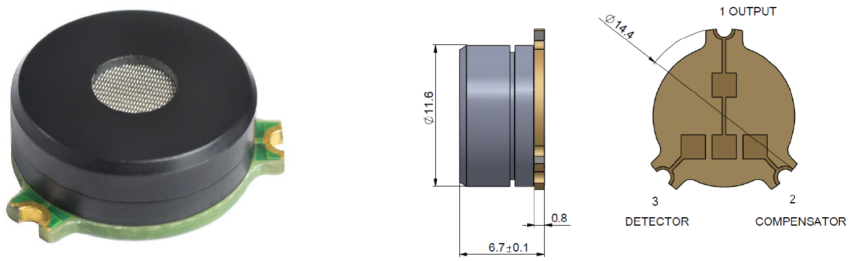

(a) MP-7217-DA pellistor. (b) Pellistor size.

Fig. 5.11 Gas measuring device. Reproduced from [91]

they permit to detect flammable gases at low concentrations (0-100% of LFL). In particular, a model manufactured by SGX, the MP-7217-DA [91], was employed due

to its extremely reduced dimensions, which permitted the embedding in the domain objects. Figure 5.11 shows that they have a cylindrical shape, with a diameter below 1.5 cm and a thickness below 7 mm. The operating principle of this devices is based on the catalytic combustion of the gas. They are constituted by a pair of planar metal heaters: the first, coated with a layer embedding a noble metal catalyst, constitutes the detector, the second, coated with an inert film, constitutes the compensator [91]. During its use, the device is heated up to 400/500 °C in order to permit an oxidizing reaction on the catalyst branch when a flammable gas passes through it. The reaction generates heat which causes an increase of temperature that is detected as an increase in the resistance. The compensator has the role to compensate for the environmental factors (temperature and air composition), therefore, any increase of temperature that is not due to the gas oxidation does not affect the measure. The thermal compensation process is not perfect as the detector and compensator branch are not perfectly identical, nonetheless due to the high reaction temperature, it is not expected to have a relevant external temperature influence. The device provides a measuring rate of 1 Hz. In addition, as provided by the datasheet, these devices are highly resistant to mechanical shocks, a fundamental feature if highly inertial jets are involved. Moreover, they have a low orientation effect, and since the sensors are embedded in a complex and irregular environment where it is likely to have randomly oriented impinging gas jets on the sensor rather than perpendicular ones, this is another fundamental feature. Before the sensors plugin in the mockup, an initial calibration was performed by the supplier company, putting each one in a vacuum box in which a known amount of gas was gently injected. The output electric signal was associated to the known concentration, and a characteristic curve was built. Since the sensor calibration was performed in conditions of flow at rest, the sensor response when hit by a high inertia flow was investigated. In particular, the precision of the instrument under such conditions was tested by performing several free-jet tests. A 2.2% CH_4- 97.8% air mixture is used as experimental gas to avoid methane concentration above 0.5·LFL. With reference to figure 5.12, four different configurations of free jets were considered varying both the release point-sensor distance L and the release pressure $p_{free jet}$. These parameters are presented in table 5.1. These sets were defined in order to obtain four different levels of gas sample at the sensor location, which resulted respectively around 200, 300, 400, 600 ppm of methane, representative of the amount of gas plausibly involved in the platform release tests. For each set, the experiment was repeated ten times obtaining the

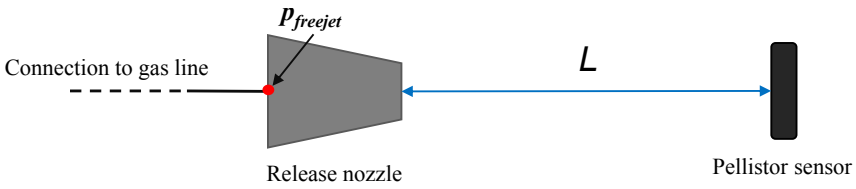

Fig. 5.12 Free jets test arrangement.

	$p_{free\,jet}$ [bar]	L [m]
1st set	6	4.3
2nd set	8	2
3rd set	12	1.8
4th set	8	1

Table 5.1 Free-jet tests parameters.

results listed in table 5.2 in terms of a mean value (E_i) and a standard deviation (σ_i) for each i-th measure. At this point an average value E_{set} and a pooled standard deviation σ_{set} are evaluated for each set through Eq. 5.2 and 5.3.

$$E_{set} = \frac{\sum_{i=1}^{N} E_i}{N} \tag{5.2}$$

$$\sigma_{set} = \sqrt{\frac{\sum_{i=1}^{N} \sigma_i^2}{N}} \tag{5.3}$$

Where i=1,...,N and N=10. The results, summarized in table 5.3, show that the device precision is almost constant with respect to the amount of gas sample measured, as the pooled standard deviation is about 6-7 ppm. A slight increase in this value is observed from set 1 to 4, and this seems counterintuitive as for larger gas samples a larger measure stability is expected. This behavior can be ascribed to the fact that reducing L or increasing $p_{free\,jet}$ lead to a larger inertia of the jet impacting the sensor, hence to a larger turbulence which causes a larger oscillation of the measure. However, the differences in the σ_{set} are negligible, and it can be deduced that the sensor maintain the same level of precision in this range of measure. A last check on the accuracy of the device was made by comparing the mean values for each set E_{set}, with the value obtained with one of the most widely used empirical models for turbulent free jets, the Chen and Rodi one [12]. The input of the model are the data available in table 5.1, and the composition of the released mixture.

	1st set		2nd set		3rd set		4th set	
	E_i	σ_i	E_i	σ_i	E_i	σ_i	E_i	σ_i
#1	113.00	5.57	300.73	11.31	407.45	4.76	608.00	6.39
#2	119.73	5.90	301.36	6.44	396.27	7.88	630.18	6.66
#3	130.45	5.26	295.82	5.86	395.73	5.55	593.82	8.33
#4	119.36	3.75	298.91	5.94	395.45	4.76	617.64	7.06
#5	119.55	4.50	301.55	5.92	392.18	7.67	617.82	14.16
#6	122.09	10.00	298.82	4.19	391.36	6.53	608.09	6.28
#7	126.45	8.20	297.09	4.11	392.18	5.88	601.45	5.28
#8	119.27	7.24	286.73	10.27	393.73	5.57	584.45	5.20
#9	112.91	5.54	293.27	3.72	388.36	10.69	585.36	4.50
#10	132.73	4.38	288.27	2.94	399.36	5.35	583.82	4.56

Table 5.2 Free-jet tests results: mean value and standard deviation.

	1st set	2nd set	3rd set	4th set
E_{set}	121.56	296.25	395.21	603.06
σ_{set}	6.30	6.61	6.69	7.35

Table 5.3 Average value and pooled standard deviation for each free-jet test set.

Table 5.4 shows that the measures are in good agreement with the theoretical values as the largest relative difference is obtained for the 4th set and it is equal to 4.3 %. This comparison with a validated experimental model, helped in having confidence in the quality of the measurements related to the case study tests.

	Experimental	Chen&Rodi	Relative difference
1st set	121.56	124.05	0.02
2nd set	296.25	303.12	0.023
3rd set	395.21	404.43	0.023
4th set	603.06	630.28	0.043

Table 5.4 Free-jet tests results comparison with Chen&Rodi model.

5.1.3 Gas distribution line and release

The gas release is accomplished out thanks to a nozzle connected to a gas distribution line, which schematic representation is shown in figure 5.13. It should be remarked

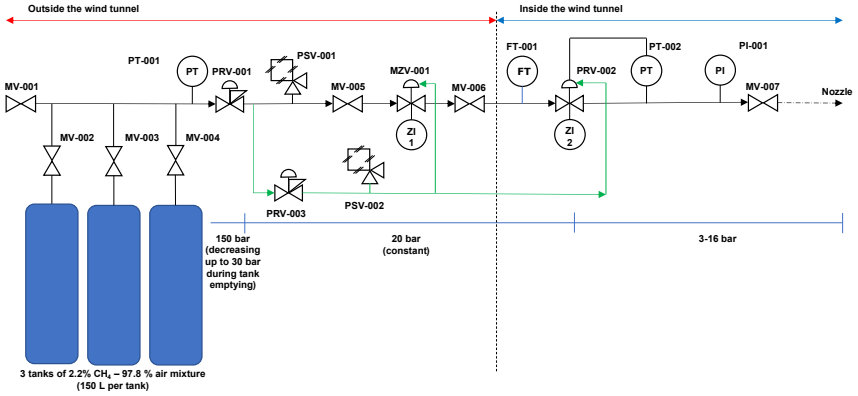

Fig. 5.13 Gas distribution line.

that for safety reasons a mixture of air and CH_4 at 2.2 % in volume is used instead of pure methane. In fact, 2.2 % corresponds to about half of the LFL for methane and it is thereby able to ensure a non-hazardous release of gas inside the wind tunnel. The release mixture was provided by Linde S.p.A. in 50 litres gas cylinders at 150 bars. The scheme in figure 5.13 shows that three tanks are connected in parallel to feed the distribution line. A manual valve is installed per each tank, (MV-002, MV-003, MV-004) to isolate them during the substitution or in case of a tank failure. In this last case, the manual valve MV-001 can be operated to safely discharge the line residual mixture in the atmosphere. The distribution line can be divided in two regions: outside and inside the wind tunnel. The portion located outside, is contained in a dedicated room where also the tanks are stored. A first pressure reduction is performed by the pressure regulator PRV-001 which is auto-regulated and guarantees a pressure reduction from the storage pressure (150 bar, which will decrease up to 30 bar as the tanks are emptied) to 20 bar. The pressure level inside the tanks can be monitored by the pressure transmitter PT-001. After that, a pressure safety valve is installed (PSV-001) to safely discharge the mixture in case the pressure overcomes 27 bar. Another safety measure is the pneumatic shut-off valve MZV-001 which closes in case of failure and is of the type fail to close. Maintenance operations can be performed by isolating part of the line by closing the manual valves MV-005 and MV-006. A second pressure reduction is operated by PRV-002, which provides a reduction from 20 bar to the needed release pressure (which is in the range 3–16 bar)

and is regulated through a Proportional-Integral- Derivative controller (PID) basing on the signal of the pressure transmitter PT-002. The signal of this last component is used in the WT control room to check if the desired pressure is reached. In this point of the line a redundant measure of the pressure is given by the pressure indicator PI-001, which measure can be used to validate the PT-002 response. The release mass flow rate is obtained by the measure of the flow transmitter FT-001. The PRV-002 has also the function to start and stop the release thanks to a remote signal given by the software installed in the control room PC. The manual valve MV-007 is positioned inside the tunnel and must be opened and closed before and after each test session. Each pneumatic valve is actuated by spilled mixture at 5 bar through a parallel line (green line) equipped with a pressure reducer PRV-003 and a pressure safety valve PSV-002. This gas line is connected through a 5 m flexible hose to the release nozzle mounted on the mockup, as shown in figure 5.14.

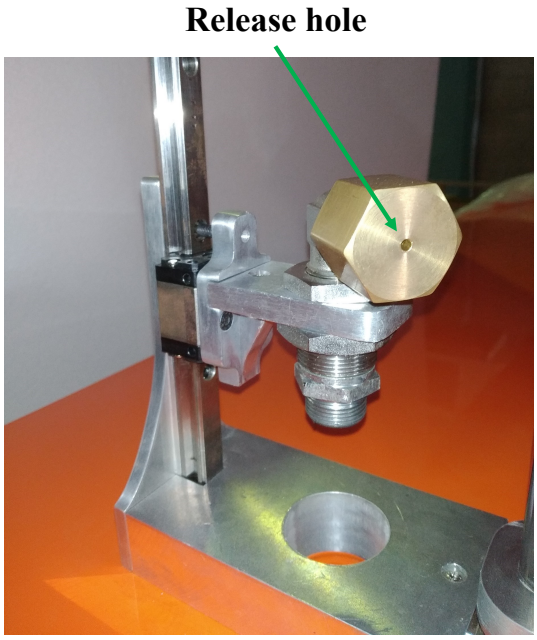

Fig. 5.14 Picture of the nozzle used for the experimental gas releases.

5.2 Scaling procedure

The present work considers accidental gas releases on a O&G platform, therefore, full scale experiments are obviously out of consideration. For these reason, a set of reduced scale experiments was defined basing on some *ad hoc* scaling rules [55]. In general, a scaling procedure strongly depends on the features of the main physical phenomena to be experimentally reproduced and involve the preserving of some relevant dimensionless parameters, in order to assure the fluid dynamic similarity between the *real* scale and the experimental model scale phenomenon. Assuring a proper scaling is a typical problem that arises in wind tunnel experiments of pollutant dispersion in urban environment, but also in the scaled-down experimental analysis of hazardous gas releases in closed spaces such as tunnels or warehouses. The literature about this topic is quite extended, encompassing both papers specifically devoted to scaling procedures [92, 93], guidelines for modelling atmospheric diffusion [94, 95], plume dispersion [96], experimental validation of CFD simulations of near-field pollutant dispersion [97–100] and experimental and/or numerical investigation on hydrogen releases in confined spaces [101–103].

In the present work, the first step relates on the definition of a geometric scaling factor, S_c, which represent the ratio between the *real* scale length L and the *model* scale length l, see Eq. 5.4. Basing on the wind tunnel test chamber dimensions, S_c=0.1 is adopted for the platform mockup sizing, in order to assure that it is invested by the uniform flow region.

$$S_c = \frac{l}{L} \tag{5.4}$$

At this point, once the geometry scaling is defined basing on some structural constraints, a scaling procedure to assure the correct reproduction of the phenomenon at the reduced scale must be defined. The general approach for gaseous releases scaling is presented in [104], where a reduced scale field experiment of CO_2 release was performed to validate numerical simulations. It considers three dimensionless numbers:

- Density ratio
- Froude number
- Richardson number

which are defined for both the gas flow velocity (V: real scale, v: model scale) and the wind velocity (U: real scale, u: model scale) in Eq. 5.5, 5.6 and 5.7 respectively, with ρ_g gas density and ρ_a air density.

$$\frac{\rho_g}{\rho_a} \tag{5.5}$$

$$Fr = \frac{U}{\sqrt{g \cdot L}} \quad Fr = \frac{V}{\sqrt{g \cdot L}} \tag{5.6}$$

$$Ri = g\frac{\rho_g - \rho_a}{\rho_a}\frac{L}{U^2} \quad Ri = g\frac{\rho_g - \rho_a}{\rho_a}\frac{L}{V^2} \tag{5.7}$$

To satisfy the fluid dynamic similitude, Eq. 5.5 and 5.6 must keep the same value in the real and the model scale, once this is obtained, this is true also for equation 5.7. Considering this procedure, the velocities scale according to Eq. 5.8.

$$\frac{v}{V} = \frac{u}{U} = S_c^{0.5} \tag{5.8}$$

This approach is very general and widely applicable, nonetheless, it does not fit the present case studies for several reasons. Firstly, it proposes an approach suitable for gas dispersions characterized by gas release velocities (V) and wind velocities (U) of the same order of magnitude, while the initial pressure of accidental gas releases here analyzed involve a supersonic discharging velocity, hence implying $V \gg U$. Secondly, the wind velocity scaling is badly addressed as it does not account for the typical profile of the atmospheric boundary layer, i.e. logarithmic or exponential wind profile, in fact, the wind velocity (U) is scaled using the same rules of the release velocity (V).

Another interesting scaling methodology is presented in [105], where small-scale wind tunnel experiments for gaseous jets are studied. Here, an approach based on a dimensional analysis is proposed, with the aim of obtaining a gas distribution in the small-scale experiment which is in fluid-dynamic similitude with the real scale one. As a first step, the authors used the Buckingham theorem to derive an *ad hoc* dimensionless parameter involving the gas concentration. This one and a set of other dimensionless parameters are then considered to assure the similarity between the real and model scales. Also in this case, both the density ratio and the Froude number are considered for the scaling of the gas jet, with the addition of the Reynolds number. A key difference with respect to [104] is that the wind velocity scaling is

addressed considering the atmospheric boundary layer, and a parameter which relates the gas jet velocity and the wind velocity is introduced. Even though this approach is more complete and involves more parameters, it is not applicable to the present case studies since the number of dimensionless parameters involved is quite large and it is difficult to satisfy their equality between real and model scale as many conflicts may arises. It is likely that some constraints will have to be relaxed. Moreover, it does not fit the accidental release under consideration as it refers only to the dispersion phase, neglecting the initial jet expansion. This limit is well represented by the importance given to the Froude number, typically used in subsonic/dispersion models, where the gravity strongly affects the phenomena evolution (e.g. the pollutant cloud dimension and position). An alternative simplified strategy is proposed in [106] where the authors introduce a parameter to link the gas flow regime and the wind one, see Eq. 5.9, which represents the ratio between the wind and the gas jet inertia.

$$\frac{\rho_a \cdot U^2}{\rho_g \cdot V^2} \tag{5.9}$$

The authors have assured the similarity in the experiment, keeping this parameter constant. In this case, there are no more difficulties arising from the managing of many dimensionless parameters: once the wind velocity is scaled according to Eq. 5.8, the gas velocity scaling follows from Eq. 5.9. Nonetheless, the proposed parameter is not representative for high-pressure gas releases, since the gas release velocity (equal to the speed of sound in critical flows) is two orders of magnitude larger than the wind one and the ratio of their power of two leads to extremely small values and largely affected by uncertainties. Another parameter is given in [92] where the authors proposed some scaling rules for a reduced scale field release of hydrogen fluoride. They stated that to comply with the similarity between the real scale case and the model scale, a parameter called *dimensionless discharge momentum flux* should be kept constant, i.e. the relation in Eq. 5.10 must be satisfied.

$$\frac{M_f}{U^2 \cdot L^2} = \frac{m_f}{u^2 \cdot l^2} \tag{5.10}$$

M_f and m_f are respectively the *source momentum flux* for the real and model scale and are defined according to Eq. 5.11 and 5.12 where A and a are the release hole areas and $\rho_{g,R}$ and $\rho_{g,m}$ are the densities of the involved gases at the release hole conditions. All the parameters referring to the real scale are defined with the subscript

R while the model ones with the subscript m.

$$M_f = V^2 \cdot A \cdot \frac{\rho_{g,R}}{\rho_a} \tag{5.11}$$

$$m_f = v^2 \cdot a \cdot \frac{\rho_{g,m}}{\rho_a} \tag{5.12}$$

This seems to be the most complete dimensionless parameter for the scaling of a gas release, under wind conditions in a scaled geometry, as all the main parameters are involved: the gas release velocity, the gas-air density ratio, the jet orifice dimensions, the geometric length scales and the wind velocities. Moreover, this methodology is general, without any specific reference to subsonic or supersonic release, the wind velocity is scaled considering its logarithmic profile and a single equation relates the geometry, the wind velocity and the supersonic release scaling. This approach was employed several times in the past to design experiments of gas leakages and dispersions at low speeds [96, 101–103] however, it cannot be directly applied to the proposed case studies as the supersonic release presence makes it necessary to introduce some new hypotheses. An adaptation of the procedure to underexpanded jets is one of the purposes of the methodology presented in the following. Moreover, for practical reasons linked to the design definition, it is useful to express the main scaling parameters as a function of the release pressure and the hole diameter. As a first hypothesis, the stratification phenomena in the atmospheric wind are neglected and the wind direction is assumed steady reproducing only the average real wind direction. At this point, the wind velocity scaling is evaluated as a function of S_c. A logarithmic law is considered to describe the wind velocity profile, since the lower part of the atmospheric boundary layer is of interest, see Eq. 5.13.

$$\frac{U}{U_*} = \frac{1}{k} \ln\left(\frac{Z}{Z_0}\right) \tag{5.13}$$

Where U_* is the friction velocity, k=0.41 is the Von Kármán constant, Z [m] is the vertical coordinate and Z_0 [m] is the surface roughness. Analogously the reduced scale velocity can be written as in Eq. 5.14.

$$\frac{u}{u_*} = \frac{1}{k} \ln\left(\frac{z}{z_0}\right) \tag{5.14}$$

Having in mind that all the length scales according to S_c, i.e. $z/Z = z_0/Z_0 = S_c$, combining Eq. 5.13 and 5.14, the following scaling rule is derived:

$$\frac{u}{U} = S_c^{0.5}\left(1 - \frac{\ln(S_c)}{\ln(\frac{Z}{Z_0})}\right) \tag{5.15}$$

From Eq. 5.15 a scaled value of the wind velocity u can be derived accounting also for the geometry scaling factor S_c. The only variable appearing in the equation is Z, a reference height to which corresponds U. At this point, the release parameters scaling can be addressed by combining Eq. 5.10 with Eq. 5.4 and 5.15. The accidental scenarios considered in this work are methane releases characterized by a release diameter $D_{e,R}$ and a release pressure $p_{0,R}$, as summarized in table 3.2. The objective is to define the corresponding scaled parameters ($D_{e,m}$, $p_{0,m}$) per each scenario as schematically shown in figure 5.15. If the gas used in the experimental facility is the

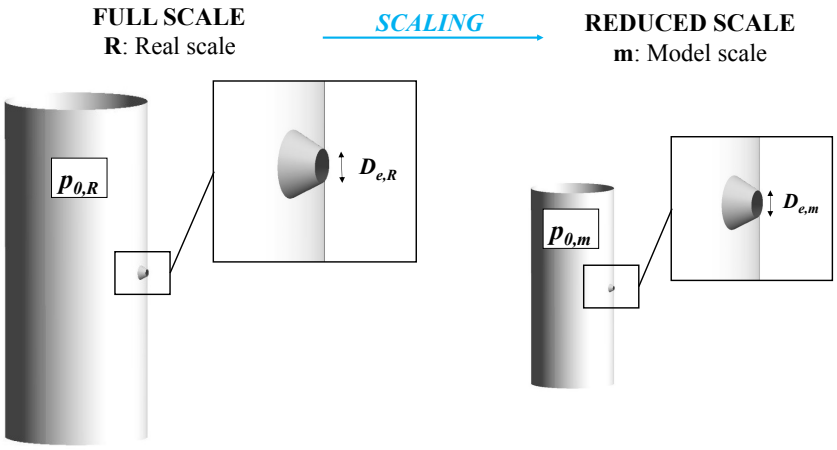

Fig. 5.15 Schematic representation of the scaling from the real to the model scale.

same involved in the real scale accident, the reproduction of the event will certainly be more reliable, and the scaling simpler. Unfortunately, in many cases, a different gas must be chosen for several reasons: cost, safety and traceability. In case the gas is different, several properties have to be considered in the calculations. Table 5.5 summarizes these properties.

Properties	Real scale	Model scale
Density [kg/m^3]	$\rho_{g,R}$	$\rho_{g,m}$
Adiabatic constant [-]	γ_R	γ_m
Critical ratio [-]	$R_{cr,R}$	$R_{cr,m}$
Gas constant [J/kg/K]	R_R	R_m

Table 5.5 List of gas properties involved in the scaling procedure.

Substituting Eq. 5.11 and 5.12 in Eq. 5.10, and introducing S_c, the relation in Eq. 5.16 can be found.

$$\frac{v^2 \cdot a \cdot \rho_{g,m}}{V^2 \cdot A \cdot \rho_{g,R}} = \left(\frac{u}{U}\right)^2 \cdot (S_c)^2 \tag{5.16}$$

On the right-hand side of Eq. 5.16, the first term in the brackets is the wind velocity scaling ratio, while the second term is the geometry scaling factor. On the left hand side, only the release parameters (release velocities, release hole areas and density of the released gases) appear. Therefore, it is important to notice that the ratio between the release parameters in the real and model scales, is written as a function of the wind and geometry scaling, which is the purpose of the work. The next step is to re-write Eq. 5.16 as a function of the parameters of interest for this work, the release pressure and the hole diameter. Gas densities and release velocities can be related to the release pressure considering that only critical flows are considered in this work, as discussed in section 2.1, hence, the pressure at the exit section p_e can be evaluated through Eq. 2.4. In this case, Eq. 5.17 and 5.18 can be written.

$$p_{e,R} = R_{cr,R} \cdot p_{0,R} \tag{5.17}$$

$$p_{e,m} = R_{cr,m} \cdot p_{0,m} \tag{5.18}$$

The release velocities at the exit sections can be evaluated according to the formulas for sonic flows, and can be related to the inner conditions (0) by supposing an adiabatic process between the inner and the exit conditions. The resulting formulations are shown in Eq. 5.19 and 5.20.

$$V = \sqrt{\frac{2\gamma_R \cdot R_R \cdot T_{0,R}}{\gamma_R + 1}} \tag{5.19}$$

$$v = \sqrt{\frac{2\gamma_m \cdot R_m \cdot T_{0,m}}{\gamma_m + 1}} \tag{5.20}$$

The gas densities at the exit section ($\rho_{g,R}$, $\rho_{g,m}$) can be written as a function of pressure and temperature through the ideal gas law as in Eq. 5.21 and 5.22.

$$\rho_{g,R} = \frac{p_{e,R}}{R_R \cdot T_{e,R}} = \frac{R_{cr,R} \cdot p_{0,R}}{R_R \cdot T_{e,R}} \tag{5.21}$$

$$\rho_{g,m} = \frac{p_{e,m}}{R_m \cdot T_{e,m}} = \frac{R_{cr,m} \cdot p_{0,m}}{R_m \cdot T_{e,m}} \tag{5.22}$$

In this work, releases at ambient temperature are considered, therefore $T_{0,R}$=$T_{0,m}$=300 K is assumed. Moreover, since an adiabatic process is assumed between the inner (0) and exit (e) conditions, the temperatures at the exit section results similar to the inner one, $T_{e,R} \sim T_{0,R}$ and $T_{e,m} \sim T_{0,m}$, and consequently a further simplification is made: $T_{e,R} \sim T_{e,m}$. Substituting Eq. 5.19, 5.20, 5.21, 5.22 in Eq. 5.16, the relation in Eq. 5.23 is found.

$$\frac{D_{e,m}^2 \cdot p_{0,m}}{D_{e,R}^2 \cdot p_{0,R}} = \frac{\gamma_R \cdot (\gamma_m + 1) \cdot R_{cr,R}}{\gamma_m \cdot (\gamma_R + 1) \cdot R_{cr,m}} \cdot \left(\frac{u}{U}\right)^2 \cdot S_c^2 \tag{5.23}$$

The critical pressure ratios ($R_{cr,R}$, $R_{cr,m}$) are expressed in Eq. 5.24 and 5.25.

$$R_{cr,R} = \left(\frac{2}{\gamma_R + 1}\right)^{\frac{\gamma_R}{\gamma_R - 1}} \tag{5.24}$$

$$R_{cr,m} = \left(\frac{2}{\gamma_m + 1}\right)^{\frac{\gamma_m}{\gamma_m - 1}} \tag{5.25}$$

The release areas are expressed as a function of the real scale diameter $D_{e,R}$ and the model scale diameter $D_{e,m}$, since only circular holes are considered. Eq. 5.23 can be used to find the couple of reduced scale values ($p_{0,m}$, $D_{e,m}$) corresponding to a certain couple of real scale parameters ($p_{0,R}$, $D_{e,R}$). At this point, the real scale case studies listed in table 3.2 can be translated in a set of reduced scale case studies, reproducible in the wind tunnel assuring the similitude. Having fixed S_c=0.1, u can be derived from Eq. 5.15 considering that the full scale wind intensities ($|\vec{U}_1|$=$|\vec{U}_2|$) are both equal to 6 m/s measured at a reference height Z= 15 m and that the roughness Z_0 can be assumed equal to 0.1 for the open sea. The resulting value is u= 2.77 m/s. While the real case studies refers to a pure methane release (γ_R=1.3, $R_{cr,R}$=0.546), due to

	Real scale			Model scale		
case study	$p_{0,R}$ [bar]	$D_{e,R}$ [cm]	$\|\vec{U}_1\| = \|\vec{U}_2\|$ [m/s]	$p_{0,m}$ [bar]	$D_{e,m}$ [cm]	$\|\vec{u}_1\| = \|\vec{u}_2\|$ [m/s]
cs#1	30	3	6	6.4	0.3	2.77
cs#2	40	3	6	8.5	0.3	2.77
cs#3	50	3	6	10.6	0.3	2.77
cs#4	30	3	6	6.4	0.3	2.77
cs#5	50	3	6	10.6	0.3	2.77
cs#6	30	3	6	6.4	0.3	2.77
cs#7	40	3	6	8.5	0.3	2.77
cs#8	50	3	6	10.6	0.3	2.77
cs#9	30	3	6	6.4	0.3	2.77
cs#10	50	3	6	10.6	0.3	2.77
cs#11	30	3	6	6.4	0.3	2.77
cs#12	40	3	6	8.5	0.3	2.77
cs#13	50	3	6	10.6	0.3	2.77

Table 5.6 List of case studies (cs) considered for the numerical and experimental analyses, with the corresponding parameters.

safety reasons the experimental release is performed using a 2.2% CH_4-97.8% air mixture, thus, avoiding the possibility of flammability related risks in the wind tunnel since the methane dilution is below 0.5·LFL. The properties of the experimental mixture can be approximated with the air ones, hence $\gamma_m = 1.4$ and $R_{cr,m}$=0.528. Eq. 5.23 can be now used to evaluate $p_{0,m}$ per each case study considering that $D_{e,m}$=$D_{e,R} \cdot S_c$. Table 5.6 summarizes the real scale parameters and the corresponding model scaled ones. It can be easily checked that all the model scale case studies involve pressure levels assuring a critical flow condition, thus assuring that the initial assumption is verified.

5.3 CFD modeling and results

The model scale case studies listed in table 5.6 are reproduced both experimentally and numerically. This section deals with the numerical setup of the simulations, and a qualitative discussion on the results. In particular, a deeper discussion is devoted to the dimensioning of the fluid domain for a correct wind field generation, assuring a fully developed wind velocity profile impacting the platform.

5.3.1 Simulations setup and computational domain design

Since the simulations are carried out employing SBAM, at first the SB simulations must be discussed. The dimensioning of the SB is the first step of the implementation and it is based on Eq. 4.1, that in this case takes in input $D_{e,m}$ and η_0=$p_{0,m}/p_a$. It was decided to set L_{SB} at the largest possible pressure reproducible in the experimental setup ($p_{0,m}$=16 bar) since the resulting size is still small compared to the dispersion domain, thus not violating point 4 of the model applicability range (section 4.1.4). Moreover, exploiting the possibility to design the SB at the largest possible pressure permits to use the same geometry for all the cases with lower pressure values by assuring the compliance with the criterion of having a subsonic flow at the SB outlet. The resulting value is L_{SB}=0.078 m. The case of an impinging jet on a cylindrical obstacle is considered, hence the SB geometry is qualitatively similar to the one shown in figure 4.5, as well as the same symmetries are assumed. A cylinder with diameter d_{cyl}=2 cm at a distance l_{obs}=3 cm is considered to represent the case of an impinging jet on a pipeline with dimension one order of magnitude larger with respect to $D_{e,m}$. Since three values of $p_{0,m}$ are considered in the case studies, three SB simulations are performed. The numerical setup is analogous to the one presented in section 4.2.1 apart from the BCs which can be summarized as follows:

- Nozzle inlet: a *pressure inlet* is imposed. An absolute pressure equal to the three $p_{0,m}$ values is prescribed for each SB simulation, as well as a temperature equal to 300 K and a CH_4 mass fraction equal to 0.022 in accordance with the experimental mixture
- SB faces: a *pressure outlet* is imposed. An absolute pressure equal to p_a=1 bar is prescribed at the SB faces (back, front, lateral, up)

- Symmetry planes XY and XZ: a *symmetry* boundary condition is imposed (see figure 4.5)
- Cylinder and nozzle walls: a *wall* with no-slip condition is imposed

The adopted mesh is also in this case an unstructured tetrahedral mesh, consisting of $\sim 2 \cdot 10^6$ elements. A grid independence study was carried out to optimize the spatial discretization considering the case with the highest pressure ($p_{0,m}$=10.6 bar), which is described in appendix C as well as the convergence criteria. The results in terms of CH_4 m.f. and velocity distributions on the SB faces are shown in figure 5.16.

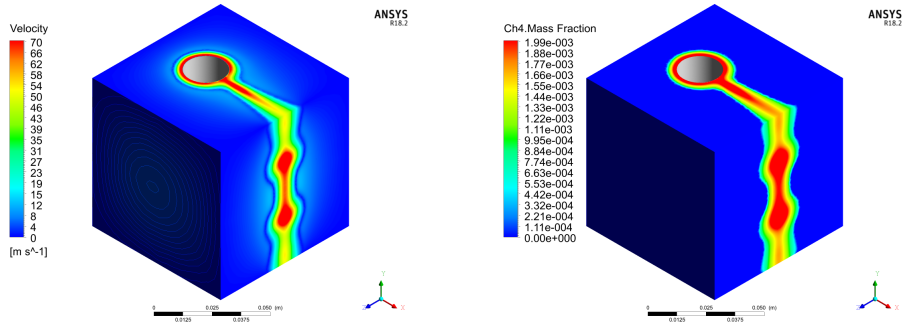

(a) Magnitude velocity distribution on the outlet faces.

(b) CH_4 m.f. distribution on the outlet faces.

Fig. 5.16 SB contour plots related to the model scale case studies with $p_{0,m}$=10.6 bar.

These results are used as BCs on the *black-box* in the dispersion simulations. Before the implementation of the dispersion, a study is performed to define the computational domain. To generate a wind velocity field around the platform, similarly to what happens in the experimental case, a computational domain which contains the platform has to be generated. The standard procedure to obtain a wind field correctly interacting with a body is to build a bigger computational domain containing the object of interest and imposing the wind velocity boundary condition as far as necessary from the object. In literature, several authors studied the interaction of big objects, like tall buildings, with the wind field proposing some criteria for the definition of the computational domain size [107–109]. These authors suggest that the wind inlet BCs should be imposed at a distance of $5H$ from the object, while the outlet at $15H$ and the height of the domain should be $6H$, where H is the height of the object (in this case the deck height). The objective of these studies is the evaluation of a pressure coefficient on the object, therefore the proposed

criteria are optimized to guarantee a fully developed pressure field behind the object. The study here proposed, aims at a more efficient dimensioning of the computational domain for the purposes of a gas release under wind field simulation and follows the procedure presented in Moscatello et al. [110]. The objective is to define the smallest possible domain size which assures a fully developed velocity profile impacting the platform borders, in view of a computational cost saving. In fact, having such a big domain as suggested in [107–109] would lead to an unsustainable computational cost if a gas dispersion must be simulated in the domain, since a fine grid resolution must be guaranteed in the volume. In this analysis, the computational domain is generated considering a box with the walls at a distance L_{box} from the platform borders as shown in figure 5.17.

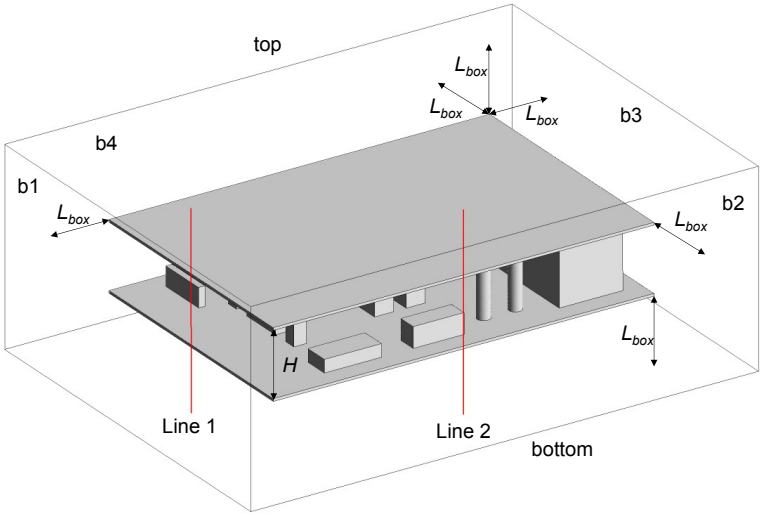

Fig. 5.17 Scheme of the external box around the platform CAD with its boundaries names (b1, b2, b3, b4, top, bottom). Representation of the probe lines (in red) for the results analysis.

The coordinate system has the origin in the center of the platform floor and is analogous to the one presented for the full scale CAD in figure 3.2. The parameter L_{box} is varied as in the following: L_{box}=H, L_{box}=2H, L_{box}=3H, L_{box}=4H where H=0.5 m is the platform height. The analysis is performed considering the wind intensity and direction of $\vec{u}_1$ (see figure 3.2). The simulations are performed in ANSYS Fluent setting up a steady-state formulation of the RANS equations. In particular, the k-ω SST model is used as it is suggested for most of the industrial applications [80]. A *velocity inlet* is prescribed on the b1-b2 boundaries to impose the

45° oriented wind $\vec{u}_1$. A *pressure outlet* with an absolute pressure of p_a is imposed on the remaining external box boundaries to simulate the surrounding environment. The fluid is assumed incompressible due to the low Ma flow involved, and the energy equation is not solved as there is no thermal imbalance. The platform surfaces are set as walls with no-slip conditions. The results obtained simulating the different domain sizes are compared by taking the velocity profiles on the two probe lines depicted in red in figure 5.17, which are dimensioned on the smallest domain (L_{box}=H). Figure 5.18 shows that the far is imposed the inlet BC the similar are the velocity profiles impacting the platform, in fact, a progressive superimposing of the profiles can be observed as L_{box} increases.

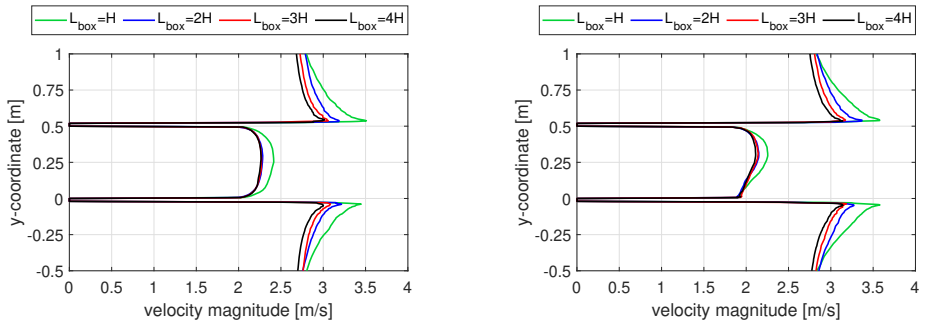

(a) Velocity profiles along line 1.

(b) Velocity profiles along line 2.

Fig. 5.18 Comparison of the velocity profiles along two probe lines obtained adopting different domain sizes characterized by different L_{box}.

Since both the probe lines are adjacent to the platform, in the correspondence of the deck floor and ceiling ($y = 0$ m and $y = 0.5$ m) there is a velocity discontinuity due to the no-slip condition imposed at the walls. The behavior observed for line 1 is replicated for line 2, as the bigger L_{box} the closer the velocity profiles. Moreover, the velocity profiles obtained with L_{box}=3H and L_{box}=4H are qualitatively similar, hence no further development of the velocity field is expected. This result is confirmed by the relative percentage errors with respect to the case with L_{box}=4H of the mean velocity shown in table 5.7. It can be concluded that the domain with L_{box}=3H is sufficient to obtain a fully developed velocity profile impacting the platform, since the relative percentage error is below 1.6% for all the probe lines. This methodology permits to reduce the domain, thus the computational effort, with respect to the methodology proposed in literature, assuring the full development of the velocity profile. At this point, all the 13 case studies dispersion simulations are run employing

	L_{box}=H	L_{box}=2H	L_{box}=3H
Line 1	0.076	0.032	0.014
Line 2	0.071	0.034	0.016

Table 5.7 Relative errors on the mean velocity obtained along lines 1 and 2 in the simulation with L_{box}=H, L_{box}=2H, L_{box}=3H with respect to case L_{box}=4H.

the domain with L_{box}=3H. An unstructured tetrahedral mesh consisting of $\sim 5 \cdot 10^6$ elements is generated in the domain. A grid independence study is presented in appendix C as well as a detailed description of the different mesh refinements. The numerical setup is analogous to that presented in section 4.2.1 about the dispersion simulation, except for the BCs. These last are described separately for the case studies involving the different wind velocity. With respect to $\vec{u_1}$ and with reference to figure 5.17 the following BCs are imposed:

- b1: a *velocity inlet* is imposed prescribing a velocity magnitude and direction according to $\vec{u_1}$, and prescribing an absolute pressure equal to p_a
- b2-b3-b4-top-bottom: a *pressure outlet* is imposed prescribing an absolute pressure equal to p_a
- Platform walls: a *wall with no-slip condition* is imposed
- Black-box: a *velocity inlet* is imposed. The velocity components as well as the CH_4 m.f. profile obtained by one of the SB simulations (figure 5.16) are prescribed according to the case study.

With respect to $\vec{u_2}$ and with reference to figure 5.17 the following BCs are imposed:

- b1-b2: a *velocity inlet* is imposed prescribing a velocity magnitude and direction according to $\vec{u_2}$, and prescribing an absolute pressure equal to p_a
- b3-b4-top-bottom: a *pressure outlet* is imposed prescribing an absolute pressure equal to p_a
- Platform walls: a *wall with no-slip condition* is imposed
- Black-box: a *velocity inlet* is imposed. The velocity components as well as the CH_4 m.f. profile obtained by one of the SB simulations (see figure 5.16) are prescribed according to the case study.

5.3.2 Model scale case studies CFD results

A qualitative discussion on the CFD results is proposed analyzing three types of plots obtained on a horizontal plane containing the release point, which is represented by the *black-box*. The velocity field is discussed looking at a velocity magnitude contour plot and at a streamlines plot while the gas distribution is analyzed through a contour plot showing the CH_4 concentration in ppm. The results related to cs#3 are shown in figure 5.19.

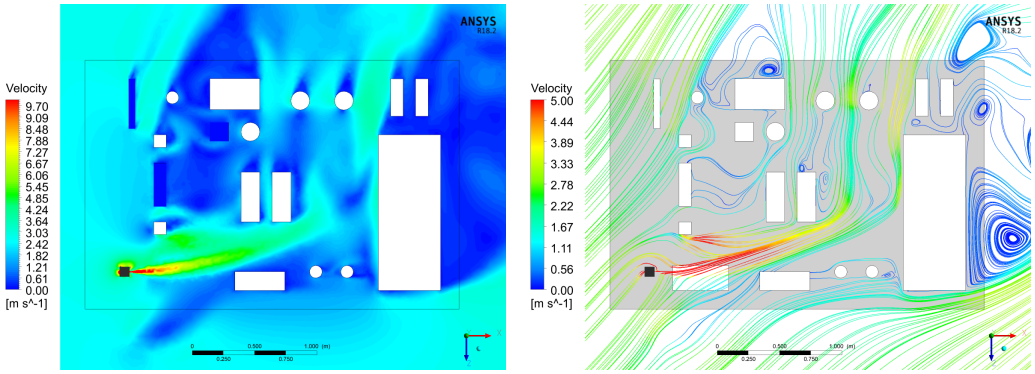

(a) Velocity magnitude contour plot.

(b) Velocity streamlines plot.

(c) CH_4 ppm contour plot.

Fig. 5.19 CFD results in terms of velocity field and gas concentration plots related to cs#3.

In this case, the release source is positioned at a corner of the domain and the wind direction (45° with respect to the x-axis) tends to advect the gas towards the internal portion of the domain. The streamlines plot shows the high inertia of the exiting jet represented by the red region, which after a certain distance is strongly affected by the wind direction and by the resistance of the big object in the right bottom corner. Several recirculation flows can be observed behind the objects,

especially near the outlet boundaries, but also in central region of the domain where the gas tends to accumulate. In fact, the gas distribution is clearly affected by the wind direction, but the picture shows also an amount of CH_4 in the central region in correspondence of low speed values. Analogous qualitative considerations can be derived for cs#1 and cs#2 as these case studies differ from cs#3 only for the pressure level, hence, the same pattern in the flow field and gas distribution are obtained (see plots in appendix D). The results related to cs#5 are presented in figure 5.20.

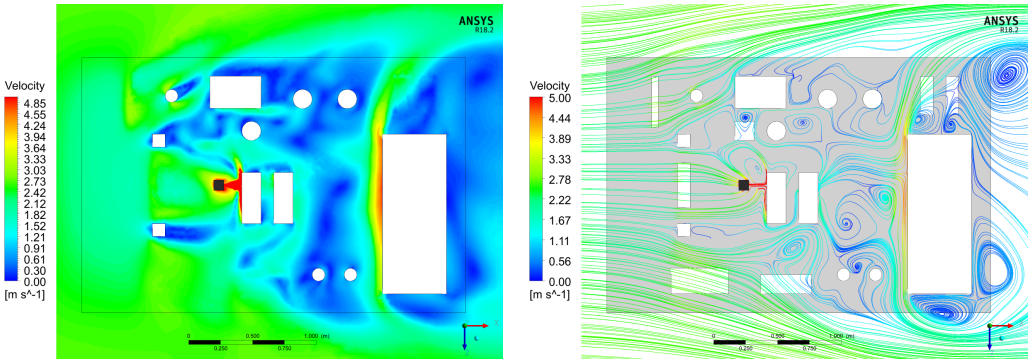

(a) Velocity magnitude contour plot.

(b) Velocity streamlines plot.

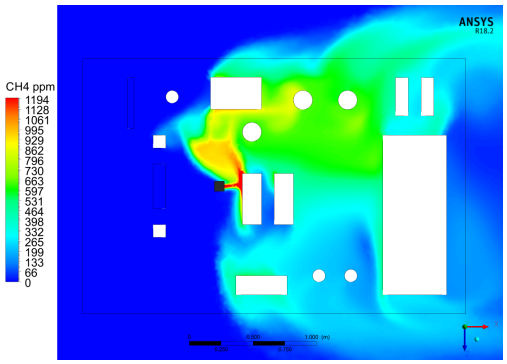

(c) CH_4 ppm contour plot.

Fig. 5.20 CFD results in terms of velocity field and gas concentration plots related to cs#5.

In this case the wind is directed according to the release (x-direction), hence it is expected that the gas distributes in a region in front of the leak source. A lot of low speed and recirculating flow regions can be observed in velocity field, which appears more complex with respect to the previous case. The most interesting result is related to the gas distribution plot which presents a surprisingly non symmetric behavior. An accumulation zone appears on the left of the release point (being consistent with the x-axis), moreover, it seems that the gas tend to flow in the backward direction

with respect to its initial release direction. In fact, the region of accumulation is at a lower x-coordinate with respect to the leak position, i.e. behind the release position. Figure 5.21 can be used to explain this behavior. It shows a 3D streamlines plot of the flow exiting from the black-box. It can be seen that the lower part of the emitted gas impacts on the object in front of the release point causing a splitting of the flow in two lateral portion.

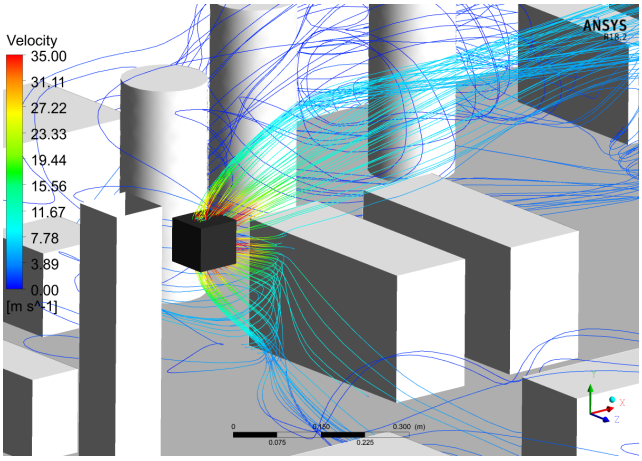

Fig. 5.21 3D streamlines of the flow exiting the black-box in the cs#5.

Moreover, after the impingement, the gas gains a certain amount of inertia in the backward direction which will be soon counterbalanced by the wind intensity. This impingement explains the lateral spreading of the gas distribution, which in different amounts is accumulated both on the left and right regions with respect to the release point. The largest amount of gas on the left of the leak point can be explained looking at figure 5.20(b). Due to the asymmetry in the geometry, some recirculating flows appear on the left of the release point, while not on the other side where the wind advection is more dominant, since there is a lower resistance to the flow having a smaller number of equipment objects. For this reason, the gas on the left side is trapped in these recirculating regions, while the gas on the right side is advected enhancing its mixing with the surrounding air. Analogous qualitative considerations hold for cs#4 since the only difference is a lower release pressure value (see appendix D). Figure 5.22 shows the results related to cs#8. This case study has some analogies with cs#5 since also in this case the release and wind direction are concordant and the leak is positioned on one of the deck axis. Differently from the previous case, there is no an asymmetric behavior and the spreading of the gas is

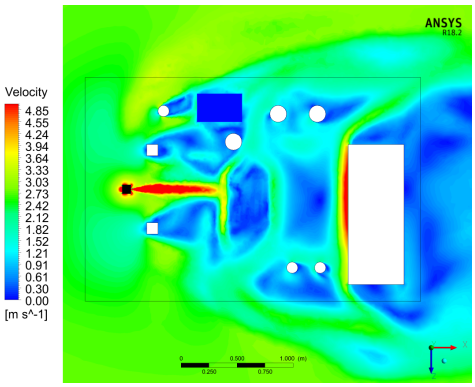

(a) Velocity magnitude contour plot.

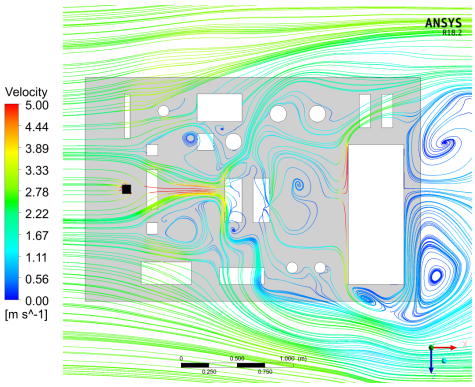

(b) Velocity streamlines plot.

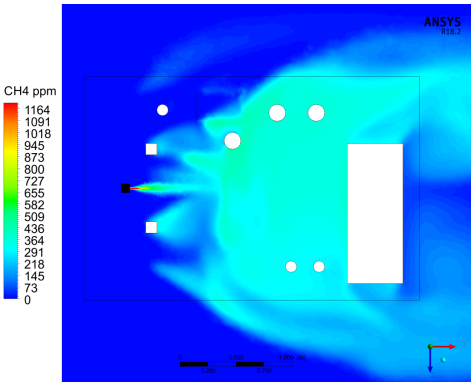

(c) CH_4 ppm contour plot.

Fig. 5.22 CFD results in terms of velocity field and gas concentration plots related to cs#8.

consistent with the release and wind directions. The gas in uniformly mixed in the domain, and no accumulation regions are observed. Analogous qualitative results are obtained in cs#6 and cs#7 as shown in appendix D since the only difference is a lower pressure value. Finally, the results related to cs#13 are shown in figure 5.23. In the velocity streamlines plot, a large inertia region can be identified along the release direction. The wind influence seems negligible as the jet follows an almost straight path from the leak point to the opposite boundary. The last discussion about cs#13 can be extended to cs#11 and cs#12, which differs only for the pressure levels, but also to cs#9 and cs#10 configurations since the only difference is the release height and the results are qualitatively similar (see appendix D).

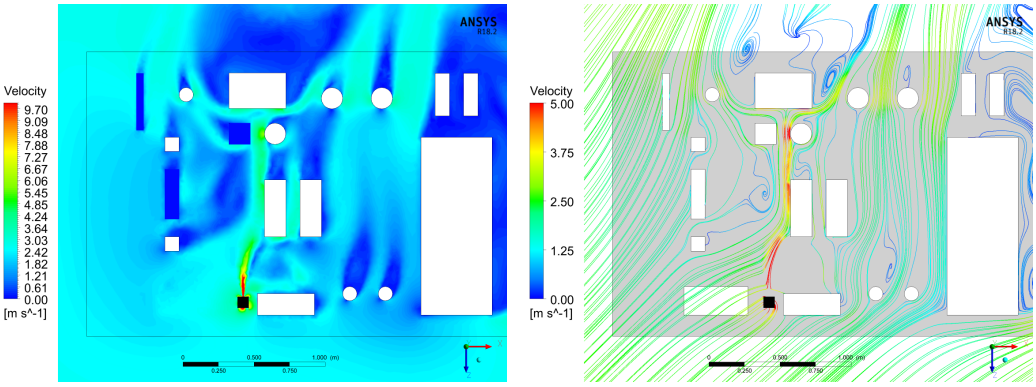

(a) Velocity magnitude contour plot.

(b) Velocity streamlines plot.

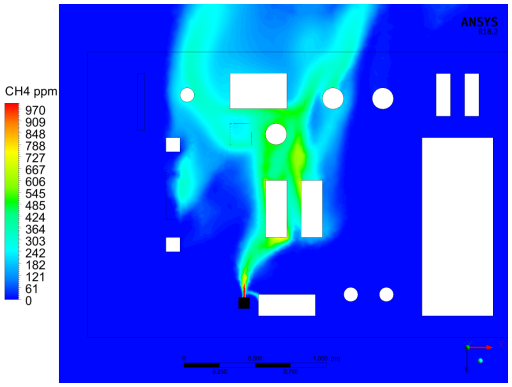

(c) CH_4 ppm contour plot.

Fig. 5.23 CFD results in terms of velocity field and gas concentration plots related to cs#13.

5.4 Experimental procedure and results discussion

5.4.1 Experimental procedure

A rigorous procedure was followed for each experimental test to avoid influence on the measurements by possible external factors. At first, the geometrical setup is prepared placing the mockup at the center of the WT test chamber and regulating the instrumented deck height to assure that it is invested by the uniform flow region. As an example, figure 5.24 shows the mockup tilted arrangement in the test chamber, adopted to reproduce a 45° impacting wind direction. Moreover, to have an overall picture of the setup, the connection by the black flexible hose between the release line (figure 5.13) and the nozzle (figure 5.14) is highlighted and a zoomed view of one cylindrical object with three pellistors plugged inside it is shown.

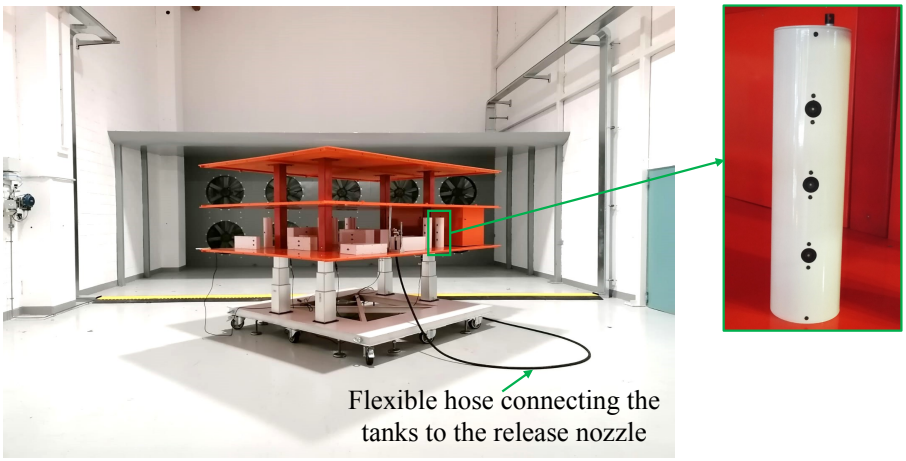

Fig. 5.24 Picture of platform mockup inside the wind tunnel with a zoomed view of an object to highlight the hidden gas sensors.

The nozzle is mounted in the deck position corresponding to each case study release position, with the correct orientation, and it is connected to the gas feed line through the hose. Once the geometry is set, all the connections are checked to avoid possible unintended gas leakages. At this point, the fans are remotely activated, set to the test wind velocity and are run up for 10 minutes. This phase is fundamental to assure that possible pollutant accumulation on the gas sensors are removed and to permit a full development of the wind field. In the meantime, from the software in the control room PC, the status of all the sensors is checked, to assure that the test is run only if all the sensors are properly working. Finally, the release pressure is

set from the software and the gas starts to exit. The target pressure is reached with a confidence interval of 10 %, after a short transient of the PID regulator, when the system is stabilized, the data acquisition starts and it is stopped after 45-50 seconds. For each of the gas sensors, the system acquires a measure with a 1 second time step. As an example, figure 5.25 (a) shows the measure on a sensor which highlights that there is an initial transient until the target pressure is reached, and then a stabilization with the formation of a plateau. Figure 5.25 (b) shows the measure on another sensor, highlighting that in some cases the plateau-like behavior is not obtained, while the measure oscillates around a certain value.

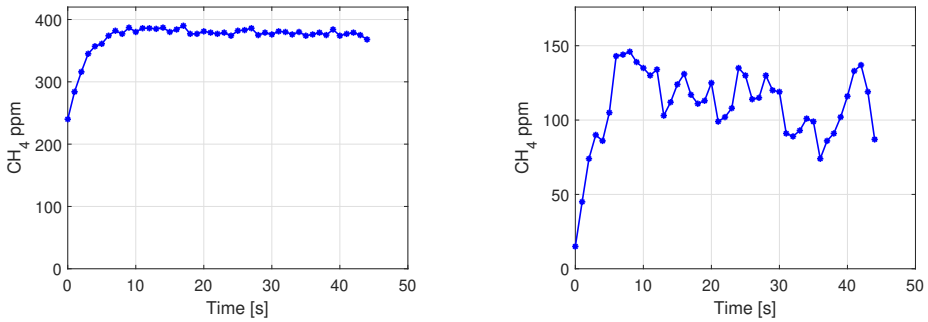

(a) (b)

Fig. 5.25 Example of measure for a single sensor: concentration vs time.

These different behaviors can be explained considering that the measure is largely influenced by the position of the sensor in the domain, indeed, regions characterized by less turbulence permit more stable measurements, while on the other hand high turbulent and unsteady flow locations lead to oscillating measures. However, a mean value is considered for each point of measure to be compared to the CFD steady state one, and a standard deviation is provided for each measure in order to have an idea about their quality. Basing on some preliminary tests, the duration of the tests was fixed at 45-50 seconds since the initial transient runs out in 5-10 seconds. This duration was judged as a good compromise to obtain a converged measure and reducing at minimum the gas depletion, thus permitting a large number of tests. The data related to the initial 5-10 seconds of transient are discarded, therefore the last 40-45 seconds of the measure are considered to evaluate the mean value. For each case study, 30 measurement points are considered among the available 38 for the discussion of the results. In fact, the gas sensors distribution is designed to have measurement points distributed throughout the mockup, thus allowing for a

greater flexibility in the availability of data as the case study changes. On the other hand, is also clear that, for each case study, a limited number of poorly significant measurement points can be identified, e.g. at marginal points on the platform with respect to the position of the jet.

5.4.2 Model performance criteria

The comparison between the predicted (numerical) concentration data C_P and the observed (experimental) data C_0 is performed at first through a qualitative comparison of the concentration levels at each considered point, and successively employing the approach suggested by Hanna et al. [111, 112]. This methodology was used by several authors for the evaluation of gas dispersion models [113–116] and involves several statistical parameters, namely, the fraction of predictions within a factor of two $FAC2$ (Eq. 5.26), the fraction of predictions within a factor of five $FAC5$ (Eq. 5.27), the fractional bias FB (Eq. 5.28), the geometric mean bias MG (Eq. 5.29), the normalized mean square error $NMSE$ (Eq. 5.30) and the geometric variance VG (Eq. 5.31).

$$FAC2 = \text{fraction of data that satisfy } 0.5 \leq \frac{C_P}{C_0} \leq 2 \tag{5.26}$$

$$FAC5 = \text{fraction of data that satisfy } 0.2 \leq \frac{C_P}{C_0} \leq 5 \tag{5.27}$$

$$FB = \frac{(\overline{C_0} - \overline{C_P})}{0.5(\overline{C_0} + \overline{C_P})} \tag{5.28}$$

$$MG = e^{(\overline{\ln C_0} - \overline{\ln C_P})} \tag{5.29}$$

$$NMSE = \frac{\overline{(C_0 - C_P)^2}}{\overline{C_0 C_P}} \tag{5.30}$$

$$VG = e^{\overline{(\ln C_0 - \ln C_P)^2}} \tag{5.31}$$

The comparison of the numerical and experimental sets of data (C_P, C_0) can be performed in several ways, depending on whether the data represent a space distribution, a time distribution or both. Thus, the matching can be only in time (i.e. comparing values at several points in the domain but considering the same time instant), only in space (i.e. comparing the time evolution at the same location) and matching both time and space. In this case, the time evolution is not analyzed whilst different measure locations are involved, hence, the model predictions and experimental data are paired in time, considering the steady-state configuration. The *FAC*2 and *FAC*5 are considered as the most robust measures because they are not affected by high and low outliers that may be present in the data sets. FB and MG are both measures of the mean bias and account for systematic errors that may lead to under/over estimation of measured values. On the other hand, $NMSE$ and VG account for both systematic and random errors. In a perfect model MG, VG, *FAC*2 and *FAC*5 would be equal to 1, while FB and $NMSE$ would be equal to 0. Nevertheless, due to the stochastic nature of turbulent flows and experimental measurement errors, there is no ideal dispersion model. For this reason, in [112] the authors propose a range of acceptability for each parameter, such that the performance of the model can be considered satisfactory. According to the authors, the fraction of predictions within a factor of two of observation, should be at least 50 % (*FAC*2>0.5). There is no explicit mention of the minimum *FAC*5 acceptable value, but since this requirement is soft, it is reasonable to expect that is met by at least 90 % of points. Since FB and MG are different expressions of the same statistical meaning, it is sufficient that at least one of them falls within the criterion of acceptability, that is the mean bias should be within $\pm$30 % of the mean ($|FB|$<0.3 or 0.7<MG<1.3). Lower values of the mean bias correspond to an over prediction of the model and, conversely, higher values are indicative of an under prediction. The considerations made for the previous parameters apply also to $NMSE$ and VG, i.e. at least one of the indicators corresponding to the random dispersion should be within a factor of two of the mean ($NMSE$<4 or VG<1.6). All the measures defined above, should be considered together as each one has pros and cons. For example, FB and $NMSE$ are linear measures and can be influenced by infrequently occurring high/low values in the predicted or measured concentrations, while MG and VG can provide a more balanced treatment as they are logarithmic measures.

5.4.3 Numerical and experimental results comparison

At first, a qualitative comparison between the numerical and the experimental methane concentrations obtained on each measuring point is presented in a barplot, where the mean experimental value (blue bar) is associated with a standard deviation (in red). This last is evaluated on the last 40 seconds of the measurements, which are the ones considered to evaluate the mean value as well, and serves as an indication about the oscillating nature of the measurement related to each sensor. This data comparison provides useful insights on the similarities/differences on the gas distributions in the domain although is a very rough analysis of the results. Figure 5.26 shows the sensors tags and distribution on the domain, and can be taken as reference for the following discussion on the bar plots.

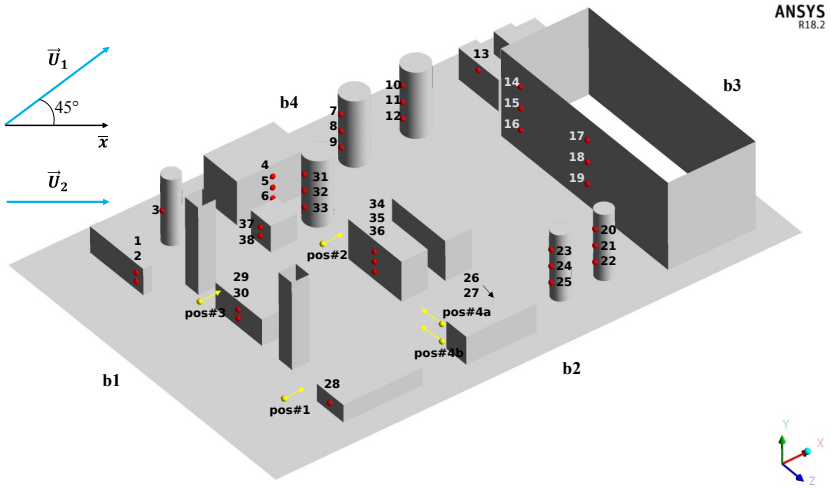

Fig. 5.26 3D CAD of the platform deck with the measuring points (in red), the leak source positions and directions (in yellow) and the schematic representation of the two wind directions considered.

In figure 5.27, the results related to cs#1-2-3 are presented. These case studies differs only in the release pressure value, whilst the other parameters are kept constant. In the plot related to cs#1, three regions can be identified: an overestimation between sensors 4-9 and 34-38, a good prediction between 10-21 and an underestimation between 21-27. With reference to figure 5.26 it can be observed that the region of underestimation is located in front of the release point (pos#1), whilst the region of overestimation in the center of the domain and towards boundary b4. These suggest that the gas jet is more influenced by the wind direction ($|\vec{U}_1|$) in the CFD simulation

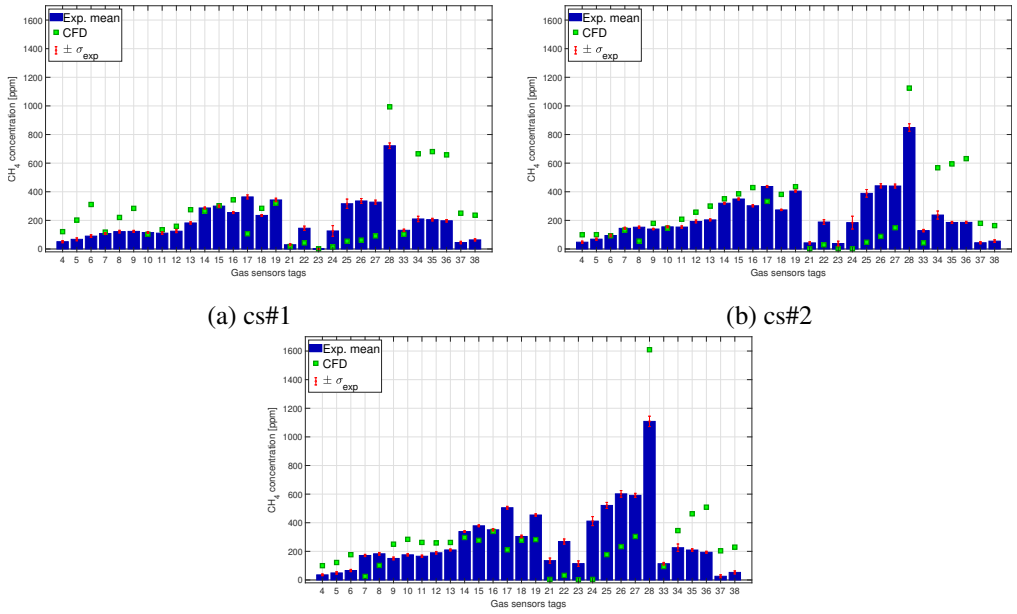

(a) cs#1 (b) cs#2

(c) cs#3

Fig. 5.27 Case studies cs#1-3: comparison of the experimental data (blue bars) with their standard deviations (red lines) and the SBAM results (green squares) in terms of measured gas concentration at sensors location.

(as also observable from D.1) with respect to the experimental case. In other words, from the experimental measure it results a higher gas concentration in the release frontal region, rather than in the central are of the domain, suggesting that the gas jet inertia is less influenced by the wind direction in this case. The peak concentration occur in both cases at sensor 28, located in front of the release point, and a slight CFD overestimation is observed. Analogous considerations can be made for cs#2 and cs#3, where the only difference with the previous case study is the increasing pressure. According to that, a progressive increase in the gas concentrations is registered going from cs#1 to cs#3, consistently with the increasing amount of discharged gas. Moreover, in cs#2-3 the discrepancies between the CFD and experimental values tend to reduce, suggesting that for a fixed configuration the model behavior is better as the release jet inertia increase. Figure 5.28 shows the results related to cs#4-5 (related to pos#2). In cs#4 the CFD predicted gas concentrations appear consistent with the experimental ones almost on all the sensors locations. Significant overestimations are registered for the sensors 4-6, 31-32 and 35-36. The peak concentration is almost perfectly matched on the sensor 34, that is the one in front of the release point. It can be noticed a slight enhancing of the model prediction with respect to the previous

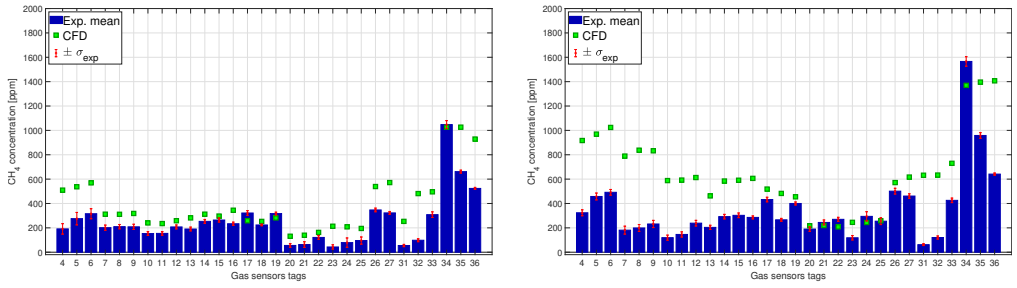

(a) cs#4 (b) cs#5

Fig. 5.28 Case studies cs#4-5: comparison of the experimental data (blue bars) with their standard deviations (red lines) and the SBAM results (green squares) in terms of measured gas concentration at sensors location.

cases, at least in the overall gas distribution in the domain, which can be ascribed to the fact the the wind ($|\vec{U_2}|$) and release direction are in this case coincident. In cs#5 a large model overestimation is observed in correspondence of sensors 4-12, 31, 32, 36. This can be explained considering that, as shown in 5.20, the gas jet is split in two lateral regions and tend to spread towards boundaries b2, b4 (see figure 5.26), while the experimental results suggest that the gas is mainly distributed in front of the release point. Moreover, a large gas concentration is observed in the CFD plots (see figure 5.20) in the region of the 4-12, 31, 32, 36 sensors. A special discussion can be made for sensor 36 that is in front of the leak source, near the floor. In the CFD calculation the cylindrical obstacle inside of the SB has a finite height, equal to L_{SB}, while in the experiment there is a through cylinder. This approximation in the CFD, could be responsible of some prediction errors near the leak point, on the other hand, it greatly simplifies the numerical implementation. Figure 5.29 shows the results related to cs#6-7-8 which differs only in the release pressure, whilst the other parameters are maintained constant. Also in the configuration of these three case studies, the release and wind directions are concordant, and also in this cases, an overall good model prediction is observed, except for few sensor locations. The only large discrepancies occur at sensors 29-30, where a large over estimation can be observed. These two sensors are positioned in front of the release point (pos#3), at a lower height, and the over prediction can be ascribed also in this case to the SB obstacle approximation as for cs#5. In the end, the results related to cs#9-13 are presented in figure 5.30. Analogous considerations can be derived for these case studies, since the test arrangement are similar. Two regions can be distinguished in the plots, one characterized by extremely low concentration levels (sensors 17-25)

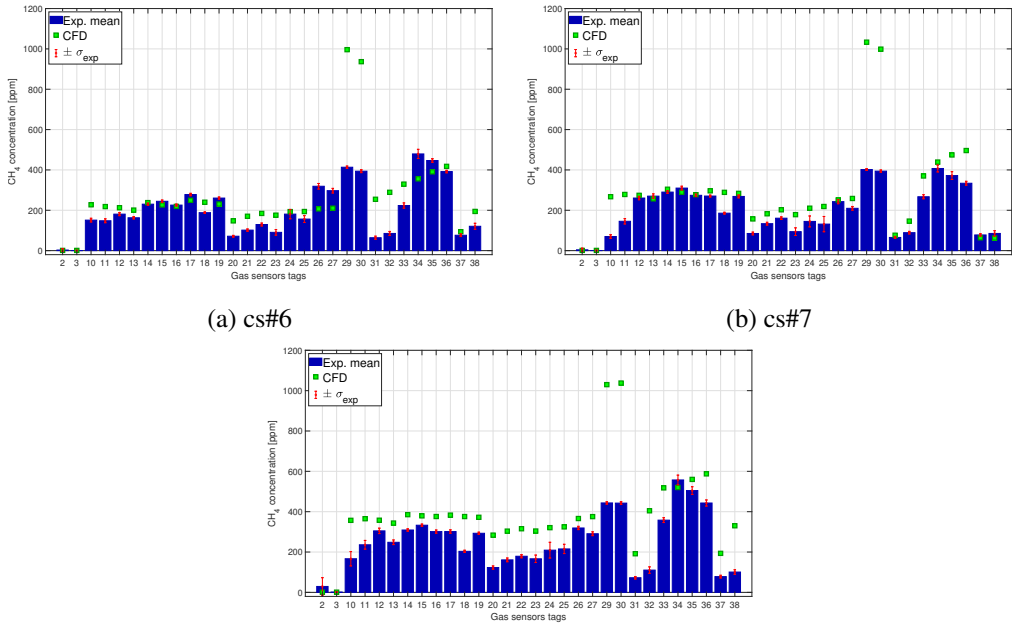

(a) cs#6

(b) cs#7

(c) cs#8

Fig. 5.29 Case studies cs#6-8: comparison of the experimental data (blue bars) with their standard deviations (red lines) and the SBAM results (green squares) in terms of measured gas concentration at sensors location.

and one where the gas presence is clearly visible (sensors 3-10, 31-38). These lasts, are located in front of the release points, towards boundary b4. In the CFD simulation the gas spreads in front of the release point, as shown also in figure 5.23, and the wind direction ($|\vec{U}_2|$) does not influence noticeably the jet behavior. The same behavior is obtained in the experimental measure, since the gas distribution seems analogous, at least qualitatively, from the barplots, therefore, it can be deduced that the model well predicts the gas spreading in the domain. However, also in this case the wind advection seems larger in the CFD results. In fact, the gas concentration at sensors 7-10 is always overestimated, and these lasts are located near boundaries b4-b3, which are the outlet with respect to the wind direction. This suggests that the gas is advected by the wind in that points, while in the tests the jet is more aligned with the release direction and has less lateral spreading.

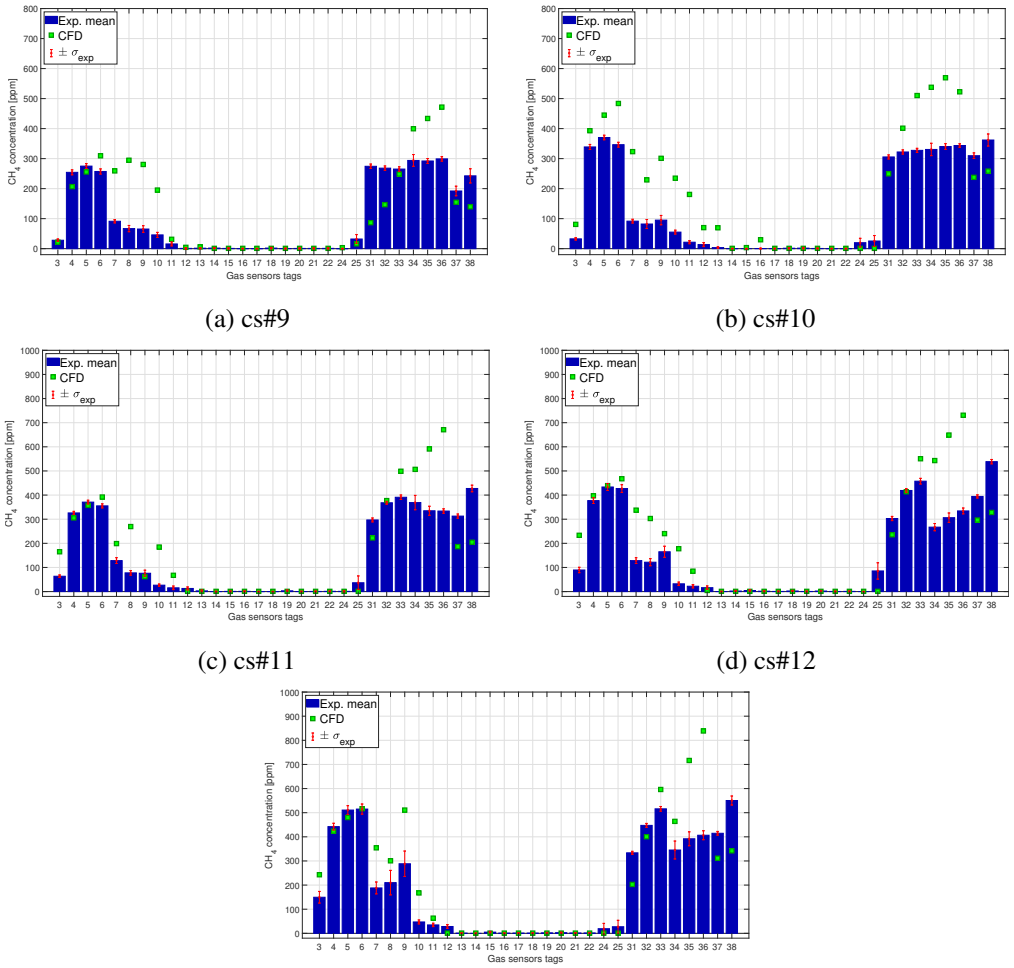

(a) cs#9

(b) cs#10

(c) cs#11

(d) cs#12

(e) cs#13

Fig. 5.30 Case studies cs#9-13: comparison of the experimental data (blue bars) with their standard deviations (red lines) and the SBAM results (green squares) in terms of measured gas concentration at sensors location.

At this point, the discussion can be focused on the quantification of the model prediction error through the evaluation of the statistical parameters for each case study. Results are summarized in table 5.8 where the values falling in the acceptability criteria are highlighted in bold. It can be noticed that the *FAC*2 criterion is always satisfied as no values under 50% are obtained, and the *FAC*5 assumes always values larger than 80% and in several cases it reaches the 100%. The performance in terms of this two parameters can be easily visualized through some scatter plots, as shown in figures 5.31 and 5.32, where the two sets (C_0, C_P) are directly related.

case study	*FAC*2	*FAC*5	*FB*	*MG*	*NMSE*	*VG*
cs#1	**50%**	87%	**-0.257**	**0.917**	**0.627**	2.686
cs#2	**50%**	80%	**-0.092**	1.482	**0.419**	10.647
cs#3	**50%**	80%	**0.070**	1.462	**0.378**	14.862
cs#4	**73%**	100%	-0.431	0.581	**0.24**	1.634
cs#5	**50%**	93.3%	-0.589	0.5	**0.51**	2.377
cs#6	**83.3%**	100%	**-0.268**	**0.768**	**0.373**	**1.29**
cs#7	**90%**	100%	-0.353	**0.752**	**0.385**	**1.234**
cs#8	**70%**	96.7%	-0.434	**0.703**	**0.321**	2.06
cs#9	**83.3%**	100%	**-0.188**	**0.886**	**0.326**	**1.448**
cs#10	**63.3%**	80%	-0.384	0.657	**0.242**	8.036
cs#11	**73.3%**	90%	**-0.193**	**1.001**	**0.229**	2.72
cs#12	**66.7%**	93.3%	**-0.263**	**0.933**	**0.269**	2.812
cs#13	**83.3%**	90%	**-0.165**	**1.198**	**0.186**	3.262

Table 5.8 Statistical parameters values for each case study. In bold, the values that fall within the acceptable ranges.

A perfect correlation is obtained when all the points belong to the bisector, as it means that C_0 and C_P assume the same value. Since this is impossible to be obtained, due to the presence of numerical errors, and experimental ones as well, a good correlation plot can be considered the one with the largest number of points distributed around the bisector with the lowest possible scattering. Moreover, the *FAC*2 and *FAC*5 limits, represented respectively by the red and green dotted lines, help in the identification of a good correlation regions. The best correlation plots are obtained for cs#6-7-8, where the points are almost aligned on a straight line, while the more scattered plots are obtained for cs#2-3-10-11-12-13 where several points appear in the lowest portion of the plot. In these last cases, the out of bounds points mostly appear in the region of the plot where $C_0 \gg C_P$ and are related to regions where the model predicts near zero concentrations while the measures reveal the gas presence. It should be emphasized that in some measuring points, ppm numerical values of the order of magnitude of 10^{-4} or lower are obtained in the numerical solution. Since this has no physical meaning, these values were rounded up to unity to permit the calculation of the statistical parameters, which otherwise would result impossible in some cases. This assumption is consistent with the fact that the

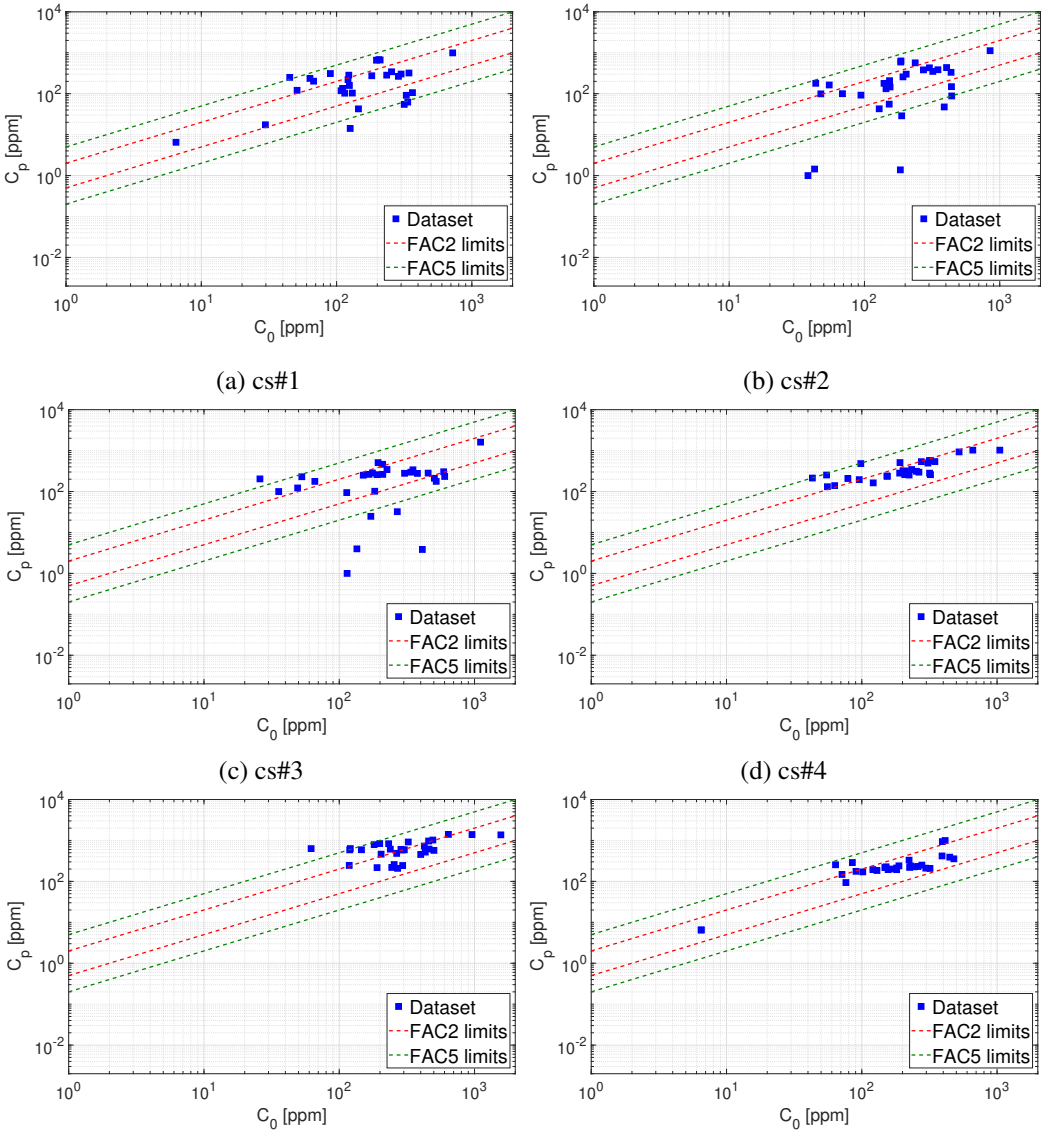

(a) cs#1

(b) cs#2

(c) cs#3

(d) cs#4

(e) cs#5

(f) cs#6

Fig. 5.31 Correlation plots for case studies cs#1-6.

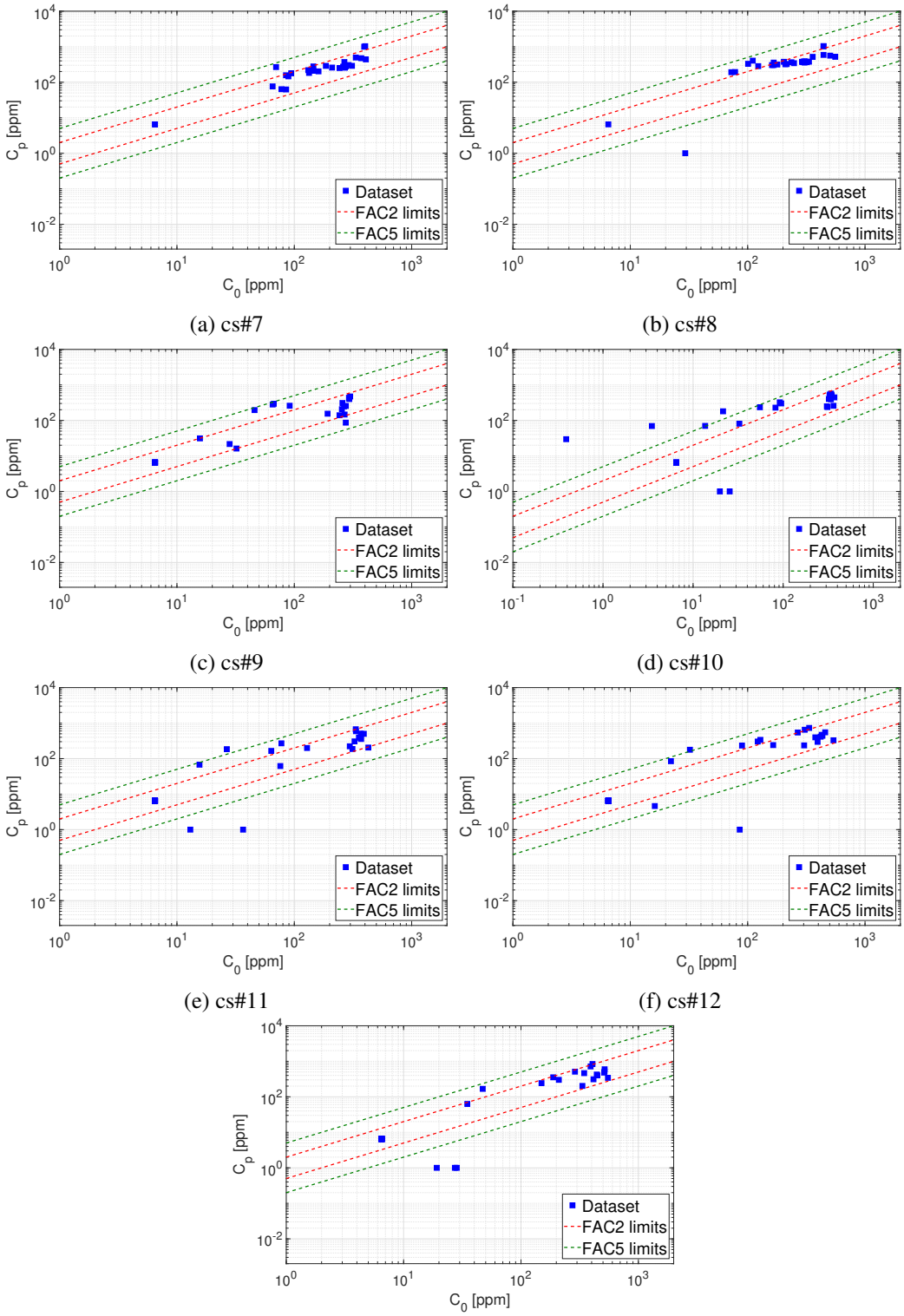

(a) cs#7

(b) cs#8

(c) cs#9

(d) cs#10

(e) cs#11

(f) cs#12

(g) cs#13

Fig. 5.32 Correlation plots for case studies cs#7-13.

predicted concentration in that points is extremely low, and a value of 1 ppm can be reasonably considered representative of that situation. The fact that the FB assumes only negative values except one case, emphasize that the numerical predictions globally overestimates the experimental ones, as deduced by the barplot discussion. For most of the case studies the value fell inside the acceptability range, and the other assumes values near the minimum threshold (-0.3) suggesting that the overestimation is not very large. The MG values are all around the acceptability range (0.7-1.3) no matter they are inside or not. Also in this case in most of the cases the requirement is met, and more importantly, this happen also for some case studies with FB outside the acceptable range. In fact, model predictions with a fractional bias (FB) of 0.0 are relatively free from bias values, while values of -2.0 and +2.0 correspond respectively to extreme overestimation and extreme underestimation, being FB symmetric and bounded. Consistently, values of the MG that are equal to 0.5 and 2 are equivalent respectively to an overprediction and an underprediction of the model by a factor of two. The $NMSE$ values are all within the acceptable ranges for all the different case studies while on the other hand, VG falls outside the acceptable range in most of the cases. The small values obtained for $NMSE$ suggest that the data sets are normally distributed, in fact, having $NMSE \gg 1$ would imply a log-normal distribution of the data. This suggests that VG is not suitable for the evaluation of the model as it expresses the scatter of a log-normal distribution [112], therefore, this can explain the VG non-compliance with the acceptability criteria. However, it should be considered that usually, for the calculation of MG and VG a minimum threshold value for both C_0 and C_P should be defined, since both parameters are influenced by extremely low values and are undefined for zero values. Since the threshold value definition is not trivial, as the concentrations are generally very low, no thresholds are introduced and all the selected measurements are considered, even though this might influence the values assumed by the parameters. The choice of a certain threshold could in fact facilitate compliance with the conditions necessary to consider the values obtained acceptable.

5.4.4 SBAM performance: practical considerations

From the previous results, some considerations can be drawn about the overall model performance. At first, it can be noted that SBAM well predicts the general trend of the experimental gas distributions in all the case studies. For example, with reference to figure 5.30 it can be appreciated how near-zero values are predicted at the same locations of the experimental tests, and analogously for the high gas concentration locations. Results hint also that SBAM prediction capabilities results more effective in case studies characterized by concordant wind and gas release directions. In fact, from the comparison of the numerical and experimental measures on case studies involving a gas release direction discordant with respect to the wind one (cs#1-3 and cs#9-13) it can be deduced that the gas distribution is more influenced by the wind inertia in the numerical simulation rather than in the experimental tests. Moreover, the results comparison in the bar plots related to case studies with a concordant wind and release direction (cs#4-8) show that the predicted gas distribution resemble the experimental ones, at least in the shape despite some systematic overestimations are also observed. Another important hint comes from the observation of the model prediction capabilities in proximity of the release point. In fact, predictions in measuring point in front of the release position are generally largely overestimated, as can be observed on sensors 29, 30 in cs#6-8 (related to pos#3). This consideration hint that the approximation or spatial discontinuity introduced by the SB presence in the numerical solution have a certain influence on the model prediction in proximity of the leakage point.

At this point, to summarize the model prediction quality for all the case studies, the parameters listed in table 5.8 can be grouped according to their statistical significance to check if the acceptability requirements are met or not.

- at least 50% of measuring points with $FAC2 > 0.5$
- $|FB| < 0.3$ or $0.7 < MG < 1.3$
- $NMSE < 4$ or $VG < 1.6$

The results for the different case studies under analysis are shown in table 5.9, that shows the acceptability in the various cases, denoting with Y and N the cases in which the criteria are respectively fulfilled or not.

case study	$FAC2$	FB or MG	$NMSE$ or VG
cs#1	Y	Y	Y
cs#2	Y	Y	Y
cs#3	Y	Y	Y
cs#4	Y	N	Y
cs#5	Y	N	Y
cs#6	Y	Y	Y
cs#7	Y	Y	Y
cs#8	Y	Y	Y
cs#9	Y	Y	Y
cs#10	Y	Y	Y
cs#11	Y	Y	Y
cs#12	Y	Y	Y
cs#13	Y	Y	Y

Table 5.9 Acceptance of the statistical parameters values for each case study.

In all the case studies except cs#4-5, the three requirements are met. The condition not satisfied for these two cases is the one related to the mean bias, in fact it is observable from the bar plots that a systematic and large model overestimation occurs. The cs#4-5 are the ones where the SB is placed in front of a blocking object which causes a strong impingement and a consequent strong flow lateral spreading, hence the low accuracy in the modeling of these phenomenon may be the cause of the larger discrepancies with respect to the other case studies.

Figure 5.33 helps to visualize the overall model performance in a single plot, where the $NMSE$ values *vs* the FB values with a confidence interval of 95% are shown. The vertical black dashed lines represent the limits of the factor-of-two mean bias for prediction. All the case studies fall in the negative FB region except one, suggesting an overall tendency of the model to overestimates the experimental values, confirming the considerations derived from the bar plots. Most of the points are inside the range $-0.4 \lesssim FB \lesssim -0.2$, that means an overestimation of about 20–40 %, while the worst performance is registered for a test inducing almost a 60 % of discrepancy. The only one point falling in the underprediction region, induces a discrepancy of about 10 %. The graph permits to easily judge the overall behavior of SBAM, which can be defined conservative from a safety-oriented point of view as the involved gas quantities in the scenario are overestimated. In general, also the parameters that fall within the range of acceptability have values that indicate a

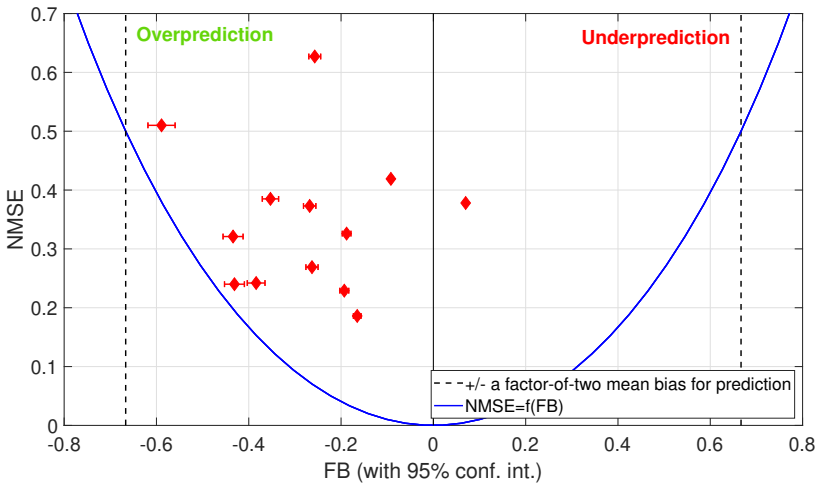

Fig. 5.33 NMSE *vs* FB for the case studies with a 95 % confidence interval.

slight overestimation. Overall, these results demonstrate that, although there is not a perfect match between expected and measured concentrations for all the cases, at the very least the model turns out to be acceptable from the point of view of risk analysis, which follows conservative approaches that allow to retrieve more cautious estimates. It can be concluded that SBAM is capable to reproduce with sufficient accuracy several accidental scenarios characterized by a numerous combination of pressure levels, leak locations and directions and wind directions. The discrepancies between the predicted results and the experimental data could be ascribed to different factors: the observed values are affected by uncertainties due to random turbulence in the test environment (that is the open-channel of the WT), slight oscillations of the release pressure and wind velocity values due to physical systems non-ideality, measurements errors, presence of combustible gas particles in the test chamber due to air pollution. Additionally, the uncertainties related to the CFD simulations can play a key role: physics modeling errors, numerical error etc., can affect the solution.

A final remark is needed about the model performance. According to the criteria defined in Hanna et al. [112], the model is validated, since the requirements on the statistical parameters are met in the large majority of the case studies (11 out of 13, as shown in table 5.9). However, the model was tested considering only one type of gas and not considering significant configurations, e.g. counter wind ones, hence, it is more appropriate to refer to a *preliminary* or *partial* validation of the model, seeking for future activities aiming at a *complete* validation.

Chapter 6

Final discussion, conclusions and perspectives

In this thesis, a novel CFD approach targeted for QRA-oriented accident simulations is presented. In particular, the model design choices, its applicability range and its novelties are defined and discussed after a description of the main features of the target physical phenomenon. Moreover, the model prediction capabilities are assessed through a *numerical benchmark* analysis and an *experimental validation*.

The CFD approach here proposed, is called Source Box Accident Model (SBAM) and is oriented to the simulation of high-pressure gas releases in congested domains. It is developed adopting a design philosophy which fits between the two main CFD approaches already available in literature for these kind of scenarios: hybrid empirical model-CFD approaches and full numerical ones. Like the first ones, SBAM entails the splitting in two steps of the phenomenon, the initial gas *release* jet expansion and the subsequent gas *dispersion*, but provides a higher level of accuracy in the modeling of the *release*. Like the second ones, SBAM is based on a full numerical approach, but guarantees a lower computational cost.

This *two-steps* strategy resulted advantageous from a simulation implementation point of view as demonstrated by the *numerical benchmark* analysis. In fact, it simplifies the handling of the multi physics nature of the phenomenon with respect to a «classical» CFD approach. Simulating the high inertia underexpanded jet in the SB and only the subsonic incompressible flow in the case study domain permits to differentiate models and methods, and permits to easily address the mesh generation

issues. Moreover, results show that the risk metrics evaluated through SBAM are in good accordance with the one obtained in the *benchmark* simulation, having that relative errors on these output parameters are under the 20%. It must be emphasized that this is considered an acceptable outcome from a QRA point of view, while it can represent a limitation for other engineering applications of CFD. On the other hand, simulating an extremely underexpanded jet in a small domain, such as the SB, represented a real challenge from the numerical solution point of view. It required deep investigations on suitable methodologies for prescribing the inlet boundary conditions as well as assuring a stable convergent solution, in fact, the higher the release pressure the harder the convergence. This could represent a possible limitation of the model, seeking for extremely high-pressure gas releases (>100 bar, which is the current maximum pressure modeled in SBAM). In this respect, strategies to enlarge the applicability range of the model should be investigated in view, for example, of future scenarios involving high-pressure H_2 storage technologies (up to 350 or 700 bar [117]) for the transport sector. The adoption of adaptive mesh algorithms coupled with a pseudo-transient formulation of the governing equations could represent a possible strategy to help the solution convergence in presence of extremely high gradients. Moreover, the implementation of real gas models should be foreseen to evaluate the gas density at very high pressure values, since in that conditions the ideal gas law could be no more applicable, especially in some cases where the substance could behave as a supercritical fluid (e.g. CO_2). The *two-steps* strategy resulted convenient also from a computational cost point of view, having proved the feasibility of a Reduced Order Model (ROM) to reproduce the SB behavior. In fact, the main computational burden is associated to its simulation ($\sim$24 h against $\sim$3 h of the dispersion) and results show that the ROM can accurately provide SB-like results in few seconds, thus, completely cutting out the computation time, with an extremely low impact on the final risk metrics evaluation (less than 7%).

A comparison with two industrial CFD tools, FLACS and KFX, demonstrates that SBAM can guarantee a comparable computational time (if the SB ROM is exploited), assuring a higher level of modeling flexibility and results output quality, thanks to the general purpose nature of ANSYS Fluent. On the other hand, a slightly greater effort is required to the user for the simulation implementation, since FLACS and KFX are specific purpose tools for safety analyses with a user interface tailored on the simulation of accidental scenarios.

The outcomes of these numerical investigations, suggest that SBAM reflects the principle of *fast-calculation and simple use* introduced in chapter 1.1.2 and represents a step towards the demonstration of the CFD-QRA integration feasibility. However, despite it permits a significantly faster evaluation with respect to a *standard* CFD approach (employing general purpose CFD codes), its computational cost is still too high for the simulation of a complete set of QRA scenarios, hence, integral and empirical models still represent the more practical solution. Nonetheless, the number of critical scenarios analyzed through CFD could be significantly increased, and the possibility of generating high accuracy CFD results without a huge computational burden, could represent a strategy to help the development, calibration and validation of simplified integral tools for consequences assessment. Moreover, it can be employed to generate a large quantity of data to be exploited as training and validation sets for novel artificial intelligence (AI) models to predict the consequences of a large number of scenarios. In fact, a synergistic use of CFD and machine learning algorithms could represent a possible answer to the necessity of more accurate and fast models, which consider the actual geometry of the domain. As an example, the design optimization of gas sensors locations in a specific plant could be performed by using AI tools trained by a set of CFD predictions of several leakage scenarios.

The *experimental validation* required to reproduce a set of gas release scenarios on a scaled platform mockup in a wind tunnel. These tests, required the development of an *ad hoc* scaling procedure, (described in detail in the present work) to define reduced scale case study parameters. Results show a good agreement between the numerical (predicted) and the experimental (observed) data, in fact, a *preliminary* or *partial* validation of the model is achieved. A slight overestimation tendency of the model is registered, and this is a positive outcome from a safety assessment point of view, since a conservative approach is always preferred.

As a final consideration, this research aimed at contributing to the know-how of high-pressure gas releases modeling, providing useful insights from both the numerical and the experimental side, setting the basis for other future activities. Among the others, it suggests alternative solutions to the convergence issues of the CFD simulation of such events, it provides useful hints on their experimental testing, and provides a scaling procedure tailored on high-pressure gas releases under wind conditions closing the literature gap on this topic. Future numerical and experimental activities should be carried out to enlarge the model applicability range as well as to achieve a *complete* validation. A possible follow up of SBAM could

be the modeling of chemical reactions, perhaps considering fires, as well as the SB ROM could be improved by considering the variation of other parameters apart from the release pressure, e.g. the hole size, in order to extend its range of application. More in general, this work could represent the basis for other investigations on more accurate modeling of fires and explosions, which can exploit the two steps nature of SBAM, or the SB itself as an input which avoid to simulate the complex compressible flow near the leak source. Moreover, the model performance could be investigated by considering extremely heavy or light gases (e.g. CO_2, H_2), for which buoyancy effects could strongly affect the concentration spatial distribution and, as a consequence, the hazardous zones estimation in the risk assessment. This would be a crucial improvement, since the design and optimization of safeguards such as gas detection systems, is strongly influenced by this phenomenon, which must therefore be accurately modeled.

References

[1] IPCC. Carbon dioxide capture and storage, 2005.

[2] J. Andersson and S. Grönkvist. Large-scale storage of hydrogen. *International journal of hydrogen energy*, 44(23):11901–11919, 2019.

[3] B.G. Pollet, I. Staffell, J.L. Shang, and V. Molkov. Fuel-cell (hydrogen) electric hybrid vehicles. In *Alternative Fuels and Advanced Vehicle Technologies for Improved Environmental Performance*, pages 685–735. Elsevier, 2014.

[4] R.L. Murray. Chapter 7 - fusion. In Raymond L. Murray, editor, *Nuclear Energy (Sixth Edition)*, pages 83–90. Butterworth-Heinemann, Boston, sixth edition edition, 2009.

[5] U. Hauptmanns. *Process and Plant Safety*. Springer, 2020.

[6] J. Casal. *Industrial safety Series: Evaluation of the Effects and Consequences of Major Accidents in Industrial Plants*, volume 8. Elsevier Science, 2008.

[7] H. Kumamoto and E.J. Henley. *Probabilistic Risk Assessment and Management for Engineers and Scientists*. IEEE Press, 1996.

[8] Council Directive. 96/82/ec of 9 december 1996 on the control of major-accident hazards involving dangerous substances. *Official Journal of the European Communities, L*, 10(13):0013–0033, 1997.

[9] C. Kirchsteiger, M. D. Christou, and G. A. Papadakis. *Industrial Safety Series: Risk assessment and management in the context of the seveso II directive*, volume 6. Elsevier Science, 1998.

[10] EU Parliament. Directive 2013/30/eu of the european parliament and of the council of 12 june 2013 on safety of offshore oil and gas operations and amending directive 2004/35/ec. *Official Journal of the European Union*, 2013.

[11] J. Vinnem and W. Røed. *Offshore Risk Assessment Vol. 2*. Springer, 2014.

[12] C. J. Chen and W. Rodi. Vertical turbulent buoyant jets: a review of experimental data. *NASA Sti/Recon Technical Report A*, 80:23073, 1980.

[13] H.A. Becker, H.C. Hottel, and G.C. Williams. The nozzle-fluid concentration field of the round, turbulent, free jet. *Journal of Fluid Mechanics*, 30(2):285–303, 1967.

[14] G.A. Davidson. Simultaneous trajectory and dilution predictions from a simple integral plume model. *Atmospheric Environment (1967)*, 23(2):341–349, 1989.

[15] TNO. *Methods for the calculation of physical effects, Yellow Book*. The Hague, 2005.

[16] E. Zamejc. Api standard 521 new alternative method to evaluate fire relief for pressure relief device sizing and depressuring system design. *Journal of Loss Prevention in the Process Industries*, 27:21–31, 2014.

[17] Q.A. Baker, M.J. Tang, E.A. Scheier, and G.J. Silva. Vapor cloud explosion analysis. *Process Safety Progress*, 15(2):106–109, 1996.

[18] DNV. PHAST. https://www.dnv.com/software/services/plant/consequence-analysis-phast.html. [Online; accessed 21-June-2022].

[19] EPA US. ALOHA software. https://www.epa.gov/cameo/aloha-software. [Online; accessed 21-June-2022].

[20] A. Dasgotra, G.V.V. Varun Teja, A. Sharma, and K.B. Mishra. Cfd modeling of large-scale flammable cloud dispersion using flacs. *Journal of Loss Prevention in the Process Industries*, 56:531–536, 2018.

[21] M. Derudi, D. Bovolenta, V. Busini, and R. Rota. Heavy gas dispersion in presence of large obstacles: selection of modeling tools. *Industrial & Engineering Chemistry Research*, 53(22):9303–9310, 2014.

[22] A.M. Schleder, E. Pastor, E. Planas, and M.R. Martins. Experimental data and cfd performance for cloud dispersion analysis: The usp-upc project. *Journal of Loss Prevention in the Process Industries*, 38:125–138, 2015.

[23] C. Zuliani, C. De Lorenzi, and S. Ditali. Application of cfd simulation to safety problems–challenges and experience including a comparative analysis of hot plume dispersion from a ground flare. *Chemical Engineering Transactions*, 53:79–84, 2016.

[24] M. Pontiggia, V. Busini, M. Ronzoni, G. Uguccioni, and R. Rota. Effect of large obstacles on high momentum jets dispersion. In *Conference on Safety & Environment in Process & Power Industry-CISAP6*, pages 523–528, 2014.

[25] M. Gerbec, M. Pontiggia, G. Antonioni, A. Tugnoli, V. Cozzani, M. Sbaouni, and R. Lelong. Comparison of udm and cfd simulations of a time varying release of lpg in geometrical complex environment. *Journal of Loss Prevention in the Process Industries*, 45:56–68, 2017.

[26] M. Gerbec, P. Vidmar, G. Pio, and E. Salzano. A comparison of dispersion models for the lng dispersion at port of koper, slovenia. *Safety science*, 144:105467, 2021.

[27] M. Bellegoni, F. Ovidi, L. Tempesti, A. Mariotti, L. Tognotti, G. Landucci, and C. Galletti. Optimization of gas detectors placement in complex industrial layouts based on cfd simulations. *Journal of Loss Prevention in the Process Industries*, 80:104859, 2022.

[28] G. Landucci, M. Pontiggia, N. Paltrinieri, and V. Cozzani. Computational fluid dynamics modeling: Tutorial and examples. *Dynamic Risk Analysis in the Chemical and Petroleum Industry*, pages 115–125, 2016.

[29] G. Landucci, A. Tugnoli, V. Busini, M. Derudi, R. Rota, and V. Cozzani. The viareggio lpg accident: lessons learnt. *Journal of Loss Prevention in the Process Industries*, 24(4):466–476, 2011.

[30] R. Shen, Z. Jiao, T. Parker, Y. Sun, and Q. Wang. Recent application of computational fluid dynamics (cfd) in process safety and loss prevention: A review. *Journal of Loss Prevention in the Process Industries*, 67:104252, 2020.

[31] IPCC. Global warming of 1.5°, 2018.

[32] IEA. The future of hydrogen energy, 2019.

[33] IOGP. Process leak frequencies, 2010.

[34] C. Vivalda, R. Gerboni, and A. Carpignano. A practical approach to risk-based gas monitoring system design for oil and gas offshore platforms. In *Proceedings of the 14th Probabilistic Safety Assessment and Management Conference*, 2018.

[35] Y. Deng, H. Hu, B. Yu, D. Sun, L. Hou, and Y. Liang. A method for simulating the release of natural gas from the rupture of high-pressure pipelines in any terrain. *Journal of Hazardous Materials*, 342:418–428, 2018.

[36] X. Liu, A. Godbole, C. Lu, G. Michal, and P. Venton. Study of the consequences of co2 released from high-pressure pipelines. *Atmospheric Environment*, 116:51–64, 2015.

[37] A.D. Birch, D.R. Brown, M.G. Dodson, and F. Swaffield. The structure and concentration decay of high pressure jets of natural gas. *Combustion Science and Technology*, 36(5-6):249–261, 1984.

[38] I.C. Tolias, S.G. Giannissi, A.G. Venetsanos, J. Keenan, V. Shentsov, D. Makarov, S. Coldrick, A. Kotchourko, K. Ren, O. Jedicke, D. Melideo, D. Baraldi, S. Slater, A. Duclos, F. Verbecke, and V. Molkov. Best practice guidelines in numerical simulations and cfd benchmarking for hydrogen safety applications. *International Journal of Hydrogen Energy*, 44(17):9050–9062, 2019.

[39] J. Hu, D.M. Cristopher, and X. Li. Simplified partitioning model to simulate high pressure under-expanded jet flows impinging vertical obstacles. *International Journal of Hydrogen Energy*, 43(29):13649–13658, 2018.

[40] X. Li, D.M. Christopher, E.S. Hecht, and I.W. Ekoto. Comparison of two-layer model for hydrogen and helium jets with notional nozzle model predictions and experimental data for pressures up to 35 mpa. *International Journal of Hydrogen Energy*, 42(11):7457–7466, 2017.

[41] C. Colombini, G. Maugeri, G. Zanon, R. Rota, and V. Busini. Unignited high-pressure methane jet impinging a pipe rack: practical tools for risk assessment. *Journal of Loss Prevention in the Process Industries*, 69:104378, 2021.

[42] C. Colombini, E. Carminati, A. Parisi, R. Rota, and V. Busini. Safety evaluations on unignited high-pressure methane jets impacting a spherical obstacle. *Journal of Loss Prevention in the Process Industries*, 74:104631, 2022.

[43] C. Colombini, C. Iannantuoni, R. Rota, and V. Busini. Unignited high-pressure methane jet impacting a cylindrical obstacle: An assessment tool for consequences analysis. *Journal of Loss Prevention in the Process Industries*, 76:104593, 2022.

[44] W. Houf, R. Schefer, G. Evans, E. Merilo, and M. Groethe. Evaluation of barrier walls for mitigation of unintended releases of hydrogen. *International journal of hydrogen energy*, 35(10):4758–4775, 2010.

[45] Gexcon US. Flacs v10.4 user's manual, 2019.

[46] DNV GL. Kfx exism v3.4 user's manual, 2019.

[47] P. Bénard, A. Hourri, B. Angers, and A. Tchouvelev. Adjacent surface effect on the flammable cloud of hydrogen and methane jets: Numerical investigation and engineering correlations. *International Journal of Hydrogen Energy*, 41(41):18654–18662, 2016.

[48] A. Hourri, B. Angers, P. Bénard, A. Tchouvelev, and V. Agranat. Numerical investigation of the flammable extent of semi-confined hydrogen and methane jets. *international journal of hydrogen energy*, 36(3):2567–2572, 2011.

[49] O.R. Hansen, F. Gavelli, M. Ichard, and S.G. Davis. Validation of flacs against experimental data sets from the model evaluation database for lng vapor dispersion. *Journal of Loss Prevention in the Process Industries*, 23(6):857–877, 2010.

[50] H. Wilkening and D. Baraldi. Cfd modelling of accidental hydrogen release from pipelines. *International journal of hydrogen energy*, 32(13):2206–2215, 2007.

[51] X. Liu, A. Godbole, C. Lu, G. Michal, and P. Venton. Source strength and dispersion of co2 releases from high-pressure pipelines: Cfd model using real gas equation of state. *Applied Energy*, 126:56–68, 2014.

[52] A.O. de Souza, A.M. Luiz, A.T.P. Neto, A.C.B. de Araujo, H.B. da Silva, S.K. da Silva, and J.J.N. Alves. Cfd predictions for hazardous area classification. *Chinese journal of chemical engineering*, 27(1):21–31, 2019.

[53] A. Moscatello, A.C. Uggenti, R. Gerboni, and A. Carpignano. A novel approach to high-pressure gas releases simulations. *Journal of Loss Prevention in the Process Industries*, 72:104531, 2021.

[54] SEASTAR. Seastar wind tunnel. http://www.seastar-wt.polito.it/. [Online; accessed 11-February-2022].

[55] A. Moscatello, A.C. Uggenti, G. Iuso, D. D'Ambrosio, G. Cafiero, R. Gerboni, and A. Carpignano. Scaling procedure for designing accidental gas release experiment. *Engineering Computations*, 38(3):1350–1367, 2021.

[56] R. Gerboni, G. Ledda, A. Moscatello, A.C. Uggenti, and A. Carpignano. Fluid-dynamic calibration of an atmospheric wind tunnel applied to test offshore infrastructures. In *OMC Med Energy Conference and Exhibition*. OnePetro, 2021.

[57] A. Moscatello, R. Gerboni, G. Ledda, A.C. Uggenti, A. Piselli, and A. Carpignano. Cfd gas release model performance evaluation through wind tunnel experiments. *Journal of Loss Prevention in the Process Industries*, 75:104715, 2022.

[58] B.R. Munson, T.H. Okiishi, W.W. Huebsch, and A.P. Rothmayer. *Fluid mechanics*. Wiley Singapore, 2013.

[59] Y. Otobe, H. Kashimura, S. Matsuo, T. Setoguchi, and H.D. Kim. Influence of nozzle geometry on the near-field structure of a highly underexpanded sonic jet. *Journal of Fluids and Structures*, 24(2):281–293, 2008.

[60] J.L. Palmer and R.K. Hanson. Application of method of characteristics to underexpanded, freejet flows with vibrational nonequilibrium. *AIAA journal*, 36(2):193–200, 1998.

[61] R.T. Driftmyer. A correlation of freejet data. *AIAA journal*, 10(8):1093–1095, 1972.

[62] E. Franquet, V. Perrier, S. Gibout, and P. Bruel. Free underexpanded jets in a quiescent medium: A review. *Progress in Aerospace Sciences*, 77:25–53, 2015.

[63] A.J. Saddington, N.J. Lawson, and K. Knowles. An experimental and numerical investigation of under-expanded turbulent jets. *The Aeronautical Journal*, 108(1081):145–152, 2004.

[64] C. Donaldson and R. Snedeker. A study of free jet impingement. part 1. mean properties of free and impinging jets. *Journal of Fluid Mechanics*, 45(2):281–319, 1971.

[65] A.L. Addy. Effects of axisymmetric sonic nozzle geometry on mach disk characteristics. *AIAA Journal*, 19(1):121–122, 1981.

[66] P. Birkby and G.J. Page. Numerical predictions of turbulent underexpanded sonic jets using a pressure-based methodology. *Proceedings of the Institution of Mechanical Engineers, Part G: Journal of Aerospace Engineering*, 215(3):165–173, 2001.

[67] A. Krothapalli, G. Buzyna, and L. Lourenco. Streamwise vortices in an underexpanded axisymmetric jet. *Physics of Fluids A: Fluid Dynamics*, 3(8):1848–1851, 1991.

[68] N.J. Dam, M. Rodenburg, R.A.L. Tolboom, G.G.M. Stoffels, P.M. Huisman-Kleinherenbrink, and J.J. Ter Meulen. Imaging of an underexpanded nozzle flow by uv laser rayleigh scattering. *Experiments in fluids*, 24(2):93–101, 1998.

[69] X. Tang, M. Asahara, A.K. Hayashi, and N. Tsuboi. Numerical investigation of a high pressure hydrogen jet of 82 MPa with adaptive mesh refinement: The starting transient evolution and Mach disk stabilization. *International Journal of Hydrogen Energy*, 42(10):7120–7134, 2017.

[70] T.C. Adamson Jr and J.A. Nicholls. On the structure of jets from highly underexpanded nozzles into still air. *Journal of the Aerospace sciences*, 26(1):16–24, 1959.

[71] H. Ashkenas and F.S. Sherman. Structure and utilization of supersonic free jets in low density wind tunnels. Technical report, 1965.

[72] R. Khaksarfard, M.R. Kameshki, and M. Paraschivoiu. Numerical simulation of high pressure release and dispersion of hydrogen into air with real gas model. *Shock Waves*, 20(3):205–216, 2010.

[73] F. Péneau, G. Pedro, P. Oshkai, P. Bénard, and N. Djilali. Transient supersonic release of hydrogen from a high pressure vessel: A computational analysis. *International journal of hydrogen energy*, 34(14):5817–5827, 2009.

[74] S. Crist, D.R. Glass, and P.M. Sherman. Study of the highly underexpanded sonic jet. *AIAA journal*, 4(1):68–71, 1966.

[75] B.A. Mamedov, E. Somuncu, and I.M. Askerov. Evaluation of speed of sound and specific heat capacities of real gases. *Journal of Thermophysics and Heat Transfer*, 32(4):984–998, 2018.

[76] RSE. Atlanteolico. http://atlanteeolico.rse-web.it/. [Online; accessed 20-December-2020].

[77] J.M. Kuchta. *Investigation of fire and explosion accidents in the chemical, mining, and fuel-related industries: a manual*. Number 678-688. US Department of the Interior, Bureau of Mines, 1985.

[78] Decreto del Presidente del Consiglio dei Ministri. Linee guida per la predisposizione del piano d'emergenza esterna di cui all'articolo 20, comma 4, del decreto legislativo 17 agosto 1999, n. 334e. 2005. https://www.anci.it/. [Online; accessed 1-January-2020].

[79] S. Doroudi, A. Pophali, M. Bussmann, D. Tandra, and H. Tran. Modelling sootblower jet effectiveness with ansys fluent. *Journal of Science & Technology for Forest Products and Processes*, 4(4):30–35, 2014.

[80] UDF Manual. Ansys fluent 18.2. *Theory Guide*, 2018.

[81] N. Novembre, F. Podenzani, and E. Colombo. Numerical study for accidental gas releases from high pressure pipelines. 2006.

[82] P.L. Eggins and D.A. Jackson. Laser-doppler velocity measurements in an under-expanded free jet. *Journal of Physics D: Applied Physics*, 7(14):1894, 1974.

[83] A.C. Benim, M. Cagan, A. Nahavandi, and E. Pasqualotto. Rans predictions of turbulent flow past a circular cylinder over the critical regime. In *Proc. 5th IASME/WSEAS International Conference on Fluid Mechanics and Aerodynamics, Athens, Greece*, pages 232–237, 2007.

[84] D.P. Georgiou, K. Milidonis, and A.I. Geniketzidis. Comparisons between experimental measurements and rans-based simulations on the aerodynamics of a horseshoe vortex configuration. 2015.

[85] A.M. Levchenya, E.M. Smirnov, and V.D. Goryachev. Rans-based numerical simulation and visualization of the horseshoe vortex system in the leading edge endwall region of a symmetric body. *International Journal of Heat and Fluid Flow*, 31(6):1107–1112, 2010. 7th World Conference on Experimental Heat Transfer, Fluid Mechanics and Thermodynamics (ExHFT-7), Krakow and The Conference on Modelling Fluid Flow (CMFF '09), Budapest.

[86] N.D. Katopodes. Chapter 6 - ideal fluid flow. In N.K. Katopodes, editor, *Free-Surface Flow*, pages 428–515. Butterworth-Heinemann, 2019.

[87] T.P. Chong, P.F. Joseph, and P.O.A.L. Davies. Design and performance of an open jet wind tunnel for aero-acoustic measurement. *Applied acoustics*, 70(4):605–614, 2009.

[88] R. Merino-Martínez, A.R. Carpio, L.T.L. Pereira, S. van Herk, F. Avallone, D. Ragni, and M. Kotsonis. Aeroacoustic design and characterization of the 3d-printed, open-jet, anechoic wind tunnel of delft university of technology. *Applied Acoustics*, 170:107504, 2020.

[89] K. Pascioni, R. Reger, A. Edstrand, and L. Cattafesta. Characterization of an aeroacoustic wind tunnel facility. In *43rd International congress and exposition of noise control engineering*, pages 16–19, 2014.

[90] Y. Yang, Y. Liu, R. Liu, C. Shen, P. Zhang, R. Wei, X. Liu, and P. Xu. Design, validation, and benchmark tests of the aeroacoustic wind tunnel in sustech. *Applied Acoustics*, 175:107847, 2021.

[91] Sensortech SGX. Mems pellistor - mp-7217 - datasheet. https://www.sgxsensortech.com/products-services/industrial-safety/mems-pellistor/. [Online; accessed 10-February-2023].

[92] D.J. Hall and S. Walker. Scaling rules for reduced-scale field releases of hydrogen fluoride. *Journal of hazardous materials*, 54(1-2):89–111, 1997.

[93] E.D. Obasaju and A.G. Robins. Simulation of pollution dispersion using small scale physical models—an assessment of scaling options. In *Urban Air Quality: Monitoring and Modelling*, pages 239–254. Springer, 1998.

[94] W.H. Snyder. *Guideline for fluid modeling of atmospheric diffusion*, volume 81. Environmental Sciences Research Laboratory, Office of Research and Development, US, Environmental Protection Agency, 1981.

[95] W.H. Snyder. Fluid modeling of pollutant transport and diffusion in stably stratified flows over complex terrain. *Annual Review of Fluid Mechanics*, 17(1):239–266, 1985.

[96] I. Mavroidis, R.F. Griffiths, and D.J. Hall. Field and wind tunnel investigations of plume dispersion around single surface obstacles. *Atmospheric Environment*, 37(21):2903–2918, 2003.

[97] P. Gousseau, B. Blocken, T. Stathopoulos, and G.J.F. Van Heijst. Cfd simulation of near-field pollutant dispersion on a high-resolution grid: a case study by les and rans for a building group in downtown montreal. *Atmospheric Environment*, 45(2):428–438, 2011.

[98] A. Gupta, T. Stathopoulos, and P. Saathoff. Wind tunnel investigation of the downwash effect of a rooftop structure on plume dispersion. *Atmospheric Environment*, 46:496–507, 2012.

[99] Y. Tominaga and T. Stathopoulos. Cfd simulation of near-field pollutant dispersion in the urban environment: A review of current modeling techniques. *Atmospheric Environment*, 79:716–730, 2013.

[100] M.F. Yassin. A wind tunnel study on the effect of thermal stability on flow and dispersion of rooftop stack emissions in the near wake of a building. *Atmospheric Environment*, 65:89–100, 2013.

[101] I. W Ekoto, W.G. Houf, G.H. Evans, E.G. Merilo, and M.A. Groethe. Experimental investigation of hydrogen release and ignition from fuel cell powered forklifts in enclosed spaces. *International journal of hydrogen energy*, 37(22):17446–17456, 2012.

[102] W.G. Houf, G.H. Evans, E. Merilo, M. Groethe, and S.C. James. Releases from hydrogen fuel-cell vehicles in tunnels. *international journal of hydrogen energy*, 37(1):715–719, 2012.

[103] W.G. Houf, G.H. Evans, I.W. Ekoto, E.G. Merilo, and M.A. Groethe. Hydrogen fuel-cell forklift vehicle releases in enclosed spaces. *International Journal of Hydrogen Energy*, 38(19):8179–8189, 2013.

[104] J. Xing, Z. Liu, P. Huang, C. Feng, Y. Zhou, R. Sun, and S. Wang. Cfd validation of scaling rules for reduced-scale field releases of carbon dioxide. *Applied energy*, 115:525–530, 2014.

[105] J. Donat and M. Schatzmann. Wind tunnel experiments of single-phase heavy gas jets released under various angles into turbulent cross flows. *Journal of Wind Engineering and Industrial Aerodynamics*, 83(1-3):361–370, 1999.

[106] I. Kanda, K. Uehara, Y. Yamao, Y. Yoshikawa, and T. Morikawa. A wind-tunnel study on exhaust gas dispersion from road vehicles—part i: Velocity and concentration fields behind single vehicles. *Journal of wind engineering and industrial aerodynamics*, 94(9):639–658, 2006.

[107] Y. Abu-Zidan, P. Mendis, and T. Gunawardena. Optimising the computational domain size in cfd simulations of tall buildings. *Heliyon*, 7(4):e06723, 2021.

[108] B. Blocken. Computational fluid dynamics for urban physics: Importance, scales, possibilities, limitations and ten tips and tricks towards accurate and reliable simulations. *Building and Environment*, 91:219–245, 2015.

[109] J. Revuz, D.M. Hargreaves, and J.S. Owen. On the domain size for the steady-state cfd modelling of a tall building. *Wind and structures*, 15(4):313, 2012.

[110] A. Moscatello, G. Ledda, A.C. Uggenti, R. Gerboni, and A. Carpignano. Wind impact assessment of a sour gas release in an offshore platform. *Safety*, 8(4):80, 2022.

[111] S.R. Hanna. Uncertainties in air quality model predictions. In *Transport and Diffusion in Turbulent Fields*, pages 3–20. Springer, 1993.

[112] S.R. Hanna, O.R. Hansen, and S. Dharmavaram. Flacs cfd air quality model performance evaluation with kit fox, must, prairie grass, and emu observations. *Atmospheric Environment*, 38(28):4675–4687, 2004.

[113] L. Dong, H. Zuo, L. Hu, B. Yang, L. Li, and L. Wu. Simulation of heavy gas dispersion in a large indoor space using cfd model. *Journal of loss prevention in the process industries*, 46:1–12, 2017.

[114] A.M. Schleder and M.R. Martins. Experimental data and cfd performance for co2 cloud dispersion analysis. *Journal of Loss Prevention in the Process Industries*, 43:688–699, 2016.

[115] A. Stohl, M. Hittenberger, and G. Wotawa. Validation of the lagrangian particle dispersion model flexpart against large-scale tracer experiment data. *Atmospheric Environment*, 32(24):4245–4264, 1998.

[116] D. Toscano, M. Marro, B. Mele, F. Murena, and P. Salizzoni. Assessment of the impact of gaseous ship emissions in ports using physical and numerical models: The case of naples. *Building and Environment*, 196:107812, 2021.

[117] H.T. Hwang and A. Varma. Hydrogen storage for fuel cell vehicles. *Current Opinion in Chemical Engineering*, 5:42–48, 2014. Energy and environmental engineering / Reaction engineering.

[118] F. Pappalardo, A. Moscatello, A.C. Uggenti, R. Gerboni, Andrea C., F. Di Maio, R. Mereu, and E. Zio. Comparison of cfd numerical approaches for the simulation of accidental gas release in energy applications. In *Proceedings of the 30th European Safety and Reliability Conference and the 15th Probabilistic Safety Assessment and Management Conference*, pages 4067–4074. Research Publishing, Singapore, 2020.

[119] F. Pappalardo, A. Moscatello, G. Ledda, A.C. Uggenti, R. Gerboni, A. Carpignano, F. Di Maio, R. Mereu, and E. Zio. Quantification of uncertainty in cfd simulation of accidental gas release for o & g quantitative risk assessment. *Energies*, 14(23):8117, 2021.

[120] B.H. Hjertager. Computer modelling of turbulent gas explosions in complex 2d and 3d geometries. *Journal of hazardous materials*, 34(2):173–197, 1993.

[121] J. Puttock, F. Walter, D. Chakraborty, S. Raghunath, and P. Sathiah. Numerical simulations of gas explosion using porosity distributed resistance approach part-1: Validation against small-scale experiments. *Journal of Loss Prevention in the Process Industries*, 75:104659, 2022.

[122] B.R. Cormier, R. Qi, G. Yun, Y. Zhang, and M.S. Mannan. Application of computational fluid dynamics for lng vapor dispersion modeling: A study of key parameters. *Journal of Loss Prevention in the Process Industries*, 22(3):332–352, 2009.

[123] A. Moscatello, G. Ledda, A.C. Uggenti, R. Gerboni, and A. Carpignano. Cfd modelling of pressurized gas releases: sensitivity analysis of driving parameters. In *Proceedings of 30th European Safety and Reliability Conference and the 15th Probabilistic Safety Assessment and Management Conference Accepted Paper*, 2020.

[124] N. Abrate, A. Moscatello, G. Ledda, N. Pedroni, F. Carbone, E. Maffia, and A. Carpignano. A novel approach combining bootstrapped non-intrusive reduced order models and unscented transform for the robust and efficient cfd analysis of accidental gas releases in congested plants. *Journal of Loss Prevention in the Process Industries*, 83:105015, 2023.

[125] N. Pedroni and E. Zio. An adaptive metamodel-based subset importance sampling approach for the assessment of the functional failure probability of a thermal-hydraulic passive system. *Applied Mathematical Modelling*, 48:269–288, 2017.

[126] N. Pedroni. Computational methods for the robust optimization of the design of a dynamic aerospace system in the presence of aleatory and epistemic uncertainties. *Mechanical Systems and Signal Processing*, 164:108206, 2022.

[127] F. Casenave, A. Gariah, C. Rey, and F. Feyel. A nonintrusive reduced order model for nonlinear transient thermal problems with nonparametrized variability. *Advanced Modeling and Simulation in Engineering Sciences*, 7(1), 2020.

[128] S. M. Rahman, O. San, and A. Rasheed. A hybrid approach for model order reduction of barotropic quasi-geostrophic turbulence. *Fluids*, 3(4), 2018.

[129] D. Kumar, M. Raisee, and C. Lacor. An efficient non-intrusive reduced basis model for high dimensional stochastic problems in CFD. *Computers and Fluids*, 138:67–82, 2016.

[130] N. Demo, M. Tezzele, and G. Rozza. A non-intrusive approach for the reconstruction of POD modal coefficients through active subspaces. *Comptes Rendus - Mecanique*, 347(11):873–881, 2019.

[131] B. Efron. Nonparametric estimates of standard error: The jackknife, the bootstrap and other methods. *Biometrika*, 68(3):589–599, 1981.

[132] R. Kohavi. A study of cross-validation and bootstrap for accuracy estimation and model selection. In *Proceedings of the 14th International Joint Conference on Artificial Intelligence - Volume 2*, IJCAI'95, page 1137–1143, San Francisco, CA, USA, 1995. Morgan Kaufmann Publishers Inc.

[133] S.J. Julier and J.K. Uhlmann. New extension of the Kalman filter to nonlinear systems. In Ivan Kadar, editor, *Signal Processing, Sensor Fusion, and Target Recognition VI*, volume 3068, pages 182 – 193. International Society for Optics and Photonics, SPIE, 1997.

[134] N. Abrate. *Methods for safety and stability analysis of nuclear systems*. PhD thesis, Politecnico di Torino, Dipartimento Energia, 2022.

[135] R.L. Hardy. Multiquadric equations of topography and other irregular surfaces. *Journal of Geophysical Research (1896-1977)*, 76(8):1905–1915, 1971.

[136] E. Zio. A study of the bootstrap method for estimating the accuracy of artificial neural networks in predicting nuclear transient processes. *IEEE Transactions on Nuclear Science*, 53(3):1460–1478, 2006.

[137] P. Secchi, E. Zio, and F. Di Maio. Quantifying uncertainties in the estimation of safety parameters by using bootstrapped artificial neural networks. *Annals of Nuclear Energy*, 35(12):2338–2350, 2008.

[138] F. Menter. Zonal two equation kw turbulence models for aerodynamic flows. In *23rd fluid dynamics, plasmadynamics, and lasers conference*, page 2906, 1993.

[139] D. C. Wilcox. *Turbulence modeling for CFD*, volume 2. DCW industries La Canada, CA, 1998.

[140] P. J. Roache. Perspective: A Method for Uniform Reporting of Grid Refinement Studies, 1994.

Appendix A

Comparison between SBAM and two industrial safety-oriented CFD tools

This appendix proposes a comparison between SBAM and two widely used CFD tools for safety analyses, FLACS and KFX, respectively developed by Gexcon US [45] and DNV GL [46]. These are two of the more commonly used software in the industry for the CFD simulation of accidental scenarios such as gas dispersion, fires and explosions. These are specific purpose tools which aim at a simple and fast numerical simulation of common industrial accidents, providing a larger accuracy with respect to empirical or integral models. The comparison is made by simulating the same case study and by discussing similarities and discrepancies in the results as well as advantages and disadvantages about the usability, the physical modeling, the numerical methods, the meshing features and the computational cost. The case study considered in this comparison is the same of the numerical investigations proposed in chapter 4. In particular, it is the cs#3 (see table 3.2), which main parameters are here summarized: p_0=50 bar, D_e=3 cm, wind intensity=6 m/s ($\vec{U}_1$), d_{cyl}=30 cm and l_{obs}=45 cm. Part of the work presented in this appendix was previously published in Pappalardo et al. [118, 119].

A.1 Physical modeling approach in FLACS and KFX

In FLACS and KFX an empirical model is coupled with the numerical code. In fact, the underexpanded jet that forms near the release point is not solved numerically, but

it is approximated with the Birch model [37]. This model is applicable in a range of release pressure between 2 and 70 bar, and it evaluates an equivalent diameter and velocity at the location of complete expansion of the gas, i.e. when the jet pressure equals the ambient one. The model assumes an isentropic expansion from the inner conditions (0) and the exit section conditions (e), see figure A.1.

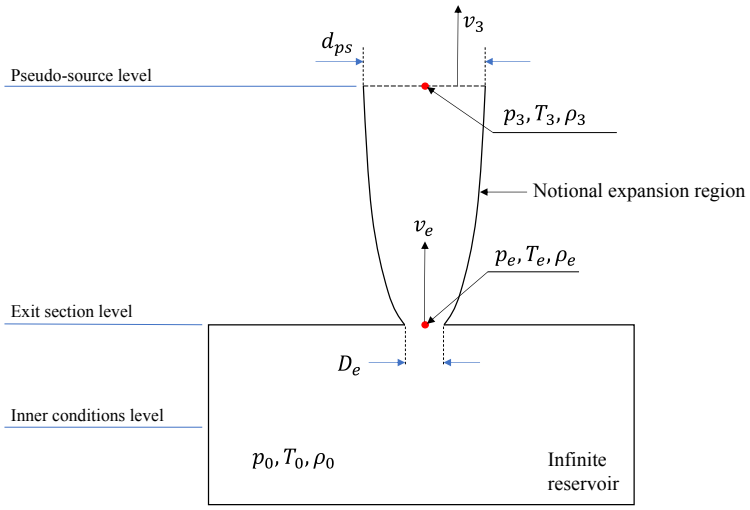

Fig. A.1 Schematic representation of the notional expansion of the jet in the Birch model.

Moreover, it is based on the mass and momentum conservation in the free expansion region, where the *notional* expansion occur, that is between (e) and the maximum expansion point (3). Viscous forces on the expansion surface are neglected as well as the surrounding air entrainment, and the ideal gas assumption is made. With reference to figure A.1, three levels can be identified:

- Inner conditions level (0), where the gas is at the equipment conditions
- Exit section level (e), where the gas is at the exit conditions, which derives from the isentropic expansion from (0) to (e)
- Pseudo-source level (3), where the gas is in equilibrium with the surrounding environment, hence, it fully expanded to atmospheric pressure

The model evaluates a *pseudo source*, defined by a pseudo diameter and a pseudo velocity, at the location of full expansion, whilst it does not provide details about the gas conditions in the expansion region. This last is to be considered a *notional*

region, as highlighted in figure A.1, in fact, the pseudo diameter does not physically exists.

The derivation of the pseudo velocity and diameter starts from the mass flowrate released into the environment, which can be expressed as in Eq. A.1.

$$Q_e = \frac{\pi}{4} D_e^2 \rho_e v_e C_D \tag{A.1}$$

Note that here the velocity is indicated with the letter v instead of u. Analogously at the pseudo source level a mass flowrate can be defined as in Eq. A.2.

$$Q_3 = \frac{\pi}{4} d_{ps}^2 \rho_3 v_3 \tag{A.2}$$

In this last case, the discharge coefficient (C_D) is assumed equal to 1 since the velocity profile is assumed uniform in the definition of the pseudo source. Assuming no air entrainment, the two mass flowrates must be equal due to mass conservation, hence, equalizing Eq. A.1 and A.2, Eq. A.3 can be derived.

$$\left(\frac{d_{ps}}{D_e}\right)^2 = C_D \frac{v_e \rho_e}{v_3 \rho_3} \tag{A.3}$$

Parameters at level (e) can be derived through the correlation for chocked flow conditions, hence, pressure and temperature can be written as in Eq. A.4 and A.5 while the density can be expressed using the ideal gas law as in Eq. A.6.

$$p_e = p_0 \left(\frac{2}{\gamma+1}\right)^{\left(\frac{\gamma}{\gamma-1}\right)} \tag{A.4}$$

$$T_e = T_0 \left(\frac{2}{\gamma+1}\right) \tag{A.5}$$

$$\rho_e = \frac{p_0 \left(\frac{2}{\gamma+1}\right)^{\left(\frac{1}{\gamma-1}\right)}}{T_0 R} \tag{A.6}$$

Due to sonic flow conditions at the exit, the velocity can be expressed as in Eq. A.7.

$$v_e = \sqrt{\gamma R T_e} = \sqrt{2 \frac{\gamma}{\gamma+1} R T_0} \tag{A.7}$$

The density at the pseudo source level can be written through the ideal gas law as in Eq. A.8 and the velocity using the same approach of location (e) through Eq. A.9.

$$\rho_3 = \frac{p_3}{RT_3} \tag{A.8}$$

$$v_3 = \sqrt{\gamma RT_3} \tag{A.9}$$

Substituting Eq. A.4, A.5, A.6, A.8 and A.9 in Eq. A.3 the expression in Eq. A.10 can be found.

$$\left(\frac{d_{ps}}{D_e}\right)^2 = C_D \left(\frac{T_3}{T_0}\right)^{\frac{1}{2}} \frac{p_0}{p_3} \left(\frac{2}{\gamma+1}\right)^{\frac{\gamma+1}{2(\gamma-1)}} \tag{A.10}$$

Assuming that the released gas is at ambient temperature and that after the notional expansion it is at ambient temperature and pressure, Eq. A.10 can be simplified obtaining Eq. A.11.

$$\left(\frac{d_{ps}}{D_e}\right)^2 = C_D \frac{p_0}{p_a} \left(\frac{2}{\gamma+1}\right)^{\frac{\gamma+1}{2(\gamma-1)}} \tag{A.11}$$

If the considered gas is methane, as in this case, γ is assumed equal to 1.35 since this is an average value between 1.3 and 1.4, which are the values corresponding to the pressure range in which this model is valid. The final expression for the pseudo diameter is in Eq. A.12.

$$d_{ps} = D_e \cdot \sqrt{\frac{p_0}{p_a} 0.582 C_D} \tag{A.12}$$

The pseudo velocity can be now defined by Eq. A.13.

$$v_{ps} = \frac{Q_e}{\frac{\pi}{4} d_{ps}^2 \rho_3} \tag{A.13}$$

These two values are imposed on the surface of the mesh cell located at the point of complete expansion, which represent the effective leakage source point in the simulation. Once the leak source is characterized by the Birch model, the flow field is then solved numerically by employing a *Porosity Distributed Resistance* (PDR) formulation of the governing equations [120, 121], i.e. the Navier-Stokes equations for momentum, the energy equation and a gas species transport equation. This approach treats small-scale obstacles as sub-grid elements in the form of porosity and resistance elements, while large-scale obstacles are resolved. Objects with length scales lower than the grid size are not fully resolved, in fact their presence affects the governing equations in two ways. First, only a portion of the total volume is

available to the flow, and secondly their presence generates additional flow resistance, turbulence and heat transfer. In FLACS and KFX solvers, all governing equations are written in a general conservation form as in Eq. A.14.

$$\frac{\partial}{\partial t}(\beta_v \rho \Phi) + \frac{\partial}{\partial x_i}(\beta_i \rho v_i \Phi) = \frac{\partial}{\partial x_i}\left(\beta_i \rho \Gamma_\Phi \frac{\partial \Phi}{\partial x_i}\right) + \beta_v (S_\Phi + R_\Phi) \tag{A.14}$$

The equation is written for the i-th direction, where β_v is the volume porosity, β_i is the area porosity, v_i is the velocity, Φ is a general quantity, Γ_Φ is the effective turbulence coefficient, S_Φ is a source term and R_Φ represents an additional drag (additional turbulence or heat transfer caused by solid obstruction). All the porosities can assume values between 0, completely blocked, or 1, completely free space. This approach permits to model complex geometries such as O&G installations or industrial sites, characterized by a wide range of geometry length scales, by defining a suitable grid resolution for larger scales [122], and special sub-grid models for drag and turbulence to account for smaller geometries. From the general formulation given in Eq. A.14, the modified Navier-Stokes momentum equations can be derived as in Eq. A.15.

$$\frac{\partial}{\partial t}(\beta_v \rho v_i) + \frac{\partial}{\partial x_j}(\beta_i \rho v_j v_i) - \frac{\partial}{\partial x_j}(\beta_i \sigma_{ij}) = -\beta \frac{\partial p}{\partial x_i} + F_i + \beta G_b \tag{A.15}$$

Where v_i and v_j are the velocities along the i-th and j-th directions, β is the volume porosity, β_i is the area porosity in the i-th direction, σ_{ij} is the stress tensor, G_b is a buoyancy term. An additional term appear in the modified Navier Stokes equations, which is a drag modelled through the term F_i, the flow resistance in the i-th direction. As shown in Eq. A.16, this term has two contributions: F_{ci}, resistance constant and F_{Ri} the speed resistance factor in the i-th direction.

$$F_i = -\beta (F_{ci} + F_{Ri}|v_i|)v_i \tag{A.16}$$

Due to the turbulent nature of the problem, a RANS formulation of the equations is solved and additional equations are considered for the turbulence closure problem. In both FLACS and KFX, the Standard k-ε is the only available turbulence model, which related equations are written in the PDR form in Eq. A.17 and A.18.

$$\frac{\partial}{\partial t}(\beta_v \rho k) + \frac{\partial}{\partial x_j}(\beta_j \rho v_j k) = \frac{\partial}{\partial x_j}\left(\beta_j \frac{\mu_{eff}}{\sigma_k}\frac{\partial k}{\partial x_j}\right) + \beta_v P_k - \beta_v \rho \varepsilon \tag{A.17}$$

$$\frac{\partial}{\partial t}(\beta_v \rho \varepsilon) + \frac{\partial}{\partial x_j}(\beta_j \rho v_j \varepsilon) = \frac{\partial}{\partial x_j}\left(\beta_j \frac{\mu_{eff}}{\sigma_\varepsilon}\frac{\partial \varepsilon}{\partial x_j}\right) + \beta_v P_\varepsilon - \frac{\beta_v \rho \varepsilon^2}{k} \tag{A.18}$$

Where k is the turbulent kinetic energy, ε is the rate of dissipation of the turbulent kinetic energy, σ_ε and σ_k are the turbulent Prandtl and Schmidt numbers, μ_{eff} is the effective viscosity, P_k and P_ε are respectively the production rate of k and ε. P_k is modeled as a sum of four distinct terms contributing to turbulence generation due to fluid-shear (G_s), wall-shear (G_w), buoyancy (G_b) and sub-grid objects (G_0). The latter term considers the additional turbulence during the interactions between fluid and solid through the defined drag coefficient.

A.2 Mesh and boundary conditions features in FLACS and KFX

In FLACS and KFX only a structured Cartesian mesh can be generated and a constraint is imposed on the minimum cell size. In fact, once the release pseudo-diameter is evaluated (d_{ps}), the leak area ($A_{leak} = \pi \cdot d_{ps}^2/4$) is defined according to the that. Both software imposes that the cell dimensions cannot be smaller than the A_{leak}, hence the following condition must be always satisfied $A_{cell} > A_{leak}$ in the volume. This adds a level of approximation of the domain geometry, since objects with characteristic length lower than A_{leak} are neglected, and are treated with the porosity approach. Considering that d_{ps} is proportional to the square root of the release pressure, the higher this last the larger A_{leak}, the larger the number of neglected objects. Neglecting pieces of equipment could lead to significant errors, especially if they are near the release point since the impingement at high speed could strongly influence the flow path. Moreover, another limitation is represented by the fact that it is not possible to fit the mesh with inclined or curved surfaces, which are treated using stepped walls. Particular attention must be paid to the object spatial arrangement in the domain, since the code will force their surfaces to be aligned

to grid lines, hence, a user has to align the objects prior to the mesh generation to help the mesh construction. While FLACS algorithm automatically handles this alignment, KFX needs a manual intervention from the user. The mesh used for the calculations of the present analysis consisted of $\sim$ 450000 and $\sim$ 650000 elements respectively in FLACS and KFX.

Concerning the boundary condition, as a general consideration it must be noted that FLACS and KFX help the user in setting some parameters which are commonly used for accidental scenarios, as the atmospheric stability class, the turbulent intensity, the reference height for the wind profile and the surface roughness. In fact, they automatically consider a wind profile and the effect of the atmospheric stability. At the leak source the release hole size, the type of gas and its thermodynamic conditions are specified. Then, FLACS and KFX automatically evaluate the pseudo source through the Birch model. For the purposes of this analysis, a velocity inlet is imposed at the platform boundaries b1-b2 to reproduce the wind intensity, see figure A.2. At the outlets, b3-b4, the ambient pressure is imposed in KFX while a mass flow outlet is used in FLACS. This last choice is suggested in [45], in order to obtain a convergent solution.

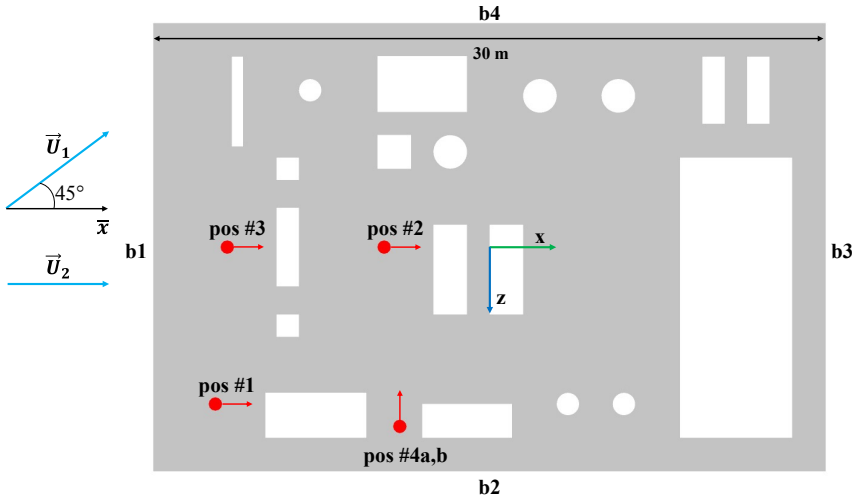

Fig. A.2 Top view of the deck CAD geometry with a schematic representation of the leak positions and directions (red bullets/arrows) and wind directions (cyan arrows).

Due to the PDR approach, in FLACS and KFX it is not possible to model the object surfaces as walls, in fact, a mass flow outlet condition is applied to all the solid objects, then the resistance to flow created by the obstacles is taken in consideration

through the porosity value in the equation, i.e. the porosity is zero when an object is encountered. The setup of SBAM simulation is the same presented in section 4.2.1.

A.3 Results discussion

At first, a qualitative comparison of the results is proposed, by comparing the flammable area at 1.5 m height (A_{flam}). In figure A.3 the contour plots related to each of the software is shown. The flammable areas shape obtained in FLACS and KFX are almost similar, and appear strongly influenced by the wind direction, while the SBAM one presents some differences. At first, in this last case the wind influence is less dominant as it is overcome by the jet inertia in the first part of the area. Secondly, while the FLACS and KFX areas have a more plume-like shape, in SBAM a more irregular behavior is observed. This is the result of the interaction of the gas with the surrounding objects, which causes a splitting of the jet and flow recirculations. Due to the PDR approach, in FLACS and KFX the boundary layer arising on the object surfaces is not solved, as they are treated as porous regions. In fact, no *wall boundary condition* is available in these tools, hence flow separation are badly modeled. However, the pieces of equipment involved in the cloud seem almost the same in FLACS and SBAM, where the rectangles in the center of the platform and the cylinder on the left are both involved, while in KFX the plume tends to rapidly bend and the rectangle at the center is not touched. If, on one hand, the PDR approach of FLACS and KFX seems to fail to reproduce the flow-obstacle interactions in a detailed way neglecting many of the geometry features (e.g. curved surfaces are badly approximated), on the other hand, it is less computationally demanding. In fact, FLACS employs 50 minutes for the steady-state analysis, KFX 3 hours for the transient analysis (steady-state solutions are not available) and SBAM 3 hours for the steady-state (note that only the computational cost associated to the *dispersion* simulation of SBAM is considered). A comparable computational power was used for the calculations, in particular FLACS and KFX were run on a Dell Tower 7820 (CPU Intel Xeon Gold 6136 3 GHz, RAM 64 GB) while SBAM on a Dell Tower 7810 (Intel Xeon e5-2630 CPU 2.4 GHz, RAM 64 GB). FLACS resulted the best performing one, and also KFX resulted a fast tool (considering that a transient solution employed the same amount of time of the SBAM steady-state). On the other hand, this last tool does not permit a steady state solution evaluation,

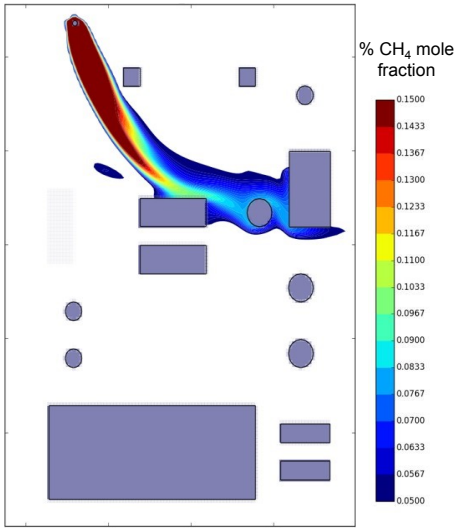

(a) FLACS

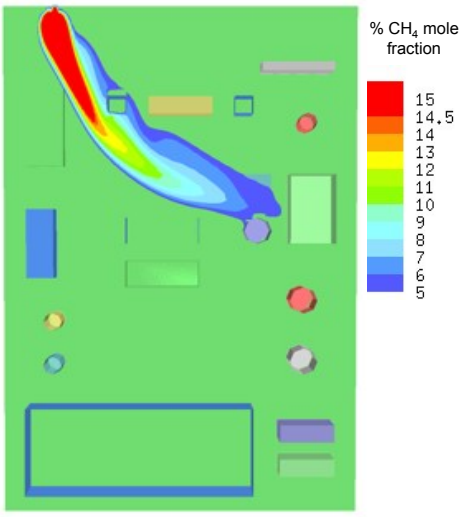

(b) KFX

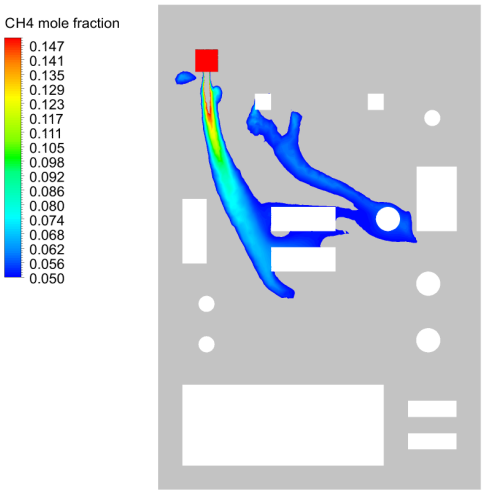

(c) SBAM (the red box represents the SB)

Fig. A.3 Flammable area comparison between FLACS, KFX and SBAM.

hence if the final configuration of the accident is of interest, a user is forced to solve the entire transient solution and this can be interpreted as a limitation. A quantitative comparison of the results is here presented by comparing some risk metrics. Table A.1 summarizes the obtained values.

tool	M_{ch4} [kg]	V_{flam} [m^3]	$M_{ch4,flam}$ [kg]
SBAM	18.0	135.9	6.1
FLACS	16.4	145.0	6.9
KFX	16.2	184.0	8.8

Table A.1 Risk metrics values for three tools: SBAM, FLACS, KFX

The values of total methane mass in the domain, M_{ch4}, suggest that a similar amount of gas is in the domain at the steady-state configuration of the accident. This suggest that at a global level the prediction of the three tools is similar, despite a slight overestimation of SBAM. Despite the total amount of gas is larger for SBAM, the flammable volume (V_{flam}) and mass ($M_{ch4,flam}$) are the lowest ones, and comparable to the one of FLACS. KFX gives the more conservative estimations on the flammable quantities. These differences can be ascribed to the larger mixing occurring in the SBAM simulation due to the more detailed modeling of the gas objects interaction which promotes the gas mixing with the surrounding air. Some general considerations can be derived from the analysis. FLACS and KFX are more rigid tools, being specific purpose codes, since provide only one type of mesh (which dimension has some constraints), one turbulence model, and in particular KFX do not permits steady-state solutions. On the other hand, being SBAM based on ANSYS Fluent, that is a general purposes code, a wide range of mesh types, turbulence, and in general numerical models can be used. The boundary conditions setting for this kind of applications, is guided in FLACS and KFX while can be more difficult in Fluent. Concerning the modeling accuracy, SBAM uses a classical formulation of the governing equations, as shown in appendix C, and fully resolve all the geometry scales, i.e. it does not neglect any obstacle. Moreover, in SBAM the underexpanded jet near the release point is numerically solved in the SB simulation, while the other tools employ the Birch model. This represent an additional source of uncertainty in the solution, that can be even more critical if near impinging jets are considered, in fact, if the pseudo source location is at a distance larger than the obstacle position, this last is completely neglected. Another crucial aspect is

related to the post processing. SBAM is largely flexible and user friendly since exploits the CFD-post of ANSYS Fluent, while FLACS and especially KFX have some criticalities in the representation of the solution which in general results in low quality plots (that can be judged by figure A.3) and in a difficult calculation of the risk metrics.

Appendix B

Feasibility study of a SB metamodel

As discussed in section 4.1.3 the two main novelties of SBAM are related to the improvement in the results accuracy with respect to the commonly employed empirical methods, and to the perspective of reducing the computational burden associated with a standard CFD approach. This last aspect is related to the two-steps nature of SBAM and particularly on the reduced simulation time of the dispersion phase, assuming that the SB results are already available. For this reason, the feasibility of the generation of a SB database, or in alternative of the design of a surrogate model that mimic the SB behavior was investigated. In the following sections, the issues related to the SB database generation are addressed and some simplification strategies are proposed. Moreover, an alternative strategy to the database is proposed introducing the possibility of designing a Reduced Order Model of the SB. Part of the work presented in this appendix was previously published in Moscatello et al. [123] and Abrate et al. [124].

B.1 Preliminary 2D analysis

Generating a comprehensive SB database translates in realizing a set of simulations including all the possible cases needed for a QRA of an industrial installation. The number of cases can be extremely high (of the order of thousands as described in the following) since the SB is defined by several parameters, namely, the release pressure p_0, the release hole size D_e, the gas type, the obstacle distance l_{obs}, the obstacle type, the obstacle dimension (d_{cyl} or L_{fp}) which can take several values in a certain

range. An estimation of this number could be given starting from the definition of a relevant range of values for each SB parameter. In this sense, the authors Vivalda et al. [34] proposed representative ranges for the release pressure and diameter which are commonly considered in QRA of offshore platforms. It is suggested that the more relevant p_0 values for this kind of analyses range between 5 and 100 bar and a 5 bar step should be used for the safety investigations, while at least four values for D_e, which are 5, 10, 30 and 100 mm, should be considered. Defining the obstacle distance and dimension is not a trivial task, since in principle any type of equipment with an arbitrary dimension could be located at an arbitrary distance. To this end, some considerations are here proposed concerning the cylindrical shape case. As the SB has a finite length, the requirement $l_{obs} + d_{cyl}/2 < L_{SB}$ must be satisfied, and a certain amount of space behind the object and the SB boundary must be left in order to avoid that the cylinder is tangent to the SB face. In addition, the presence of the Mach disk imposes that that $l_{obs} - d_{cyl}/2 > L_{MD}$ is satisfied, otherwise the obstacle would interfere with the Mach disk formation, thus dramatically complicating the flow resolution. These constraints are discussed in the model applicability range, see section 4.1.4. According to these constraints, which are discussed in the model applicability range (see section 4.1.4), a set of values for l_{obs} and d_{cyl} can be reasonably defined as done in [123], where 5 different values of distance and diameter are proposed. Summarizing the previous considerations, 20 pressure levels, 4 release diameters, 5 cylinder diameters and 5 obstacle distances are considered, leading to a total number of 2000 SB. This is a minimum estimate since the typology of obstacle could be changed to a flat plate or a different gas could be considered, i.e. this number can easily be doubled or quadrupled. Since almost 24 h of calculation time are needed on average per each SB, almost 5 years and a half would be required for the 2000 SB simulations, which is a prohibitive amount of time. For this reason a preliminary 2D study was performed [123] in order to gain insights on possible simplification to reduce the number of representative SB for the database. Two analyses are proposed respectively on the geometrical configuration of the obstacle and on the release pressure, by studying their impact on the velocity and gas concentration at the SB outlet. These quantities are monitored since are used in the *coupling* phase of SBAM. The 2D study was performed considering the plane highlighted in figure B.1, which is the midplane transversal to the obstacle and containing the jet axis. This plane contains all the geometrical information involved in the analysis as well as the maximum jet separation due to the impingement. For the study on the geometrical

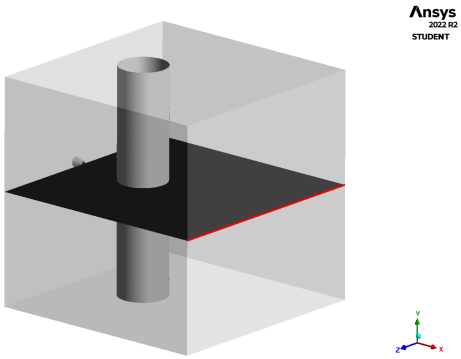

Fig. B.1 SB plane considered for the 2D analysis.

configuration of the obstacle, the release pressure and diameter were fixed at $p_0 = 10$ bar and $D_e = 1$ cm, and consequently the SB length resulted L_{SB}=0.57 m. Basing on the geometrical constraints previously described, five values of cylinder diameter were analyzed d_{cyl}=9-10-12-15-17 cm as well as five obstacle distances, expressed by the ratio l_{obs}/d_{cyl}=1-1.25-1.5-1.75-2. Figure B.2 presents the results in term of average velocity and CH_4 m.f. on the outlet boundary in front of the release point (highlighted by the red line in figure B.1).

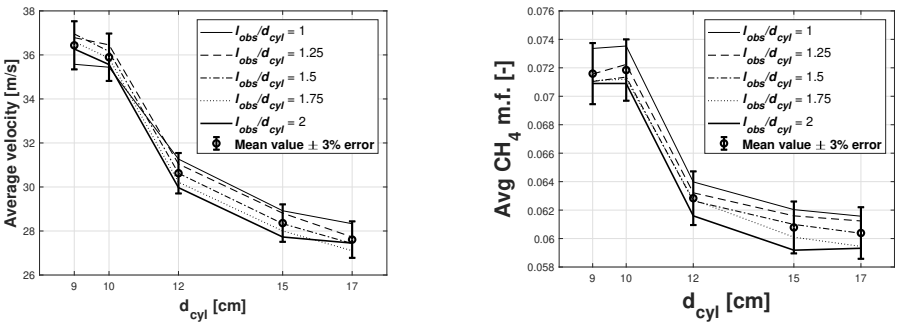

(a) Average velocity on the outlet boundary as a function of d_{cyl} for different l_{obs}/d_{cyl} ratios.

(b) Average CH_4 m.f. on the outlet boundary as a function of d_{cyl} for different l_{obs}/d_{cyl} ratios.

Fig. B.2 Results of the sensitivity study on the SB obstacle dimensions and distance: average values.

For both quantities, a sharp decrease is observed as the obstacle dimension increases, no matter the ratio l_{obs}/d_{cyl}. Moreover, a slight decrease is observed as the obstacle is positioned far away, i.e. passing from l_{obs}/d_{cyl}=1 to l_{obs}/d_{cyl}=2 for a fixed d_{cyl} value. It seems that the presence of the obstacle tends to decelerate the flow and

to enhance the mixing between the CH_4 and the surrounding air as it is bigger and further away. The obstacle dimension influences the jet causing a reduction of the velocity about $\sim$10 m/s going from 9 to 17 cm. Looking at this difference in terms of percentage on the maximum velocity value, a reduction of about 30% is noted, which is a relevant reduction with respect to the subsequent dispersion, happening at very low flow speeds. Starting from the previous point, it can be deduced how approximating an impinging jet with a free-jet by neglecting the presence of object near the release point, can induce very large over-estimations of the flow speed and CH_4 concentration. The most significant result, which can be appreciated from figure B.2, is the slight difference occurring in the velocities and methane m.f. for a fixed value of d_{cyl}. In fact, no matter the ratio l_{obs}/d_{cyl} is doubled, the velocity or mass fraction values are inside a small range defined by an error bar of 3% around the mean value. This result suggests that for a fixed d_{cyl} different configurations characterized by a different l_{obs} can be neglected as it does not influence significantly the SB output. This last consideration is valid for the average value of the output variables, but an analysis on the spatial distributions of these quantities is needed since these last represent the input of the dispersion simulation. Considering the case with d_{cyl}=10 cm, the velocity and mass fraction profiles on the outlet boundary (red line) for the different l_{obs}/d_{cyl} ratios are represented respectively in figure B.3 (a) and (b).

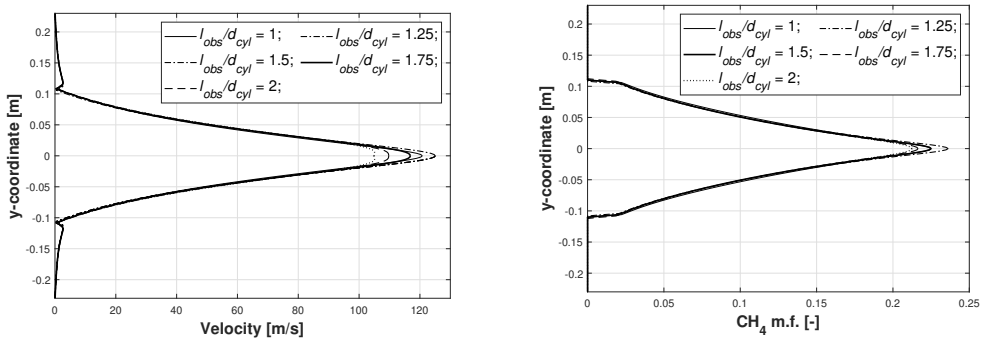

(a) Velocity profiles on the outlet boundary for different l_{obs}/d_{cyl} ratios.

(b) CH_4 m.f. profiles on the outlet boundary for different l_{obs}/d_{cyl} ratios.

Fig. B.3 Results of the sensitivity study on the SB obstacle dimensions and distance: spatial distributions.

A simil-Gaussian distribution is obtained for both quantities no matter the geometric ratio, and the profiles are all nearly coincident except for a narrow region

around the peak. This result confirms the considerations derived from the average values analysis, thus it can be concluded that for a fixed cylinder diameter, the distance l_{obs} does not influence relevantly the output. This outcome allows to neglect this parameter in the SB database construction, thus reducing the set of relevant configurations. The second sensitivity analysis consisted in analyzing the variation of the velocity and CH_4 m.f. at the outlet as a function of the pressure. In particular, p_0 is varied between 10 and 80 bar with a 5 bar step, which seems an exhaustive range for the purposes of a feasibility study. Figure B.4 shows that the average velocity and mass fraction have an almost linear increase as p_0 grows.

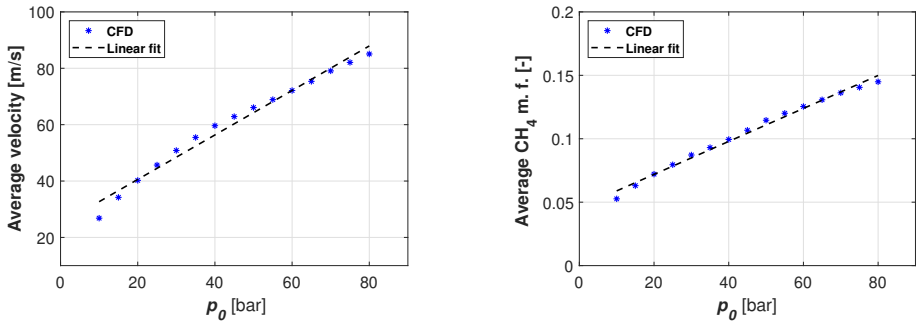

(a) Average velocity variation on the outlet boundary for different p_0 values.

(b) Average CH_4 m.f. variation on the outlet boundary for different p_0 values.

Fig. B.4 Results of the sensitivity study on the SB release pressure: average values.

Both data set can be fitted with good accuracy with a linear interpolation with relative Pearson coefficient R equal to 0.9897 and 0.9949 respectively. A more detailed information is provided in figure B.5 where the velocity and mass fraction profiles at the outlet boundary are shown as a function of the increasing pressure.

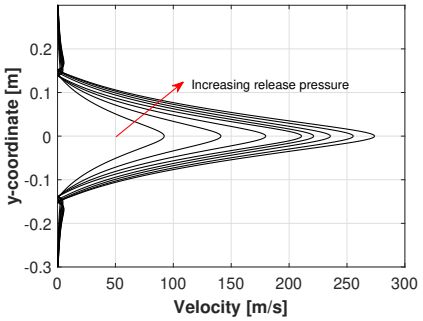

(a) Velocity profiles on the outlet boundary for different p_0 values.

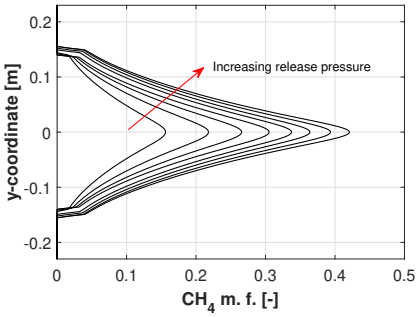

(b) CH_4 m.f. profiles on the outlet boundary for different p_0 values.

Fig. B.5 Results of the sensitivity study on the SB release pressure: spatial distributions.

It can be appreciated that the distributions, in both cases, maintain a similar "shape" no matter the pressure. They resemble a Gaussian distribution (typical of the gas jets) with an increasing peak for an increasing pressure. This result provides that for a fixed geometry the spatial distribution of the quantities is similar for all the simulations with different pressures. If on the one hand, the variation of the pressure seems to greatly influence the results and its variation could not be neglected, this 2D study hinted that a certain "regular" and "reproducible" behavior of the jet can be observed, also looking at the spatial distributions.

Despite the study on the geometrical features of the obstacles permits to cut the number of representative SB for the database generation, that in the previous minimum estimation goes from 2000 to 400, this number remains prohibitive in view of extension of the model to different type of gases and obstacles. For this reason, the regular behavior observed in the sensitivity analysis on the release pressure suggested to investigate alternative methodologies to obtain the SB results without doing the CFD simulations, as for example a Reduced Order Model based on machine learning algorithms which can dramatically reduce the computational burden.

B.2 SB metamodel

The strategy relies on the use of Reduced Order Models (ROMs) [125, 126] to overcome the computational burden associated to the database generation and, as deeply discussed in the following, to assure a high level of flexibility. In particular,

the attention is focused on *data-driven* methods which considers the high fidelity model (or Full Order Model, FOM), in this case the SB CFD simulation, as a black box and use only its inputs and outputs. For these reasons, data-driven ROMs are defined also *non-intrusive* since does not require to modify the equations of the FOM itself, making possible to use them also with commercial codes [127]. However, it must be considered that the data selection for the training and validation phases could biases the prediction capabilities and an *a priori* error prediction is difficult to be obtained [128]. No matter this drawbacks, approaches for non-intrusive model reductions resulted highly attractive for CFD applications [129, 130]. The Non-Intrusive Reduced Order Model (NIROM) here proposed is based on a novel combination of the the Proper Orthogonal Distribution (POD) and Radial Basis function (RBF) approach, together with two statistical approaches for the evaluation of two errors: the NIROM approximation error of the SB results and its propagation on the dispersion simulation output. These methods are the bootstrap method [131, 132] and the unscented transform (UT) [133].

The following sections aim just at briefly describing the main features of the NIROM, while for the detailed dissertation the reader may refer to Abrate et al. [124], where the work presented in the following was previously published.

B.2.1 The Non-Intrusive Reduced Order Model

The objective of the NIROM is to mimic the behavior of the SB simulation (the FOM), which can be represented in generic terms as a numerical model $\mathscr{M}$ acting on a P-dimensional input vector $\vec{p}$ containing the values of its input parameters, see Eq. B.1.

$$\vec{y} = \mathscr{M}(\vec{p}), \tag{B.1}$$

It returns an m-dimensional output $\vec{y}$, named *snapshot*, that in this case are the velocity and m.f. distributions on the SB faces. The input vector $\vec{p}$ contains the parameters p_0, D_e, d_{cyl}, l_{obs}, which can take several values in a certain range. This study considers only the variation of p_0, while the other parameters are fixed to D_e=1 cm, d_{cyl}=20 cm, l_{obs}=30 cm. The choice to consider only the pressure variation is based on the fact that it is the parameter with the largest impact on the final results, and it has the wider range of variation. Moreover, at this stage of the analysis, further complications due to geometry modifications induced by variations of the other

parameters can be avoided, as well as can represent a further development of the model. As a first step, the pressure range (10-80 bar) has to be sampled in order to define a suitable *training set* on which the CFD simulations have to be performed, and which results are used to train the NIROM. The sampling strategy here proposed entails the use of nested sets of points, which permits an *a posteriori* refinement of the parameters samples. As an example, at the beginning a pressure sampling step of 10 bar can be considered, but if the NIROM error results too high, new points of training can be added by considering smaller pressure steps. In particular, the pressure range is sampled with a nested Newton-Cotes quadrature rule where three different levels of discretization are considered, with reference to figure B.6: the red dots represent a discretization with a 10 bar step, the blue squares a 5 bar step and the triangles a 2.5 bar step.

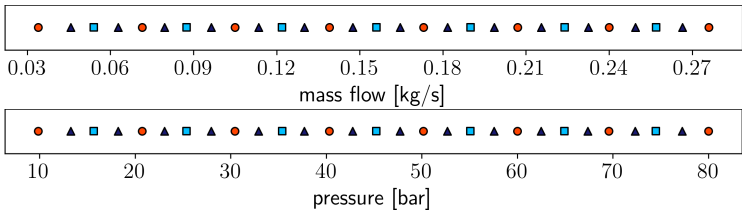

Fig. B.6 High-fidelity model samples generated with the Newton-Cotes rule. The orange circles are the first level, the light blue squares are the second level and the dark blue triangles are the third level.

Figure B.6 shows also the corresponding values of mass flow rate to the pressure levels, which can be uniquely related to the pressure considering that a chocked flow conditions is verified for all cases. The necessity to evaluate the mass flow rates arises since the CFD simulations in Fluent resulted more stable by imposing a mass flow inlet despite a pressure inlet especially at high pressures (>50 bar). As a second step, the results of the CFD simulations in correspondence of the training set values are then represented on a reduced order space by expressing them as an expansion of basis functions, namely the POD modes, extracted with a singular value decomposition. Details on the algorithms are provided in [134]. Then, the *reduced* data obtained by POD is now used to train a network of RBFs, which are adopted to interpolate the CFD solutions on new pressure values. The type of RBFs here employed rely on the inverse multi-quadrics formulated by Hardy [135]. The interpolation error of these functions is minimized employing the Leave-One-Out-Cross-Validation technique. After the training phase, the model is validated

by evaluating its responses on new pressure values chosen as far as possible from the training points. Since an extensive validation require a lot of CFD simulations to be compared to the NIROM ones, few validation points are usually considered. To complement this validation phase, a statistical sensitivity study concerning the training set is also proposed by applying the *bootstrap* method. This last consists in training a large number of NIROMs using different training sets obtained by resampling with replacement the original one. At the end, a distribution of the output responses is obtained and used to estimate the error distribution for each validation point [136, 137]. At the end of this process, there is an ensemble of metamodels, from which confidence intervals can be extracted. If these results with their own confidence intervals represent the input for another model $\mathscr{M}'$, propagating the uncertainty is not a trivial task. In this work, the unscented transform (UT) method [133] is proposed to propagate the SB NIROM error on the dispersion simulation outputs. The overall procedure is summarized by algorithm 1.

Algorithm 1: POD-RBF with uncertainty estimation

Offline procedures

1. define the p-dimensional parameter space $\mathbb{R}^p$;
2. select a parameter space sampling strategy (i.e. sparse grids, random sampling...);
3. generate full-order model snapshots $\vec{y}_i \in \mathbb{R}^m$ for each parameter sample $\vec{p}_i$;
4. divide the data into the training and the validation sets;
5. reduce dataset dimensionality, using POD;
6. train the RBF net with the POD coefficients $\vec{a}_i \in \mathbb{R}^t$;
7. apply the bootstrap method to generate a set of ROMs;
8. compute the error distribution of the ROMs on the validation set;
9. validate the ROM on the validation set. If the average error between validation data and the set of bootstrapped ROMs is not acceptable, go back to step 3, adding more training points;

Online procedure

1. interpolate with RBF the POD coefficients over a new point (i.e. not used during training) $\vec{p}_j$ in $\mathbb{R}^p$;
2. back-project the POD coefficients $\vec{a}_j \in \mathbb{R}^t$ to get the approximated snapshot in the original space, $\vec{y}_j \in \mathbb{R}^m$.
3. if the ROM response is used as input for another model, apply the UT to estimate the confidence interval.

B.2.2 The SB NIROM performance

The discussion of the results is made considering the SB faces names introduced in section 4.1.1 and which are shown here in figure B.7 for convenience. Note that the calculation are made on a reduced SB domain due to the symmetries discussed in section 4.2.1.

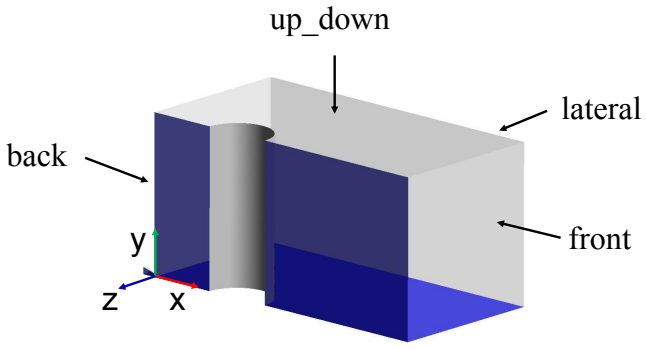

Fig. B.7 SB NIROM: SB faces denomination.

At first, the NIROM was trained on the first level of points (red circles) and validated on the second level (blue squares), see figure B.6. In figures B.8, B.9, B.10 and B.11 the percentage relative errors between the NIROM and CFD velocity components and CH_4 m.f. averages for each SB faces are presented.

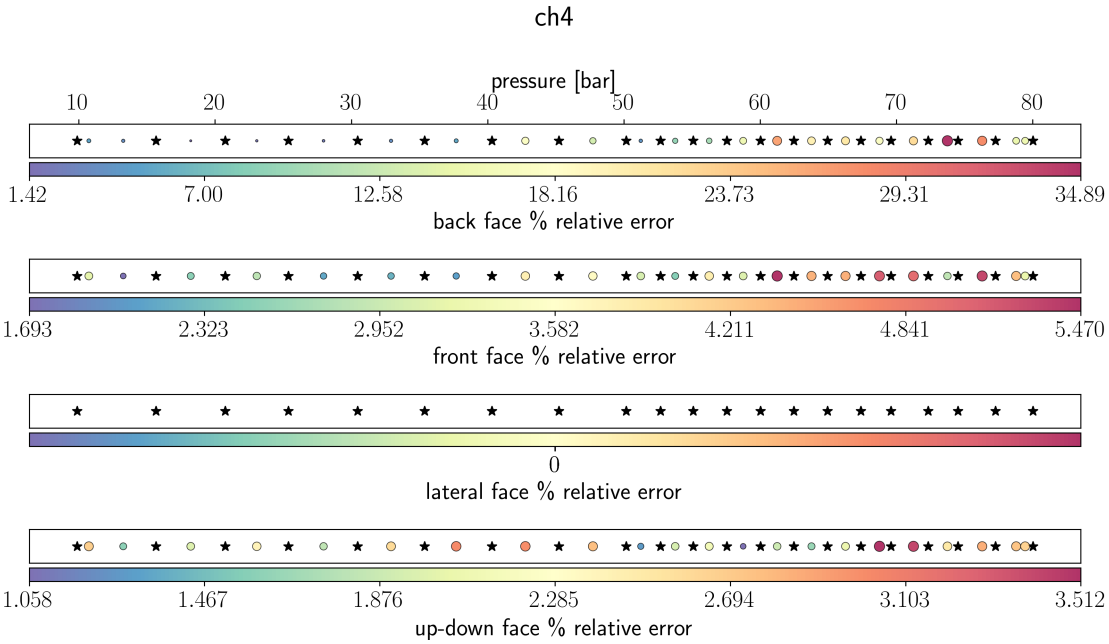

Fig. B.8 Face-wise relative L_2 error for the CH_4 concentration. The black stars represent the training cases, while the dots represent the validation cases and their color is related to the relative error.

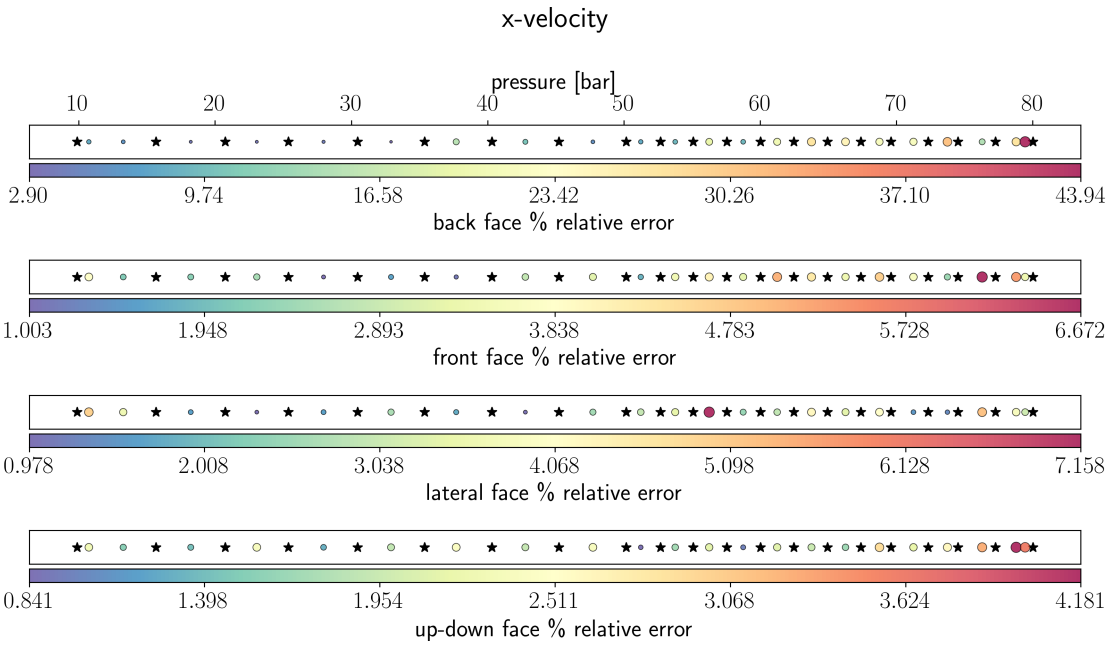

Fig. B.9 Face-wise relative L_2 error for the x-component of the velocity. The black stars represent the training cases, while the dots represent the validation cases and their color is related to the relative error.

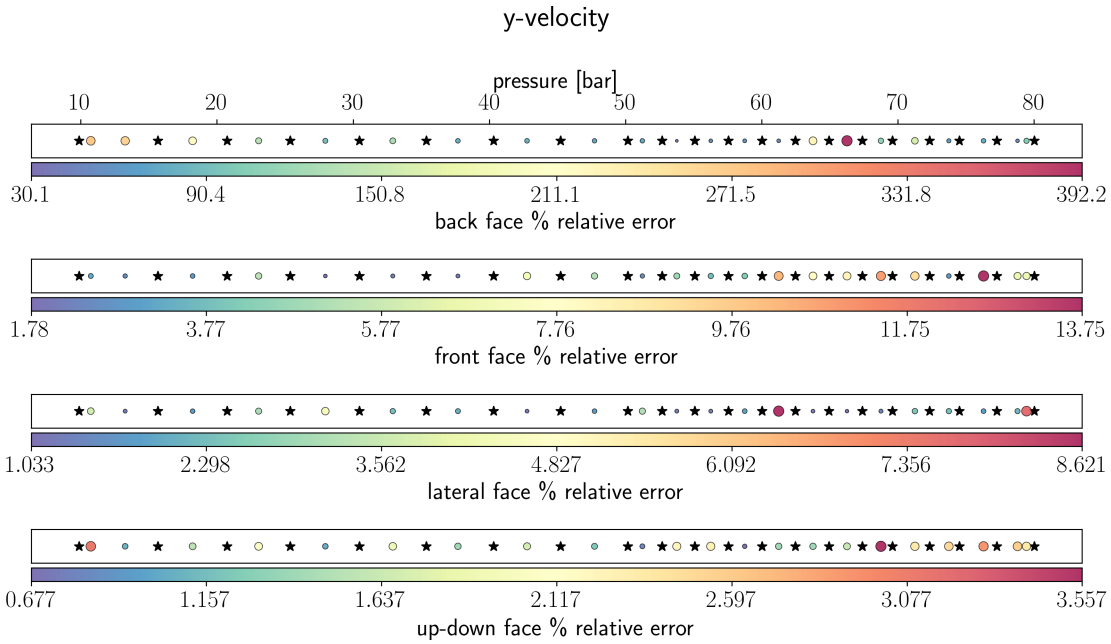

Fig. B.10 Face-wise relative L_2 error for the y-component of the velocity. The black stars represent the training cases, while the dots represent the validation cases and their color is related to the relative error.

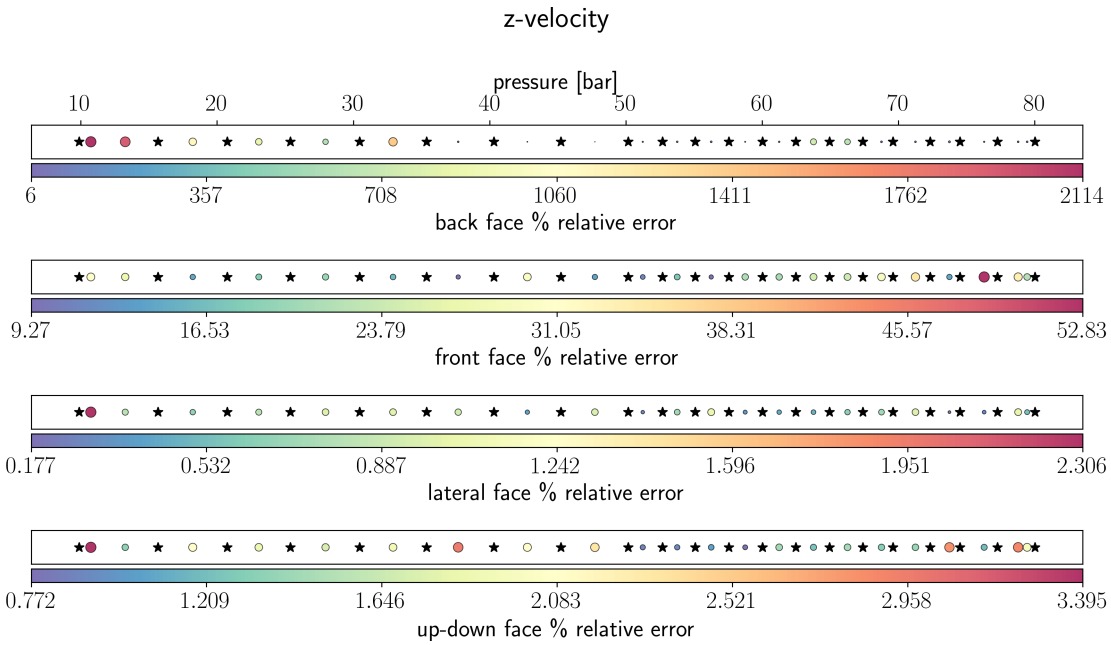

Fig. B.11 Face-wise relative L_2 error for the z-component of the velocity. The black stars represent the training cases, while the dots represent the validation cases and their color is related to the relative error.

The black stars represent the training points while the coloured circles the validation ones with a size proportional to the error magnitude. Errors on the faces *front, up-down* and *lateral* are relatively small except for the z-velocity component on the front face. The face *back* presents significant errors which can be ascribed to the steep velocity variation near the release point where a strong air entertainment phenomenon occur as shown in figure B.12.

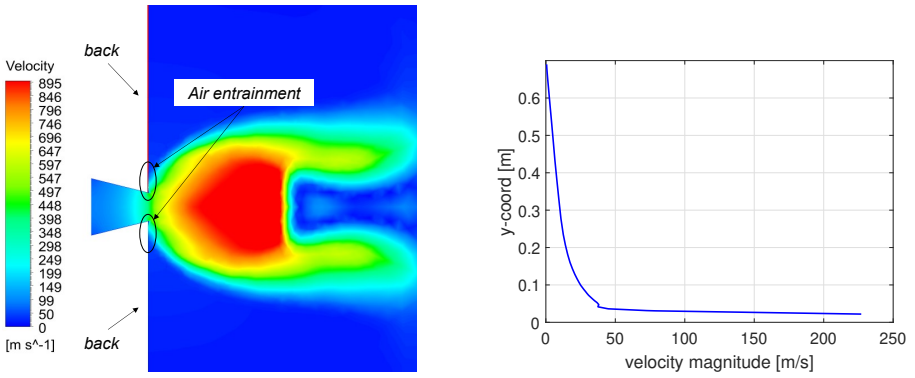

(a) Velocity contour on a SB section.

(b) Velocity profile on a line along the *back* SB face.

Fig. B.12 Air entrainment phenomenon in the SB.

Figure B.12(a) shows the regions, tangent to the *back* face, where the air is entrained by the strong inertia of the jet. Furthermore, the entrained air flows at high speed due to the extremely high inertia of the released gas, and steep velocity variations occur. These lasts are clearly visible from figure B.12(b) which presents the velocity profile along the red line on the back face shown in figure (a). The velocity reach values above 200 m/s and decrease down to 25 m/s in few centimeters, and this behavior is too complex to be reproduced by the ROM, inducing large magnitude errors. On the other hand, the overall quality of the NIROM is not affected by this error since being the *back* face tangent to the source point, it does not contribute relevantly to the overall mass flowing out of the SB. For this reason, instead of evaluating the L_2 error a more reliable error estimation is employed by weighting the face-wise errors with the mass flowrate flowing from each face. Eq. B.2 shows the new error estimation, where w_i is the weight defined according to Eq. B.3 where $\dot{m}_i$ is the mass flow from the i-th face and $\dot{m}_{tot}$ is the total mass flowrate

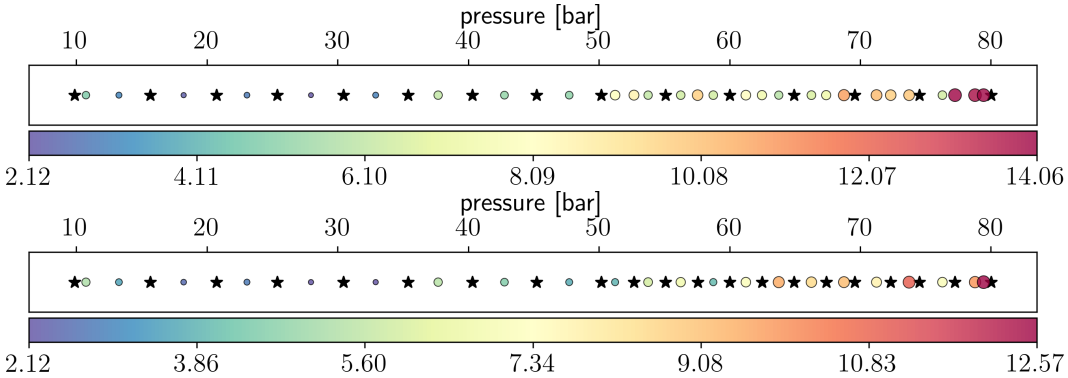

Fig. B.13 Weighted percentage relative error between NIROM and CFD using two different sets of training points. The black stars represent the training cases, while the dots represent the validation cases and their color is related to the relative error.

flowing out the SB.

$$\varepsilon = \sum_{i=1}^{faces} \frac{||\vec{y}_{\text{CFD,i}} - \vec{y}_{\text{ROM,i}}||}{||\vec{y}_{\text{CFD,i}}||} w_i \tag{B.2}$$

$$w_i = \frac{\dot{m}_i}{\dot{m}_{tot}} \tag{B.3}$$

It can be observed also that the CH_4 m.f. at the lateral face do not produced any data since no gas reaches that boundary, see figure B.8. The new error estimator permits a more realistic and physically reliable NIROM accuracy estimation, as the overall performance is now not influenced by the irrelevant larger errors at the *back* face. Figure B.13 reports the overall error per each pressure level, in particular, in the top the weighted relative error is obtained using the first samples level as training and the second as validation, while at the bottom the training employed the first and some of the second level points and the remaining for the validation. A higher density of training points were considered at p_0>50 bar in order to reduce the relative error in this region. The last figure shows that the largest global error is about 12.5%, and that the NIROM error increases for larger pressure levels, in fact a large number of training points was required in that pressure range. Velocity and m.f. profiles reproduced by the NIROM are presented and compared to the CFD ones in figures B.14, B.15, B.16 where the m.f. on the *front* face, and the normal velocity on the *front* and *up-down* faces are presented for the most critical case $p_0 = 51.25$ bar, the one with the worst statistical error [134]. Among with the profiles, the differences between them are highlighted on the right. The NIROM reproduction seems qualitatively good as the main spatial features of the flow field are preserved

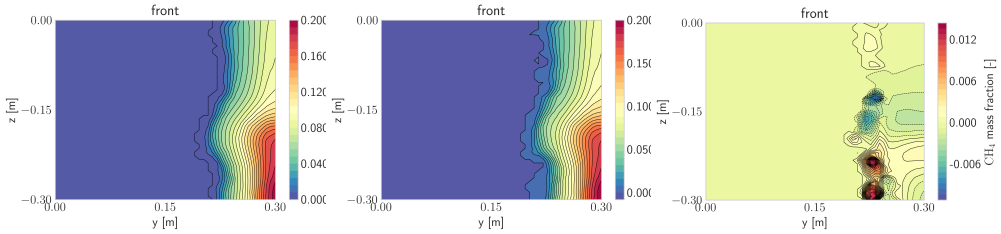

Fig. B.14 CH_4 mass fractions for CFD (left) and NIROM (centre) and their difference (right) on the front face for the validation case with p=51.237 bar.

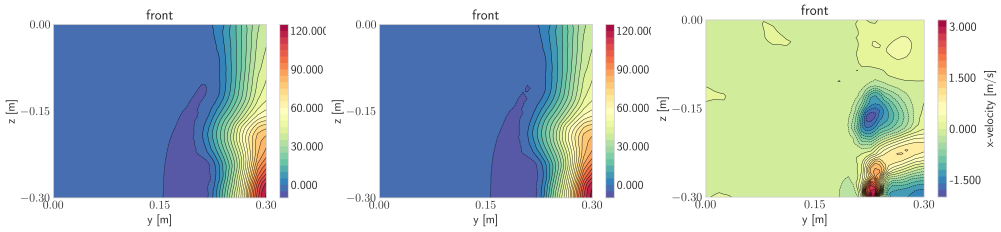

Fig. B.15 x-component of the velocity field for CFD (left) and NIROM (centre) and their difference (right) on the front face for the validation case with p=51.237 bar.

with negligible errors in most of the faces. The peak values regions, which are the ones with the highest importance, are reproduced with high accuracy, while larger error are generated at low velocity or low m.f. regions. However, considering that the aim is the QRA estimation, the prediction capability of the model is satisfactory as the error is lower than 15% in the worst case. Moreover, the acceptability of this error depends on its propagation on the final relevant results, which are the risk metrics evaluated by the dispersion simulation. For this reason, the uncertainty of the NIROM is estimated through the bootstrap method and consequently propagated to the dispersion output by the UT. As an example, the scenario where the NIROM has shown worst performance, i.e. the largest variance and mean error, is here considered to quantify the error propagation on the dispersion output. This scenario is the one

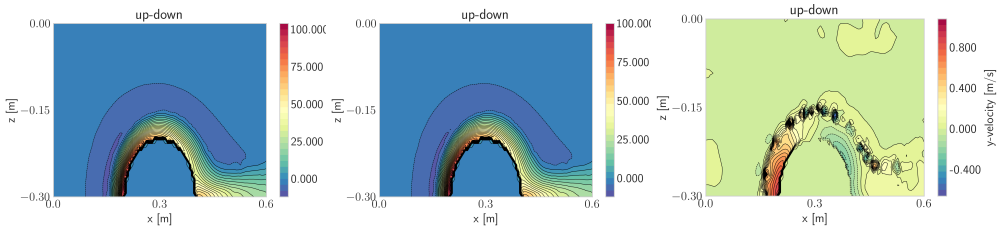

Fig. B.16 y-component of the velocity field for CFD (left) and NIROM (centre) and their difference (right) on the up-down face for the validation case with p=51.237 bar.

with p_0=51.25 bar, and the dispersion case study here considered is cs#8 (see table 3.2). Some safety-relevant output parameters are defined in order to compare the results obtained using the high-fidelity CFD profiles in one case, and the approximate NIROM profiles in the other one.

- Total dispersed CH_4 mass [kg], M_{CH4}
- CH_4 mass in the flammable cloud [kg], $M_{CH4,flam}$
- Flammable cloud volume [m^3], V_{flam}
- Irreversible Injuries (II) volume [m^3], V_{II}
- Irreversible Injuries area at 1.5 m height [m^2], A_{II}

Figure B.17 shows the irreversible injuries volumes obtained using respectively the CFD SB profiles and the NIROM SB profiles. In both cases, the gas cloud tends to split in two portions along the vertical direction, and the same platform components are invested by the gas. No significant differences can be appreciated by a visual inspection except some small discrepancies in one of the two extremity of the upper region. In fact, in the case of the CFD profile, an II volume equal to 22.2 m^3 is obtained, while in the NIROM case the II volume is 22.4 m^3, confirming that the difference is negligible ($\sim 0.9\%$). This qualitative comparison permits to deduce that the NIROM does not lead to noticeable differences in the dangerous cloud shape, however, a more detailed analysis needs to be carried out on the safety related quantities to quantify these, albeit small, discrepancies. The values obtained for each parameter are summarized in table B.1 where the results of the dispersion calculation using the original CFD profiles, provided by the SB simulation, and the surrogate profiles, computed with the NIROM, are compared. With the aim of providing a visual representation of these quantities and their uncertainties, the same quantities are normalised with respect to the CFD case and shown in figure B.18. The results obtained using the NIROM SB profiles are surprisingly similar to the CFD related ones. The relative difference in the mean values is always below 7%, and this is a remarkable result considering that these calculations refer to the worst performing case. As some parameters are slightly underestimated but from a safety point of view an overestimation of the accident consequences is preferable, a safety coefficient can be applied to the results to assure a conservative estimation. In addition, the computational cost associated with the SB profiles is dramatically reduced, since the

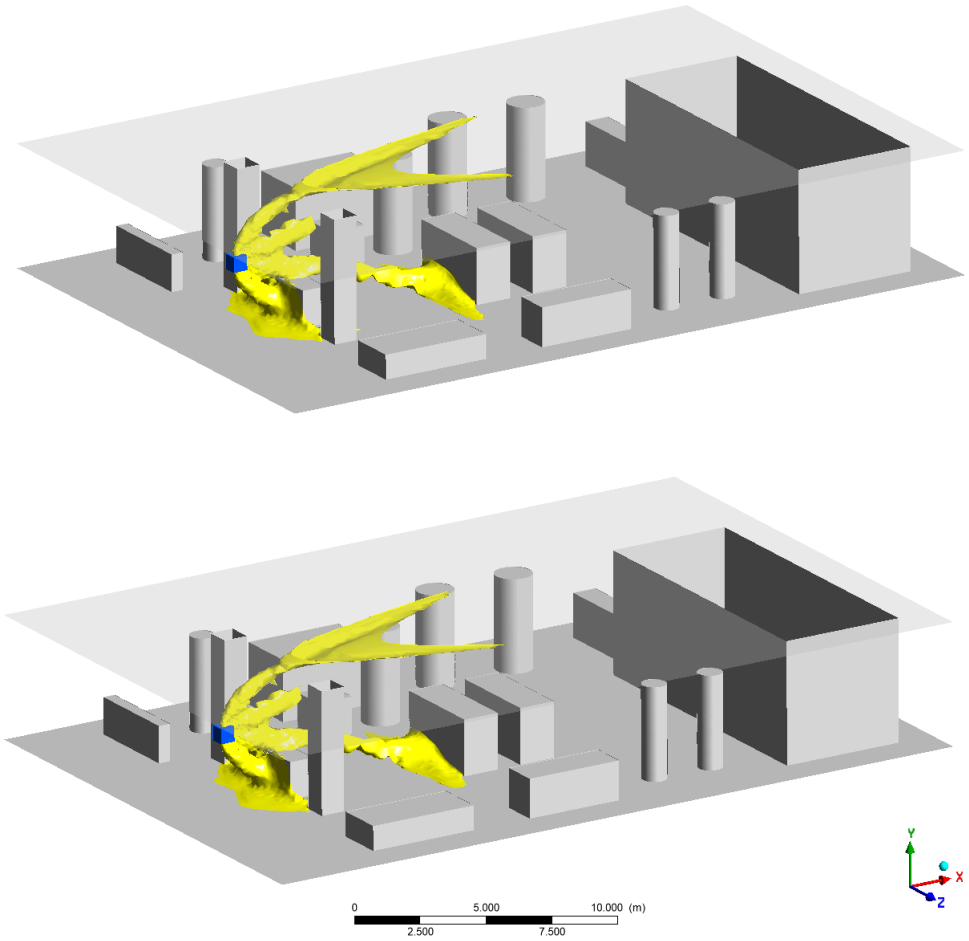

Fig. B.17 Irreversible Injuries volume obtained using the CFD SB profiles (top) and of the NIROM SB profiles (bottom).

Table B.1 Comparison of the risk metrics evaluated through the dispersion simulation using the CFD SB profiles and the NIROM SB profiles. The results of the second column are provided with an uncertainty, put in parentheses, given in terms of 1 standard deviation.

	CFD profile	ROM profile	Rel. difference
M_{CH4} [kg]	5.959	5.6(2)	∼6 %
$M_{CH4,flam}$ [kg]	0.066	0.064(4)	∼3 %
V_{flam} [m^3]	1.925	1.8(1)	∼6.5 %
V_{II} [m^3]	22	23(1)	∼4.5 %
A_{II} [m^2]	4.20	4.5(3)	∼7 %

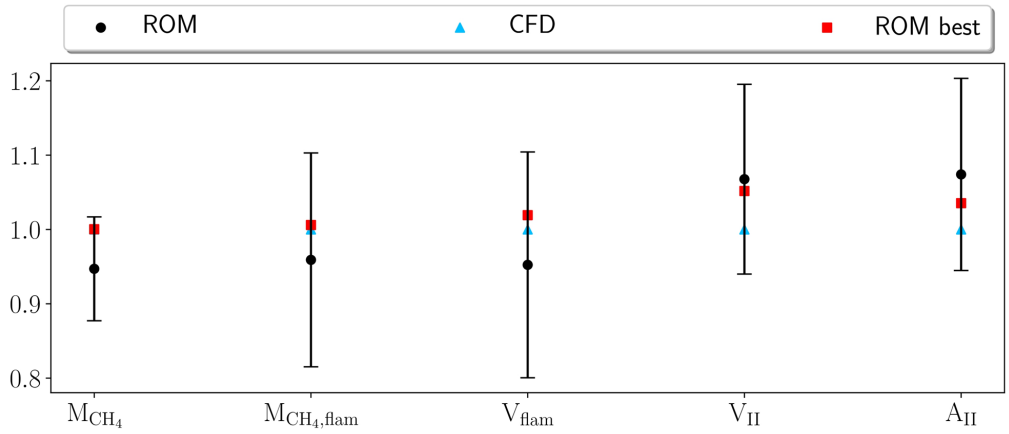

Fig. B.18 Expected value and standard deviation for the risk metrics evaluated through the dispersion simulation using the CFD SB profiles and the NIROM SB profiles. Each data is normalised with respect to the CFD case.

CFD employed almost 24 h, while the ROM runs in few seconds. This improvement permits to cut the time necessary for the SB database generation, since it needs only the simulation of a reduced set of cases for the training of the ROM (having in mind that the training set consisted only in the pressure levels with step 10 bar and few more points). Moreover, this opens the possibility to choose an arbitrary pressure value in the analyzed range and to get the results for that particular pressure instead of having a database with the results related only to a set of discretized values.

As a final consideration, the NIROM seems adequate to obtain fast yet very accurate results. In fact, the QRA related output parameters estimated through the ROM and CFD SB profiles input are in very good agreement, with a relative error between the two approaches below 7% and a reduction of the computational time of about three orders of magnitude. It should be remarked that a QRA study has an intrinsically high level of uncertainty, which makes the additional 7% introduced by the ROM model acceptable. Having proved the feasibility and the effectiveness of this approach, in future works, it can be extended by considering other input parameters affecting the SB, namely the break size and the obstacle features. Since these parameters have a strong influence on the SB dimension, a more sophisticated strategy should be devised in order to handle the snapshots $\vec{y}$ defined on a different spatial domain. In parallel to these activities, a surrogate model for the dispersion phase could be trained as well. Such a model could be efficiently coupled with the first NIROM, allowing to realise a real-time simulation framework (featured by

the capability of providing confidence intervals on the main results thanks to the combination of bootstrapping and UT), setting the basis for an effective CFD-QRA integration.

Appendix C

Governing equations, simulations setup and mesh features

In this appendix, the governing equations, the mesh features, the grid independence studies and the numerical implementation details of the simulations are presented. The ANSYS package v18.2 was employed for the pre-processing (ANSYS meshing), solving (Fluent) and post-processing (CFD-Post).

C.1 Governing equations

This section describes the governing equations solved in ANSYS Fluent through a finite volume approach [80].

C.1.1 Mass Conservation Equation

The general form of the mass conservation equation, valid for both incompressible and compressible flows can be written as follows:

$$\frac{\partial \rho}{\partial t} + \nabla \cdot (\rho \vec{v}) = S_m \tag{C.1}$$

where ρ is the density, $\vec{v}$ the velocity vector, S_m a source term representing the mass added to the continuous phase from the dispersed second phase or a user-defined source. In the Source Box (SB) and *benchmark* simulation, the density is modeled

through the ideal gas law (ρ=$\frac{p}{RT}$). The temperature field is evaluated by solving the energy equation (see Eq. C.8). In the dispersion simulation the flow is considered incompressible (ρ=const), and the energy equation is not solved.

C.1.2 Momentum Conservation Equations

The following equation describes the conservation of momentum in an inertial reference frame in three dimensions.

$$\frac{\partial}{\partial t}(\rho \vec{v}) + \nabla \cdot (\rho \vec{v} \vec{v}) = -\nabla p + \nabla \cdot (\vec{\vec{\tau}}) + \rho \vec{g} + \vec{F} \tag{C.2}$$

With p static pressure, $\vec{\vec{\tau}}$ stress tensor (see Eq. C.3), $\rho \vec{g}$ gravitational forces and $\vec{F}$ external body forces.

$$\vec{\vec{\tau}} = \mu \left[(\nabla \vec{v} + \nabla \vec{v}^T) - \frac{2}{3} \nabla \cdot \vec{v} I \right] \tag{C.3}$$

With μ molecular viscosity and I unit tensor.

C.1.3 Turbulence modeling

Since our application involves turbulent flows, the momentum conservation equations are solved in the form of Reynolds-Averaged Navier Stokes (RANS) equations. As a closure of the RANS equations, the k-ω SST model is used in the benchmark simulation and in the SB while the k-ω Standard for the SBAM dispersion simulations. In Eq. C.4 and C.5, the transport equations for the turbulent kinetic energy k and the specific dissipation rate ω are shown for the k-ω Standard model.

$$\frac{\partial}{\partial t}(\rho k) + \frac{\partial}{\partial x_i}(\rho k u_i) = \frac{\partial}{\partial x_j}\left(\Gamma_k \frac{\partial k}{\partial x_j} \right) + G_k - Y_k + S_k \tag{C.4}$$

$$\frac{\partial}{\partial t}(\rho \omega) + \frac{\partial}{\partial x_i}(\rho \omega u_i) = \frac{\partial}{\partial x_j}\left(\Gamma_\omega \frac{\partial \omega}{\partial x_j} \right) + G_\omega - Y_\omega + S_\omega \tag{C.5}$$

The subscripts i and j denotes the different Cartesian components. G_k represents the generation of turbulent kinetic energy due to mean velocity gradients. G_ω represents

the generation of ω. Γ_k and Γ_ω represent the effective diffusivity of k and ω. Y_k and Y_ω represent the dissipation of k and ω due to turbulence. The SST k-ω model involves the same couple of equations, except for an addendum in the right-hand side of Eq. C.5, that is the cross-diffusion term D_ω. Details about the turbulence models are discussed in [138, 139]. The equations of the other turbulence models employed in the benchmark analysis, k-ω BSL, k-ε Realizable and k-ε RNG are not reported here, but can be found in [80], since these models were no more used for other analyses.

C.1.4 Species Transport Equation

To predict the local mass fraction of each species, Y_i, a convection-diffusion equation for the i-th species is solved:

$$\frac{\partial}{\partial t}(\rho Y_i) + \nabla \cdot (\rho \vec{v} Y_i) = -\nabla \cdot \vec{J}_i + R_i + S_i \tag{C.6}$$

where R_i is the net rate of production of the i-th species by chemical reaction and S_i is a source term accounting for dispersed phases or user-defined sources. These two terms are imposed equal to 0 since no chemical reactions are considered. $\vec{J}_i$ is the mass diffusion term, that in this application is written for turbulent flows as:

$$\vec{J}_i = -\left(\rho D_{i,m} + \frac{\mu_t}{Sc_t}\right)\nabla Y_i - D_{T,i}\frac{\nabla T}{T} \tag{C.7}$$

where $D_{i,m}$ is the mass diffusion coefficient, $D_{T,i}$ is the thermal diffusion coefficient and Sc_t is the turbulent Schmidt number imposed equal to its default value 0.7.

C.1.5 Energy Equation

The energy equation solved by Fluent is of the following form:

$$\frac{\partial}{\partial t}(\rho E) + \nabla \cdot (\vec{v}(\rho E + p)) = \nabla \cdot \left(k_{eff}\nabla T - \sum_j h_j \vec{J}_i + (\vec{\vec{\tau}}_{eff} \cdot \vec{v})\right) + S_h \tag{C.8}$$

where E is defined as:

$$E = h - \frac{p}{\rho} + \frac{v^2}{2} \tag{C.9}$$

with h sensible enthalpy.
k_{eff} is the effective conductivity (k_{eff}=k+k_t where k_t is the turbulent conductivity defined according to the chosen turbulence model). S_h is a source term, $\vec{\vec{\tau}}_{eff}$ is the deviatoric stress tensor and $\vec{J}_j$ is the diffusion flux for the j-th species. Both the SB and the dispersion simulations are performed in steady-state.

C.2 Mesh features and numerical setup

C.2.1 Source Box simulation (full scale)

A unstructured mesh consisting of tetrahedral elements was generated in the SB domain through ANSYS meshing. Figures C.1(a) and (b) show the mesh on the symmetry planes, where the elements density variation in the domain can be appreciated. A higher mesh density near the jet source, represented by the small nozzle on the left, as well as the gradual element size growth from the jet centerline towards the outer regions are clearly shown. In figure C.1(c) a zoomed view of the mesh at the cylinder wall highlights the mesh refinement generated to fully resolve the boundary layer.

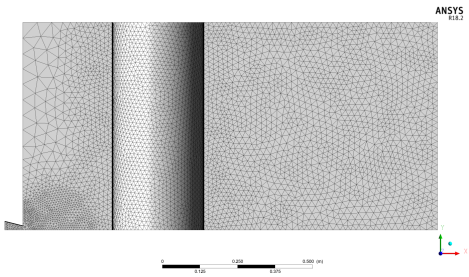

(a) Symmetry plane *xy*.

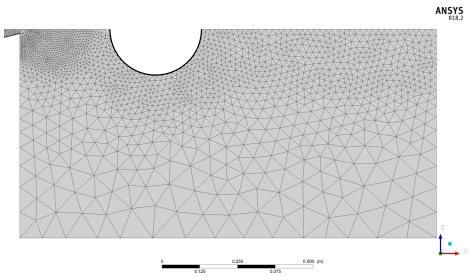

(b) Symmetry plane *xz*.

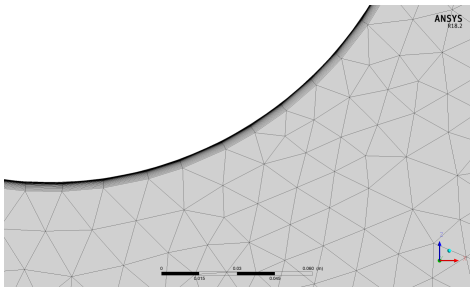

(c) Mesh refinement on the cylinder wall.

Fig. C.1 Source Box mesh in the full scale case.

The element size varies from 1.75 mm to 8 cm going from the most refined to the coarsest mesh region. This size variation was handled through the employment of 6 control volumes (CV) characterized by different element sizing, gradually increased with a 1.2 *growth rate*. The mesh refinement around the cylinder, visible in figure C.1(c), was obtained using the *inflation* layer algorithm of ANSYS meshing

by imposing the first layer thickness equal to 10^{-6} m (guaranteeing $y^+<1$) and a maximum number of layers equal to 30. The grid independence study was performed considering four different meshes consisting respectively of $\sim 1.5 \cdot 10^5$, $\sim 3 \cdot 10^5$, $\sim 4.5 \cdot 10^5$, $\sim 6 \cdot 10^5$ elements. The behaviour of the average velocity and CH_4 m.f. on the SB outlet boundaries were monitored. In addition, the generalized form of the Richardson extrapolation [140] was used to obtain an estimation of the exact solution to be compared to the numerical ones. In figure C.2(a) the numerical and extrapolated value of the average velocity are compared, while figure C.2(b) shows the relative error of the numerical solution with respect to the Richardson extrapolation. In figure C.3(a) and figure C.3(b) the analogous plots for the average CH_4 m.f. are shown.

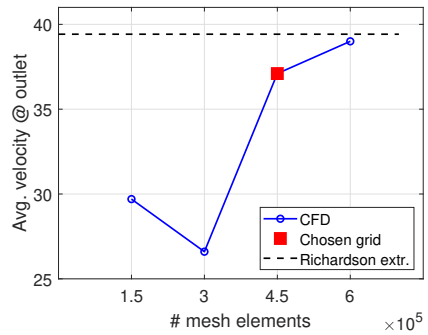

(a) Average velocity in m/s at the outlet boundary faces for different mesh sizes.

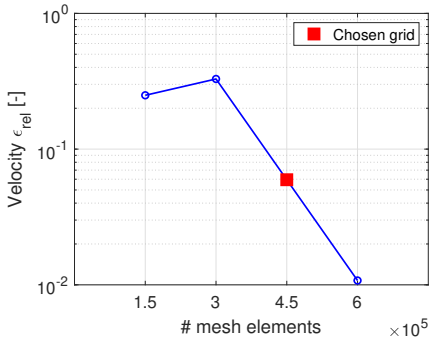

(b) Relative error (ε_{rel}) of the average velocity with respect to the Richardson extrapolation.

Fig. C.2 Full scale SB grid independence on velocity.

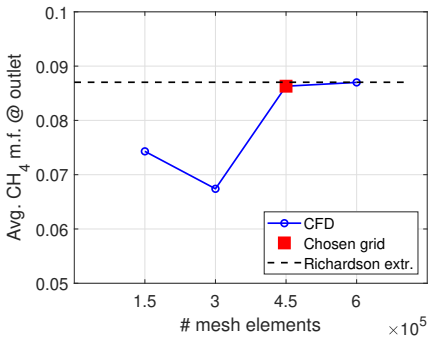

(a) Average CH_4 m.f. variation at the outlet boundary faces for different mesh sizes.

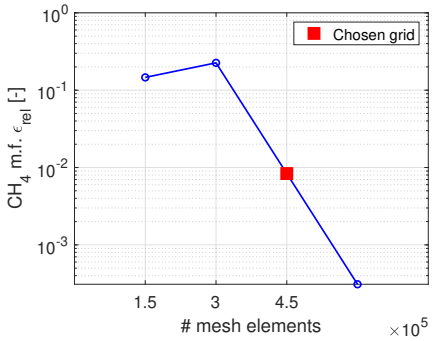

(b) Relative error (ε_{rel}) of the CH_4 m.f. with respect to the Richardson extrapolation.

Fig. C.3 Full scale SB grid independence on m.f.

The mesh consisting of $\sim 4.5e5$ was used for the calculations as it represented a trade-off between cost and accuracy. In fact, the ε_{rel} is lower than ~ 0.05 and ~ 0.01 respectively for the average velocity and the CH_4 m.f. which for the purposes of this work can be considered a sufficient accuracy. Nonetheless, the solution appears to be convergent to the estimated exact solution for both quantities.

A *steady-state* formulation of the governing equations is solved employing a *pressure based* solver. The energy equation is solved as well, and the k-ω SST model is chosen enabling the *viscous heating* term. The *species transport equation* is solved and the properties of the species are evaluated as in the following: *ideal gas law* for the density, *mixing-law* for the Cp, constant value for the thermal conductivity $k = 0.0454$ W/(m·K) and the *constant dilute approximation* for the mass diffusivity $D_M = 2.88 \cdot 10^{-5}$ m^2/s. The boundary conditions are already listed in the main text, however a deeper discussion is required for the inlet condition at the nozzle. A total pressure value is specified through a *pressure inlet* in ANSYS Fluent. A user defined function (udf) is imposed at that boundary in order to reach the target pressure (50 bar) after 200 iterations. The udf is written as in the following:

```
#include "udf.h"
int iter=0;
real final_pressure=4900000;
real initial_pressure=200000;
real p=200000;
int iter_ramp=200;

DEFINE_PROFILE(pressure_ramp, t, i)
{
  face_t f;
  iter=iter+1;

  if(iter<iter_ramp)
  {
    p = p + ((initial_pressure+final_pressure)/iter_ramp);
  }
  else
```

```
    {
      p = final_pressure;
    }
    begin_f_loop(f,t)
    {
      F_PROFILE(f,t,i) = p;
    }
    end_f_loop(f,t)
}
```

The inlet pressure (that is a gauge pressure in the udf) is linearly increased from 2 bar to 50 bar during the first 200 iterations. This methodology was employed to help the simulation convergence which resulted hardly reachable by directly imposing the target pressure due to the strong pressure gradient. A pressure-velocity *coupled* algorithm is employed. A 1^{st} order spatial discretization scheme is employed in the first 1000 iterations, while for the remaining iterations a 2^{nd} order scheme is employed until convergence is reached. A *pseudo-transient* formulation of the equations is used to help the convergence, by using an implicit relaxation factor of 0.8. In addition, the explicit relaxation terms of the continuity equation is set to 0.5. The solution convergence is judged by looking at the residuals and two monitors quantities: the released mass of CH_4 and the velocity at the outlet boundaries. The convergence criterion is based on the parameter defined in Eq. C.10.

$$\Delta_{rel} = \frac{|K(it) - K(it-1)|}{|K(it-1)|} \tag{C.10}$$

Where K is a generic monitored quantity and it is the iteration counter. Δ_{rel} permits to evaluate the relative difference of the solution at iteration it with respect to the solution at the previous iteration $it-1$. The solution was considered converged when Δ_{rel} fell below a target value of 0.1 % for both the monitored quantities. In figure C.4 the behavior of each monitored quantity is shown in function of the iterations (a, c) as well as the corresponding Δ_{rel} (b, d).

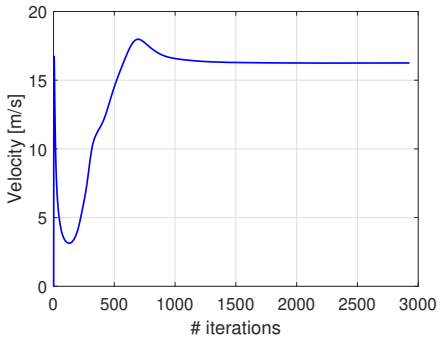

(a) Average velocity at SB outlet in function of the iterations.

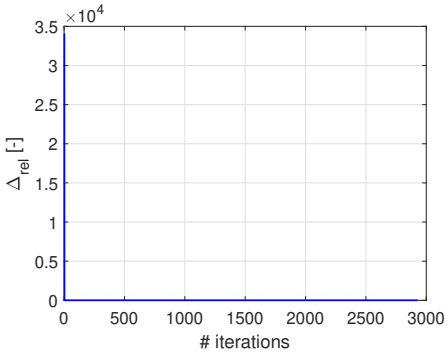

(b) Δ_{rel} of the average velocity at SB outlet at each iteration.

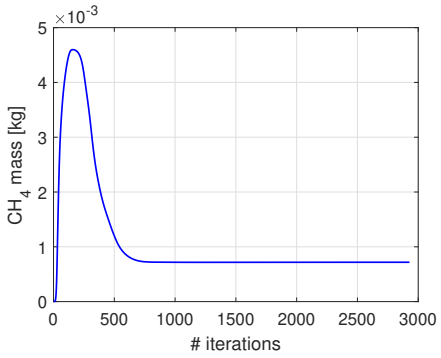

(c) CH_4 mass in the SB volume in function of the iterations.

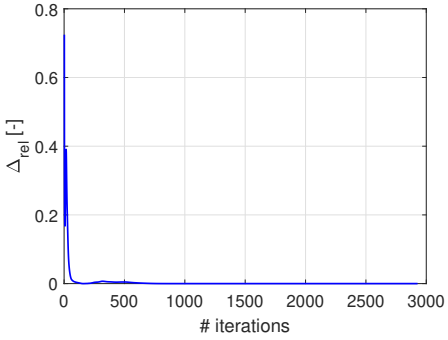

(d) Δ_{rel} of the CH_4 mass in the SB volume at each iteration.

Fig. C.4 Monitors convergence for the SB simulation convergence.

C.2.2 SBAM dispersion simulation (full scale)

An unstructured tetrahedral mesh was generated in the platform as can be seen in figure C.5(a). The mesh generation in this simulation was largely simpler with respect to the SB simulation, in fact a uniform sizing equal to 0.4 m was imposed in the domain and two *face sizing* were used: on the *black-box* faces a element size equal to 1 cm was imposed (see figure C.5(b)) and on the objects faces a 0.15 refinement was imposed. Moreover, a refinement on the walls was generated through the *inflation layer* algorithm to model the boundary layer. The first cell dimension was set equal to 5 mm to have $30<y^{+}<300$, and a maximum number of 7 layers was imposed. No control volumes was needed to generate different mesh densities is the domain.

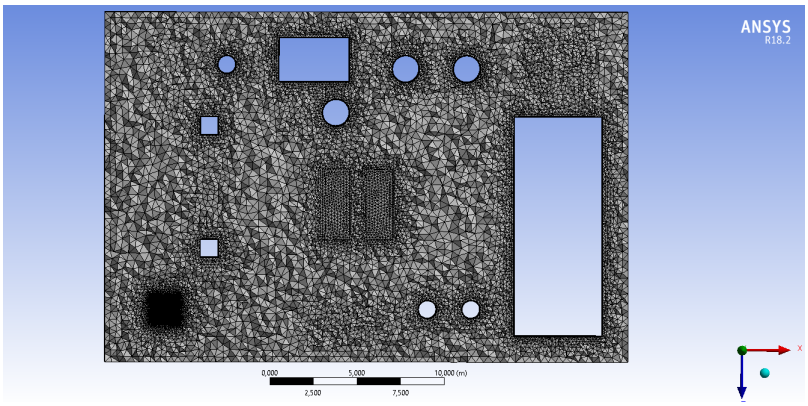

(a) Mesh overview on a xz section.

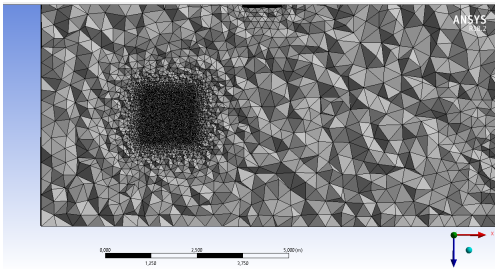

(b) Mesh refinement near the black-box

Fig. C.5 Full scale SBAM dispersion mesh.

For the grid convergence study of this simulation, the methodology of the Grid Convergence Index (GCI) [140] was adopted. The choice is due to the complexity of the geometry and the necessity to provide a fast methodology to assess the spatial grid convergence in the dispersion phase simulation. The GCI is a measure of the percentage distance of the computed value from the asymptotic numerical value. For the study, three different meshes were used: mesh 1 of $\sim 1.5 \cdot 10^6$ elements, mesh 2 of $\sim 2.8 \cdot 10^6$ elements and mesh 3 of $\sim 4.5 \cdot 10^6$ elements. The GCI was evaluated with respect to two quantities: the average velocity at the outlet boundary and the average CH_4 m.f. in the domain. In particular, the GCI related to the finest mesh (GCI12) and the GCI related to the medium mesh (GCI23) were evaluated. The methodology is the one for unstructured mesh proposed in [140]. It has also been investigated that the solution was in the asymptotic range of convergence by checking Eq. C.11. The values obtained are summarized in Table C.1. The results shows that very low values of GCI were obtained for both quantities especially for the estimation of the error related to the finest mesh (GCI12). It was important to assure that the solution was in the asymptotic range of convergence by checking that

	GCI12	GCI23
Avg. velocity	$1.36{\cdot}10^{-5}$	$1.97 \cdot 10^{-4}$
CH_4 mass	$2.36 \cdot 10^{-1}$	$3.03 \cdot 10^{-1}$

Table C.1 Full scale dispersion GCI values.

Eq. C.11 is satisfied.

$$\frac{GCI23}{r_{eff}^{p} \cdot GCI12} \simeq 1 \tag{C.11}$$

Where p is the formal order of accuracy of the algorithm and r_{eff} the effective mesh refinement factor. The following values were obtained respectively for the velocity and mass fraction cases: 1.0001 and 0.9945. These values assured that the solution is well converged, hence mesh 1 was judged sufficiently refined for the calculations.

The gravitational forces term is considered in the momentum equations, the turbulence modeling is performed employing several 2-equations models in the benchmark analysis, but the k-ω Standard is the one employed for all other analyses. The *viscous heating* term and the *shear flow correction* term are included. The remaining part of the setup is analogous to the SB one, with the difference that the explicit relaxation terms are set equal to 1. Also in this case, the total mass of released CH_4 and the average velocity at the outlet are used as monitors quantities, and the same requirement on Δ_{rel} (see Eq. C.10) was employed to obtain a converged solution. In figure C.6 the behavior of each monitored quantity is shown in function of the iterations (a, c) as well as the corresponding Δ_{rel} (b, d).

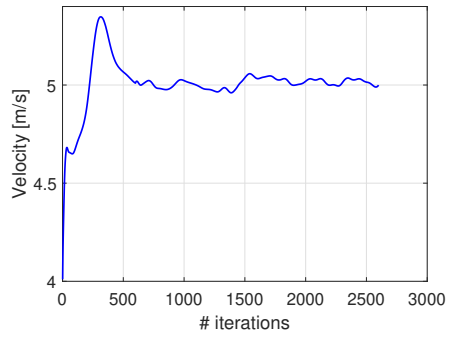

(a) Average velocity at boundaries b3-b4 in function of the iterations.

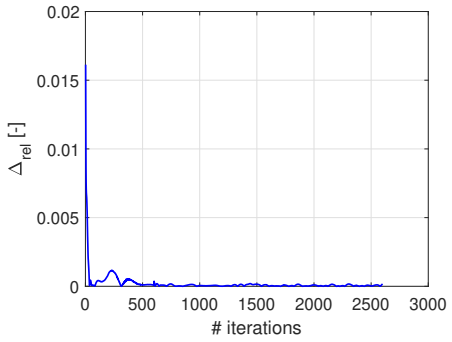

(b) Relative difference of the average velocity at boundaries b3-b4 at each iteration.

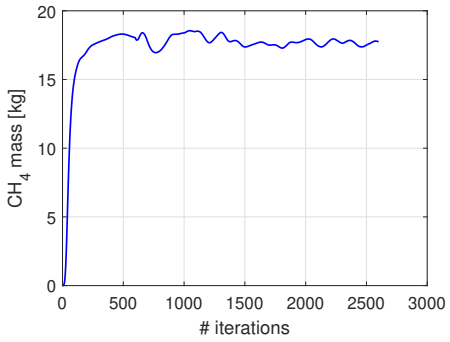

(c) CH_4 mass in the platform volume in function of the iterations.

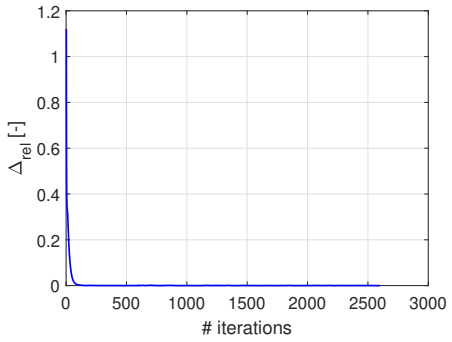

(d) Relative difference of the CH_4 mass in the platform volume at each iteration.

Fig. C.6 Monitors convergence for the SBAM dispersion simulation.

C.2.3 Benchmark simulation mesh and setup

An overview of the mesh is shown in figure C.7(a) where a transversal section of the domain is shown. The zones characterized by different element sizes are clearly distinguishable, and the large mesh density variation can be appreciated. Four control volumes were created to generate the different sizing in the range

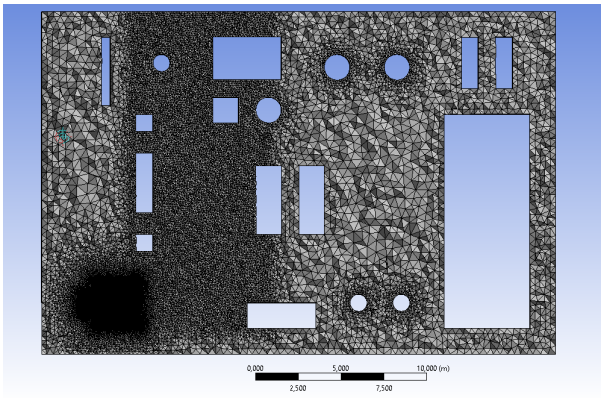

(a) Mesh overview on a *xz* section.

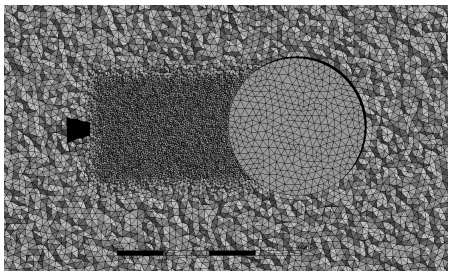

(b) Mesh refinement near the release point.

Fig. C.7 Benchmark simulation mesh.

0.005 m to 0.4 m guaranteeing a smooth transition with a 1.2 *growth rate*. In figure C.7(b) a zoomed view of the mesh near the leak source is shown. Other mesh refinements were realized on the platform objects walls through a *face sizing*. Also in this case a tetrahedral mesh was generated and a grid independence study was performed considering 5 different meshes consisting in $\sim 2.5 \cdot 10^6$, $\sim 5 \cdot 10^6$, $\sim 7.5 \cdot 10^6$, $\sim 10 \cdot 10^6$ and $\sim 12.5 \cdot 10^6$ elements. Two quantities were considered for the analysis: the average velocity on the outlet boundaries faces and the average CH_4 m.f. on transversal section at height y=1.5 m. For both quantities the exact solution was estimated through the generalized Richardson extrapolation and it was compared to the numerical values. In figure C.8 the average velocity at the outlet

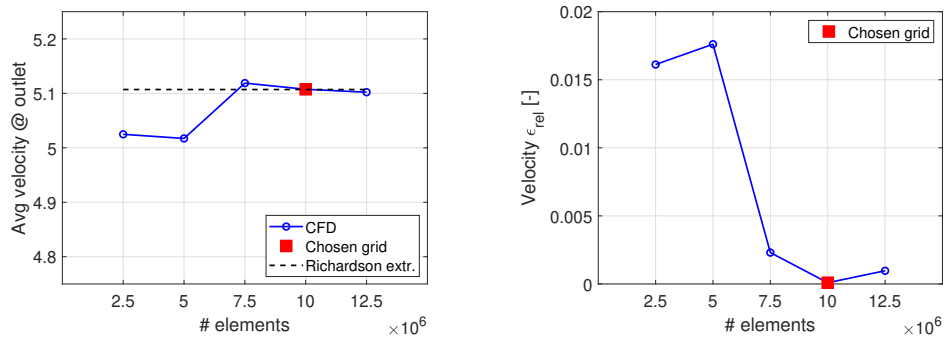

(a) Average velocity in m/s at the outlet boundary faces for different mesh sizes.

(b) Relative error (ε_{rel}) of the average velocity with respect to the Richardson extrapolation.

Fig. C.8 Benchmark grid independence on velocity.

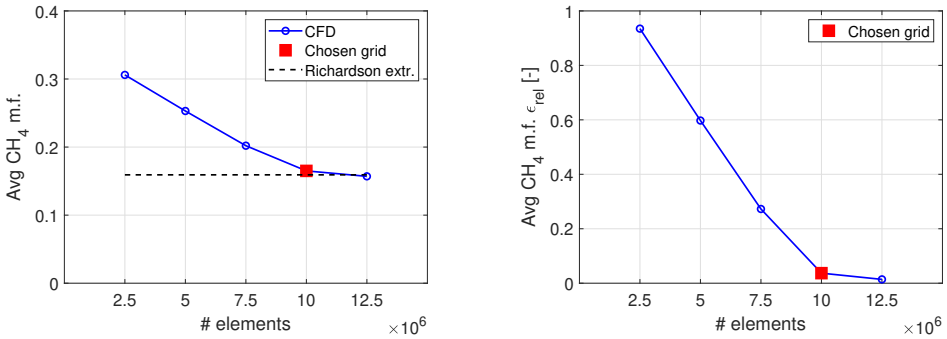

(a) Average CH_4 m.f. variation at the transversal section at y=1.5 m for different mesh sizes.

(b) Relative error (ε_{rel}) of the CH_4 m.f. with respect to the Richardson extrapolation.

Fig. C.9 Benchmark grid independence on m.f.

boundary faces in function of the different mesh sizes (a) and the relative error of the numerical solution with respect to the extrapolated value (b) are shown. The analogous results related to the average CH_4 m.f. are shown in figure C.9. The mesh consisting of $\sim 10 \cdot 10^6$ was selected for the calculation since it resulted the best compromise between accuracy and computational cost. Models and solution methods set for this simulations are analogous to the SB ones and also in this case, the total mass of released CH_4 and the average velocity at the outlet were used as monitors quantities, and the same requirement on Δ_{rel} (see Eq. C.10) was employed to judge the solution convergence. In figure C.10 the behavior of each monitored quantity is shown in function of the iterations (a, c) as well as the corresponding Δ_{rel} (b, d).

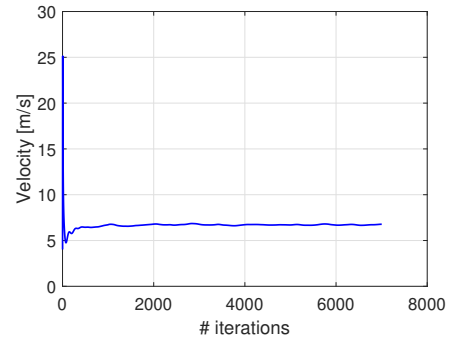

(a) Average velocity at boundaries b3-b4 in function of the iterations.

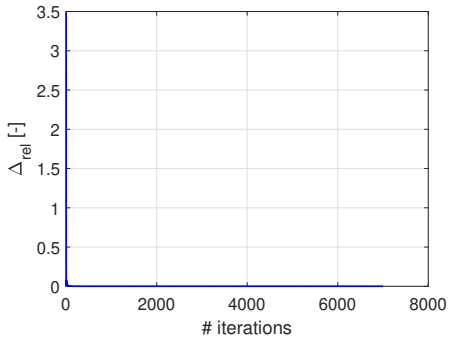

(b) Relative difference of the average velocity at boundaries b3-b4 at each iteration.

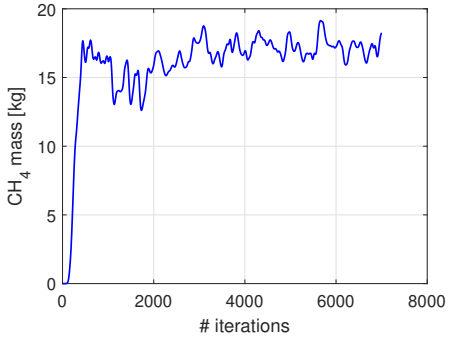

(c) CH_4 mass in the platform volume in function of the iterations.

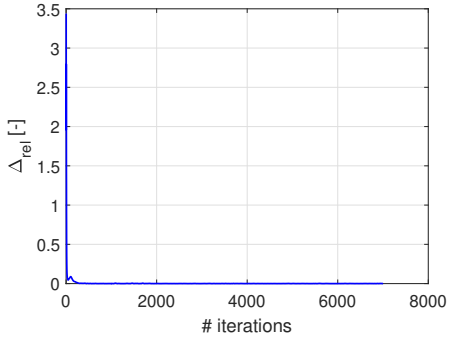

(d) Relative difference of the CH_4 mass in the platform volume at each iteration.

Fig. C.10 Monitors convergence of the benchmark simulation.

C.2.4 Source Box mesh features (model scale)

The same criteria for the full scale SB were employed for the generation of the unstructured mesh of the model scale SB. The mesh is composed of tetrahedral elements which density varies according to the region of the SB: a high density mesh was realized near the jet source and the jet centerline. Figure C.11 shows the mesh chosen for the calculations which consists of $\sim 2 \cdot 10^6$ elements. The minimum element size is 0.15 mm in the nozzle region, while the maximum one is 12 cm. Seven control volumes were employed to assure a smooth transition from the finest to the coarsest mesh region. A refinement around the cylinder was realized through the *inflation* layer algorithm of ANSYS meshing imposing a first layer thickness of 10^{-7} m to have $y^+ < 1$ and a maximum number of 30 layers. A grid independence was performed considering three mesh consisting of $\sim 8 \cdot 10^5$, $\sim 1.4 \cdot 10^6$ and $\sim 2 \cdot 10^6$ elements. The average velocity at the outlet boundaries and

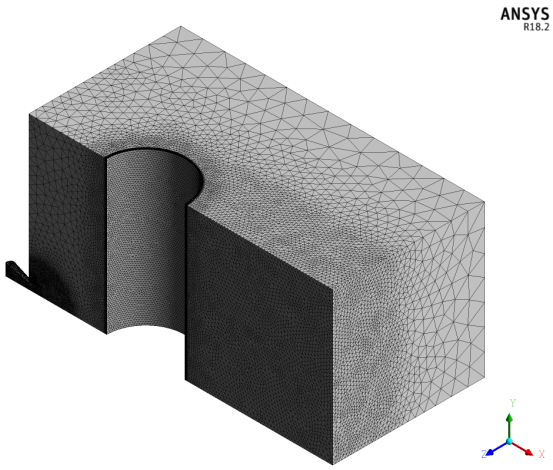

Fig. C.11 Model scale SB mesh.

the average CH_4 m.f. in the volume were monitored. The numerical solutions were compared to an estimation of the exact solution through the Richardson extrapolation [140]. In figures C.12 (a) and (b) the numerical and extrapolated value of the average velocity are compared, and the relative error of the numerical solution with respect to the Richardson extrapolation are respectively shown. In figure C.13 the analogous plots for the average CH4 m.f. are shown.

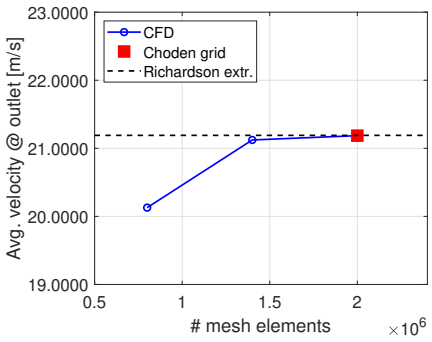

(a) Average velocity at the outlet boundary faces for different mesh sizes.

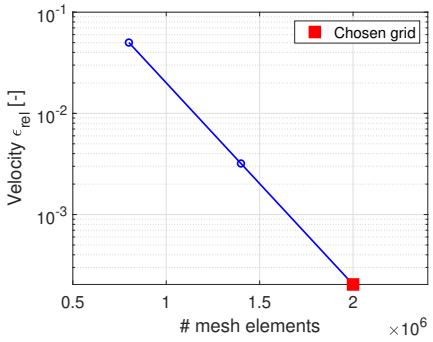

(b) Relative error (ε_{rel}) of the average velocity with respect to the Richardson extrapolation.

Fig. C.12 Model scale Source Box grid independence on velocity.

Moreover, the GCI [140] was evaluated for both quantities obtaining the results in table C.2. The convergence asymptotic range was checked in both cases with Eq. C.11 obtaining 1.003 and 1.006 respectively, assuring that the solution has converged. Figures C.12 and C.13 show that the solution tend to the exact value as

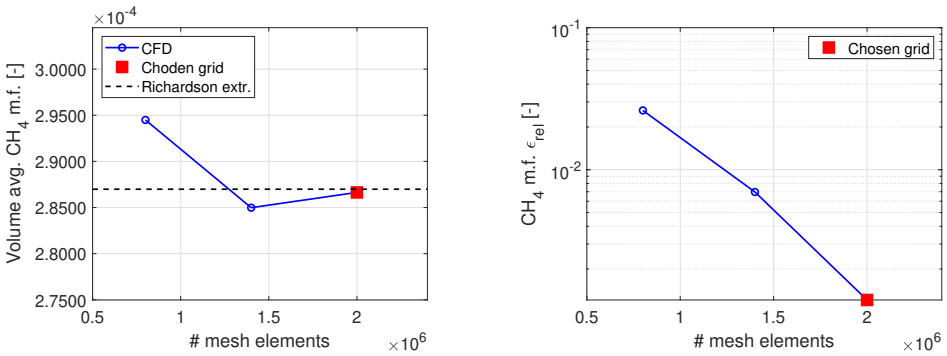

(a) Average CH_4 m.f. variation in the domain volume for different mesh sizes.

(b) Relative error (ε_{rel}) of the CH_4 m.f. with respect to the Richardson extrapolation.

Fig. C.13 Model scale Source Box grid independence.

	GCI12	GCI23
Avg. velocity	$2.55{\cdot}10^{-4}$	$4 \cdot 10^{-3}$
Avg CH_4 m.f.	$1.5 \cdot 10^{-3}$	$8.8 \cdot 10^{-3}$

Table C.2 Model scale SB GCI values.

the mesh is refined and that the errors decrease up to $2 \cdot 10^{-4}$ and 0.001 respectively for the velocity and CH_4 m.f. This suggested that the mesh consisting of $\sim 2 \cdot 10^6$ elements was enough refined for the calculations, as confirmed also by the extremely low values of the GCI12, therefore, this one was chosen for the calculations. The same models, methods and convergence criteria of the full scale SB simulation were adopted.

C.2.5 Dispersion simulation mesh features (model scale)

An unstructured tetrahedral mesh was generated in the platform as can be seen in figure C.14(a). The *proximity and curvature* algorithm was employed for the mesh generation to accurately treat edges and curves. On the black-box faces a element size equal to 1 mm was imposed (see figure C.14(b)), while on the objects faces a 0.015 m size. Moreover, a refinement on the walls was generated through the *inflation layer* algorithm to model the boundary layer. The first cell dimension was set equal to $4 \cdot 10^{-5}$ m, and a maximum number of 8 layers was imposed with a growth rate of 1.2.

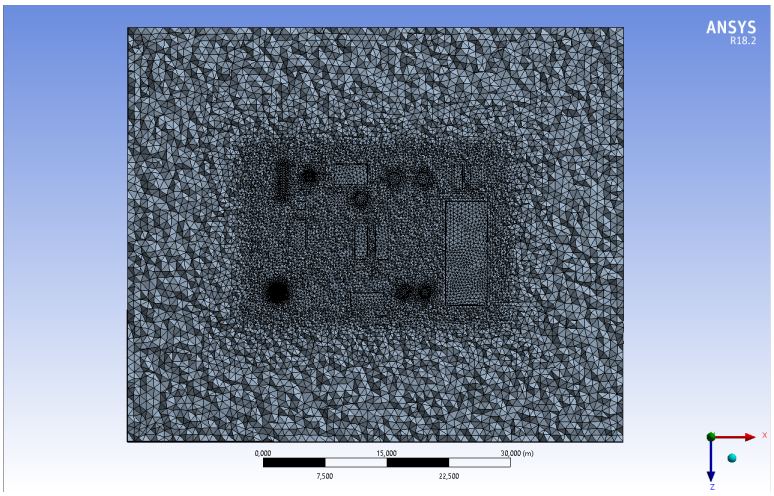

(a) Mesh overview on a xz section.

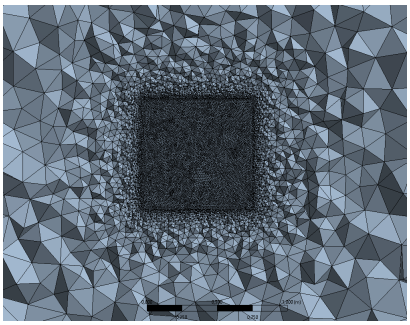

(b) Mesh refinement near the black-box.

Fig. C.14 SBAM dispersion model scale mesh.

For the grid convergence study of this simulation, the methodology of the Grid Convergence Index (GCI) [140] was adopted. For the study, three different meshes were used: mesh 1 consisting of $\sim 7.5 \cdot 10^6$ elements, mesh 2 of $\sim 6 \cdot 10^6$ elements and mesh 3 of $\sim 4.8 \cdot 10^6$ elements. The GCI was evaluated with respect to two quantities: the average velocity at the outlet boundary and the CH_4 mass in the domain. The obtained values are summarized in Table C.3.

	GCI12	GCI23
Avg. velocity	$6.14 \cdot 10^{-4}$	$3.1 \cdot 10^{-3}$
CH_4 mass	$9.3 \cdot 10^{-3}$	$2.52 \cdot 10^{-2}$

Table C.3 Model scale dispersion GCI values.

It has also been checked that the solution was in the asymptotic range of convergence by checking Eq. C.11. The following values were obtained respectively for the velocity and mass fraction cases: 1.002 and 0.9871. These values assured that the solution was well converged, hence, mesh 2 was used for the calculations since it was considered the optimal compromise between accuracy and computational cost.

Appendix D

Model scale case studies: additional results

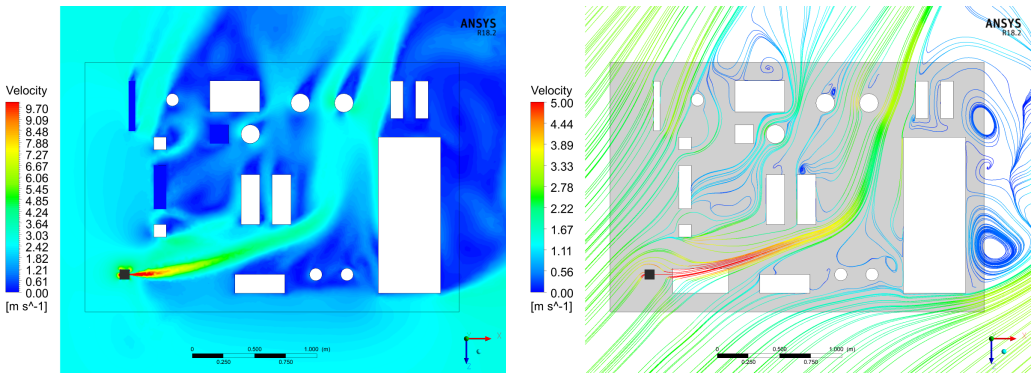

(a) Velocity magnitude contour plot.

(b) Velocity streamlines plot.

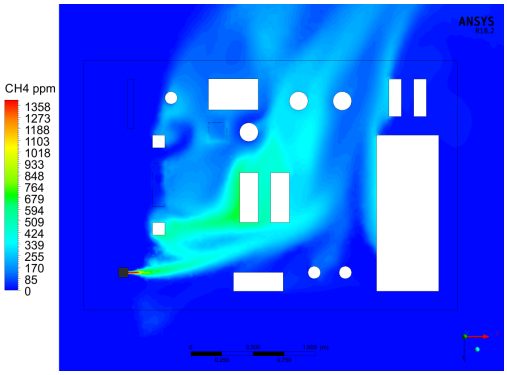

(c) CH_4 ppm contour plot.

Fig. D.1 CFD results in terms of velocity field and gas concentration plots related to cs#1.

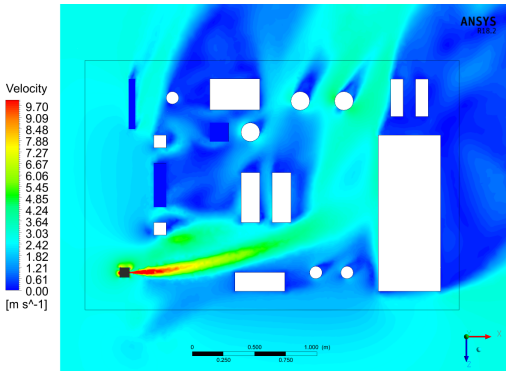

(a) Velocity magnitude contour plot.

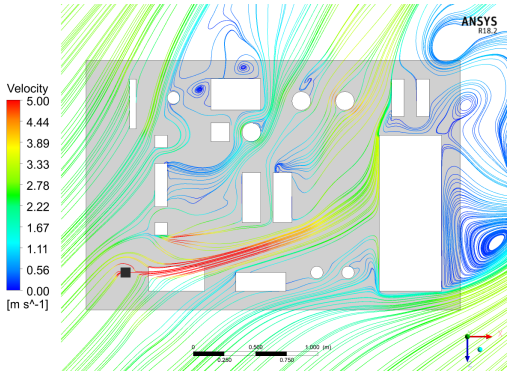

(b) Velocity streamlines plot.

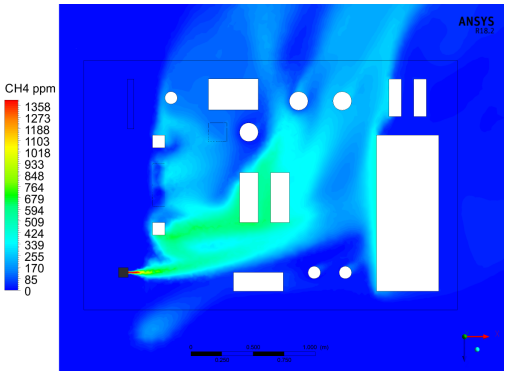

(c) CH_4 ppm contour plot.

Fig. D.2 CFD results in terms of velocity field and gas concentration plots related to cs#2.

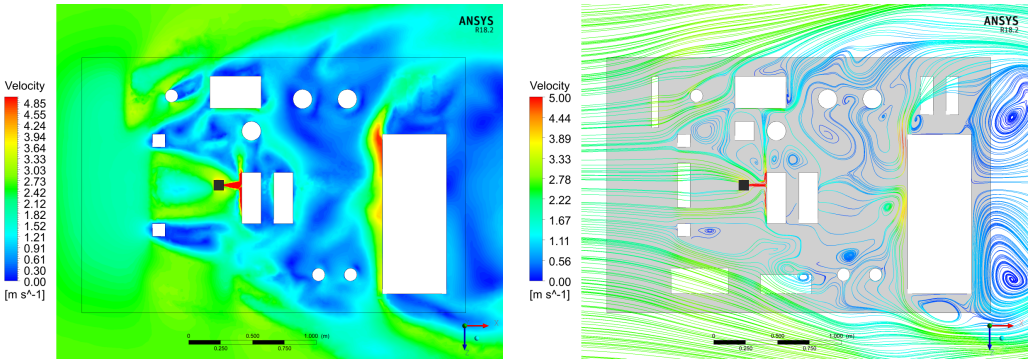

(a) Velocity magnitude contour plot.

(b) Velocity streamlines plot.

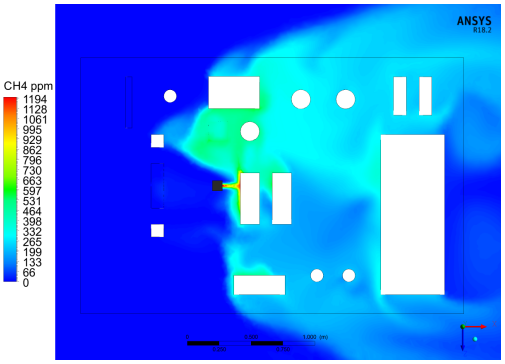

(c) CH_4 ppm contour plot.

Fig. D.3 CFD results in terms of velocity field and gas concentration plots related to cs#4.

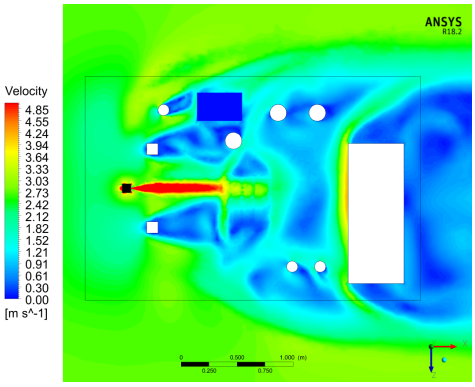

(a) Velocity magnitude contour plot.

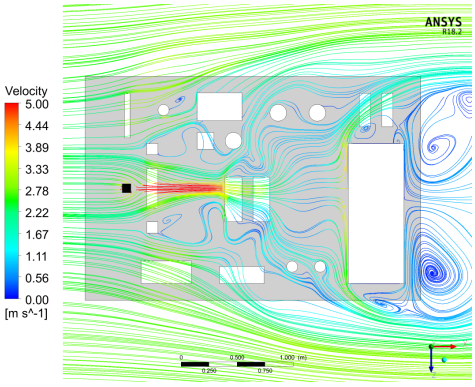

(b) Velocity streamlines plot.

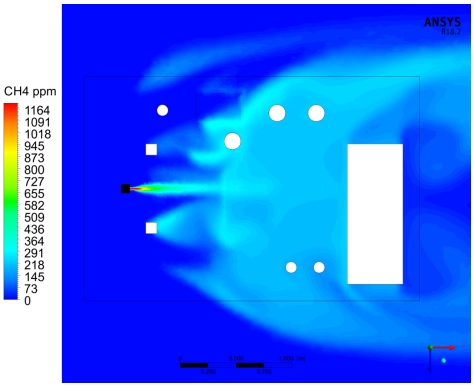

(c) CH_4 ppm contour plot.

Fig. D.4 CFD results in terms of velocity field and gas concentration plots related to cs#6.

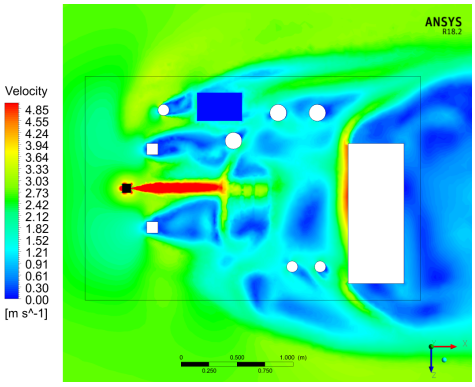

(a) Velocity magnitude contour plot.

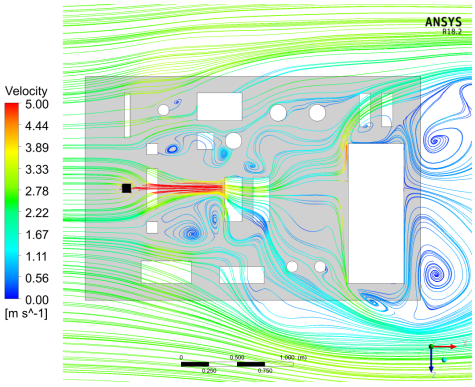

(b) Velocity streamlines plot.

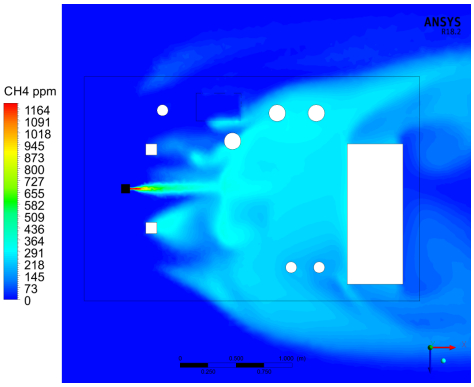

(c) CH_4 ppm contour plot.

Fig. D.5 CFD results in terms of velocity field and gas concentration plots related to cs#8.

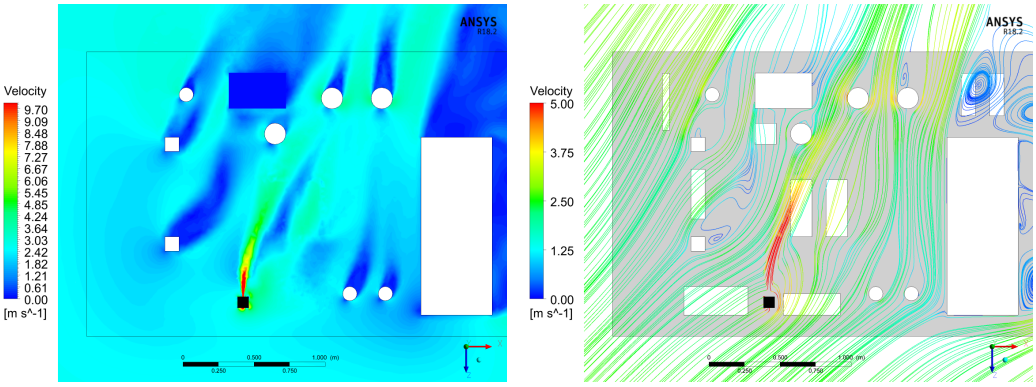

(a) Velocity magnitude contour plot.

(b) Velocity streamlines plot.

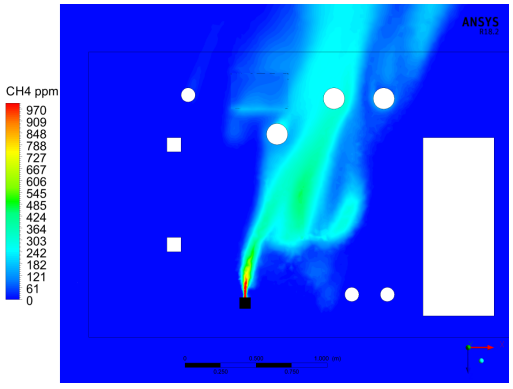

(c) CH_4 ppm contour plot.

Fig. D.6 CFD results in terms of velocity field and gas concentration plots related to cs#9.

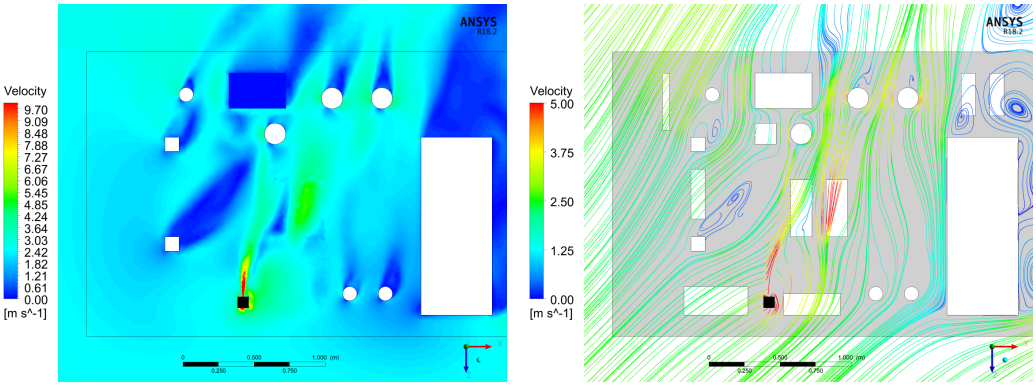

(a) Velocity magnitude contour plot.

(b) Velocity streamlines plot.

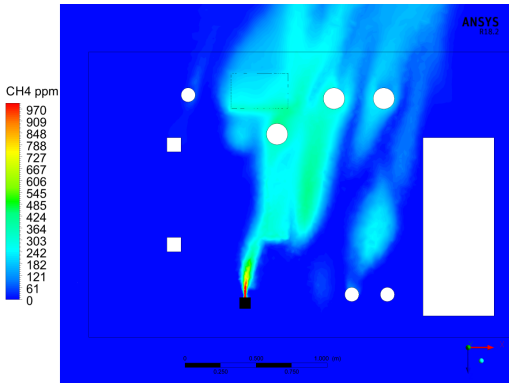

(c) CH_4 ppm contour plot.

Fig. D.7 CFD results in terms of velocity field and gas concentration plots related to cs#10.

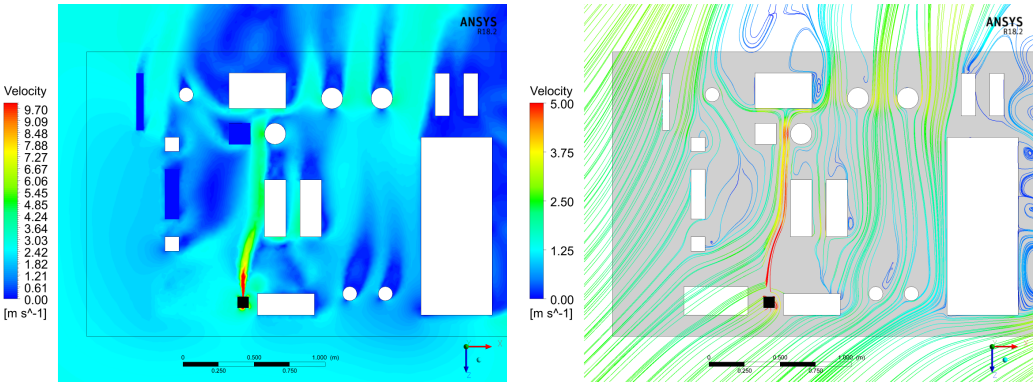

(a) Velocity magnitude contour plot.

(b) Velocity streamlines plot.

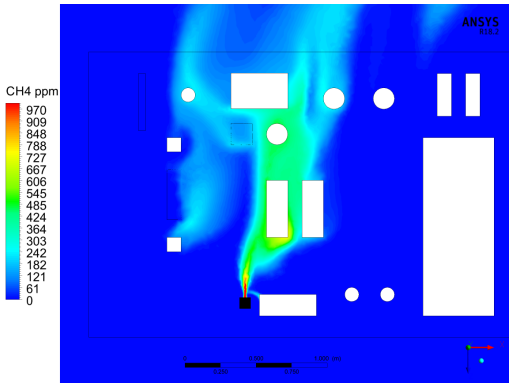

(c) CH_4 ppm contour plot.

Fig. D.8 CFD results in terms of velocity field and gas concentration plots related to cs#11.

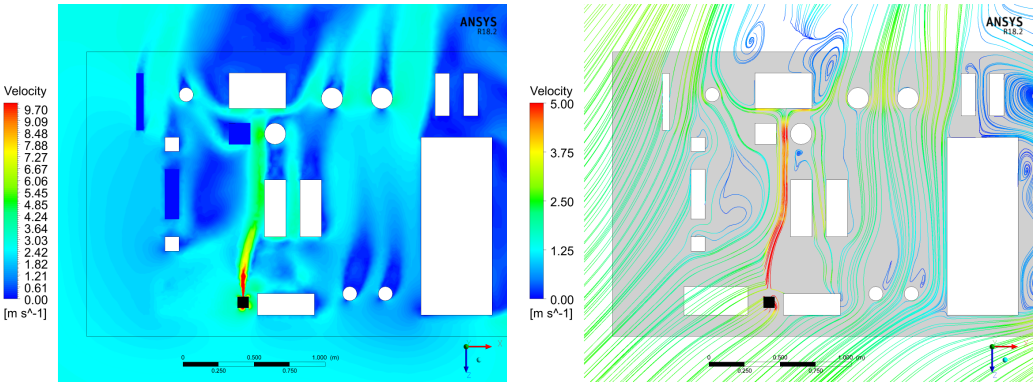

(a) Velocity magnitude contour plot.

(b) Velocity streamlines plot.

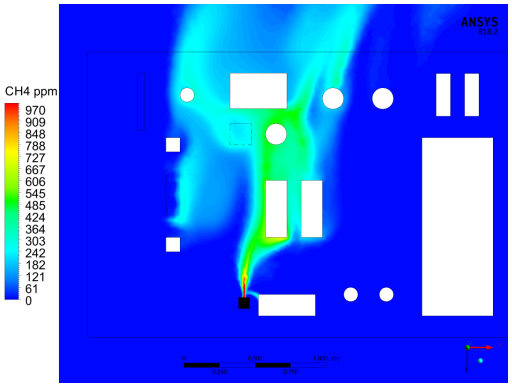

(c) CH_4 ppm contour plot.

Fig. D.9 CFD results in terms of velocity field and gas concentration plots related to cs#12.